Dissertation

submitted to the
Combined Faculties for the Natural Sciences and for Mathematics
of the Ruperto-Carola University of Heidelberg, Germany
for the degree of

Doctor of Natural Sciences

Put forward by
Dipl.-Phys. Andrea Kirsch
born in Berlin

Oral examination: July 9$^{\text{th}}$, 2014

Search for the neutrinoless double β-decay

in Gerda Phase I

using a Pulse Shape Discrimination technique

Referees:

Prof. Dr. Werner Hofmann
Prof. Dr. Norbert Herrmann

The GERmanium Detector Array (GERDA) experiment, located underground at the INFN Laboratori Nazionali del Gran Sasso (LNGS) in Italy, deploys high-purity germanium detectors to search for the neutrinoless double β-decay ($0\nu\beta\beta$) of ^{76}Ge. An observation of this lepton number violating process, which is expected by many extensions of the Standard Model, would not only generate a fundamental shift in our understanding of particle physics, but also unambiguously prove the neutrino to have a non-vanishing Majorana mass component.

A first phase of data recording lasted from November 2011 to May 2013 - resulting in a total exposure (defined as the product of detector mass and measurement time) of 21.6 kg·yr. Within this thesis a thorough study of this data with special emphasis on the development and scrutiny of an active background suppression technique by means of a signal shape analysis has been performed. Among several investigated multivariate approaches, particularly a selection algorithm based on an artificial neural network is found to yield the best performance; i.a. the background index close to the Q-value of the $0\nu\beta\beta$-decay could be suppressed by 45 % to $1 \cdot 10^{-2}$ cts/(keV·kg·yr), while still retaining a considerably high signal survival fraction of (83 ± 3) % leading to a significant improvement of the experimental sensitivity. The efficiency is derived by a simulation and further validated by substantiated consistency checks availing themselves of measurements taken with different calibration sources and physics data. No signal is observed and a new lower limit of $T^{0\nu}_{1/2}(90\,\%\,\mathrm{C.L.}) > 2.2 \cdot 10^{25}$ yr for the half-life of neutrinoless double β-decay of ^{76}Ge is established.

Suche nach dem neutrinolosen Doppelbeta-Zerfall in GERDA Phase I unter Verwendung einer Pulsformdiskriminierungs-Technik

Das GERmanium Detector Array (GERDA) Experiment, welches sich unterirdisch am INFN Laboratori Nazionali del Gran Sasso (LNGS) in Italien befindet, verwendet hochreine Germanium-Detektoren, um nach dem neutrinolosen Doppelbeta-Zerfall ($0\nu\beta\beta$) in ^{76}Ge zu suchen. Eine Beobachtung dieses leptonenzahl-verletzenden Prozesses, der in vielen Erweiterungen des Standard Modells vorhergesagt wird, würde nicht nur unser Verständnis bezüglich der Teilchenphysik fundamental wandeln, sondern auch den Nachweis einer Majorana-Natur der Neutrinos mit nicht verschwindender Massen-Komponente erbringen.

Die erste Phase der Messungen dauerte von November 2011 bis Mai 2013 an - mit einem resultierenden Produkt aus Detektormasse und Messzeit von $21,6$ kg·yr. Im Rahmen dieser Arbeit wurden die hierbei gewonnen Daten einer sorgfältigen Studie mit besonderem Augenmerk hinsichtlich der Entwicklung und Prüfung einer Technik zur aktiven Unterdrückung des Untergrundes, die sich auf der Pulsformanalyse des Detektorsignals begründet, unterzogen. Im Vergleich mit verschiedenen untersuchten multivariaten Ansätzen, erzielte dabei insbesondere ein Selektionsalgorithmus basierend auf einem künstlichen Neuronalen Netzwerk die besten Ergebnisse; u.a. konnte der Untergrundindex in der Nähe des Q-Wertes des $0\nu\beta\beta$-Zerfalls um 45 % auf $1 \cdot 10^{-2}$ cts/(keV·kg·yr), bei einer verbleibenden Signaleffizienz von (83 ± 3) %, reduziert und somit zu einer erheblichen Verbesserung der experimentellen Signifikanz beitragen werden. Die Effizienz wurde hierbei mittels einer Simulation berechnet und zusätzlich noch durch mehrere fundierte Konsistenztests, die sich auf Messungen mit verschiedenen Kalibrationsquellen sowie Physikdaten stützen, bestätigt. Es gibt keinen Hinweis auf ein Signal und die Berechnung einer neuen unteren Schranke für die Halbwertszeit des neutrinolosen Doppelbeta-Zerfalls von ^{76}Ge ergibt $T^{0\nu}_{1/2}(90\,\%\,\mathrm{C.L.}) > 2,2 \cdot 10^{25}$ yr.

Contents

1. Introduction

Ever since its postulation in the early 30s of the last century by W. PAULI [Pau30], the neutrino has attracted the interest of a whole field of research - the fundamental particle physics. However, due its small cross section almost three decades had to pass until a first experimental proof of existence could be accomplished [Rei53]. Thereby as object of past, present and certainly also future experimental as well as theoretical efforts, the neutrino is attributed a key part in even several respects. So, for example, a detailed scrutiny of their peculiar nature and properties would not only facilitate a validation of the so-called Standard Model (SM) on the different interaction processes, in which the neutrino initially has been included six-fold (electron, muon and tau neutrino plus their anitparticles) as massless particle, but also allow to introduce further extensions to the so far collected information.

Despite the successes that could be achieved within the commonly entrenched explanatory models that durably managed to interpret a wide variety of phenomena with remarkable precision, the neutrino always remained in the focus of experimental interest with respect to many still unresolved puzzles, namely as one famous example, the "Solar neutrino problem". With the detection of neutrinos originating from the internal fusion processes of the sun the theoretically derived and well established standard solar model (SSM) could be tested. Surprisingly, all experiments conducted on that topic observed a significant lack of detected electron neutrinos of about a factor of three below the expectations. This discrepancy impressively supported hypothetical assumptions on neutrino flavor transitions, also known as neutrino flavour oscillations previously concluded in [Pon67][Gri69], which have been in the past systematically confirmed by a series of experimental studies on neutrinos from the sun, the atmosphere and reactors as well as accelerators [Fuk01][Ahm02][Ara06][Ard06] [Kim08][Wan09][Mic06]. Since such a mixing of the neutrino's weak interacting states can - by theory - only occur, if the rest masses do indeed differ from each other, the observed oscillations imply, in terms of the neutrino itself, non-vanishing rest masses that are distinct from zero.

But this discovery reaches well beyond only solar neutrinos. When regarding cosmic scales on the one hand, it impacts the gravitational theory about the evolution of the universe, whereas on a subatomic level also the so far very substantial and robust SM of elementary particle physics is crucially affected. Thus a quantitative specification of the neutrino mass spectrum is assigned a high importance to the way for new, advanced theories beyond the known Standard Model. Eventhough the gathered results about neutrino flavor oscillations have provided values of the squared mass differences Δm^2 of the neutrino mass eigenstates, they do neither contain any information on the absolute scale nor the order of the different masses. In order to access the absolute mass scale, researchers instead have to revert to alternative (in-)direct, more or less model-dependend approaches such as cosmological considerations based

on Cosmic Microwave Background (CMB) and Large Scale Structures (LSS) in the Universe, supernovae observations or particle interactions involving either neutrinos or antineutrinos, like the single β-decay. Apparently for several isotopes this single β-decay mode is energetically forbidden but the simultaneous occurrence of two β-decays ($2\nu\beta\beta$) is allowed. Up to the present day this process has been observed in 11 nuclei with corresponding half-lives in the range of $10^{18} - 10^{24}$ yr [Bar11].

For the special case of the neutrinoless double β-decay ($0\nu\beta\beta$), predicted in several theoretical treatments [Bil12][Ver12][Rod11][Gom12], even additional particulars on a possible "Majorana" mass component of the neutrino can be attained, while still allowing for an indirect measurement on the absolute mass of neutrinos to cast light on the hierarchy of neutrino masses. In such a process, lepton number is no longer conserved anymore but instead violated by two units. Hence an evidence for that extremely rare process would require physics in contrast with the Standard Model, with far reaching repercussions. Consequently, a large interest to search for the hypothetical $0\nu\beta\beta$-decay engendered and a still growing number of experimental programs based on different detection techniques and isotopes are currently taking measurements or will start soon collecting first data.

The experimental signature of the neutrinoless double β process can be detected as a monoenergetic peak at the Q-value of the decay. Prior to the latest results of the GERDA experiment published in [Ago13a] and in this thesis, the two most sensitive experiments performed with the candidate nucleus ^{76}Ge ($Z = 32$), that undergoes a second order reaction into ^{76}Se ($Z = 34$) with an endpoint energy of $Q_{\beta\beta} = 2039.061 \pm 0.007$ keV [Mou10], were provided by the Heidelberg-Moscow (HdM) [Kla01] and the International Germanium Experiment (IGEX) [Aal02][Aal04]. Both of them found no indication for the $0\nu\beta\beta$-decay, yielding lower $90\,\%$ confidence limits on the half-life for the neutrinoless process in germanium of $T^{0\nu} > 1.9 \cdot 10^{25}$ yr and $T^{0\nu} > 1.6 \cdot 10^{25}$ yr, respectively. In 2004 a subgroup of the HdM Collaboration published a claim to have seen evidence of (28.75 ± 6.86) $0\nu\beta\beta$ events converting to a half-life of $T^{0\nu} = 1.19^{+0.37}_{-0.23} \cdot 10^{25}$ yr and - under the assumption of light neutrino exchange - a corresponding effective Majorana electron neutrino mass range $|m_{\beta\beta}| = 0.24 - 0.58$ eV with a central value at 0.44 eV [Kla04]. The uncertainty on the mass interval arises hereby predominantly from estimated inaccuracies in the calculations of the nuclear matrix elements (NME). This result has been even strengthened in a later work by an additional pulse shape analysis of the detector signals [Kla06]. Several inconsistencies associated to the latter publication have been pointed out in [Sch13] though.

Until recently, despite several experimental attempts, the claimed evidence for the neutrinoless double β-decay from [Kla04] has not been unambiguously scrutinized. The currently most sensitive experiments on the trail to either validate or falsify the discovery by parts of HdM are KamLAND-Zen [Gan13] and the Enriched Xenon Observatory EXO-200 [Aug12], both of them using ^{136}Xe as $\beta\beta$ emitter, and the GERDA experiment [Ack13] employing ^{76}Ge. Taking into account that strongly error-proned NME calculations are necessary to relate the different isotopes, the two

former setups availing themselves of ^{136}Xe can only allow for an examination of the claim on a model dependent basis. As GERDA instead uses the same isotope and deploys also mostly the very same detectors from HdM and IGEX, this particular experiment represents the only endeavour of relevant sensitivity performance able to perform a direct, model independent test.

The GERDA experiment is located at the Laboratori Nazionali del Gran Sasso (LNGS) of INFN in Italy and operates high-purity germanium (HPGe) diodes of semi-coaxial as well as Broad Energy Germanium (BEGe) type made from isotopically modified material with ^{76}Ge being enriched to a percentage of $\approx 86\,\%$. Each detector is mounted in a low-mass copper support and submersed inside a cryostat containing $64\,\mathrm{m}^3$ cryogenic liquid argon (LAr), serving as both coolant medium for the enriched germanium crystals and shield against external background from γ radiation. Finally the shielding is complemented by an additional $3\,\mathrm{m}$ of ultra-pure water that is instrumented with photo multipliers to detect the Cerenkov light generated by muons traversing the setup. The measurements are planned to proceed in several steps with consecutively increasing $\beta\beta$ emitter masses and more and more stringent demands on the background level. In a first period of data taking continuing from November 2011 to May 2013 denoted as "Phase I", a total exposure of $21.6\,\mathrm{kg \cdot yr}$ has been collected. Simultaneously, the background level has been determined to amount at roughly $1 \cdot 10^{-2}\,\mathrm{keV \cdot kg \cdot yr}$, which marks an order of magnitude improvement if compared to predecessor experiments. Both properties combined, allow to make a statistically conclusive statement of high probability on the assertion for the observation of the $0\nu\beta\beta$-decay in [Kla04]. The obtained result has been lately published in [Ago13a] and will be discussed in detail within this thesis.

Generally, the sensitivity of a counting experiment searching for the neutrinoless double β-decay can be drastically improved by an effective suppression of the obstructive background originating from close-by or rather distant radiation sources, provided that the signal efficiency still remains comparably high. This can, amongst other methods, be achieved by means of a carefully chosen experimental site located deep underground, massive shielding of the detectors from the environment or active muon- and LAr-veto techniques. Interestingly, it has been proven in the past, that a thoughtfull data selection in addition with an enhanced pulse shape discrimination (PSD) of the detector signals also provides a powerfull tool to significantly reduce the background level. The working principle is thereby based on the explicit distinction of events that deposit the entire released energy within a small volume $\approx 1\,\mathrm{mm}$ (= single site event, SSE), as known to be the case for the $0\nu\beta\beta$-decay, from those where the ionization takes place in several spatially well separated interaction points (= multi site event, MSE). Albeit being aware of the pivotal importance of reliable event selection tools being implemented in the analysis chain, within the GERDA experiment until lately no working pulse shape discrimination technique has been on hand for the semi-coaxial detector type, which does - considering the combined exposure of $19.2\,\mathrm{kg \cdot yr}$ - in fact constitute the major contribution to the Phase I data (the residual part of only $2.4\,\mathrm{kg \cdot yr}$ is attributed to the diodes of BEGe geometry).

Therefore the development and subsequent validation of an enhanced discrimination algorithm - called *Artificial Neural Network* (ANN) - with special regard to the adaption on the semi-coaxial HPGe detector type is the main goal of the work presented in this thesis. To avoid biases in the event selection for the $0\nu\beta\beta$-scrutiny, a blind analysis has been performed. The universally promising successes when being applied to GERDA data obtained during Phase I or from an enhanced simulation approach in the context of systematic consistency checks, which all confirmed the robustness and plausibility of the multivariate classification method, made the studies outlined in the framework of the current thesis the preferred and official PSD algorithm used for the final $0\nu\beta\beta$-analysis of the experiment. It will be ultimately shown, that the deployment of the neural network based pattern recognition program on the experimental measurement indeed permitted to perspicuously improve the sensitivity of GERDA setup.

Considering the neutrino to have such an important impact on our knowledge of particle physics that reaches far beyond the Standard Model, the first chapter 2 is exclusively dedicated to provide a brief overview of past and recent progresses in neutrino physics with special emphasis on searches for neutrinoless double beta-decay along with the therefore necessary experimental requirements.

In a next step the general concept of the GERDA experiment, as the detection principle of a semiconductor in combination with the interaction processes of particles in matter up to the final detector response to radiation as well as the time course of the commissioning period and the Phase I data taking are addressed in chapter 3.

Chapter 4 focusses on the multivariate ANN recognition technique, its explicit adaption to the data acquisition (DAQ) output and the training/testing with experimental charge traces. The performance improvements achieved with this approach are evaluated on the basis of regularly obtained ^{228}Th calibration measurements for the time resolved monitoring of the energy scale along with the Phase I physics runs.

Subsequently, in chapter 5 detailed validation test on the $0\nu\beta\beta$-signal efficiency of the pulse shape algorithm using experimental data only are prosecuted with focus on different aspects, such as a possible energy or volume dependency effects. In particular, $2\nu\beta\beta$ from the neutrino-accompanied decay mode and multi Compton scattered event are used as proxy for SSEs and MSEs. Additionally classifier response distribution of different event classes (signal- or background-like) as well as special calibration set taken with a ^{56}Co source are investigated and discussed.

Further efforts related to dedicated Monte Carlo + FEM simulations concerning the energy depositions inside the active volume along with the corresponding signal induced on the detector read-out electrode, are described in the following chapter 6.

The second last chapter 7 presents the extracted results on the half-life $T_{1/2}^{0\nu}$ on the neutrinoless double β-decay of ^{76}Ge and its implication on the claimed discovery in [Kla04] particularly with respect to the substantial contribution from the pattern recognition analysis developed throughout this work before the findings of the thesis are finally recapitulated in chapter 8.

2. Neutrino Physics

The era of neutrino physics was already heralded far back in the year 1896 and has its seeds in the accidental discovery of the natural radioactivity by A.H. BECQUEREL [Bec96]. At this time he observed the so-called β-decay, where due to the electroweak interaction a neutron is converted into a proton under emanation of an electron. However, under the assumption of such a two-body-decay, subsequent experiments conducted by J. CHADWICK resulted in a clear conflict to several laws of conservation. Instead of the expected discrete energy of the emanated electron, the β-decay showed a continuous energy spectrum [Cha14]. Hence the energy as well as the momentum were not preserved. The second, not less profound inconsistency arises from the spin conservation of the decaying atomic nuclei, which was also violated.

In order to solve this problem W. PAULI came upon an - as he said himself - "desperate remedy" and postulated an additional, third particle participating in the now three-body-decay with a small but not necessarily vanishing rest mass [Pau30]. Such a hypothetical particle could carry the missing energy (or momentum) and should, to also provide for the conservation of charge and angular momentum, have no electrical charge and be of spin $\frac{1}{2}$. The neutrino was born! Based on Pauli's idea four years later, in 1934, the italian nuclear physicist E. FERMI gave the neutrino a theoretical background by formulating a first mathematical framework of the β-decay that allowed an explanation of the observed data and has endured with only little modification into the present [Fer34]. In his theory a new weak force, so called because it was remarkably weaker than the electromagnetic force, transfers a neutron into a proton and creates instantly an electron and an anti-neutrino:

$$n \rightarrow p + e^- + \overline{\nu} \,. \tag{2.1}$$

But due to the small cross section of the neutrino not less than 29 years had to pass until a first experimental proof could be accomplished. In their Nobel Prize rewarded Savannah River experiment F. REINES and C.L. COWAN availed themselves of the induced inverse β-process, consisting of the capture of an anti-neutrino by a nucleus with an instant emission of a positron $p + \overline{\nu} \rightarrow n + e^+$ [Rei53].

particle	flavour			electr. charge	colour	spin
	1	2	3			
quarks	u	c	t	+2/3	r,b,g	1/2
	d	s	b	-1/3		
leptons	e	μ	τ	-1	-	1/2
	ν_{e}	ν_μ	ν_τ	0		

Table 2.1: Fundamental particles of the Standard Model: quarks ('up' and 'down', 'charm' and 'strange', 'top' and 'bottom') + leptons ('electron', 'muon', 'tau' and their corresponding neutrinos).

In the past tremendous efforts have been taken to draw more and more secrets from the mysterious nature of the neutrino. The following chapter is dedicated to give a brief summary of the experimental approaches and the thereby collected insight into this elusive particle we still know so little about. There are several excellent textbooks on particle physics, for more general reviews the reader is therefore referred to the literature [Gri09][Pov08].

2.1   The Standard Model of particle physics

Since its development in the early 1970s the Standard Model managed to successfully explain a wide variety of phenomena in the huge field of particle physics by laying down a simple rule: everything in the universe - or in the most general sense - matter is made from a few basic building blocks of fundamental particles, governed by four fundamental forces. A visual overview of the Standard Model is given in table 2.1 by arranging the fundamental particles according to their electrical charge Q (horizontal).

As fundamental particles 12 fermions could be identified, all of them with spin $\frac{1}{2}$, which occur in two basic types called *quarks* and *leptons*. Both groups are of the same size with six particles each, where two particles are affined in three pairs depending on their masses (vertical), also known as *flavours* or *generations*, respectively. In any case, the lightest and most stable particles are assigned to the first generation. Apart from that, the second and third generation are made up of the heavier and less stable particles. In addition, quarks also come in three different *colours* and only combine in such ways as to form colourless objects.

The interaction between different fundamental particles is mediated by four fundamental forces, each resulting from the exchange of a corresponding boson - the force carrier particle. The *electromagnetic force* is carried by the photon γ, the *strong force* is exchanged by the gluon g, and the $W^{\pm}$ and Z^0 bosons are responsible for the *weak force*. Eventhough based on the very same principle, the fundamental forces exhibit completely disparate properties as e.g. coupling constants and ranges. However, the fourth fundamental force, *gravity* with its pursuant force-carrying particle, the graviton, that applies for all massive particles, could not yet be implemented into the Standard Model.

2.1.1   The concept of antiparticles

In addition the Standard Model assigns every particle an appendant *antiparticle*, with the same mass but opposite electric charge. The existence of antimatter was first theoretically demanded by quantum mechanics and its relativistic generalization[1]

---

[1]Schrödinger's equation describes particles in nonrelativistic quantum mechanics; in the relativistic extension, particles of spin 0 are expressed by the *Klein-Gordon equation*, particles of spin $\frac{1}{2}$ by the *Dirac equation* and particles of spin 1 by the *Poca equation*.

of the *Schrödinger equation*, resulting in the *Dirac equation* that acts on the four component wave function $\psi = (\psi_1, \psi_2, \psi_3, \psi_4)$ [Dir28]

$$(-i\hbar c\,\boldsymbol{\gamma} \cdot \nabla + \gamma^0 mc^2)\psi(\mathbf{r}, t) = i\hbar\frac{\partial}{\partial t}\psi(\mathbf{r}, t) \; , \tag{2.2}$$

where $\boldsymbol{\gamma} = \gamma^k$ for $k = 1, 2, 3$ and γ^0 denote coefficients, which - when utilizing the Minkowski metric g^{lm} - have to obey the condition

$$\{\gamma^l, \gamma^m\} = \gamma^l\gamma^m + \gamma^m\gamma^l = 2g^{lm} = \begin{cases} 2 & \text{for } l = m = 0 \\ -2 & \text{for } l = m = 1, 2, 3 \\ 0 & \text{for } l \neq m \end{cases} . \tag{2.3}$$

It turns out that this can be fulfilled for matrices with a minimum size of 4×4 (here given in the standard "Bjorken and Drell" convention [Bjo64]):

$$\gamma^0 = \begin{pmatrix} 1 & 0 \\ 0 & -1 \end{pmatrix} \; , \qquad \gamma^k = \begin{pmatrix} 0 & \sigma^k \\ -\sigma^k & 0 \end{pmatrix} \tag{2.4}$$

with the 2×2 Pauli spin matrices indicated by σ^k

$$\sigma^1 = \begin{pmatrix} 0 & 1 \\ 1 & 0 \end{pmatrix} \; , \qquad \sigma^2 = \begin{pmatrix} 0 & -i \\ i & 0 \end{pmatrix} \; , \qquad \sigma^3 = \begin{pmatrix} 1 & 0 \\ 0 & -1 \end{pmatrix} . \tag{2.5}$$

The relativistic quantum mechanical wave equation provides not only a description of elementary spin-$\frac{1}{2}$ particles but also holds a troubling feature: for every positive-energy solution it admits a second solution with negative energy. This can be demonstrated by using the ansatz

$$\psi_{\mp}(\mathbf{r}, t) = u\,\mathrm{e}^{\pm i(\mathbf{pr} - Et)/\hbar} = \begin{pmatrix} u_A \\ u_B \end{pmatrix} \mathrm{e}^{\pm i(\mathbf{pr} - Et)/\hbar} \tag{2.6}$$

in form of plane waves, where u signifies a 4-dimensional spinor composed of two two-component vectors u_A and u_B. Therefore, after applying the quantum prescription $-i\hbar\nabla \to \mathbf{p}$ and $i\hbar\frac{\partial}{\partial t} \to E$ equation 2.2 becomes

$$(c\boldsymbol{\gamma} \cdot \mathbf{p} + \gamma^0 mc^2)u = Eu \tag{2.7}$$

yielding the two equations

$$u_A = \frac{c\boldsymbol{\sigma} \cdot \mathbf{p}}{E - mc^2}u_B \; , \qquad u_B = \frac{c\boldsymbol{\sigma} \cdot \mathbf{p}}{E + mc^2}u_A \; . \tag{2.8}$$

Substituting the second of these into the first and vice versa gives

$$(E - mc^2)(E + mc^2)u_{A,B} - c^2(\boldsymbol{\sigma} \cdot \mathbf{p})^2 u_{A,B} = 0 \; . \tag{2.9}$$

Since $(\boldsymbol{\sigma} \cdot \mathbf{p})^2 = (\boldsymbol{\sigma} \cdot \mathbf{p})(\boldsymbol{\sigma} \cdot \mathbf{p}) = \mathbf{p} \cdot \mathbf{p} + i\boldsymbol{\sigma} \cdot (\mathbf{p} \times \mathbf{p}) = p^2$ and $u_{A,B} \neq 0$, the equation 2.9 is only satisfied for the eigenvalues

$$E = \pm\sqrt{p^2c^2 + m^2c^4} \; . \tag{2.10}$$

This circumstance of negative energies has been interpreted as positive-energy states of a *different* particle with inverted time dependence $t \to -t$, the antiparticle. Such a symmetry operation or *charge conjugation C*, affects the sign of all quantum charges, including e.g. the electrical charge, the lepton number or the flavour charges. In contrast, the mass, spin, energy or momentum of a particle remain unchanged. Using the normalization factor $N = \sqrt{(E + mc^2)/c}$ the four canonical solutions of the Dirac equation are finalized to

$$u^{(1)} = N \begin{pmatrix} 1 \\ 0 \\ \frac{p_z c}{E+mc^2} \\ \frac{(p_x+ip_y)c}{E+mc^2} \end{pmatrix} , \qquad u^{(2)} = N \begin{pmatrix} 0 \\ 1 \\ \frac{(p_x-ip_y)c}{E+mc^2} \\ \frac{-p_z c}{E+mc^2} \end{pmatrix} \tag{2.11}$$

and

$$v^{(1)} = N \begin{pmatrix} \frac{(p_x-ip_y)c}{E+mc^2} \\ \frac{-p_z c}{E+mc^2} \\ 0 \\ 1 \end{pmatrix} , \qquad v^{(2)} = -N \begin{pmatrix} \frac{p_z c}{E+mc^2} \\ \frac{(p_x+ip_y)c}{E+mc^2} \\ 1 \\ 0 \end{pmatrix} . \tag{2.12}$$

It is customary to use the letter u for particles and v for antiparticles, respectively. In the late 1931, a first evidence of antimatter could be supplied with the discovery of the positron e^+ as the antiparticle of the electron [And33].

2.1.2   The neutrino and the weak interaction

For they do not carry electric charge or colour, neutrinos interact with quarks and leptons through the weak force only, which is either described by the charged-currend (CC) interaction from $W^\pm$ boson exchange or by the neutral-current (NC) inter-action evoked from the Z^0 boson. All phenomena based on both weak interaction modes are ultimately ascribable to the three elementary processes depicted in figure 2.1. Please notice that for these scenarios time flows *horizontally* to the right.

The diagram 2.1a) for purely leptonic charged current interaction then reads: A negative lepton l^- (either e^-, μ^- or τ^-) converts under emission of a W^- (or absorption of a W^+) into the corresponding neutrino ν_l of the same generation. In
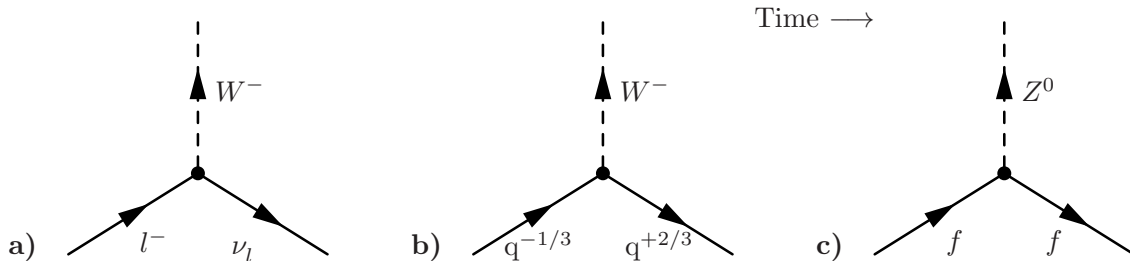

Figure 2.1: The three basic types of weakly interaction: **a)** purely leptonic charged current vertex, **b)** non-leptonic charged current vertex and **c)** neutral current vertex for fermions.

all reactions the weak force therefore underlies another conservation law: at each interaction vertex the creation or annihilation of a lepton is always associated with the creation or annihilation of an antilepton of the same flavour and one can write

$$L_l = N(l) - N(\bar{l}) + N(\nu_l) - N(\overline{\nu_l}) = \text{const.} , \tag{2.13}$$

where $l = e$, μ or τ and the L_l's are called *lepton family numbers*. However, recent experiments indicate a cross-generational mixing among the leptons with the consequence that only the sum $L = L_e + L_\mu + L_\tau$ referred to as the *lepton number* is conserved as a whole. A closer look at this effect known as neutrino oscillation and its impact on neutrino physics will be postponed to the next section 2.2.

The same interpretation schema also applies to non-leptonic processes as for the fundamental charged vertex in figure 2.1b) with a d, s or b quark of charge $-\frac{1}{3}$ that transforms into a u, c or t quark of charge $+\frac{2}{3}$, respectively. Again the difference of charge and mass is mediated by an outgoing W^- (or incoming W^+). In any case both quarks do carry the same colour, but in conformity with the first example of purely leptonic reactions, the coupling to $W^\pm$ does not have to take place strictly within a particular flavour.[2] To solve this quandary N. CABIBBO suggested in 1963 an tentative explanation [Cab63], which was later extended to a third generation of quarks by M. KOBAYASHI and T. MASKAWA [Kob73]. According to the main idea, instead of

$$\begin{pmatrix} u \\ d \end{pmatrix} , \quad \begin{pmatrix} c \\ s \end{pmatrix} , \quad \begin{pmatrix} t \\ b \end{pmatrix} \tag{2.14}$$

the weak interaction couples to different pairs

$$\begin{pmatrix} u \\ d' \end{pmatrix} , \quad \begin{pmatrix} c \\ s' \end{pmatrix} , \quad \begin{pmatrix} t \\ b' \end{pmatrix} , \tag{2.15}$$

where d', s' and b' designate linear combinations that are related to the physical d, s and b quarks by the 3×3 *Cabibbo-Kobayashi-Maskawa* (CKM) *matrix*:

$$\begin{pmatrix} d' \\ s' \\ b' \end{pmatrix} = \begin{pmatrix} V_{ud} & V_{us} & V_{ub} \\ V_{cd} & V_{cs} & V_{cb} \\ V_{td} & V_{ts} & V_{tb} \end{pmatrix} \begin{pmatrix} d \\ s \\ b \end{pmatrix} . \tag{2.16}$$

The square of the magnitude of the matrix elements $|V_{qq'}|^2$ measures the transition probability from a quark q to a quark q'. Furthermore the CKM mixing matrix V_{CKM} containing the nine (complex) elements is unitary and can thus be reduced to only four parameters: the three mixing angles θ_{12}, θ_{23}, θ_{13} and one phase factor δ. Thereby one possible standard parameterization has become

$$V_{CKM} = \begin{pmatrix} c_{12}c_{13} & s_{12}c_{13} & s_{13}e^{-i\delta} \\ -s_{12}c_{23} - c_{12}s_{23}s_{13}e^{i\delta} & c_{12}c_{23} - s_{12}s_{23}s_{13}e^{i\delta} & s_{23}c_{13} \\ s_{12}s_{23} - c_{12}s_{23}s_{13}e^{i\delta} & -c_{12}c_{23} - s_{12}s_{23}s_{13}e^{i\delta} & c_{23}c_{13} \end{pmatrix} . \tag{2.17}$$

---

[2]Such a cross-generation, or strangeness-changing, coupling could be seen for example in the decay $\Lambda \to p + e + \overline{\nu}_e$ of the lambda, where a s quark is converted into a d quark.

Here c_{ij} and s_{ij} denote $\cos\theta_{ij}$ and $\sin\theta_{ij}$, respectively. Due to various experiments the matrix elements are well known and specified to the following magnitudes [Ber12]:

$$V_{\mathrm{CKM}} = \begin{pmatrix} 0.9743 & 0.2253 & 0.0035 \\ 0.2252 & 0.9734 & 0.0412 \\ 0.0087 & 0.0404 & 0.9991 \end{pmatrix} . \tag{2.18}$$

In weak decays quark transitions are predominantly observed within a family (thus the diagonal elements of the matrix V_{CKM} differ only by a few percent from unity), but also to a smaller degree between two different families, like from the second to the first generation (specified by the nonzero entries of V_{us} and V_{cd}). Whereas other transition probabilities, like from the third to the second - or even from the third to the first - generation, are already suppressed by several orders of magnitude and much more unlikely to happen.

Last but not least, figure 2.1c) shows the primitive vertex of the missing neutral current interaction, where f can be any quark or lepton and Z^0 mediates neither charge nor mass. More complicated processes can be constructed by combining several replications of this vertices to so-called Feynman diagrams. An example of such a Feynman graph is given in figure 2.2 for the already mentioned β-decay of the neutron $(n \rightarrow p + e^- + \overline{\nu}_{\mathrm{e}})$.
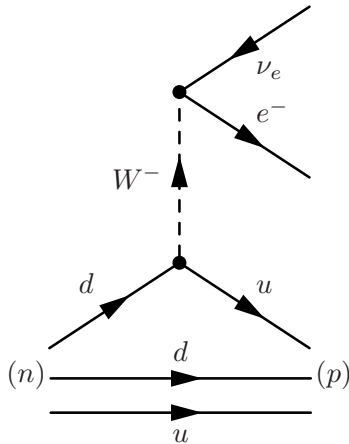
Figure 2.2: Feynman diagram for the β-decay of the neutron, which consists of two d and one u quarks. Mediated by the weak force, the d quark is converted into an u quark under the instant emission of an electron e^- and an anti-electron-neutrino $\overline{\nu}_{\mathrm{e}}$. The difference of charge is compensated by the charged weak boson W^-.

As a huge benefit, the usage of Feynman diagrams allows a quantum dynamical formulation of important physical quantities such as, in case of decays, lifetime or decay rate. According to Fermi's "Golden Rule" two specifications are needed for this calculation [Dir27][Fer50]: the *probability amplitude* $\mathcal{M}$ of the perturbation between the final and initial states, which was already introduced under the notation 'transition matrix element', and the *phase space* available. The latter contains all the kinematic information about the masses, momenta or energies of the particles and reflects the fact that a given process will as well depend on the number of possible final states. On the contrary, the amplitude is purely *dynamical* and can be mathematically evaluated by employing the *Feynman Rules* on the for the decay relevant Feynman graphs [Fey49].

One of the fundamental components of the Feynman Rules for weak interactions is, that each internal line of the diagram is associated with a factor

$$\mathcal{M} \propto \frac{-i(g_{\mu\nu} - q_\mu q_\nu/M^2 c^2)}{q^2 - M^2 c^2} \overset{q^2 \ll M^2 c^2}{=} \frac{ig_{\mu\nu}}{M^2 c^2} \qquad \text{(propagator for } W^\pm \text{ and } Z^0\text{)} \quad (2.19)$$

that contributes to the overall probability amplitude. Here M means either the mass M_W or M_Z of the two weak exchange bosons. The term $q_\mu \to i\hbar\partial_\mu$ specifies the momentum of the line in four-vector notation:

$$\partial_\mu \equiv \frac{\partial}{\partial x_\mu} \quad \text{with} \quad \partial_0 = \frac{1}{c}\frac{\partial}{\partial t}, \quad \partial_1 = \frac{\partial}{\partial x}, \quad \partial_2 = \frac{\partial}{\partial y} \quad \text{and} \quad \partial_3 = \frac{\partial}{\partial z}. \quad (2.20)$$

Since the momenta are usually much smaller than $M^2 c^2$, the corresponding terms can be neglected to further simplify the propagator factor in equation 2.19.

Furthermore the matrix element is also affected by the vertices of the diagram. A unique property of the weak interaction is parity (mirror symmetry) violation [Wu57], meaning that its reactions are not invariant under space inversion. Generally speaking, the operator of an interaction mediated by the exchange of a spin-1 particle shows a vector as well as an axial vector nature. In the special case of parity violating interactions it is observed that both, the vector part and the axial vector part, are present. The closer the strengths c_V and c_A of the two parts, the stronger the parity violation becomes, reaching its maximum when both contributions are of equal magnitude. So far experiments are consistent with charged current interactions occurring under the condition of maximum parity violation for $c_V = -c_A$, the so called *vector minus axial vector* $(V - A)$ coupling. Though, following Feynman's Rules, each vertex ploughs in another contribution to the probability amplitude, written as

$$\mathcal{M} \propto \frac{-ig_w}{2\sqrt{2}}\gamma^\mu(1 - \gamma^5) \qquad (W^\pm \text{ weak vertex factor}) \qquad (2.21)$$

By analogy to the coupling constants g_e from *quantum electrodynamics* (QED) and g_s from *quantum chromodynamics* (QCD), $g_w = \sqrt{4\pi\alpha_w}$ characterizes the 'weak coupling constant'.[3] The term $\gamma^\mu(1 - \gamma^5)$ with

$$\gamma^5 \equiv i\gamma^0\gamma^1\gamma^2\gamma^3 = \begin{pmatrix} 0 & 1 \\ 1 & 0 \end{pmatrix}, \qquad (2.22)$$

where γ^μ and $\gamma^\mu\gamma^5$ alone would express a purely vector coupling (as present in QED as well as QCD) or axial vector coupling, respectively, introduces the maximal

---

[3]The observed lifetime of the muon decay $\mu \to e^- + \nu_\mu + \overline{\nu}_e$ allowed a determination of the 'weak fine structure constant' to $\alpha_w = \frac{1}{29.5}$, which is nearly by a factor 5 larger than the 'electromagnetic fine structure' $\alpha = \frac{1}{137}$. The point-like and feeble appearance of the weak interaction can therefore not be caused due to the coupling but arises instead from the propagator term. In contrast to the gravitational, electromagnetic or strong force that are all conveyed by massless exchange bosons, the force-carriers of the weak interaction exhibit with 80 GeV/c^2 ($W^\pm$) and 91 GeV/c^2 (Z^0) heavy masses, so that for typical energies far below Mc^2 equation 2.19 becomes extremely small.

parity violating nature of the weak interaction. In case of non-leptonic transitions between quarks, the weak vertex contribution is corrected by the additional factor $|V_{qq'}|^2$ arising from the CKM matrix of equation 2.17 to also account the probability cross-generational coupling.

On the other side, the partly parity violating neutral current interaction is a combination of $V-A$ and $V+A$ coupling depending on the charge of the involved particles. The coupling of the Z^0 boson therefore changes to

$$\mathcal{M} \propto \frac{-ig_z}{2}\gamma^\mu(c_V^f - c_A^f\gamma^5) \qquad (Z^0 \text{ weak vertex factor}) \qquad (2.23)$$

In the Glashow-Weinberg-Salam (GWS) formulation [Gla61][Wei67][Sal68], in principle allowing for an unification of the electromagnetic and weak interactions into a single *electroweak force*, the values for the different coupling coefficients c_V^f and c_A^f could be affiliated to one fundamental parameter θ_w, namely the 'weak mixing angle' or 'Weinberg angle' (see table 2.2). The corresponding weak coupling constants g_z and g_w are interwined with the 'electromagnetic coupling constant' $g_e = e\sqrt{4\pi/\hbar c}$ and therefore with the electromagnetic force as follows:

$$g_w = \frac{g_e}{\sin\theta_w} \,, \qquad g_z = \frac{g_e}{\sin\theta_w\cos\theta_w} \,. \qquad (2.24)$$

Solely the neutrino represents an exception and interacts exclusively via $V-A$ coupling for both modes, CC and NC. As an example of a characteristic property that underlies changes under spatial inversion, the *helicity*

$$h = \frac{\boldsymbol{\sigma} \cdot \boldsymbol{p}}{|\boldsymbol{\sigma}| \cdot |\boldsymbol{p}|} = \pm 1 \qquad (2.25)$$

has been a convenient quantity measured by many experiments on parity violation. The scalar product of the axial vector $\boldsymbol{\sigma}$ (spin), which retains its orientation under mirror reflection, and the vector $\mathbf{p}$ (momentum), that instead reverses its direction, is a pseudoscalar and inverts the sign when the parity operator acts on it. In [Gol58] the corresponding helicity of the electron-neutrino ν_e has been measured from weak nuclear decays, yielding that neutrinos ν_L are always *left-handed* (with $h = -1$) and antineutrinos $\overline{\nu}_R$ *right-handed* (with $h = 1$). The indices L and R are supposed to indicate the handedness of the neutrino. As a consequence, in the Standard Model of particle Physics neutrinos are therefore considered to be massless.

particle	flavour			c_V^f	c_A^f
	1	2	3		
quarks	u	c	t	$\frac{1}{2} - \frac{4}{3}\sin^2\theta_w$	$\frac{1}{2}$
	d	s	b	$-\frac{1}{2} + \frac{2}{3}\sin^2\theta_w$	$-\frac{1}{2}$
leptons	e	μ	τ	$-\frac{1}{2} + 2\sin^2\theta_w$	$-\frac{1}{2}$
	ν_e	ν_μ	ν_τ	$\frac{1}{2}$	$\frac{1}{2}$

Table 2.2: Coupling strengths for the coefficients c_V^f and c_A^f according to the Glashow-Weinberg-Salam (GWS) theory. The parameter θ_w denotes the 'weak mixing angle' or 'Weinberg angle'.

2.2 Neutrino Oscillations

Even though the Standard Model allowed to successfully elucidate various aspects of particle physics, many important issues remained to be unresolved to this day. There is, for example, a large number of arbitrary empirical parameters that can not be derived by the model and had to be introduced ad hoc to delineate various unforeseen phenomena. Furthermore there is yet no sufficient answer to the question on 'how to calculate the masses of the fermions and quarks?' or even 'why there are exactly three generations of fermions (instead of four or even five...)?'. In spite of its many successes, the mere amount of controversial subjects lead to the assumption, that todays Standard Model is far from being a 'final' theory. And indeed, first definite evidence for physics *beyond* the Standard Model came up with the emergence of several experiments which indicated a "solar neutrino problem" as will be discussed in the subsequent pages.

2.2.1 The solar neutrino problem

Solar neutrinos: Stars derive their radiation energy from nuclear fusion, where four hydrogen atoms convert into one alpha particle (helium-4 nuclei of two protons and two neutrons). In heavy stars with higher temperature the route is dominated by the so-called Carbon-Nitrogen-Oxygen (CNO) cycle facilitating the process to be further catalyzed by these three elements. Whereas, in relatively light stars with lower temperature, like the sun, the mechanism is predominantly driven by the *pp*-chain, which - in simplified terms - takes place in the four following steps:

- At the beginning, a pair of protons conflates into a deuteron, composed by a proton and a neutron, under the simultaneous creation of a positron and an electron-neutrino. The other way around, the outgoing positron can optionally be replaced by an incoming electron.

$$p + p \rightarrow d + e^+ + \nu_e$$
$$p + p + e^- \rightarrow d + \nu_e \tag{2.26}$$
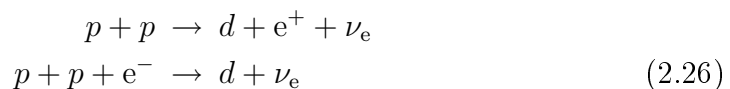
- Up next, the deuteron joins with another proton to create a helium-3 nucleus consisting of two protons and a neutron. The resulting energy is released in the form of a photon.

$$d + p \rightarrow {}^3\text{He} + \gamma \tag{2.27}$$

- In the third step, the helium-3 has three alternatives: it can pick up a free proton or another helium-3 nucleus to make an alpha particle. Also possible is a helium-3 that reacts with an alpha particle (produced in one of the previous reactions) generating beryllium-7.

$$
\begin{aligned}
{}^3\text{He} + p &\rightarrow \alpha + e^+ + \nu_e \\
{}^3\text{He} + {}^3\text{He} &\rightarrow \alpha + p + p \\
{}^3\text{He} + \alpha &\rightarrow {}^7\text{Be} + \gamma
\end{aligned} \tag{2.28}
$$
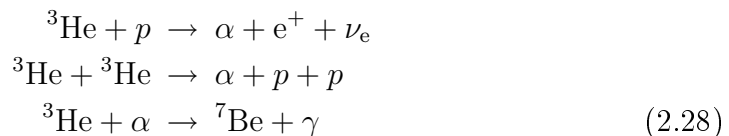
- Finally, the beryllium can either combine with an electron, creating lithium, which in turn absorbs a proton, decaying into two alpha particles, or else conjoin with a proton, making boron that instead changes to an excited state of beryllium-8 and decays from there (as well) into two alpha particles:

$$
\begin{aligned}
{}^{7}\text{Be} + \text{e}^{-} &\rightarrow {}^{7}\text{Li} + \nu_{\text{e}} \\
{}^{7}\text{Li} + p &\rightarrow \alpha + \alpha
\end{aligned}
\qquad
\begin{aligned}
{}^{7}\text{Be} + p &\rightarrow {}^{8}\text{B} + \gamma \\
{}^{8}\text{B} &\rightarrow {}^{8}\text{Be}^{*} + \text{e}^{+} + \nu_{\text{e}} \\
{}^{8}\text{Be}^{*} &\rightarrow \alpha + \alpha
\end{aligned}
\qquad (2.29)
$$
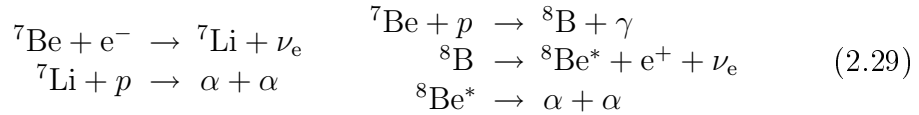
Whereas all other reaction products suffer interaction when working their way out from the core to the surface, the neutrino, due to its extremely small cross-section, endures its passage through the sun unaltered. Consequently, neutrinos bear an exciting opportunity and are the obvious probe to study the process in the center of the sun.
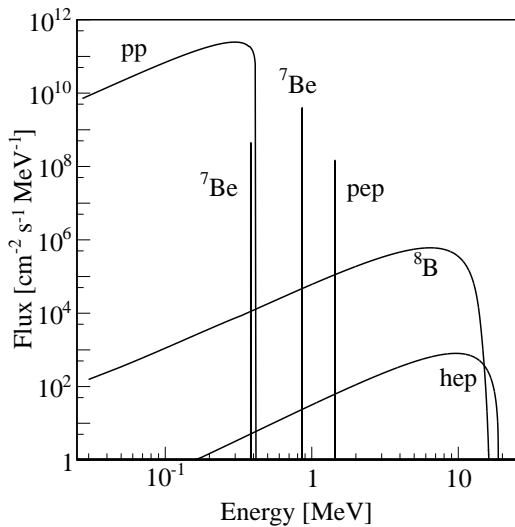
Figure 2.3: Solar neutrino energy spectrum from the *pp*-chain as derived by the BS05(AGS,OP) Standard Solar Model [Bah05]. The neutrino fluxes are presented for a distance of 1 AU corresponding to the distance between earth and sun. from the sun in units of $[\text{cm}^{-2}\text{s}^{-1}\text{MeV}^{-1}]$ for the continuous and $[\text{cm}^{-2}\text{s}^{-1}]$ for the mono-energetic neutrino sources. Further contributions from the CNO-cycle are not considered.

The solar neutrino spectrum predicted by the Solar Standard Model BS05(AGS, OP) [Bah05] for a given distance of the earth from the sun of one astronomical unit (AU) is plotted in figure 2.3. Thereby, as explained above, the *pp*-chain holds five reactions yielding neutrinos with the initial reaction 2.26 $(p + p \rightarrow d + \text{e}^{+} + \nu_{\text{e}})$ contributing by far the biggest share. Unfortunately, these neutrinos carry relatively low energies of a range up to $0.42\,\text{MeV}$, where most detectors of present and past neutrino experiments (apart from e.g. GALLEX [Ham99] or GNO [Alt00]) are insensitive to. Thus most experiments are compelled to resort to the far less abundant electron-neutrinos emerging from the boron-8 decay. So did the Davis experiment (Nobel Prize awarded in 2002) in the Homestake mine in South Dakota, consisting of a huge chlorine tank to measure the solar neutrinos [Dav68]. The detection principle was based on

$$
\nu_{\text{e}} + {}^{37}\text{Cl} \rightarrow {}^{37}\text{Ar} + e \ , \qquad (2.30)
$$

where a chlorine atom reacts with a neutrino and transmutes into argon. The collected number or argon atoms for a particular time interval then allows to draw

inferences about the solar neutrino flux. In contradiction to predictions from the Standard Solar Model (SSM) [Bah68] the experiment revealed a deficit by nearly a factor of three and marked the begin of the *solar neutrino problem*. Subsequently, the observation was also further strengthened by other neutrino experiments related to the flux of solar pp-neutrinos (e.g. GALLEX [Ham99], GNO [Alt00], SAGE [Abd99]).

2.2.2 Neutrino flavour mixing

The problem of the distinct missing neutrino flux was resolved by a simple explanation - often referred to as the famous *neutrino oscillation* - suggested by B. PONTECORVO [Pon67][Gri69]. In principle he proposed that the electron-neutrinos ν_e produced inside the sun can convert in flight into different generations (e.g. muon- or tau-neutrinos) after a characteristic length scale. So, analogous to quark mixing as already mentioned in section 2.1.2 also neutrino flavour changes can occur requiring in contrariety to the Standard Model that neutrinos do have non vanishing mass >0. Thus neutrinos interact in a given flavour eigenstate ν_l ($l = e$, μ, τ), but propagate as a linear superposition of mass eigenstates ν_i ($i = 1$, 2, 3) with masses m_i. Their interrelation is defined by the unitary Pontecorvo-Maki-Nakagawa-Sakata (PMNS) mixing matrix U_{li} [Mak62]

$$\nu_l = \sum_{i=1}^{3} U_{li}\nu_i \qquad \text{or} \qquad \begin{pmatrix} \nu_e \\ \nu_\mu \\ \nu_\tau \end{pmatrix} = \begin{pmatrix} U_{e1} & U_{e2} & U_{e3} \\ U_{\mu1} & U_{\mu2} & U_{\mu3} \\ U_{\tau1} & U_{\tau2} & U_{\tau3} \end{pmatrix} \begin{pmatrix} \nu_1 \\ \nu_2 \\ \nu_3 \end{pmatrix} . \qquad (2.31)$$

Hence the individual lepton numbers L_l are not preserved, while the full lepton number $L = L_e + L_\mu + L_\tau$ conservation is still valid. Similar to equation 2.17 for the quark sector of the Standard Model, the PMNS matrix can be expressed in terms of one phase factor (δ), often referred to as the "Dirac phase" responsible for CP violation and three mixing angles (θ_{12}, θ_{23}, θ_{13}):

$$U = \begin{pmatrix} c_{12}c_{13} & s_{12}c_{13} & s_{13}e^{-i\delta} \\ -s_{12}c_{23} - c_{12}s_{23}s_{13}e^{i\delta} & c_{12}c_{23} - s_{12}s_{23}s_{13}e^{i\delta} & s_{23}c_{13} \\ s_{12}s_{23} - c_{12}s_{23}s_{13}e^{i\delta} & -c_{12}c_{23} - s_{12}s_{23}s_{13}e^{i\delta} & c_{23}c_{13} \end{pmatrix} D \qquad (2.32)$$

with c_{ij}, s_{ij} as shortcuts for the sines $\sin\theta_{ij}$ and cosines $\cos\theta_{ij}$. But in difference to the mixing for quarks, which is rather small so that the CKM matrix almost represents a unity matrix and cross-generational transformation is largely suppressed, for leptons mixing takes place to a significant degree, where at least two of the mixing angles being quite large along with a smaller contribution from θ_{13} (see table 2.4). In addition the expression includes as well an diagonal phase matrix $D = \text{diag}(1, e^{i\alpha}, e^{i(\beta+\delta)})$ containing the two "Majorana phases" α and β. Note that these phases are, however, only physical, i.e. different from zero, if neutrinos act - in disagreement with the Standard Model - indeed as Majorana particles (further explanation can be found in section 2.3.1).

2.2.3   Implication on neutrino masses

Considering three (known) fermion families, the general formula for the oscillation probability $P(\nu_\alpha \rightarrow \nu_\beta)$ of a neutrino with flavour α and total energy E to transform into a different flavour β after traveling a certain distance $L = c \cdot t$, also called baseline, is defined by

$$P(\nu_\alpha \rightarrow \nu_\beta) = \sum_i \sum_j U_{\alpha i} U_{\alpha j}^* U_{\beta i}^* U_{\beta j} \exp\left(-i\frac{\Delta m_{ij}^2 L}{2E}\right) . \qquad (2.33)$$

Thereby the development in time has been derived by applying the Schrödinger equation, explicitly. Further the quantity $\Delta m_{ij}^2 = m_i^2 - m_j^2$ denotes the corresponding three-fold mass splittings (out of which only two are independent of each other though, since $\Delta m_{31}^2 = \Delta m_{21}^2 + \Delta m_{32}^2$). If also accounting for $\mathrm{Re}(U_{\alpha i} U_{\alpha j}^* U_{\beta i}^* U_{\beta j})$ being symmetric and $\mathrm{Im}(U_{\alpha i} U_{\alpha j}^* U_{\beta i}^* U_{\beta j})$ being antisymmetric under the interchange of i and j along with the unitary of U, the transition probability can be subsequently re-expressed as [Rod11][Cot07]

$$P(\nu_\alpha \rightarrow \nu_\beta) = \delta_{\alpha\beta} \; - \; 4\sum_{i>j} \mathrm{Re}\left(U_{\alpha i} U_{\alpha j}^* U_{\beta i}^* U_{\beta j}\right) \sin^2 \frac{\Delta m_{ij}^2 L}{4E}$$

$$+ \; 2\sum_{i>j} \mathrm{Im}\left(U_{\alpha i} U_{\alpha j}^* U_{\beta i}^* U_{\beta j}\right) \sin \frac{\Delta m_{ij}^2 L}{2E} . \qquad (2.34)$$

Moreover, when neutrinos propagate through matter additional issues can emerge due to elastic scattering via the charged current that only applies for the electron-neutrino. Depending on the energy of the beam and the density of the matter, the oscillation probability is therefore enhanced by the Mikheyev-Smirnov-Wolfenstein (MSW) effect [Wol78][Mik86].

In order for neutrino oscillations to take place, the masses have to be unequal to guarantee $\Delta m_{ij}^2 \neq 0$, or in other words at least one of them must be nonzero. Unfortunately, equations 2.33 or 2.34 also particularly exemplify that neutrino flavour transitions and hence all experiments based on them (some will be outlined in the next passage 2.2.4) are only sensitive to to the three mixing angles, the Dirac phase δ as well as the two independent mass *differences* (including their sign) and do neither contain information about the absolute mass scale nor the order (hierarchy) of the different masses. Thereby the oscillation data and the possible mass spectra/orderings are independent on whether neutrinos are Dirac or Majorana particles. Of special interest are, however, the following three conceivable constellations (of which the former two are depicted in figure 2.4) for the mass eigenstates:

- *normal* hierarchy (NH) with $m_1 < m_2 < m_3$

- *inverted* hierarchy (IH) with $m_3 < m_1 < m_2$

- *quasi-degeneracy* (QD) with $m_1 \simeq m_2 \simeq m_3$, i.e. the mass of the lightest neutrino being large compared to the mass differences.

2.2.4   Confirmation and experimental approaches

The components of the PMNS matrix elements, like in particular the mixing parameters θ_{12}, θ_{23}, θ_{31} or the *phase difference* $\Delta m_{ij}^2 \cdot L/E$ related to the squared mass splittings, the propagated distance and the energy of the neutrino, can be experimentally extracted from measurements of the transition propability. Several such efforts have been performed to study the variation with respect to distinct distances L and energies E and by that exploiting the advantage to isolate and access only particular correlated oscillation parameters. Therefore researches can draw on different suitable neutrino sources as summarized in table 2.3.

source	flavour	E [MeV]	L [km]
solar	ν_e	~ 1	10^8
atmospheric	$\nu_{e,\mu}, \overline{\nu}_{e,\mu}$	$\sim 10^3$	10^4
reactor	$\overline{\nu}_e$	~ 1	$1 - 10^2$
accelerator	$\nu_\mu, \overline{\nu}_\mu$	$\sim 10^3$	$1 - 10^3$

Table 2.3: Characteristic values of the flavour sensitivity, the kinematic energies E and length scales L for various neutrino sources [Ber12].

Solar neutrinos (as already discussed) provided subsequent evidence of neutrino oscillations when, in 2001, the Super-Kamiokande collaboration proclaimed their results on neutrino fluxes [Fuk01]. Unlike the Davis experiment that originally established the solar neutrino problem the detection principle based on elastic neutrino-electron scattering $\nu + e \rightarrow \nu + e$ in purified water was not only sensitive to electron-neutrinos but to all neutrino flavours. Since muon- and tau-neutrinos $\nu_{\mu,\tau}$ exhibit smaller cross-sections, their detection efficiency though was suppressed (by a known factor) to that of the electron-neutrino ν_e. The outgoing electron can then be verified by the emitted Cherencov radiation. Under the assumption that all neutrinos coming from the sun were still electron-neutrinos, the result revealed 45% of the predicted solar flux and the deficit was attributed to the flavour mixing and less efficient counting of the ν_μ's and ν_τ's. From there the last piece of the puzzle was to identify what exact fraction of the ν_e's had converted into the different flavours in order to finally derive the overall neutrino flux and compare with those calculated from the SSM. This could be first obtained in 2002 at the Sudbury Neutrino Observatory (SNO) [Ahm02] using heavy water D_2O, which allowed to measure not only the total but also the separate electron neutrino flux by the reactions

$$
\begin{aligned}
\nu_e + d &\rightarrow p + p + e \\
\nu + d &\rightarrow n + p + \nu \\
\nu + e &\rightarrow \nu + e \,.
\end{aligned}
$$
(2.35)

The results perfectly confirmed the interim conclusions, since the sum of the remodeled neutrino fluxes from all three flavours e, μ, τ matched the theoretical predictions, and provided all the information needed to determine the parameter elements for a conversion of an electron-neutrino to muon- or tau-neutrino, namely the mixing angle $\theta_{\text{sol}} \approx \theta_{12}$ and mass splitting $\Delta m_{\text{sol}}^2 \approx \Delta m_{21}^2$.

Atmospheric neutrinos as one terrestrial source arise predominantly from the decay of muons and pions, produced by preceding cosmic ray interactions in the upper atmosphere.

$$\pi^+ \rightarrow \mu^+ + \nu_\mu \quad \text{with} \quad \mu^+ \rightarrow e^+ + \nu_e + \overline{\nu}_\mu \;,$$
$$\pi^- \rightarrow \mu^- + \overline{\nu}_\mu \quad \text{with} \quad \mu^- \rightarrow e^- + \overline{\nu}_e + \nu_\mu \;. \tag{2.36}$$

So one would obviously expect a number of muon neutrinos that is twice as high as the corresponding number for electron-neutrinos. Anyhow, the Kamiokande experiment (predecessor to the Super-Kamiokande collaboration) counted almost equal rates for the two neutrino flavours, suggesting that the muon-neutrinos must convert into the only remaining flavour: the tau-neutrino [Hir92]. Furthermore the Kamiokande detector was able to track the direction of the incoming neutrinos and by that to investigate the dependence of the propagated distance L from the source on the transition propability, which lead to the first undeniable confirmation of neutrino oscillations. Neutrinos created in the atmosphere feature much (orders of magnitudes) higher energies than neutrinos supplied from the sun (see table 2.3) involving that transitions between the second and the third generation ($\nu_\mu \leftrightarrow \nu_\tau$) become dominant, thus: $\theta_{atm} \approx \theta_{23}$ and $\Delta m^2_{atm} \approx \Delta m^2_{32}$.

Accelerator and reactor neutrinos: are emanated from fixed sources and are therefore ideally suited for high precision measurements on neutrino oscillation. Depending on the length scales or energies one could perform detailed investigations on the sinusoidal flavour variation as motivated in equation 2.34 in order to scan the distinct matrix element parameters (for example the mixing angle θ_{31} responsible for the oscillation between the electron and the tau flavour, that remains up to now the most poorly known). Some experiments monitoring the disappearance of antineutrinos from nuclear reactors are KamLAND [Ara06], DOUBLECHOOZ [Ard06], RENO [Kim08] or DAYABAY [Wan09], not to forget about MINOS that aims to looks at accelerator-generated neutrinos from Fermilab [Mic06], and many others.

parameter		best fit	3σ range
$\sin^2 \theta_{12}$ / 10^{-1}		3.07	$2.59 - 3.59$
$\sin^2 \theta_{23}$ / 10^{-1}	NH	3.86	$3.31 - 6.37$
	IH	3.92	$3.35 - 6.63$
$\sin^2 \theta_{13}$ / 10^{-2}	NH	2.41	$1.69 - 3.13$
	IH	2.44	$1.71 - 3.15$
Δm^2_{21} / $10^{-3}(eV/c^2)^2$		7.54	$6.99 - 8.18$
$|\Delta m^2_{32}|$ / $10^{-3}(eV/c^2)^2$	NH	2.43	$2.19 - 2.62$
	IH	2.42	$2.17 - 2.61$

Table 2.4: Best fit values and uncertainties at the 3σ range for the free parameters of the PMNS matrix (except for the CP violating phase δ) obtained from the three flavour oscillation global analysis in [Fog12]. The shortcuts NH and IH signify if either normal or inverted mass hierarchy is assumed.

Conclusively, the angle θ_{12} and $\Delta m^2_{21} \approx \Delta m^2_{sol}$ are accountable for solar neutrino or long-baseline reactor neutrino oscillations, whereas atmospheric neutrinos

are instead governed by θ_{23} or $\Delta m_{32}^2 \approx \Delta m_{\mathrm{atm}}^2$ representing the same parameters which long-baseline accelerator neutrinos are sensitive to. It is worth mentioning that the sign of the (atmospheric) mass-squared difference is unknown, defining the mass ordering according to: NH for $\Delta m_{\mathrm{atm}}^2 > 0$ and IH for $\Delta m_{\mathrm{atm}}^2 < 0$. Moreover, short-baseline reactor neutrino or long-baseline $\nu_\mu \to \nu_e$ oscillations are dominated by θ_{13} (if non-zero) and Δm_{31}^2. Thereby a non-zero value for θ_{13} would further provide a connection between the solar and atmospheric sector and has become an intensively studied object in the field of neutrino research, as leptonic CP violation in oscillations would cancel out if it was indeed zero [Rod11] (compare with equation 2.32).

In table 2.4 the state of the art from the combined results of the neutrino experiments on the parameters of the PMNS matrix are collected. Especially more recent publications such as [Dwy12][An12][Kim12][Abe12] allowed to scrutinize the numbers up to a relatively good precision, which implies that ν_3 almost consists of a two-component blend of ν_μ and ν_τ with only a tiny residue from ν_e, whereas (approximately) ν_2 is equally composed of all types and ν_1 is dominated by the electron-flavour. It also appears that the mass spectrum of the three neutrinos is created by a "doublet" of relatively close-by states and a third isolated neutrino state. Two possible scenarios for normal and inverted hierarchy are depicted in figure 2.4.

Figure 2.4: Schematic sketch of the neutrino mass scale configuration as suggested by measurements on neutrino oscillation. Currently the experimental results do not allow to distinguish between normal (left) and inverted (right) hierarchy. Also delineated in different grey shadings is the flavour composition consisting of ν_e, ν_μ and ν_τ for the neutrino mass eigenstates ν_1, ν_2 and ν_3.

2.2.5 Measurements of absolute neutrino mass

Despite its impact on neutrino physics, the observation of neutrino oscillation only allowed an *indirect* evidence of finite neutrino rest-masses. To gain further knowledge about the absolute mass scale thus other direct and model independent approaches have to be evoked. Therefore, during the current subsection and the upcoming section 2.3, dedicated to the "double β-decay", the most relevant approaches pursued on that matter are intended to be described in more or less detail.

Cosmology: As neutrinos are so abundant and known to carry mass, they potentially affect the evolution of the universe and cosmological observations play there-

fore a powerful role to set bounds on the sum of the mass eigenstates $m_\nu = \sum m_{\nu_i}$ with $i = 1, 2, 3$. Currently the most stringent constraints on neutrino properties could be derived by analyzing the anisotropies of the cosmic microwave background (CMB) radiation delivered from the Wilkinson Microwave Anisotropy Probe (WMAP) satellite experiment [Lim11]. In combination with the distribution of large-scale structure/growth of matter perturbations newest cosmological observations lead to a present upper limit of $\sum m_{\nu_i} < 0.24\,\mathrm{eV}/c^2$ at 68% confidence level [Mor12].

Supernovae, since most of the energy produced is radiated in short time range as a huge beakout burst of neutrinos, do represent a different, not less promising approach to study neutrino properties. In case of the famous supernova SN1987A, a gravitational collapse event discovered in 1987 on February 24$^{\text{th}}$ in the Large Magellanic Cloud (LMC) outside our Galaxy, two water Cerenkov detectors, Kamiokande-II (Japan) [Hir87] and Irvine-Michigan-Brookhaven IMB experiment (USA) [Bio87], as well as the Baksan scintillator detector (Russia) [Ale87] were in operation and observed an unusual high neutrino event rate within a time window of $\approx 10\,\mathrm{s}$ several hours before the optical detection of the stellar explosion.[4] Because neutrinos interact via the weak force only and can escape easily right after the core collapse, whereas photons suffer interactions within the stellar envelope and are therefore trapped until the shock wave emerges from the surface, neutrinos arrive at earth first. Also neutrinos with non-vanishing rest mass do have a traveling speed which is smaller than that of light resulting in a distance and energy dependent time-of-flight delay[Pir81]. Already a few weeks after the discovery of SN1987A an upper limit of $m_{\nu_e} < 11\,\mathrm{eV}/c^2$ could be set on the electron-neutrino mass [Bah87], assuming that the observed events all originated with electron-antineutrinos and disregarding any neutrino flavour-mixing.

Single β-decay: Investigations on absolute neutrino masses can be performed on any decay involving either neutrinos or antineutrinos. Such a reaction is for example provided by the already mentioned single β-decay

$$\begin{align}{}^A_Z X \rightarrow {}^A_{Z+1} Y + e^- + \overline{\nu}_e\,, \tag{2.37}\end{align}$$

of a mother nucleus $X(A, Z)$ into its progeny $Y(A, Z + 1)$ with same mass number A but atomic number Z increased by one, while simultaneously ejecting an electron and an antineutrino.

The resulting mass difference between the initial and the final state determines the released decay energy to $Q_\beta = M_X c^2 - M_Y c^2 - m_e c^2$ for the leptons minus the electron mass m_e, when neglecting the recoil-energy of the nuclei. Thus, the Q-value equals the maximal kinetic energy $E_{e,\max}$ of the electron for massless neutrinos. In case of an electron-neutrino with non-vanishing mass $m_{\nu_e} > 0$ the maximum kinetic energy is instead decreased by $E_{e,\max} = Q - m_{nu_e} c^2$ though. Consequently the study of the end-point of the continuous energy spectra of the electron emitted by the

---

[4]The LSD (France) also reported observations, which were controversially evaluated by the community, because the events were recorded several hours early [Agl87].

β-decay (e.g. with a so-called Kurie-plot) can shed light on the effective electron-neutrino mass given as a superposition of mass eigenstates and hence defined by the incoherent sum $m_{\nu_l}^2 = \sum |U_{li}|^2 m_{\nu_i}^2$ with $i = 1,\, 2,\, 3$ and $l = \text{e},\, \mu,\, \tau$.

For the analysis the fraction of events in the relevant energy interval δE close to the end-point of the electron spectrum is approximately inverse proportional to the third power of the Q-value $\propto (\delta E/Q)^3$ [Ran12] and it is therefore experimentally preferred to employ β-decaying isotopes with the lowest end-point energies possible. Two suitable isotopes meeting this requirement are the hydrogen isotope tritium (^{3}H) with $Q = 18.6\,\text{keV}$ and rhenium (^{187}Re) with $2.47\,\text{keV}$, respectively. So far the most accurate results based on single β-decay, have been reported by the Mainz and Troisk experiments, which evaluated upper boundaries of $m_{\nu_\text{e}} < 2.3\,\text{eV}/c^2$ [Kra05] and $m_{\nu_\text{e}} < 2.05\,\text{eV}/c^2$ [Lob03], respectively.

Future setups currently under construction, such as the Karlsruhe Tritium Neutrino (KATRIN) experiment [Wei02] or the Microcalorimeter Array for a Rhenium Experiment (MARE) [Gat06], are designed to further improve the sensitivity to the sub-eV neutrino mass range.

2.3 Double beta-decay

The double β-decay as one of the rarest known nuclear decay processes, was first theoretically proposed by M. GOEPPERT-MAYER in [Goe35]. However, for 35 isotopes $X(A, Z)$ the single β-decay is forbidden or strongly suppressed since the neighbouring nuclei $Y(A, Z + 1)$ exhibits a higher binding energy, but the double β-decay is allowed:

$$_Z^A X \rightarrow \ _{Z+2}^A Y + 2e^- + 2\overline{\nu}_\text{e} \qquad (2\nu\beta\beta) \qquad (2.38)$$
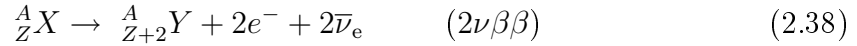
where a pair of protons undergoes a simultaneous single β-decay emanating two electrons and two electron-neutrinos (see corresponding Feynman graph in figure 2.5a) on the left-side).
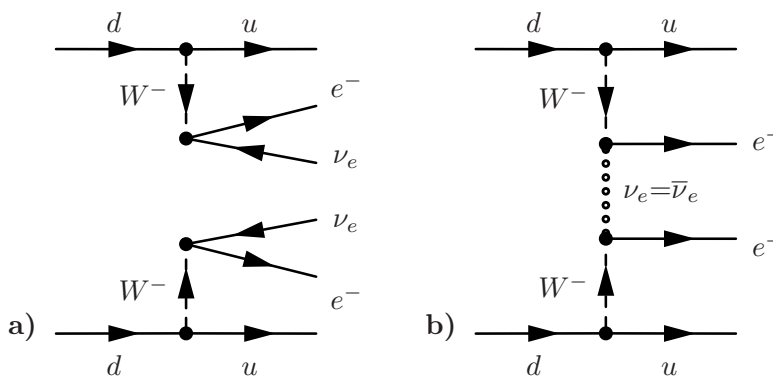

Figure 2.5: Feynman diagrams for the double β-decay with **a)** $2\nu\beta\beta$ and **b)** $0\nu\beta\beta$ under exchange of a Majorana neutrino.

As the neutrinos carry away an indeterminate part of the released energy, the sum of the electron energies displays a continuous spectrum up to the Q-value, $Q_{\beta\beta}$.

Apparently this second-order process of the weak interaction only happens for even-even but not for even-odd or odd-odd nuclei and has been, so far, directly monitored for in total 11 isotopes, all listed in table 2.5. In the special case of ^{48}Ca, the single β-decay ^{48}Ca $\to$ ^{48}Sc with $Q_{\beta\beta} = 278\,\text{keV}$ is indeed energetically allowed, albeit highly forbidden due to the large difference of angular momenta between the initial and final state [Bru00]. For ^{100}Mo and ^{150}Nd the so-called two-neutrino double β-decay was also verified for the transition to the 0^+ excited state of the daughter nucleus [Bar13].

$^A_Z X$	$^A_{Z+2} Y$	$Q_{\beta\beta}$ [keV]	$T^{2\nu}_{1/2}$ [10^{20}yr]	Nat.ab. [%]	$G_{0\nu}$ [$\frac{10^{-14}}{\text{yr}}$]
^{48}Ca	^{48}Ti	4273.7	0.44	0.187	6.35
^{76}Ge	^{76}Se	2039.1	16.0	7.8	0.623
^{82}Se	^{82}Kr	2995.5	0.92	9.2	2.7
^{96}Zr	^{96}Mo	3348	0.23	2.8	5.63
^{100}Mo	^{100}Ru	3035.0	0.071	9.6	4.36
^{116}Cd	^{116}Sn	2809.1	0.285	7.6	4.62
^{128}Te	^{128}Xe	866	2.0×10^4	31.7	0.164
^{130}Te	^{130}Xe	2530.3	6.9	34.5	4.09
^{136}Xe	^{136}Ba	2457.8	22.0	8.9	4.31
^{150}Nd	^{150}Sm	3367.3	0.082	5.6	19.2
^{238}U	^{238}Pu	1.1×10^3	20	99.3	-

Table 2.5: List of the double β-decay candidates observed to date and their corresponding characteristics (without errors). Values for half-lifes $T^{2\nu}_{1/2}$ of $2\nu\beta\beta$ taken from [Bar13] represent averages or recommendations concluded from a combination of previous experiments. The phase space factors $G_{0\nu}$ for $0\nu\beta\beta$ have been scaled to $g_A=1.25$ and can be found along with the Q-values as well as natural abundances in [Rod11] (for ^{128}Te in [Suh98][Sci09]).

Table 2.5 also states the rate or half-life $T^{2\nu}_{1/2}$ derived from experimental data, which can be - according to Fermi's Golden Rule - mathematically written as

$$(T^{2\nu}_{1/2})^{-1} = G_{2\nu}(Q_{\beta\beta}, Z)|\mathcal{M}_{2\nu}|^2 \ , \tag{2.39}$$

where $G_{2\nu}(Q_{\beta\beta}, Z)$ and $\mathcal{M}_{2\nu}$ represent the four-particle phase-space factor and the nuclear matrix element for the neutrino-accompanied double β-decay, respectively. The underlying process does preserve the lepton number conservation, thus can not distinguish whether the neutrino is of Dirac or Majorana nature, and neither depends on any charge conjugation properties nor on the neutrino mass [Avi08].

2.3.1 Majorana Neutrinos

The following paragraph is anticipated to provide a brief exposition on the mathematical formulation of the neutrino that holds in contrast to charged fermions, apart from the general Dirac theory of spin $\frac{1}{2}$ particles, also an alternative so-called Majorana description.

Neutrinos are neutral particles, which entirely interact via the electroweak force described by the SU(2)$_L$×U(1) gauge symmetry.[5] Herein the subscript L denotes the phenomenology that, according to all accumulated experiences from experiments, the charged weak current is of purely left-handed nature. It is also experimentally well known, that solely left-handed neutrinos participate in the weak interactions [Gol58]. Hence right-handed neutrino components are not considered in the theory and the lepton sector of the Standard Model is formed by doublets and singlets

$$\psi_{lL} = \begin{pmatrix} \nu_{lL} \\ l_L \end{pmatrix}, l_R \quad \text{with} \quad l = \text{e}, \mu, \tau . \tag{2.40}$$

As already mentioned in section 2.1.1, in the relativistic quantum theory fermions are described by four-component spinors ψ, which obey the Dirac equation 2.2. For $m > 0$ the solution in form of plane waves

$$\psi_- = u \, e^{i(\boldsymbol{pr} - Et)} \quad \text{and} \quad \psi_+ = v \, e^{-i(\boldsymbol{pr} - Et)} . \tag{2.41}$$

yields the four linearly independent basic spinor fields $u^{(1)}$, $u^{(2)}$ for particles and $v^{(1)}$, $v^{(2)}$ for antiparticles, given in equations 2.11 and 2.12. On the other hand, for massless fermions only two of the basic Dirac spinors remain independent of each other. Hereby a particle is transformed into its antiparticle and vice-versa via charge conjugation. This antiparticle field thus has to satisfy the Dirac equation and is defined by [Avi08][Gro90][Bil87]

$$\psi^C = C\overline{\psi}^T \quad \text{with} \quad \overline{\psi} = \psi^\dagger \gamma_0 \quad \text{and} \quad C = i\gamma^2\gamma^0 . \tag{2.42}$$

By further applying the chiral projection operator

$$P_{L,R} = \frac{1}{2}(1 \mp \gamma_5) , \tag{2.43}$$

the left- and right-handed parts $\psi_L = P_L\psi$ and $\psi_R = P_R\psi$ can be easily obtained.

Parity and charge conjugation: So far only left-handed neutrinos ν_L and right-handed antineutrinos $\overline{\nu}_R$ have been be experimentally verified, which can thereby not be displayed as the charge-conjugate particle of the other. This is due to the fact that the C operator does not affect the spin and momentum, and thus the helicity, of a particle. Strictly speaking, ν_L and $\overline{\nu}_R$ are instead intertwined by the combined operation CP of charge *plus* parity conjugation $(\nu_L)^{CP} = \overline{\nu}_R$, where explicitly the parity operator P is responsible for the change in the chirality [Kla95]. Herefrom two possible scenarios for the mass term $m\overline{\psi}\psi$ of particles in the effective Lagrangian can be concluded:

- The charge-conjugate particles of ν_L, $\overline{\nu}_R$ represent independent, not yet experimentally observed particles and the neutrino is said to be of Dirac type

---

[5]The corresponding group of the weak hypercharge U(1) is required by the unification of the weak and the electromagnetic interactions in the Glashow-Weinberg-Salam model [Gla61][Wei67][Sal68].

entailing four distinct physical states $\nu_D = \nu_L + \nu_R$ and $\nu_D^C = \nu_L^C + \nu_R^C$. Following the Standard Model (SM) ansatz of Yukawa coupling to the Higgs-field to generate particle masses, a Dirac mass term for the neutrino in the Lagrangian then reads

$$-\mathcal{L}_D = M^D \overline{\nu}_D \nu_D = M^D \overline{(\nu_L + \nu_R)}(\nu_L + \nu_R) = M^D \overline{\nu}_R \nu_L + h.c. \ , \qquad (2.44)$$

where M^D signifies the Dirac mass and the terms $M^D \overline{\nu}_L \nu_L$ and $M^D \overline{\nu}_R \nu_R$ vanish according to the definition of the projection operator $P_{L,R}$ and with γ_0 flipping the chirality. Thus the lepton number is conserved.

- The neutrino represents his own charge-conjugate particle (or antiparticle), equivalent to $\nu_L^C = \nu_L$ and $\overline{\nu}_R^C = \overline{\nu}_R$ (as suggested in 1937 by E. MAJORANA [Maj37]). In this case one defines the neutrino to be of Majorana type with only two distinguishable states and since

$$(\psi_L)^C = (P_L \psi)^C = C\overline{P_L \psi}^T = P_R(C\overline{\psi}^T) = P_R \psi^C = (\psi^C)_R \quad \text{with} \quad (\psi_L)^C \equiv (\psi^C)_L \tag{2.45}$$

(the same of course also applies for inverted handedness) the corresponding Majorana mass term of the Lagrangian becomes:

$$-\mathcal{L}_M = \frac{1}{2} M_L^M \overline{\nu}_L \nu_L^C + \frac{1}{2} M_R^M \overline{\nu_R^C} \nu_R + h.c. \tag{2.46}$$

with the Majorana masses M_L^M and M_R^M acting as coupling parameters. Such a possible coupling between the neutrino and the antineutrino field would, in any way, imply that the lepton number is not preserved.

As neutrinos are known to have mass (from oscillation measurements) but no electric charge, in its most general form the mass term of the Lagrangian containing all possible transitions therefore becomes

$$\begin{aligned} -\mathcal{L}_{Yuk} &= M^D \overline{\nu}_R \nu_L + \frac{1}{2} M_L^M \overline{\nu}_L \nu_L^C + \frac{1}{2} M_R^M \overline{\nu_R^C} \nu_R + h.c. \\ &= \frac{1}{2}(\overline{\nu}_L, \overline{\nu_R^C}) \begin{pmatrix} M_L^M & M^D \\ M^D & M_R^M \end{pmatrix} \begin{pmatrix} \nu_L^C \\ \nu_R \end{pmatrix} + h.c. \end{aligned} \tag{2.47}$$

2.3.2   Neutrinoless double beta-decay

As one conceivable approach to gain insight concerning the possible Dirac or Majorana nature of the neutrino, the *neutrinoless double β-decay* ($0\nu\beta\beta$) was first considered in [Fur39]. The process is thereby defined as the transition of a mother nucleus $X(A, Z)$ into its progeny $Y(A, Z + 2)$ with proton number increased by two units under the emission of two electrons e^- but (in difference to the neutrino-accompanied $2\nu\beta\beta$ mode) without any electron antineutrinos $\overline{\nu}_e$:

$$^A_Z X \rightarrow\ ^A_{Z+2}Y + 2e^- \qquad (0\nu\beta\beta) \tag{2.48}$$

The experimental signature of the proposed decay mode would be a line at the summed electron energy spectrum appearing at the $Q_{\beta\beta}$ value (as shown in figure 3.3) and, since the lepton number is violated corresponding to $\Delta L = 2$, undoubtedly require the presence of physics beyond the SM. For this reason a huge amount of experimental (a brief outline will be given in subsection 2.3.4) and theoretical efforts have been endeavoured in order to establish and predict this process.[6]

It should be noted that via the *blackbox* or *Schechter-Valle* theorem [Sch82], all possible realizations of the $0\nu\beta\beta$-decay do involve the existence of a Majorana neutrino mass. However, in [Due11] the Majorana mass term induced by radiative corrections, was recently pointed out to be only in the range of 10^{-24} eV and thus many orders of magnitude too small to account for the mass scales implied by neutrino oscillation experiments. As a consequence, if the neutrinoless decay mode is observed, other mechanisms mediating the $0\nu\beta\beta$ process have to be considered.

Thereby the standard assumption, where the exchange of a light Majorana neutrino generates the decay, is not only the simplest theoretical treatment, but also presumably the best motivated one and will be hence exclusively discussed in the following though. Anyhow, there are still several more possible contributions, with the underlying physics being driven by the exchange of particles associated to either heavy Majorana neutrinos (here the heavy neutrinos are considered to be responsible for light neutrino mass via the famous seesaw mechanism), R-parity violating SUSY, left-right symmetric theories, Higgs triplets or leptoquarks, that might dominate the process instead. Also conceivable is an extended number of particles in the final states (e.g. modes with additional Majoron emission) and many other examples (for more information on that topic and a review on how to distinguish the different mechanism from another, the reader is further referred to [Rod11]).

The Feynman diagram for neutrinoless double β-decay based on light Majorana neutrino exchange in the nucleus is sketched in figure 2.5b). When the right-handed electron anti-neutrino is emitted at one vertex, it can be decomposed into the mass eigenstates ν_i ($i = 1, 2, 3$) and helicity eigenstates:

$$\overline{\nu}_{e,R} = \overline{\nu}_e \frac{1}{2}(1 + \gamma^5) = \sum_{i=1}^{3} U_{ei}\left(\overline{\nu}_{i,h=+1} + \frac{m_i}{E}\overline{\nu}_{i,h=-1}\right) . \qquad (2.49)$$

Here U denotes the mixing matrix, m_i are the mass eigenvalues and E represents the neutrino energy. Thus the neutrino contains a mixture of a first, almost total positive plus a second, strongly suppressed (by the factor m_i/E) negative helicity component, whereas the latter one can be - in turn - absorbed at the other vertex. Clearly, such a process is only possible, if the neutrino is not only a massive (therefore not in a pure helicity state) particle, but also of Majorana nature (tantamount with being identical to its antiparticle).

---

[6]There are several similar processes called neutrinoless double β^+-decay ($0\nu\beta^+\beta^+$), β^+-decay electron capture ($0\nu\beta^+$EC) or double electron capture (0νECEC) of bound state electrons e_b^-, which can be searched for and those discovery would also imply the non-conservation of lepton number.

Hence an observation of the neutrinoless double β-decay would unambiguously prove neutrinos to be Majorana particles, while simultaneously providing access to the absolute mass scale, for its half-life is directly related to the neutrino mass by

$$(T_{1/2}^{0\nu})^{-1} = G_{0\nu}(Q_{\beta\beta}, Z)|\mathcal{M}_{0\nu}|^2 \left(\frac{m_{\beta\beta}}{m_{\mathrm{e}}}\right)^2 , \tag{2.50}$$

with the phase space integral $G_{0\nu}$, the nuclear matrix element $\mathcal{M}_{0\nu}$ for the two electrons and the electron mass m_{e}. Furthermore, the effective coupling strength, namely the "Majorana mass" or "effective electron neutrino mass", is defined as the the coherent sum over all neutrino mass eigenvalues

$$m_{\beta\beta} = |\sum_{i=1}^{3} U_{\mathrm{e}i}^2 m_i| \overset{\mathrm{Eq.\,2.32}}{=} |c_{12}^2 c_{13}^2 m_1 + s_{12}^2 c_{12}^2 m_2 \mathrm{e}^{2i\alpha} + s_{13}^2 m_3 \mathrm{e}^{2i\beta}| . \tag{2.51}$$

As the phase space factor can on the one side be calculated with good accuracy, the nuclear matrix element, unfortunately, is on the contrary less well understood and accompanied by a high uncertainty preventing a precise extraction of the absolute neutrino mass from the observed rate $T_{1/2}^{0\nu}$. Several theoretical models have been deployed to improve the reliability of the $\mathcal{M}_{0\nu}$ calculations, some of which are the Interacting Shell Model (ISM) [Men09][Men11], the Quasiparticle Random Phase Approximation (QRPA, either with UCOM corrections for short range correlation of Jastrow type) [Sim09][Suh10][Fae12], the Interacting Boson Model (IBM) [Bar09a][Iac11], the Generating Coordinate Method (GCM) [Rod10] and the projected Hartree-Fock-Bogoliubov (pHFB) method [Rat10] (references from e.g. [Sch13][Rod11]).

Without going further into detail concerning the working principles of the individual procedures, figure 2.6 compares recent results from the NME calculations of the different methods for the seven most used isotopes in double β-decay experiments. Following this attempts the uncertainty of the nuclear matrix element for a given isotope still remains to be in the order of a factor 2-3 though.
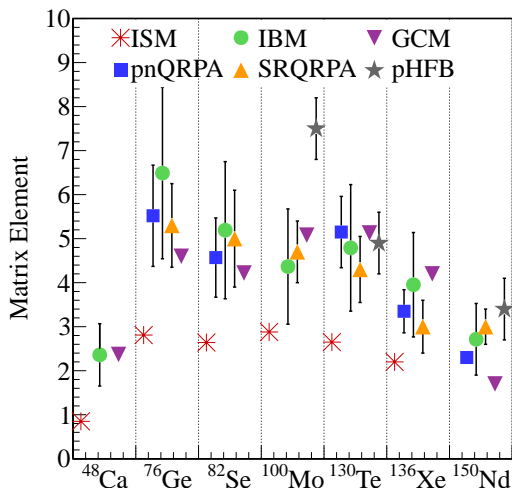

Figure 2.6: Nuclear matrix element calculations for $0\nu\beta\beta$ and light neutrino exchange. Values are compared for different techniques: ISM [Men09][Men11], IBM (results are scaled by 1.18 to estimate the difference between Jastrow and UCOM short range correlations, also an error is set to be of 30%) [Bar09a][Iac11], GCM [Rod10], pnQRPA (=proton-neutron Quasi-particle Random Phase Approximation) [Suh10], SRQRPA (=Self-consistent Renormalized Quasi-particle Random Phase Approximation) [Fae12] and pHFB [Rat10].

2.3.3 Experimental constraints for $0\nu\beta\beta$-decay

A way to encounter the half-life of neutrinoless double β-decay - and therefore the effective neutrino mass - can be achieved in counting experiments. When assuming a direct proportionality to the detector mass M_{det}, the number of background events is hereby related to

$$N_{\mathrm{bkg}} = M_{\mathrm{det}} \cdot t \cdot B \cdot \Delta E \; , \tag{2.52}$$

where next to the measurement time t also the background index B (typically in units of $\mathrm{cts}/(\mathrm{keV} \cdot \mathrm{kg} \cdot \mathrm{yr})$) and the width ΔE of the searched energy window, which depends on the experimental energy resolution, enter the equation.

Up to now, all observations of event counts in the region of interest (ROI) around $Q_{\beta\beta}$ made in different, independently from each other pursued experimental approaches were consistent with the expected background contribution N_{bkg} - except one. In [Kla04] part of the Heidelberg-Moscow collaboration went public claiming to have evidence of a signature for ^{76}Ge at a 4σ level. The corresponding half-life was specified to $T_{1/2}^{0\nu} = 1.19^{+0.37}_{-0.23} \cdot 10^{25}$ yr and has been scrutinized in various subsequent experiments ever since (see next section 2.3.4).

However in case of $N_{\mathrm{bkg}} \ll 1$, the number of counted signal events N_{sig} can be converted to the half-life $T_{1/2}^{0\nu}$ for the $0\nu\beta\beta$-decay of a given isotope $X(A, Z)$ with mass number A according to

$$T_{1/2}^{0\nu} = \frac{\ln 2 \cdot N_{\mathrm{Avg}}}{N_{\mathrm{sig}} \cdot m_A} \, \varepsilon_{\mathrm{det}} \cdot \eta \cdot M_{\mathrm{det}} \cdot t \qquad \text{for } N_{\mathrm{bkg}} \ll 1 \; . \tag{2.53}$$

Here N_{Avg} denotes the Avogadro constant, $\varepsilon_{\mathrm{det}}$ the signal detection efficiency, η the mass fraction of the isotope and m_A the molar mass of the isotope. If instead $N_{\mathrm{bkg}} \gg 1$ is the case, the e.g. $90\,\%$ confidence limit (C.L.) on the half-life is given by the slightly different expression

$$T_{1/2}^{0\nu}(90\%\mathrm{C.L.}) > \frac{\ln 2}{1.64} \frac{N_{\mathrm{Avg}}}{m_A} \, \varepsilon_{\mathrm{det}} \cdot \eta \cdot \sqrt{\frac{M_{\mathrm{det}} \cdot t}{B \cdot \Delta E}} \qquad \text{for } N_{\mathrm{bkg}} \gg 1 \; . \tag{2.54}$$

Equations 2.53 and 2.54 already suggest several requirements experiments in search for neutrinoless double β decay should meet. It is of crucial importance to have for instance a high exposure $M_{\mathrm{det}} \cdot t$, which can be either accomplished by having very long run times t (usually in the range of several years) or by increasing the detector mass M_{det} as well as the mass of the investigated $0\nu\beta\beta$ isotope (due to naturally high abundance, enrichment, ...).

If a significant background is present, meaning $N_{\mathrm{bkg}} \gg 1$, another important issue arises with keeping its contribution in form of the background index B as small as possible. Therefore several experiments have developed and continuously enhanced various rejection methods, some of which are active veto techniques, mostly based on detection of scintillation light, or purely non-hardware analysis routines extracting information from the measured signal shapes that will be further discussed in the next

chapter 3 as well as in the course of the whole thesis in context of their application in the Germanium Detector Array (GERDA) experiment. Another way to ensure low background experiments goes along with a prescreening and purification of the materials used for the construction, a graded shielding concept with the $0\nu\beta\beta$ isotope in the inner, most pure region and a carefully chosen setup site.

But, since there exists the proportionality $T^{0\nu}_{\beta\beta} \propto 1/Q^5_{\beta\beta}$ between the half-life and the $Q_{\beta\beta}$ value of the decay [Avi08], also the choice of the $0\nu\beta\beta$ isotope has an impact on the experimental sensitivity. However, despite their endpoint-energies most of the isotopes listed in table 2.5 take part in (current and past) $\beta\beta$ research programs.

Apart from the specifications on the experiments indicated by equations 2.53 and 2.54, there exist two general strategies for a source-detector setup:

Detector and source are identical. This can be for example realized by means of semiconductor detectors, scintillating materials or gas and liquid Time Projection Chambers (TPC). Having the detector acting simultaneously as source offers two advantageous opportunities: the electrons created in the double β-decay can get completely absorbed in the detector, resulting in a high efficiency. Also inferences on the nature (background- or signal-like) of the observed events can be drawn. This is because the energy emitted from a double β-decay is deposited locally within the detector, whereas background (say from closeby naturally present radioactive contaminants or in particular, radioactive isotopes occurring in the decay chain of ^{238}U and ^{232}Th) interacts with the detector material (via Compton scattering, pair production, etc.) and thus results in several, non-localized energy depositions.

Detector and source are distinct parts. In such experiments the decaying isotope is confined in thin foils placed between the detectors, providing the possibility to easily exchange the source and test several isotopes of interest. Also the escaping electrons of the decay can be tracked allowing to study their kinematical behaviour and by that reaching a very high background suppression. However, some of the disadvantages for this kind of experiments, where the source is not intrinsic to the detector, are the very low source masses and the often poor energy resolution.

2.3.4   Current status of $0\nu\beta\beta$-experiments

Since the beginning of this millennium, mainly a handfull of experiments conduced to set new limits in the $0\nu\beta\beta$ search and many more are either currently in the period of data taking, assembled or in process of planning. An overview about the chronology sequence along with the used source material, masses and detection techniques of past, present and future contributions is collated in table 2.6. A more detailed overview can be further found in [Avi08][Bar11][Sch13].

So far, Heidelberg-Moscow (HdM) and the International Germanium Experiment (IGEX), both operating enriched high purity germanium detectors, were the most sensitive approaches in the search for the neutrinoless double β-decay in the isotope ^{76}Ge and set quite similar 90% C.L. limits at $T^{0\nu}_{1/2}(^{76}\text{Ge}) > 1.9 \cdot 10^{25}$ yr [Kla01]

or $T_{1/2}^{0\nu}(^{76}\text{Ge}) > 1.57 \cdot 10^{25}$ yr [Aal02], respectively. A subgroup of the HdM Collaboration reported post hoc in 2004 positive observation of the $0\nu\beta\beta$-decay with $T_{1/2}^{0\nu}(^{76}\text{Ge}) = 1.19^{+0.37}_{-0.23} \cdot 10^{25}$ yr [Kla04]. In a later publication this claim has been even strengthened to $T_{1/2}^{0\nu}(^{76}\text{Ge}) = 2.23^{+0.44}_{-0.31} \cdot 10^{25}$ yr [Kla06] and explained due to an subsequently applied pulse shape discrimination. Anyhow, the latter analysis holds various known inconsistencies criticized by the scientific community that have been repeatedly pointed out in e.g. [Chk08][Sch13].

For other isotopes apart from ^{76}Ge the best limits on the half-life of the $0\nu\beta\beta$ process have been achieved so far for ^{130}Te, ^{100}Mo and ^{136}Xe.

Thereby the scrutiny in the former isotope ^{130}Te was conducted by the CUORICINO experiment, which operated an array of 62 tellurium oxide (TeO$_2$) crystals with a total mass of 40.7 kg (corresponding to 11.3 kg of ^{130}Te) at cryogenic temperatures < 10 mK as bolometers. Due to the very low heat capacitance, an energy deposition inside the crystal results in a temperature rise of typically 0.1 mK/MeV that in turn was read-out by neutron transmutation doped germanium thermistors. Applying the described technique yielded a reasonably good energy resolution of about $FWHM = 6 - 10$ keV close to $\simeq 2.6$ MeV, the Q-value of the isotope. After a data recording period between 2003-2008 with a total exposure of 19.75 kg·yr and a background of 0.17 cts/(keV·kg·yr) at $Q_{\beta\beta}$, no signal was observed. Instead a lower limit of $T_{1/2}^{0\nu}(^{130}\text{Te}) > 2.8 \cdot 10^{24}$ yr (at 90% C.L.) that is not sensitive enough to either refute or approve the HdM result, was found [And11].

In a different approach based on a tracking method, namely the NEMO-3 experiment, the measurement was performed by means of thin foils made out of seven different enriched $0\nu\beta\beta$ candidate isotopes (9 kg in total) located inside a drift chamber within a magnetic field. Furthermore, the drift region is surrounded by a calorimeter consisting of several plastic scintillator blocks with photomultiplier tube (PMT) read-out to monitor the individual particle energies. While the track reconstruction allows for a remarkably enhanced background reduction down to a level of $1.2 \cdot 10^{-3}$ cts/(keV·kg·yr) and an at least modest energy resolution around $FWHM \approx 15\%/\sqrt{E[\text{MeV}]}$ for electrons, the detection principle suffers on the other side from a very poor $0\nu\beta\beta$ reconstruction efficiency of only 8%. Again the limits on the individual isotopes obtained by the collaboration, with $T_{1/2}^{0\nu}(^{100}\text{Mo}) > 1.0 \cdot 10^{24}$ yr and $T_{1/2}^{0\nu}(^{82}\text{Se}) > 3.2 \cdot 10^{23}$ yr (each of them at 90% C.L.) being the most stringent ones, were not sensitive enough to scrutinize the HdM claim [Sim12].

Currently, two new-generation experiments are taking data, but reported recently first results though: the Enriched Xenon Observatory EXO-200 as well as KamLAND-Zen - both are using ^{136}Xe as $\beta\beta$ emitter and both of them yield experimental limits (at 90% C.L.) precise enough to test the HdM discovery. The EXO experiment, for instance, is a liquid xenon time projection chamber (TPC) of 40 cm diameter and length, filled with a total of 175 kg of liquid Xe. Since there is a strong anti-correlation present between the measured ionization signal and the scintillation light amplitude, a combination of these two quantities fa-

cilitates a greatly improved energy resolution as good as $\approx 4\%$ at the $Q_{\beta\beta}$-value of ^{136}Xe. When deploying topological as well as temporal cuts, the background could be reduced to $\simeq 1.5 \cdot 10^{-3}$ cts/(keV·kg·yr), which leads on to a half-life limit of $T_{1/2}^{0\nu}(^{136}\text{Xe}) > 1.6 \cdot 10^{25}$ yr for a (by then) collected exposure of 32.5 kg·yr [Aug12]. KamLAND-Zen, on the other hand, operates 13 tons of xenon-doped liquid scintillator ($\simeq 290$ kg of ^{136}Xe) inside a $25\,\mu$m thick nylon balloon filled with a radius of 1.54 m. An additional outer balloon with 13 m diameterthe and filled with liquid scintillator serves as an active shield, whereas the energy ($FWHM \approx 10\%$ at 2.5 MeV, the Q-value of ^{136}Xe) and position (resolution $\approx 15\,\text{cm}/\sqrt{\text{E(MeV)}}$) of the decay are reconstructed by surrounding PMTs. Compared to other experiments, the energy resolution is the poorest but redeemed by the large mass of target material, thus high exposure of 89.5 kg·yr and the low background level, resulting in $T_{1/2}^{0\nu}(^{136}\text{Xe}) > 1.9 \cdot 10^{25}$ yr [Gan13]. However, a comparison of two different double β isotopes, here ^{136}Xe and ^{76}Ge in order to enable a statement on the Heidelberg-Moscow claim, relies always on nuclear matrix element calculations though and is therefore strongly model-dependent.

In the near future, many other experiments with eagerly awaited results, like CANDLES, CUORE, SNO+, SuperNEMO, NEXT or COBRA, are in queue to resolve the Majorana nature of the neutrino. And also a new experimental ^{76}Ge effort, named GERmanium Detector Array (GEDRA), designed to improve the present limit by an order of magnitude, is already in process, using in a first phase the same germanium detectors as HdM and IGEX, whereas in a second phase new ones will be added. Since the work presented in this thesis has been carried out within this very approach, the next chapter 3 will be dedicated for a detailed overview on the GERDA experiment.

Experiment	Isotope $^A_Z X$	Mass [kg]	Detection method	Start-end	Ref.
IGEX	^{76}Ge	6.4	semiconductor detector	1991-2000	[Aal02]
HdM	^{76}Ge	11	semiconductor detector	1990-2003	[Kla04]
CUORICINO	^{130}Te	11	bolometer	2003-2008	[And11]
NEMO-3	^{100}Mo, ^{82}Se	7.8	calorimeter+tracking	2003-2011	[Sim12]
EXO-200	^{136}Xe	100	liquid TPC	2011- ?	[Aug12]
KamLAND-Zen	^{136}Xe	304	liquid scintillator	2011- ?	[Gan13]
GERDA I(II)	^{76}Ge	15(35)	semiconductor detector	2011- ?	[Ack13]
CANDLES	^{48}Ca	0.35	scintillation crystal	2011- ?	[Oga12]
CUORE(-0)	^{130}Te	200(10)	bolometer	2012- ?	[Gor12]
Majorana	^{76}Ge	~ 30	semiconductor detector	2013- ?	[Wil12]
SNO+	^{150}Nd	44	liquid scintillator	2013- ?	[Har12]
SuperNEMO	^{82}Se	~ 100	calorimeter+tracking	2014- ?	[Bar12]
NEXT	^{136}Xe	100	gas TPC	2015- ?	[Mon12]
COBRA	^{116}Cd	?	semiconductor detector	?	[Old12]

Table 2.6: Selection of past, present and future $0\nu\beta\beta$-decay experiments along with their target isotopes and corresponding masses, detection techniques as well as time scales.

3. The GERDA Experiment

The GERmanium Detector Array (GERDA) experiment is designed to search for the neutrinoless double β-decay in the ^{76}Ge isotope and has been first proposed in 2004 [Abt04] with the aim to either confirm or reject the claim of positive evidence for the lepton violating $0\nu\beta\beta$-process by part of the Heidelberg-Moscow (HdM) Collaboration [Kla04][Kla06]. An inauguration with a completed experimental setup could be celebrated in November 2010, subsequently a commissioning phase was aspired for first data collection with yet non-enriched germanium detectors.

Phases and physics reach: To achieve the best learning curve possible, the experiment is planned to proceed in several steps with consecutively increasing $\beta\beta$ emitter masses and more and more stringent demands on the background level. Hence, the first ground was broken in November 2011, almost one year after commissioning, when "Phase I" launched with the successful installation of the enriched conventional p-type high-purity germanium (HPGe) detectors from the previous HdM and IGEX experiments (combined = 17.7 kg). The determined background index was determined to be at roughly $1 \cdot 10^{-2}$ counts/(keV·kg·yr) (after applying the PSD algorithm developed and presented in the framework of this thesis), showing an order of magnitude improvement compared to all preceding experiments. Note that this would facilitate a statistically conclusive statement of high probability regarding neutrinoless double β-decay with a lifetime as asserted by [Kla04] within about one year. On this basis, only recently, after a total exposure of 21.6 kg·yr, the data taking was interrupted and the results attained from a blind analysis, which will be discussed in great depth in the following chapters, were presented in [Ago13a].

The next step, "Phase II", is currently in preparation, but scheduled to already start in 2014 featuring another new set of $\sim$20 enriched detectors of Broad Energy Germanium (BEGe) type, whose total mass amounts to 20.8 kg and thus allows to supplementary increase the overal exposure on a notable level. Additionally the background index is anticipated to further improve by a factor of $\sim$10 with the aid of several precautions, e.g. a liquid argon scintillation light veto and enhanced pulse shape discrimination (PSD) techniques will be provided. According to [Abt04], this second phase is foreseen to be accomplished with an accumulated exposure of 100 kg·yr, which would yield a sensitivity in the range of $\sim$2 $\cdot 10^{26}$ yr corresponding to an effective neutrino mass $|m_{\beta\beta}|$ of $(0.09-0.29)$ eV.

Future prospects for an ultimate ^{76}Ge experiment, capable of conquering the $(15-20)$ meV mass range, include a merging of the different $0\nu\beta\beta$ Collaborations in a world-wide conjoint effort towards a conceivable "Phase III". The measured and expected sensitivities of the first two experimental phases as well as an hypothetical 1 ton experiment on the effective Majorana mass $|m_{\beta\beta}|$ are emphasized as red lines in figure 3.1 as a function of the lightest neutrino mass m_{min}. Both possible mass orderings, normal (blue) and inverted (orange) hierarchy, are displayed. For the
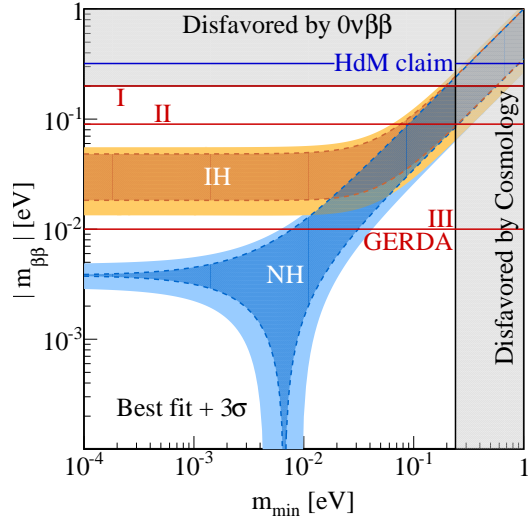
Figure 3.1: Effective Majorana mass $|m_{\beta\beta}|$ as a function of the lightest neutrino mass $m_{\min}$ for the case of normal (blue) and inverted (orange) mass hierarchy. Distributions within a 3σ range are calculated for values from [Fog12] (see summary of table 2.4), whereas the darker areas exclude the experimental errors to give prominence to the effect of the CP-violating Majorana phases. Different sensitivities of the first two GERDA phases and a future 1 ton experiment as well as the HdM claim are indicated by red and blue lines, respectively.

calculation of the colored bands, mixing parameters obtained from the three flavour oscillation global analysis in [Fog12] (collected in table 2.4) and equation 2.51 have been used. In case of normal mass hierarchy (NH), the neutrino masses $m_{2,3}$ are associated with the smallest mass $m_{\min} = m_1$ by the relations [Bil12]

$$m_2 = \sqrt{m_1^2 + \Delta m_{\mathrm{sol}}^2} \quad \text{and} \quad m_3 = \sqrt{m_1^2 + \Delta m_{\mathrm{sol}}^2 + \Delta m_{\mathrm{atm}}^2} \,, \qquad (3.1)$$

whereas for the scenario of inverted mass hierarchy (IH) with $m_{\min} = m_3$ one can conclude that

$$m_1 = \sqrt{m_3^2 + \Delta m_{\mathrm{atm}}^2} \quad \text{and} \quad m_2 = \sqrt{m_3^2 + \Delta m_{\mathrm{atm}}^2 + \Delta m_{\mathrm{sol}}^2} \,. \qquad (3.2)$$

Three important regimes can be recognized: hierarchical ($m_{\min} < 10^{-3}$), cancellation ($m_{\min} \sim 10^{-2}$, requires normal mass ordering) and quasi-degenerate ($m_{\min} > 10^{-1}$). Additionally the regions which are disfavored by $0\nu\beta\beta$-experiments (most stringent limit so far from GERDA Phase I) or cosmology [Mor12] as well as the HdM claim [Kla04] are marked as gray shades and a blue line, respectively. As one can see, only a future Phase III of the GERDA experiment would - in case of evidence for the $0\nu\beta\beta$-signal - enable access to an unambiguous clarification about whether the neutrino mass hierarchy is of normal or inverted nature.

The setup description as well as the detection principle of the GERDA experiment are reviewed in section 3.1 along with the main properties, mechanisms and application procedures of semiconducting germanium detectors in the following section 3.2. Subsequently in section 3.3 a brief discussion of the data processing flow of the software framework, called GEANA, used for the analysis presented in this work, is provided. The procedure performed to monitor the long term energy resolution and data quality performance of the measurements is introduced in section 3.4. Finally the different run configurations during the first phase, Phase I, of the experiment are summarized and the resulting physics data are discussed in terms of the expected sensitivity of the experiment in the last two sections 3.6 and 3.5 of this chapter.

3.1   Setup description and detection principle

As illustrated in figure 3.2 a), the experiment site is chosen to be located at Hall A of the INFN Laboratori Nazionale del Gran Sasso (LNGS) in a depth of 1400 m, where the surrounding rocks correspond to an average of about 3400 m of water equivalent (m.w.e.) from all directions. Functioning as a vast shielding against cosmic rays, the Gran Sasso massif allows to suppress the flux of muons compared to that at the surface by about six orders of magnitude.

Figure 3.2 b) shows a schematic view of the experimental setup, where the Ge-detector array is deployed naked and submersed in 64 m³ of liquid argon (LAr), which serves as closeby shield against radioactivity from external sources and as cooling medium at the same time. Using this design, instead of installing the detectors alternatively in a customary vacuum cryostat (as it has been done in HdM and IGEX), provides the benefit of further reducing the background to a significantly lower level. Both, the germanium crystals and the LAr coolant, are contained in a low-activity stainless steel cryostat (^{232}Th and ^{238}U are far below 1 mBq/kg) of 4.16 m diameter and 5.88 m height (if the neck is not included). A coating of high-purity copper covers the inner surface of the cryostat walls and marks the very next shield layer for the sake of a low background environment.

The shielding consisting of several components is finally completed by an outer water tank of 10 m diameter and 8.3 m height (corresponding to a nominal capacity of 590 m³) filled with purified H$_2$O, which is envisaged to reduce the neutron flux arising from the huge amount of rocks/concrete surrounding the laboratory. Additionally the water is used as an active scintillation veto against remnant high-energy muons
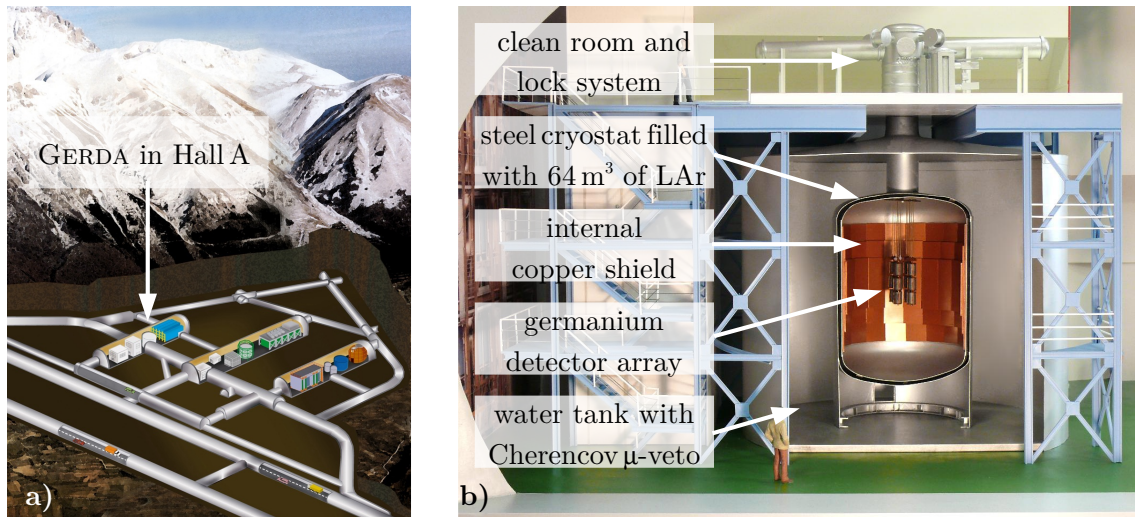

Figure 3.2: a) Location of the GERDA experiment in Hall A at the Laboratori Nazionale del Gran Sasso (LNGS) underground laboratory. **b)** Schematic view of the GERDA experiment with the enriched germanium detector array not in scale. The main parts, as discussed in the text, are superscribed.

by the detection of their Cherencov light with 66 photomultiplier tubes. Since the suppression due to the water tank is expected to be less efficient for muons entering from the top, a second part of the veto system composed of 36 plastic scintillator panels is arranged on the roof of the GERDA setup to also sufficiently shield the neck region of the cryostat (for more information regarding this topic see [Kna09][Rit11]).

The mounting scheme of the germanium detectors holds as well some challenging requirements, as the holder structure has to be constructed out of as little material as possible to minimize sources of radiation near the crystals. On the other hand, still a save suspension and sufficient support of the cables for detector bias and read-out has to be accomplished (a detailed study on this issue is given in [Bar09b]). On this basis, low mass detector holders made of only selected high radiopurity materials (about 80 g copper, 10 g PTFE and 1 g silicon) have been developed, which can be connected to strings and assembled in an array. The detector handling, or in particular, the installation and lowering into the LAr, is thereby performed using a lock system located in a clean-room (class 10.000) on top of the cryostat/water tank structure. For a description 'in-depth' about the design, construction and first operational results of the GERDA experiment [Ack13] is recommended.
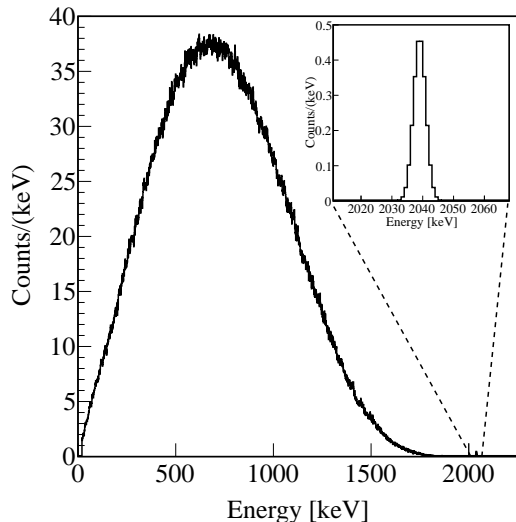

Figure 3.3: Simulated spectrum for the sum of electron energies from the neutrino-accompanied and neutrinoless double β-decay in ^{76}Ge. The energy spectrum of the $2\nu\beta\beta$-decay (here: scaled according to the "golden" data set of Phase I, for more information on the different data sets see upcoming section 3.6.1) is continuous since neutrinos that escape do carry parts of the total energy with them, whereas the signature of the $0\nu\beta\beta$-decay (here: normalized by the current upper limit on the half-life $T_{1/2}^{0\nu}$) is a monoenergetic line at $Q_{\beta\beta} = 2039\,\text{keV}$ (see inset at top right).

Howbeit, according to the detection scenario, the $0\nu\beta\beta$-signal is caused by a full absorption of the two ejected electrons inside the active detector material. In figure 3.3 a Monte Carlo simulation[1] of the expected double β-decay distribution of ^{76}Ge is shown true to scale for the "golden" data set of the first phase of data taking within the GERDA experiment, including six of the enriched of the enriched HPGe detectors from the Heidelberg-Moscow and IGEX experiments with an exposure-averaged $FWHM$ energy resolution of 4.8 keV (the terminology of the different data sets will be explained in section 3.6.1). The continuous $2\nu\beta\beta$-spectrum features an

---

[1]Monte Carlo simulations for the GERDA experiment are performed with MAGE, a general and flexible GEANT4 based framework that has been developed in a joint effort with the MAJORANA Collaboration [Ago03][All06][Bos11].

energy deficit towards the $Q_{\beta\beta}$-value of the germanium isotope, since the neutrinos escape with parts of the total energy released by the decay. In event of the hypothetical $0\nu\beta\beta$-decay, where no neutrino are left to escape, the measured electron energy amounts instead to a monoenergetic peak at $Q_{\beta\beta} = 2039\,\mathrm{keV}$. Hereby the signature is normalized with respect to the ratio of the known half-life $T^{2\nu}_{1/2}$ for the neutrino-accompanied decay to the currently best upper limit $T^{0\nu}_{1/2}$ for the concurrent neutrinoless mode. In order to resolve the two distributions, the region of interest (ROI) close to the $0\nu\beta\beta$-signal has to be kept quasi background free. Unfortunately in spite of all possible precautions an irreducible background will be always present due to the $2\nu\beta\beta$-decays occurring up to the energy of $Q_{\beta\beta}$. In this respect the plot also stresses the importance of the energy resolution, which is for the GERDA experiment obviously sufficient enough to distinguish the peak from the high energy tail of the broad spectrum (see inset at the top right).

3.2 Germanium detectors

When operating high-purity germanium detectors (HPGe) for the neutrinoless double β-decay search, several absolutely essential advantages engender straightaway (remember that still the most stringent experimental limits were achieved with this detection technique):

As detector material for semiconductors, germanium does not only provide a prominent spectroscopic performance with an excellent energy resolution of $\sim 0.1\%$ at $Q_{\beta\beta}$ and several powerful background rejection techniques (for instance pulse shape analysis, segmentation) but is as well available in neato intrinsic radio-purity. Also a very high detection efficiency is on hand, since the germanium crystals act simultaneously as detector and as source for the $0\nu\beta\beta$-decay. Not to forget about HPGe detectors being a well known, commonly used technique, thus well established for long-term γ-ray spectroscopy experiments. All in all, reasons enough to particularly thematise aspects like the functional principle, material properties or the main mechanisms of signal formation and read-out of semiconducting germanium detectors in the following section. A detail-rich review on semiconductors or radiation detection and measurement techniques in general, that covers - if not pointed out otherwise - most of what will be presented below, can be found in [Kno89].

3.2.1 Semiconductor properties

Band structure: In principle solids can be classified into three different types depending on their conduction properties: insulator, semiconductor and conductor (like any metal). The ability of conduction is thereby defined by the periodic lattice of the crystalline substance, which evokes allowed energy bands for electrons that exist within that solid. A simplified depiction of the two main distinguishable band structures corresponding to the non-metallic types of solid is shown in figure 3.4. Here

those electrons that are bound to specific lattice sites inside the material via covalent bonding are represented by the lower band, namely the *valence band*. In the next higher-lying, so-called *conduction band* electrons can instead freely migrate through the crystal and contribute therefore to the electrical conductivity of the material. Furthermore the two bands are separated by a forbidden *bandgap* of distinct size, determining the material to be of non-, semi- or conducting type.

Typically for an insulator the width of the bandgap, or to be precise, the bandgap energy E_g is bigger than $5\,\text{eV}$, whereas semiconductors exhibit considerably less gabs in the range of $\sim 1\,\text{eV}$. The amount of electrons is just enough to completely fill all available sites of the valence band, so that in absence of thermal excitation, at zero temperature, insulators as well as semiconductors are characterized by a configuration where the valence band is fully occupied and the conduction band is completely empty. Thus neither of them would feature any electrical conductivity. In a metal, the other way around, electrons can easily drift throughout the substrate with only very few additional energy needed (no bandgap has to be crossed), since the highest occupied energy band is not entirely filled. As a result, conductors usually show very high electrical conductivities.
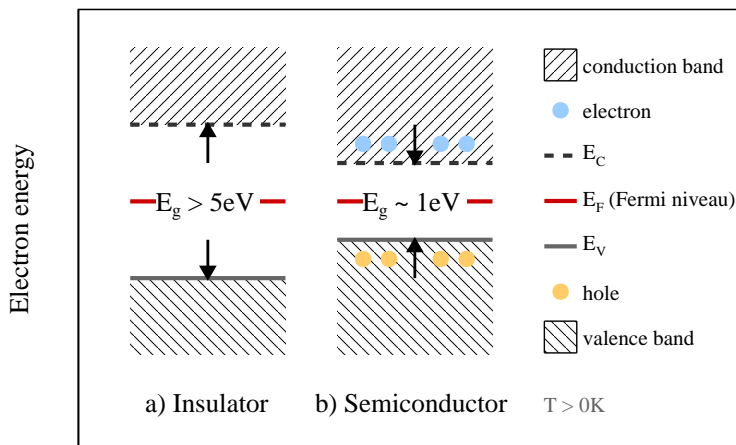

Figure 3.4: Simplified model of the band structure in **a)** insulators and **b)** semiconductors. For the latter, the thermal energy is just adequate to promote electrons to the higher-lying conduction band under the simultaneous creation of an appendant hole in the valence band.

Charge carriers: However, at non-zero temperature $T > 0\,\text{K}$, electrons of a non-metal share a certain thermal energy, such that some valence electrons do indeed gain sufficient energy to be lifted into the conduction band. So from a physical point of view, an electron which is normally part of a covalent bond experiences an excitation, leaves the specific bonding site and can move unopposed inside the crystal. In this excitation process, not only an electron in the formerly empty conduction band, but also a vacancy or *hole*, representing a net positive charge, in the otherwise full valence band is generated. The combination of both is usually called an *electron-hole* pair.

The thermal equilibrium concentration n_0 of the electrons in the valence band can be derived by integrating over the product of the density of conduction electron states and the probability that an available state at energy E is occupied. Of course the same argumentation also applies for the calculation of the hole density p_0. Using

the Fermi-Dirac distribution function $f(E,T)$ for electrons and $1 - f(E,T)$ for holes with the approximations

$$f(E,T) \;=\; \frac{1}{\mathrm{e}^{(E-E_{\mathrm{F}})/k_{\mathrm{B}}T}+1} \approx \mathrm{e}^{-(E-E_{\mathrm{F}})/k_{\mathrm{B}}T} \text{ for } E > E_{\mathrm{F}}$$

$$1 - f(E,T) \;=\; \frac{1}{\mathrm{e}^{(E_{\mathrm{F}}-E)/k_{\mathrm{B}}T}+1} \approx \mathrm{e}^{-(E_{\mathrm{F}}-E)/k_{\mathrm{B}}T} \text{ for } E < E_{\mathrm{F}} \tag{3.3}$$

then yields [Hun11]

$$n_0 \cdot p_0 = 4 \left(\frac{k_{\mathrm{B}}T}{2\pi\hbar^2} \right)^3 (m_n^* \cdot m_p^*)^{3/2} \, \mathrm{e}^{-E_{\mathrm{g}}/k_{\mathrm{B}}T} \; , \tag{3.4}$$

where T is the absolute temperature, k_{B} the Boltzmann constant, E_{F} the Fermi energy defining the energy level of 50% occupation and $m_{n,p}^*$ the effective mass characteristic of the used material for the electron or hole. As elucidated by the exponential term of equation 3.4 the electron-hole concentration due to thermal excitation is crucially dependent on the ratio of the bandgap energy E_{g} to the absolute temperature T. Consequently, substrates with a large bandgap (like insulators) will have a low charge concentration $n_0 \cdot p_0$ due to thermal energy and therefore show a negligible electrical conductivity. But in the special case of materials with relatively small bandgaps, sufficient energy can be procured to cause a conductivity significant enough to be classified as semiconductor.
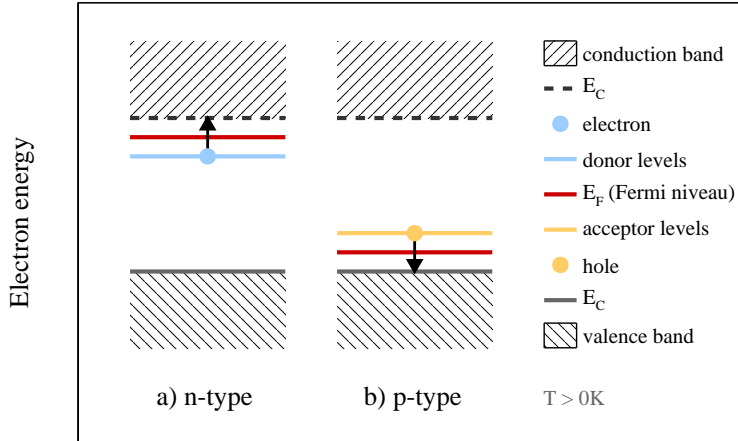

Figure 3.5: Schematics for the **a)** n-type and **b)** p-type semiconductor created by an impurity with one surplus or fewer valence electron occupying a substitutional site in the crystal along with the corresponding donor and acceptor levels.

Effect of dotation: A completely pure semiconductor, where each electron that is raised into the conduction band leaves a hole in the valence band, is called an *intrinsic* semiconductor. In practice, such a kind of material is impossible to generate, leaving the residual impurities, whatever rare they may be, to dominate the electrical properties of a "real" material. This as well accounts for germanium semiconductors, which are available in the highest practical purity. But it is also possible to take advantage of this circumstance via adding surplus electrons or holes resulting from deliberate contamination to increase the conductivity. In a solid doped with a *donor* impurity or atom with one extra valence electron, the number of lightly bound

electrons is excessed, generating a n-type superconductor. These "loose" electrons can occupy quite high energy levels within the initially forbidden bandgap making it easier to energetically lift them into the conduction band. Vice versa *acceptor* impurities feature one fewer valence electron compared to the surrounding atoms, so that covalent bonds remain unsaturated and result in a vacancy similar to a hole. As the energy differences between the top of the valence band and the acceptor sites are typically quite small, a large fraction of these vacancies gets filled by thermally excited electrons. Hence in this kind of semiconductors, that is said to be of p-type, conduction partly happens in the valence band. The influence of n- or p-type dotation on the energy levels of the donor and acceptor sites as well as the Fermi niveau is illustrated in figure 3.5.
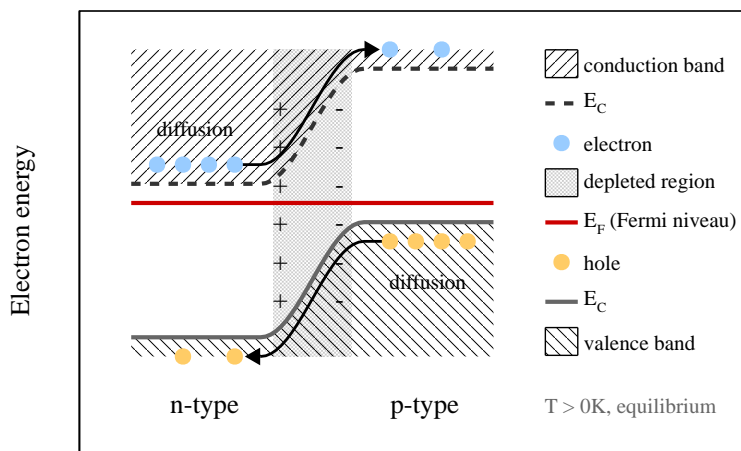
Figure 3.6: Schematic energy band diagram of a n-p junction in thermal equilibrium. With respect to one another, valence as well as condiction band edges are shifted across the junction by the potential difference V_C resulting from the contact between n- and p-type material.

N-p junction: In order to construct a convenient radiation detector composed of a semiconductor, a junction as shown in figure 3.6 between n- and p-type material is required. Due to the strikingly increased density of conduction electrons in the n-type material on the left and of holes in the p-type material on the right, respectively, a net diffusion across the junction from regions of high concentration to those of lower concentration takes place to compensate the sharp gradient of electric potential. As the electron-hole pairs quickly annihilate, they leave positively and, likewise on the opposite side of the n-p interface, negatively charged immobile ions. That is why, in regions nearby the junction (where free charges do not exist anymore), neutrality becomes extinct with a net positive space charge on the n-side and a net negative space charge on the p-side. The more charge is accumulated the more increases the resulting electric field and the tendency for further diffusion decreases continuously. At equilibrium, when the field is just about sufficient to suppress additional net diffusion across the interface, a region of stationary charge imbalance, called *depletion layer*, is established.

Consequently, any electron-hole pair, which is created by ionizing radiation depositing energy within the depleted layer, will drift in the electric field fromwards the region of charge imbalance. With their motion, influence charges engender at the contacts and an electrical signal is created making n-p junctions a very attractive

detection technique. But still, eventhough such an unbiased semiconductor diode functions as a detector, it would show a very poor performance for several reasons. For instance, the contact potential V_C in the order of $\sim$1 V resulting from the junction of the n- and p-type semiconductor material is by far too small and generates electric fields of insufficient strength, so that charge carriers can get lost to a non-negligible extend owing to trapping or recombination. Besides incomplete charge collection, the performance of an unbiased interface is also limited by the very small depletion region as well as the high capacitance involving fatal noise behaviour. This can be eluded by operating the semiconductor diode reverse biased with an applied external voltage V_{bias} that is large compared with the contact potential ($V_{\mathrm{bias}} \gg V_C$). In case of reverse biasing, the natural potential difference from one side of the junction to the other is then greatly enhanced by a factor $(V_C + V_{\mathrm{bias}})/V_C \approx V_{\mathrm{bias}}/V_C$ such that only minority carriers (meaning holes on the n-side or electrons on the p-side) are conducted across the junction. In this way, the n-p junction serves as a rectifying device that allows a relatively unimpeded flow of current in one direction but effectively blocks charge movements in the opposite direction. As an additional positive effect, also the width d of the depletion layer, which confines the active volume of the detector, is noticeably increased. The effect is directly proportional to the square root of the external bias voltage and can be estimated by the relation

$$d \approx \sqrt{\frac{2 \cdot \epsilon \cdot V_{\mathrm{bias}}}{e \cdot P}} = \sqrt{2 \cdot \epsilon \cdot V_{\mathrm{bias}} \cdot \mu \cdot \rho}\,, \tag{3.5}$$

where ϵ is the dielectric constant, μ the mobility and $\rho = 1/(\mu \cdot e \cdot P)$ the resistivity, which depends on the impurity concentration P of the material. To achieve the largest depletion thickness possible for a given applied voltage, it is therefore favourable to have a very high resistivity, tantamount to a very low concentration of impurities. A large applied voltage is not only advantageous for the size of the depletion layer, but also positively affects the detector capacitance

$$C = \frac{\epsilon}{d} \approx \sqrt{\frac{e \cdot \epsilon \cdot P}{2 \cdot V_{\mathrm{bias}}}} = \sqrt{\frac{\epsilon \cdot \rho}{2 \cdot V_{\mathrm{bias}}}} \tag{3.6}$$

to become as small as possible and thus allows to measure an ionization induced charge signal well above the noise level. Here equation 3.6 is only valid prior to the configuration of full depletion, when the depletion depth covers the entire provided material [Kno89].

3.2.2 Interaction of particles with matter

When a particle - heavy-charged, light-charged or uncharged, like a photon - passes through the active volume of a n-p junction, the ultimate effect is a deposition of energy and the subsequent production of electron-hole pairs along the track that can be detected by the semiconducting diode. However, different particles show also different interaction mechanisms with matter and significantly varying processes of energy deposition, making it necessary to regard them separately.

Heavy-charged particles, like for instance α's, interact mainly electromagnetically and loose their energy through processes like ionization and excitation of atoms. Thereby the average energy loss per unit length $\mathrm{d}E/\mathrm{d}x$ strongly depends on the product of the number density N and atomic number Z of the absorber as well as on the charge z of the primary particle and can be expressed by the *Bethe formula*

$$-\frac{\mathrm{d}E}{\mathrm{d}x} = \frac{4\pi e^4 z^2}{m_e c^4} N Z \left(\ln\frac{2m_e v^2}{I} - \ln(1-\beta^2) - \beta^2 \right). \tag{3.7}$$

Here I denotes the average ionization and excitation potential of the absorber atom. The other quantities e, m_e and v describe the charge, rest mass and velocity of the electron, respectively, whereas $\beta = v/c$ is simply used as short cut for the ratio of the velocity and the speed of light c. Since the particle randomly undergoes various microscopic interactions, energy loss symbolizes a statistical process, where the width of energy distribution varies with the passed distance. Anyhow, several implications are revealed by the above expression: First, materials with high atomic number plus density will eventuate in the most effective stopping power and, secondly, particles with greater charge will suffer a more enhanced absorption rate than less charged ions of the same velocity. The progression of the specific energy loss $-\mathrm{d}E/\mathrm{d}x$ versus particle energy is illustrated in figure 3.7 for a helium-4 or α ion along its track in germanium. An explicit maximum for energies around $1\,\mathrm{MeV}$ can be seen. Also plotted in figure 3.7 is a calculation of the average range curve with respect to the particle energy, where a continuous-slowing-down approximation has been performed by integrating the reciprocal of the total stopping power [Ber05]. Typical energies of α particles emitted in an radiative process vary between mostly $1-10\,\mathrm{MeV}$, yielding very short penetration depths in the range of $\sim 10\,\mu\mathrm{m}$.
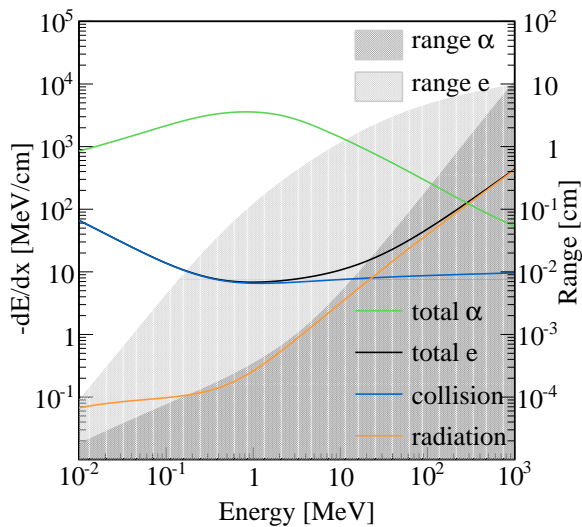

Figure 3.7: Stopping power and range as a function of energy in germanium as absorber. The total energy loss of a heavy charged helium-4 ion (green) and a lightly charged electron (black) are depicted, in case of the electron also the particular contributions, collisional (blue) and radiative (orange), are shown. Further the different gray shades display the respective range-energy curves of the α and e particle. For the calculations data from [Ber05] (online database) was used, assuming a density of $5.32\,\mathrm{g/cm^3}$ for germanium.

Light-charged particles as electrons or positrons do in principle show the same interaction mechanisms like heavy-charged particles. In direct comparison they lose energy at a much lower rate though (at least for moderate energies below $100\,\mathrm{MeV}$,

see figure 3.7). Hence, in order to derive the average energy loss per unit length evoked by collisions equation 3.7 has to be modified and is written

$$-\left(\frac{\mathrm{d}E}{\mathrm{d}x}\right)_{\mathrm{col}} = \frac{2\pi e^4 NZ}{m_\mathrm{e}v^2}\left(\ln\frac{m_\mathrm{e}v^2 E}{2I^2(1-\beta^2)} \ - \ \ln 2\cdot\left(2\sqrt{1-\beta^2}-1+\beta^2\right)\right.$$
$$\left. + \ (1-\beta^2)+\frac{1}{8}\left(1-\sqrt{1-\beta^2}\right)^2\right) \quad (3.8)$$

with E representing the electron energy. For an increasing energy, electrons more and more tend to additionally experience radiative processes in form of *bremsstrahlung* or electromagnetic radiation when being accelerated, equivalent to any kind of deflections or scattering. The specific energy loss caused by radiation is then

$$-\left(\frac{\mathrm{d}E}{\mathrm{d}x}\right)_{\mathrm{rad}} = \frac{NEZ(Z+1)e^4}{137m_\mathrm{e}c^4}\left(4\ln\frac{2E}{m_\mathrm{e}c^2}-\frac{4}{3}\right). \quad (3.9)$$

By summing both contributions up, one can calculate the total stopping power for electrons $(\mathrm{d}E/\mathrm{d}x) = (\mathrm{d}E/\mathrm{d}x)_{\mathrm{col}} + (\mathrm{d}E/\mathrm{d}x)_{\mathrm{rad}}$. In figure 3.7 the total specific energy loss and its separate contributions from the collisional and radiative processes as well as the average penetration depth of the electron are depicted as a function of E for germanium as stopping material. An electron, for example, ejected during a hypothetical $0\nu\beta\beta$-decay that carries an initial energy of $Q_{\beta\beta} = 2.039\,\mathrm{MeV}$ will traverse a mean distance of $\sim 2.5\,\mathrm{mm}$ until it is completely halted.

Photons or γ-rays are emitted when excited nuclear states, evoked by the decay of a parent nuclide, transition into lower-lying levels. Because the daughter nucleus deexcitates into its ground state after one or several state-to-state transitions between quantized energy levels, the radiated γ particles do carry characteristic, well-defined energies assignable to a specific isotope. In principle the interaction with matter is dominated by three major mechanisms, whose cross-sections are energy dependent:

- In case of lower energies *photoelectric absorption* plays the most important role. In this process the incident γ undergoes an interaction with an atom by transferring its entire energy to an orbital electron, which is ipso facto freed from the atomic bound. As a consequence a *photoelectron* gets ejected with a kinetic energy $E_\mathrm{e} = h\nu + E_\mathrm{b}$, given by the incident photon energy $h\nu$ minus the binding energy E_b of the electron in its original shell, and the absorber atom is ionized. Thereby the vacancy in the electron shell is rapidly filled by electron rearrangement and the redundant energy - in turn - released in form of either an Auger electron or a characteristic radiation ($=$ *X-ray fluorescence* that can create, when being reabsorped, further Auger electrons). In the end, the process of photoelectric absorption is ultimately reducible to the liberation of photoelectric electrons along with several low-energy electrons. Assuming an ideal scenario, where the entire kinetic energy of the electrons is fully absorbed in the detector, the corresponding signal in the recorded spectrum will show up as a *full energy peak* (FEP) equal to the incident photon energy.
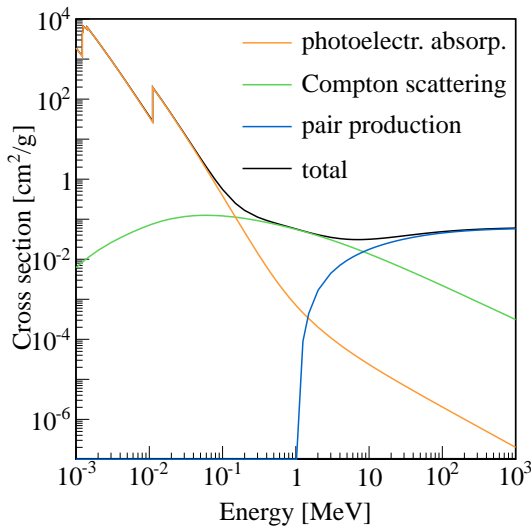
Figure 3.8: Total photon cross sections as a function of energy with germanium as absorber material. Data are taken from [Ber10] (online database). The main contributions, here emphasized in different colour code, are the photoelectric effect (orange, dominant for energies $> 10^{-1}$ MeV), Compton scattering (green, dominant for energies $< 10^{-1}$ MeV and < 10 MeV) and pair production (blue, dominant for energies > 10 MeV).

- For intermediate energy regions the predominant interaction mechanism is the *Compton scattering* between a photon and an electron accompanied by a partial energy transfer. The amount of energy conveyed in this process is closely related to the angle θ by which the γ is deflected compared to its incident direction. When availing the conservation of energy and momentum, the correlation

$$h\nu' = h\nu \cdot \left(1 + \frac{h\nu}{m_\mathrm{e}c^2}(1 - \cos\theta)\right)^{-1} \tag{3.10}$$

  in terms of the original photon energy $h\nu$ and the outgoing photon energy $h\nu'$ can be derived, where $m_\mathrm{e}c^2$ represents the rest mass of the electron. Equation 3.10 also allows to draw conclusions on the energy that is transferred from the γ to the recoil electron. Since the difference of incoming and outgoing photon energy becomes maximal for a scattering angle of $\theta = \pi$, one obtains a maximum possible electron energy according to $E_\mathrm{e,max}|_{\theta=\pi} = 2h\nu/(m_\mathrm{e}c^2 + 2h\nu)$. In a radiation detector usually all scattering angles occur and a continuous energy distribution, ranging from zero up to the predicted maximum, will arise. In practice this behaviour is directly observable as a *Compton edge* (CE) in the energy spectrum. Apart from the so far explained *single* Compton scattering, the gap between Compton edge and full energy peak can be, to some extend, filled by an additional event type of so-called *multiple Compton scattering* (MCS) events.

- The third physical interaction, *pair production*, can only occur in the electric field near the atomic nuclei and corresponds to the complete disappearance of the incident photon. In its place, an electron-positron pair with a rest mass of $2m_\mathrm{e}c^2$ is produced. Therefore a minimum γ energy of at least 1.022 MeV is required to make this process energetically possible. Any abundant energy above this critical value appears in form of kinetic energy equally shared among the electron and positron. As the positron is not a stable particle, it will

annihilate with another electron once its kinetic energy is reduced to a certain point due to thermalization. The result are two annihilation γ's of energy $m_ec^2 = 0.511$ MeV each, moving in exact opposite direction to preserve the conservation of mommentum. From now on three different border cases, which occur quite frequently, are conceivable: If the entire energy of both annihilation γ's is deposited in the detector, events arise that accumulate to the full energy peak discussed previously. In another detection prospect, only the energy of one γ is completely absorbed but the other escapes without any interaction in the active material, resulting in the *single escape peak* (SEP) that appears at an energy of $m_ec^2 = 0.511$ MeV below the FEP in the spectrum. If even both annihilation γ's manage to escape unaltered, another, so-called *double escape peak* (DEP), reduced by an energy of $2m_ec^2 = 1.022$ MeV with respect to the FEP, is engendered. Events where the photons are instead partially translated into electron energy, e.g. via Compton scattering, rather contribute to a broad continuum.

In figure 3.8 the contributions of the above described three major interaction types to the total photon cross section are depicted explicitly for germanium as a function of energy.

3.2.3 Germanium as detector material

[76]Ge is one of the few isotopes that undergoes the double β-decay and is therefore favourably used as source (and detector material) in the GERDA experiment to search for the, next to the two neutrino emitting, also hypothetically possible, but much rarer neutrinoless decay mode. Apart from $0\nu\beta\beta$-research, germanium is also a reasonable choice for common high-resolution radiation detectors because of its advantageous semiconductor characteristics (some have been already mentioned at the beginning of this section). In table 3.1 the main properties of natural germanium relevant for γ-spectroscopy are summarized.

Atomic number Z		32
Density	[g/cm^3]	5.32
Band gap E_g	[eV]	0.665
Pair creation energy E_{pair}	[eV]	2.96
Fano factor F		0.129
Dielectric constant ϵ	[F/m]	1.4×10^{-10}
Electron mobility μ_e	[cm^{2}V^{-1}s^{-1}]	3.6×10^4
Hole mobility μ_h	[cm^{2}V^{-1}s^{-1}]	4.2×10^4

Table 3.1: Properties of natural germanium [Kno89]. The Fano factor F, electron-hole pair creation energy E_{pair} and mobilities $\mu_{e,h}$ are given for the liquid nitrogen temperature of 77 K, whereas all other values are valid for room temperatures at $T = 300$ K.

By featuring a higher atomic number and density, germanium yields increased absorption coefficients for all significant interaction processes of the main particles

in matter compared with silicon, which is predominantly used for the majority of conventional applications. This behaviour can be directly retrieved from equations 3.7, 3.8 or 3.9 for heavy- and lightly-charged particles, but also accounts in particular for γ-radiation that is converted into electron energy via the tree main processes photoelectric absorption, Compton scattering and pair production. As also mentioned earlier, out of all conceivable detector materials, germanium can be manufactured in the very purest conditions and techniques capable of reducing the impurity level to approximately $\sim 10^{10}$ atoms/cm^3 have been developed. According to equation 3.5 this immediately allows the largest widths of a depletion layer for a given bias voltage possible. Typically the maximum applicable high voltage is limited by breakdown of the diode blocking to regions up to about 5 kV, depending on the particular detector, so that depletion depths of several centimeters can be achieved. The combination of its superior absorption characteristics and the considerably larger active volumes thus provides a remarkable detection efficiency for germanium semiconductors.

Further from equation 3.6 follows, that operating germanium also offers the smallest value for the capacitance (since it is producible with very low impurity concentration P) and therefore the best noise level when using the largest applied voltage possible up to the point where the detector becomes fully depleted.

As noted in table 3.1, for germanium the energy difference of $E_g = 0.67$ eV between the conduction band and the valence band is comparatively small and already in the order of a region where thermal excitation is relevant in a way that the detector properties will be significantly deteriorated. Because of this thermally induced *leakage current* spoiling the energy resolution performance, detector handling at room-temperature is impossible. By implication, a reduction of the operational temperature is absolutely necessary and normally accomplished by cooling mediums like liquid nitrogen (LN$_2$), with a temperature of 77 K, or liquid argon (LAr) of $T = 87$ K.

But in the exceptionally low width of the energy gap, even if compared with other semiconducting materials or compounds like Si ($E_g = 1.12$ eV), InP ($E_g = 1.35$ eV) and GaAs ($E_g = 1.43$ eV), also lies the reason for the excellent energy resolution. The less energy is needed to promote an electron into the conduction band, the bigger the mean number and smaller the fluctuation or variance of charge carriers (here electron-hole pairs), which are generated within a single energy deposition, becomes. As a result the signal-to-noise ratio is improving with the amount of created "information" carriers. Thereby the ionization process is limited by the discrete atomic shell structure. Furthermore, careful measurements of the energy resolution have also manifested the process, that gives rise to the creation of the individual charge carriers, to be not completely independent and thus not predictable by pure *Poisson* estimations. As a measure for the deviation of the observed statistical fluctuations as well as the number of charge carriers from a simple Poisson process, the so-called *Fano factor F* has been introduced. The net result is a statistical limit on the *full width half maximum* (FWHM) resolution $R_{\text{statistical}}$ for measuring the particle energy E as

$$R_{\text{statistical}} = 2.35\sqrt{\frac{F \cdot E_{\text{pair}}}{E}} \ , \tag{3.11}$$

where the factor of 2.35 relates the standard deviation σ to the FWHM $= 2.35 \cdot \sigma$. On average, in a semiconductor the pair excitation energy E_{pair} has been empirically found to be about $3-4$ times larger than the band gap energy E_{g}. This circumstance is attributed to the requirement on the conservation of energy and momentum with the excess energy thermalizing via additional phonon emission [Ali75].

Supplementary, the relatively high mobilities for electron as well as holes in germanium facilitate charge carriers to move very rapidly in a given electric field, which prevents trapping and recombination. By that complete charge collection in even large detector volumes can be enabled.

3.2.4 High Purity Germanium (HPGe) diodes

High Purity Germanium (HPGe) diodes are usually operated in a fully depleted mode, where the electrical contacts are provided by introducing abundant doping impurities at the surface of the semiconductor. This can be either managed with evaporation, diffusion or ion implantation.

For a p-type material, a $n+$ layer of high donor concentration acts as the first n-p junction and is formed by doping the germanium with interstitial lithium atoms via diffusion onto the appropriate parts of the detector, resulting in a fast falling concentration profile starting from saturation at the surface. This creates a conductive contact, which is typically rectifying, meaning majority charge carriers (here electrons) can move unhindered, and initiates the depletion caused by the applied positive bias voltage. The $n+$ layer itself represents a roughly 1 mm wide inactive region at the outer surface that can not be depleted and is therefore also called *dead layer*. However, as one important advantage this thick electrode allows to effectively absorb external contaminations arising from α-, β- or low energy γ-radiation, as their penetration depths are comparatively shorter than the width of the dead layer (see figure 3.7). The second, hole-collecting $p+$ contact is used as read-out electrode and serves simultaneously as blocking junction for the minority carriers. In practice, the $p+$ layer is generated by ion-implantation of boron atoms onto the surface with a very thin thickness in the order of several $0.1\,\mu$m. Hence it does (different from the n+ layer) not in the least prevent incident external radiation from depositing energy in the detector.

In the alternative case of n-type materials, the two doped layers are arranged inversely. Apart from these general considerations, HPGe detectors are available in a number of different geometries from which particularly two special configurations are deployed in the GERDA experiment.

Coaxial configration: The need for the largest active volumes possible with manageable depletion voltage, favours a cylindrical detector geometry where the core of the crystal is either removed completely (*true-coaxial*) or partially (*semi-coaxial*),

leaving a central bore. The $p+$ and $n+$ contacts are then located inside the bore-hole and on the mantle, respectively, such that the depleted zone grows from the outer surface inwards when applying the reverse bias voltage. An additional groove separates the conductive "wrap-around" lithium layer from the boron implanted hole.

The capacitance C, which has a huge effect on the energy resolution, strongly depends on the shape and dimensions of the detector, like the height h or the inner, outer radii r_1, r_2. When comparing a fully depleted true-coaxial diode with a cylindrical capacitor, one retrieves

$$C = \frac{2\pi\epsilon h}{\ln(r_2/r_1)} \ .$$ (3.12)

To minimize the capacitance, the radius r_1 of the central core is usually reduced to a minimum, consistent with feasible fabrication techniques for a suitable electrical contact. In case of semi-coaxial detectors, the capacitance is slightly different though, but equation 3.12 still represents a reasonable approximation.

Within the period of commissioning and Phase I of the GERDA experiment, in total a number of 13 coaxial HPGe detectors have been employed, five made from natural germanium and eight from material isotopically enriched in the isotope ^{76}Ge (see also section 3.5.1). Out of these, all have been operated in preceding experiments from Heidelberg-Moscow, IGEX as well as GENIUS-TF and were originally

detector name	total mass [kg]	^{76}Ge abundance [%]	total height h [mm]	outer radius r_2 [mm]	inner radius r_1 [mm]	bore hole depth [mm]	dead layer [mm]	bias voltage [kV]
ANG1	0.958	85.9(29)	68	29.25	6.75	51	1.8	4.0
ANG2	2.833	86.6(25)	107	40	7	94	2.3	3.5
ANG3	2.391	88.3(26)	93	39	7.5	83	1.9	3.5
ANG4	2.372	86.3(13)	100	37.5	7	89	1.4	3.5
ANG5	2.746	85.6(13)	105	39.25	6.25	94	2.6	2.5
RG1	2.110	85.51(10)	84	38.75	6.75	73	1.5	4.5
RG2	2.166	85.51(10)	84	38.75	6.5	72	2.3	4.0
RG3	2.087	85.51(10)	81	39.5	6.5	71	1.4	3.3
GTF32	2.321	7.8(1)	71	44.5	6	41.5	–	3.0
GTF42	2.467	7.8(1)	82.5	42.5	5.75	42.5	–	–
GTF45	2.312	7.8(1)	75	43.5	5.75	43	–	3.0
GTF110	3.046	7.8(1)	105	42	5.75	69	–	3.5
GTF112	2.965	7.8(1)	100	42.5	5.75	63	–	3.0

Table 3.2: Characteristics for the Phase I enriched and natural detectors of coaxial configuration. Values for the isotopic abundances in ^{76}Ge are taken from [Ack13] with their 1σ uncertainties being given within parentheses. All other numbers for total masses, dimensions and bias voltages can be found in [Bar09b].

manufactured by ORTEC. Before their application in GERDA, the detectors passed through a complete refurbishment at Canberra Olen, including a change of the electrode geometries and surface treatments to optimize the operational performance in LAr [Bar09b]. All main current dimensions, total masses and abundances in ^{76}Ge of the specific detectors *after* the modifications are reported in table 3.2 along with the applied bias voltages during operation.

Moreover, a schematic cross section of a semi-coaxial detector is depicted at the top of figure 3.9 a) with a color profile of the weighting potential overlayed. The latter constitutes the induced signal at the read-out electrode for an energy deposition with subsequent (electron-hole) charge drifting at a given position in the diode [He01] and
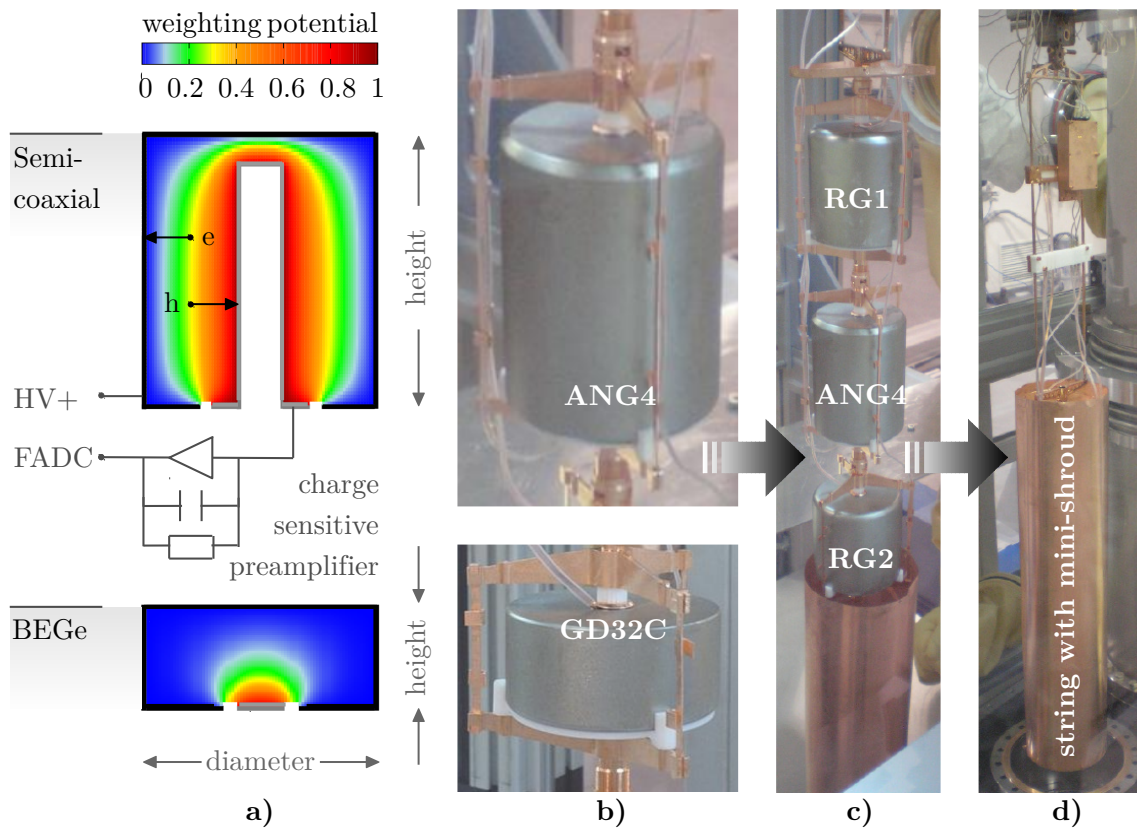
Figure 3.9: **a)** Schematic cross section of a semi-coaxial (top) and a BEGe (bottom) detector, where the $p+$ and $n+$ layers are drawn in gray and black, respectively (thicknesses not to scale). Also shown is the insulating groove separating the electrodes and an overlayed weighting potential [He01] with indicated color profiles. Further the read-out with a charge sensitive preamplifier is sketched for the case of the semi-coaxial detector. **b)** Photographic image of the ANG4 (top) and the GD32C (bottom) detector (exemplarily for the semi-coaxial and BEGe configuration) mounted upside down in a low-mass holder. **c)** String of three enriched semi-coaxial crystals (RG1, ANG4 and RG2) that is inserted into the copper mini-shroud. **d)** Finally closed detector string with a three channel CC2 preamplifier stored inside a copper box about 30 cm above the uppermost diode. The detectors are connected to the amplifier and the bias voltage supply by Teflon insulated copper stripes.

is defined by the electric field distribution based on the detector geometry. As can be seen, the weighting field peaks at the inner $p+$ contact (grey) and decreases with a low gradient towards the outer $n+$ layer (black). Hence a large portion of the volume, where electrons and holes both have significant influence, contributes to the current signal. The marked length of the diameter (at the bottom) corresponds to two times the outer radius r_2 of a coaxial detector.

BEGe configuration: In order to increase the active mass, an additional set of $\sim$30 new germanium detectors assigned for Phase II has been produced, of which five have already been operated for part of Phase I (see table 3.3 and the corresponding caption for further information regarding characteristics like total mass, dimensions, isotopic abundances or bias voltages). For this purpose a special geometry called *Broad Energy Germanium* (BEGe) type was chosen, whereas the name refers to the exceptionally wide energy range the detector is sensitive to. Like the coaxial variant from above, the BEGe detectors are fabricated from HP Ge enriched in the isotope ^{76}Ge, but instead of a bore hole the $p+$ layer is represented by a point like contact on one of the flat surfaces of the cylinder. Again the electrode is separated from the $n+$ contact by an insulating groove. A schematic illustration of the corresponding cross section and the distribution of its weighting potential can be found at the bottom of figure 3.9 a). One salient drawback of this configuration making it mandatory to produce the detector with a strongly reduced height to still achieve a full depletion, is the much smaller active volume.

detector name	total mass [kg]	total height [mm]	diameter [mm]	dead layer [mm]	bias voltage [kV]
GD32B	0.717	32.2	71.8	1.0	4.0
GD32C	0.743	33.2	72	0.8	4.0
GD32D	0.723	32	72.2	0.7	4.0
GD35B	0.812	32	76.6	0.8	3.5
GD35C	0.635	26.4	74.8	0.8	3.5

Table 3.3: Characteristics for the five enriched BEGe detectors deployed during part of Phase I (values taken from [Ago13b]). All diodes feature an uniform isotopic abundance of $f_{76} = 87.7(13)\%$ in ^{76}Ge with the region of 1σ uncertainty given within parentheses.

But the resulting planar assembly also holds one main advantage over the semi-coaxial geometry: due to a much higher inhomogeneity of the electric field and a therefore large weighting potential gradient, BEGe detectors feature an enhanced *pulse shape discrimination* (PSD) performance. This is because the charge carriers drift through volumes of extremely varying field strengths, whereby electrons mostly pass regions of low weighting (blue) and thus hardly contribute to the signal formation. On the other hand, holes are caused to approach the $p+$ electrode through the volume of the highest weighting potential (red), along very similar trajectories, notwithstanding of the location where the energy is deposited. As a result, the maximum amplitude A of the current pulse can be regarded as almost directly proportional to the energy E for a localized deposition. Mathematically, the current pulses can be easily extracted by differentiation from the measured charge pulses.

However, events with several non-localized energy depositions reveal a different, distinguishable signal-time structure. This behaviour offers the use of the ratio A/E as a powerfull PSD technique to decide whether an event is of *single site* (SSE) or *multi site* (MSE) topology [Ago11a][Bud09][Ago13b].

3.2.5 Mounting scheme

During the implementation of Phase I, the detectors of both configurations were mounted upside down (meaning borehole and groove structure do point downwards) in low-mass holders as exemplarily shown in the two photographic images of figure 3.9 b) for the ANG4 detector of semi-coaxial type (top) and the GD32C detector of BEGe geometry (bottom). To realize the signal contact, a conical copper piece, called "Chinese hat", is pressed by a silicon spring onto the $p+$ contact at the estuary of the bore hole (not visible for this camera angle). High voltage, in turn, is applied to the $n+$ layer on the facing page of the diode. The bias contact is thereby accomplished with the assistance of a copper strip that is clamped with adjustable force by a electrically insulated copper disc. Withal the whole mounting procedure is performed in the glove box of the clean room. To ensure as less contamination of the background level as possible, also only selected high radiopurity materials - mostly copper ($\sim 80\,\mathrm{g}$) but also some minor PTFE ($\sim 10\,\mathrm{g}$) and silicon ($\sim 1\,\mathrm{g}$) contributions - were used for the star-shaped design of the support structure. From the combined result of γ-ray spectroscopy and Monte Carlo simulations, an upper limit on the BI contribution could be estimated to $\leq 10^{-3}\,\mathrm{cts}/(\mathrm{keV}\cdot\mathrm{kg}\cdot\mathrm{yr})$, which is compatible with the demands confined for GERDA Phase I.

The single detectors, each stored in a custom made holder, are then connected to strings via bayonet joints at the very top and bottom of the support structure and further assembled into an array. For the sake of vividness, in figure 3.9c) one of the assembled strings, consisting of three diodes (RG1, ANG4 and RG2), is depicted. Also shown at the lower picture margin is a $60\,\mu\mathrm{m}$ thin and cylindrically formed copper foil that is intended to enclose the string to act as a "mini-shroud". In the original design of the experiment the mini-shroud was not purposed though, but has been compulsorily introduced during the commissioning phase in order to mitigate an unforeseen, $^{42}\mathrm{K}$ induced background of high intensity. Hereby the charged potassium ion emerges directly in LAr due to the decay of the cosmogenic-activated $^{42}\mathrm{Ar}$ isotope with a half-life of $T_{1/2} = 32.9\,\mathrm{yr}$ and is subsequently drifting in the electric field (resulting from the applied bias voltages) towards the germanium detector array. After several validation runs with changing configurations, the $^{42}\mathrm{K}$ background was found to be minimized when deploying the Cu foil grounded and, in so doing, separating the inner part electrically as well as physically from the outer volume.

Figure 3.9d) displays a picture taken from the finally mounted and strung enriched detectors after being inserted into the mini-shroud. At this very moment the closed string is right about to be lowered into the cryostat filled with the liquid coolant below the clean room/glove box facility.

3.2.6   Signal read-out

The front-end electronics serve as connective between germanium detectors operated in LAr and the data acquisition (DAQ) system. In order to meet the requirements in stability and low noise, the read out in HPGe spectroscopy is preferably accomplished by DC-coupled *charge sensitive preamplifiers* (CSP), which integrate the collected charge on the feedback capacitor that is, in turn, transformed into a voltage pulse. Conclusively, the output voltage from the preamplifier exhibits an amplitude V_0, and a decay time constant τ, given respectively by

$$V_0 = \frac{Q_{\mathrm{det}}}{C_{\mathrm{fb}}} \quad \text{and} \quad \tau = R_{\mathrm{fb}} \cdot C_{\mathrm{fb}} \, , \qquad\qquad (3.13)$$

where Q_{det} denotes the charge released by the detector, C_{fb} the feedback capacitor and R_{fb} the feedback resistor. Due to constraints arising from the experimental setup (e.g. the long distance between detectors and the cryogenic coolant) the CSPs are entirely deployed within LAr in vicinity to the germanium crystals with the minimum allowed distance being restricted by their radioactivity. In particular, the front-end electronics developed for the GERDA experiment (called CC2 with $C_{\mathrm{fb}} \approx 1\,\mathrm{pF}$, $R_{\mathrm{fb}} \approx 500\,\mathrm{M\Omega}$) [Rib10] is custom made from only screened components of sufficiently low background contamination and placed about $30\,\mathrm{cm}$ above the uppermost detector of the string. Each device holds three separate channels and is located inside a small copper box that acts as electrical shielding (see figure 3.9d) at the top picture margin). Typical values for the sensitivity realized with this specific device are, according to equation 3.13 along with $E_{\mathrm{pair}} = 2.96\,\mathrm{eV}$, in the range of $V_0/E \approx 50\,\mathrm{mV/MeV}$. The read-out electrodes of the detectors are connected to the amplifier by Teflon insulated copper stripes (with a cross section of $2.0 \times 0.4\,\mathrm{mm}^2$) that have to be fixed tightly to avoid further noise induced by microphonics (the same scheme applies for the electrical contacts between $n+$ electrode and bias voltage supply).

Starting from the copper box housing the CC2, thin coaxial cables with a length of $\sim 10\,\mathrm{m}$ from Habia (type SM50) for the analog preamplifier output and otherwise from Sami RG178 as well as Teledyne Reynolds 167-2896 for the high voltage supply are used until they enter welded BNC feedthroughs that provide a seal between the cryostat/lock system and the outer environment. Another coaxial cable type, RG178, of the same length transmits the signals onwards to the electronics cabinet located adjacent to the clean room where they are further amplified and digitzed by 14-bit flash-ADCs (FADC) before being saved to disk for energy reconstruction and off-line analysis. The stored raw data comprises for each event and detector channel two sets of traces, both aligned such that the beginning of the pulse leading edge is centered. To reduce the data rate and readout time, a first compressed trace, with relatively low sampling rate of $25\,\mathrm{MHz}$ and length $160\,\mu\mathrm{s}$ is recorded. It will be afterwards used for operations within the off-line data processing, as for example energy reconstruction, which involve the integration of the pulse. The second, with $4\,\mu\mathrm{s}$ four times shorter trace is sampled with an increased frequency of $100\,\mathrm{MHz}$ and thus well suited for the analysis of the signal time-structure.
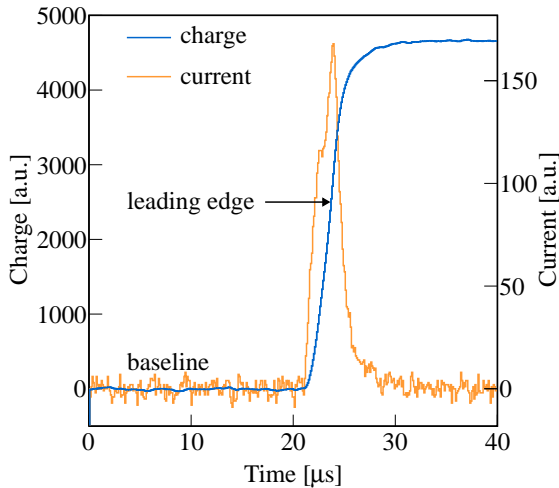
Figure 3.10: Trace from the FADC output as recorded by the ANG4 detector in January 2012 during a calibration with ^{228}Th within Run 28 with 100 MHz sampling rate, $4\,\mu$s length and an energy of 2614.4 keV. The shape is characteristic for a charge signal (blue) induced by the collection of electron hole pairs previously created through interactions of charged particles or γ rays within the active material of the diode. Mathematically the corresponding current pulse (orange) represents the first derivative of the charge signal.

Typically the recorded charge pulses are composed of a rising part with fast (rise) times of $\sim 1\,\mu$s, determined by the charge collection inside the semiconductor as given by equation 3.15, plus a superimposed exponential decay tail with long (decay) times τ of $\sim 100\,\mu$s, resulting from the charge sensitive preamplifier CC2 (see equation 3.13, i.e. product of feedback resistance and capacitance). An example for such an induced charge trace at the output of the FADC with high-frequency (100 MHz) and short-length ($4\,\mu$s) is illustrated in figure 3.10 as well as its first derivative which corresponds to the current signal. For the chosen interval the long exponential decay tail is not visible yet. This particular signal was measured by the ANG4 detector in January 2012 shortly after beginning of GERDA Phase I during a calibration run with a close-by ^{228}Th source[2] and lies within the full energy peak (FEP) of the thorium spectrum (energy reconstruction yields a value of 2614.4 keV). The corresponding energy spectrum can be found in figure 3.13 of section 3.5.2. Besides this visual impression of the charge and current pulses recorded in GERDA, a more detailed discussion concerning the formation of the signal time structure will be pursued in the next section 3.2.7.

3.2.7 Signal time structure

The mechanism of signal formation when an incoming radiation generates within the detection apparatus free charge carriers that are caused to drift towards the electrodes by an applied electric field (holes and electrons travel to contacts of opposite polarity) can be numerically described by the *Ramo-Shockley theorem*. Accordingly the charge Q and current I induced on an electrode are written as [He01]

$$Q(t) = -q_0 \times [\phi_w(\boldsymbol{r}_{\rm h}(t)) - \phi_w(\boldsymbol{r}_{\rm e}(t))]$$
$$I(t) = {\rm d}Q(t)/{\rm d}t = q_0 \times [\mathcal{E}_w(\boldsymbol{r}_{\rm h}(t)) \cdot \boldsymbol{v}_{\rm h}(t) - \mathcal{E}_w(\boldsymbol{r}_{\rm e}(t)) \cdot \boldsymbol{v}_{\rm e}(t)] \,, \qquad (3.14)$$

---

[2]Such calibrations are regularly performed in GERDA in order to track the energy resolution or instabilities of single germanium detectors and to reconstruct the respective energy scales. More details are provided in section 3.4.

where $\boldsymbol{r}_{\mathrm{e}}(t)$, $\boldsymbol{r}_{\mathrm{h}}(t)$ denote the instantaneous position and $\boldsymbol{v}_{\mathrm{e}}(t)$, $\boldsymbol{v}_{\mathrm{h}}(t)$ the instantaneous velocity of the moving electron or hole within the device as a function of time t. Further q_0 is the total charge carried by both charge carriers, the quantities $\mathcal{E}_w(\boldsymbol{r})$ and $\phi_w(\boldsymbol{r})$ represent the position-dependent weighting field and weighting potential, respectively. The latter satisfies the Poisson equation $\nabla^2 \phi_w(\boldsymbol{r}) = 0$ and can be calculated for each electrode when solving the boundary conditions $\phi_w(\boldsymbol{r}) = 1$ for the corresponding and $\phi_w(\boldsymbol{r}) = 0$ for all other electrodes.

In case of the semi-coaxial detector geometry, the relevant one for the work presented in this thesis, it is extremely difficult to calculate an analytical expression. But the above equation 3.14 can be in good approximation simplified to a radial symmetry when limiting the considerations to a true coaxial configuration, and the charge as a function of time is found to be [Kno89]

$$Q(t) = \frac{q_0 \cdot a}{V_{\mathrm{bias}}} \left[(r_0 + v_{\mathrm{e}} \cdot t)^2 - (r_0 - v_{\mathrm{h}} \cdot t)^2 \right] + \frac{q_0 \cdot b}{V_{\mathrm{bias}}} \left[\ln \left(1 + \frac{v_{\mathrm{e}} \cdot t}{r_0} \right) + \ln \left(1 - \frac{v_{\mathrm{h}} \cdot t}{r_0} \right) \right] \quad (3.15)$$

with the shortcuts

$$a = \frac{en_{\mathrm{A}}}{4\epsilon} \quad \text{and} \quad b = \frac{V_{\mathrm{bias}} - a(r_2^2 - r_1^2)}{\ln(r_2/r_1)} \; . \quad (3.16)$$

In addition also the interaction radius r_0 and the applied bias voltage V_{bias} responsible for the electric field

$$E_{\mathrm{field}}(r_0) = 2ar_0 + \frac{b}{r_0} \quad (3.17)$$

enter the equation. For a detector made of mildly p-type bulk material n_{A} represents the acceptor concentration of the remaining low-level impurity. Obviously the time structure of the charge signal $Q(t)$ depends on predictions made for the motion of the electrons and holes as reflected in v_{e} and v_{h}. Since the electric field E_{field} of a coaxial HPGe diode, changes with respect to the radius r_0 within the detector, also the velocity v_{d} of the drifting carriers will show some variation while the charges are collected. This correlation can be fitted with sufficient accuracy by the empirical derived function

$$v_{\mathrm{d}} = \frac{\mu_0 \cdot E_{\mathrm{field}}}{[1 + (E_{\mathrm{field}}/E_0)^c]^{1/c}} - \mu_n \cdot E_{\mathrm{field}} \quad (3.18)$$

as proposed in [Can75]. The last term is additionally added to account for the differential mobility of the electrons at very high electric fields. Here μ_0 symbolizes the mobility at low E_{field} values and is along with c, E_0, μ_n an adjustable parameter evaluated experimentally from drift velocity measurements.

In practice not only the electric field, but also the crystal structure turned out to have an effect on the motion and trajectories of charge carriers. It can be due to charge trapping and detrapping or actually different physical properties (e.g. distinct energy levels for the electrons) depending on the orientation in the crystal. As pictured in figure 3.11 (small inset left top) germanium crystals exhibit a face-centered cubic (*fcc*) lattice with the main crystallographic axes $\langle 001 \rangle$, $\langle 100 \rangle$, $\langle 110 \rangle$ and $\langle 111 \rangle$

direction	parameter		electrons	holes
$\langle 100 \rangle$	c		0.72	0.744
	μ_0 [cm^2/(Vs)]		40180	66333
	E_0 [V/cm]		493	181
	μ_n [cm^2/(Vs)]		589	–
$\langle 111 \rangle$	c		0.87	0.580
	μ_0 [cm^2/(Vs)]		42420	107270
	E_0 [V/cm]		251	100
	μ_n [cm^2/(Vs)]		62	–

Table 3.4: Fit parameters from experimental data for the drift velocities along the $\langle 100 \rangle$ and $\langle 111 \rangle$ directions in germanium. Values are taken from [Mih00][Reg77] and valid for $T = 77\,\text{K}$ of liquid nitrogen, close to the temperature of LAr.

of the corresponding tetrahedron structure highlighted in red colour. The resulting fit parameters for the experimental dependence of drift velocities v_d on the applied electric field E_{field} along the $\langle 100 \rangle$ and $\langle 111 \rangle$ directions are summarized in table 3.4 and plotted according to equation 3.18 for electrons as well as holes in figure 3.11. At low field strengths, the charge velocity increases linearly, at high values, well into the region where HPGe detectors are operated, it reaches a state of saturation though. Also visible is the effect of the lattice orientation with respect to the applied field (e.g. of the $\langle 111 \rangle$ direction the drift velocity is systematically lower than for $\langle 100 \rangle$).
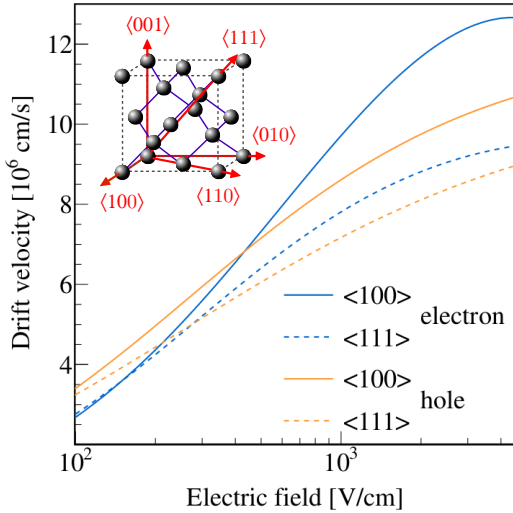
Figure 3.11: Schematic view of the unit cell for the face centered cubic lattice of a germanium crystal (*small inset left top*). The main crystallographic axes of the tetrahedron structure are marked with red arrows. Also shown for the two directions $\langle 111 \rangle$ and $\langle 100 \rangle$ within the lattice are the drift velocities v_d for electrons (blue) and holes (orange) as a function of the electric field E_{field} at $T = 77\,\text{K}$. Calculations have been performed with equation 3.18, the values used for the experimentally derived fit parameters are reported in table 3.4 and taken from [Mih00][Reg77].

During the drifting procedure of the generated electron-hole pairs, the charge carriers will be gradually collected at the electrodes, inducing a signal that feature a specific time structure. But in contrast to the BEGe configuration, charge-time signals of detectors with semi-coaxial geometry do vary drastically in their shape, even if the event is of SSE topology with a localized energy deposition. Primarily this is because of the rather homogeneous weighting potential (at least if compared with a BEGe type detector) which favours both, holes as well as electrons to contribute to the signal. But also the orientation of the crystal axes within the diode will slightly affect the time behaviour. All in all, the ambiguous signal formation of semi-coaxial diodes massively spoils the discrimination performance in pulse shape analysis.

3.3   Geana - an independent analysis software

The stored binary raw data format including the traces sampled either in 25 MHz or 100 MHz rate, are further used for an off-line digital signal processing. Therefore two different software frameworks, namely GELATIO (GErda LAyouT for Input/Output) [Ago11b][Ago12][Zav12] and GEANA (GErda ANAlysis) [Miz13], have been independently developed and used for cross checks to verify their reliability. From these two the latter has been used for the data analysis presented in the framework of this thesis and will be thus briefly presented in the following.

The GEANA software is provided as C source code (C++ compatible) with the data processing flow being composed of several main steps. First the incoming traces from the FADC are checked for their polarity which is, if needed, changed to always have positive charge pulses with a rising or leading edge. Afterwards the low-frequency traces are further analyzed by calculating the average value, the root-mean-square deviation (RMS) and the linear slope before the rising part so that a baseline restoration of the signal can be performed. Hereby it is as well important to detect possible so-called "pile-up" events generated by the superposition of multiple physical pulses that can occur if high detection rates are present, for instance during a calibration measurement with radioactive sources, while they are almost negligible in the physics data sets.

Additional information concerning the events, such as the signal position or beginning of the leading edge are also extracted to track the data quality. Since the trace exhibits, owing to the charge-sensitive preamplifier, a certain decay slope with the corresponding decay time $\tau \sim 100 \, \mu$s that creates a small overshoot in the current signal shape, another so-called *polezero correction* based on an inverse highpass filter is needed to deconvolve the exponential declining tail from the pulse form. For noise reduction the signal is further integrated with a moving average (MWA) filter, whereas the smoothing parameters are chosen such that they enhance the identification efficiency for pile-up or single physical events.

Finally the energy reconstruction of the spectrum is then accomplished by using an approximated Gaussian filter, where the incoming traces are first differentiated and then integrated for several times by a multiple-pass moving average filter (here: four times). The width of this filter, also called *shaping time*, is thoughtfully optimized for each detector channel to achieve the best energy resolution possible and lies typically in the range of $5 - 10 \, \mu$s. One of the tremendous advantages of such moving average filters is that they can be included according to the recursive implementation

$$y[i] = y[i-1] + x[i+p] - x[i-q] \, , \qquad (3.19)$$

which still keeps the data processing very fast [Smi99]. Notice that in the above equation 3.19 two sources of data are used to calculate the output $y[i]$ at the i-th entry: points $x[i+p]$, $x[i-p]$ from the input and previously calculated points $y[i-1] = \frac{1}{M} \sum_{j=0}^{M-1} x[i-1+j]$ from the output signal. Hereby M with $p = (M-1)/2$ and $q = p+1$ describes the number of samples in the moving average that is related to the

already mentioned shaping time. However, the maximum amplitude of the gaussian shaped output signals are eventually proportional to the respective event energies and can be therefore used to compute the absolute energy scale when comparing with known characteristic features of a calibration spectrum.

Apart from the analyzing procedures described yet, the GEANA framework also allows to efficiently identify and tag corrupted signals that are either (i) produced by non-physical processes, like cross-talk, electromagnetic noise and discharges, or (ii) not properly processed along the data analysis chain, as for example pile-up events. In principle the first event type (i) can be easily rejected due to their anomalous shape, extremely long/short rise times or the saturation of the dynamic range of the FADC, whereas the second class (ii) of multiple superimposed physical pulses features an salient non-flat baseline or several leading edges.

Physical events that pass the set of quality cuts are further excluded from the analysis if they occur simultaneously within a time period of 8 μs with a positive detection of the muon-veto system. Another quality cut which addresses the single-site or multi-site topology of the signal, as implied by the coincident energy deposition within more than one HPGe detector, can be applied on the data. The output can be afterwards stored in either ASCII or binary file format.

3.4 Calibration with ^{228}Th source

To monitor the energy resolution and track a possible degraded performance or even instability of the single germanium detectors, regular calibration measurements with radioactive γ sources provide the necessary information. In GERDA the calibration is performed by dedicated intervals of data taking, which involve the introduction of three ^{228}Th sources into the cryostat that are brought into close vicinity to the crystals in the LAr (every one or two weeks) and their removal during physics runs. Thereby from the sub-decay chain following the decay of ^{228}Th only the contribu-
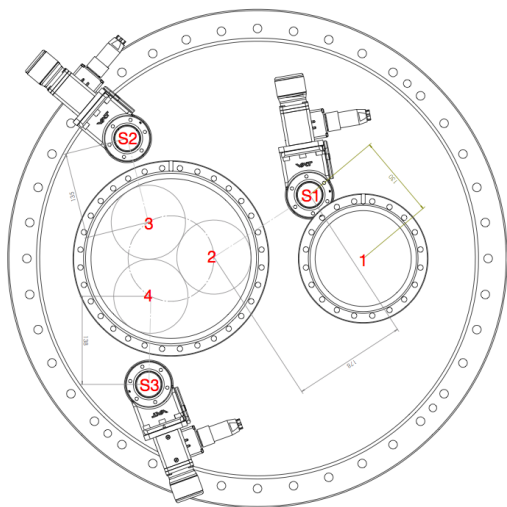
Figure 3.12: Technical drawing of the CF360 cluster flange mounted above the cryostat neck (for a view from top). The three electro-mechanical, vacuum-sealed units of the source insertion system (SIS) are shown. Also insinuated are the connections of the 3-string (left) and 1-string (right) lock to the flange. The inscriptions in red label the location of the sources S1, S2 and S3 as well as the four detector strings positions in the experimental setup of Phase I.

tions from the ^{212}Bi and ^{208}Tl progenies do emit high energetic γ rays or electrons that can reach the detectors. For a reconstruction of the energy scale the seven most prominent γ-lines of the resulting spectrum at the energies of 510.8 keV, 583.2 keV, 727.3 keV, 860.6 keV, 1620.5 keV, 2103.5 keV and 2614.5 keV are then used with the latter denoting rearwards the full energy peak (FEP) from the thallium decay followed by the corresponding single escape peak (SEP) of an energy reduced by 511 keV and the analog FEP from bismuth. To preserve disk space, energy thresholds in calibrations are set to a higher value than for normal physics runs. For the fit of the gamma lines, a Gaussian combined with a constant coefficient and sigmoid function (to also account for the slope in the background distribution) is used, the calibration function is provided by a second order polynomial. A typical calibration measurement with ^{228}Th sources is shown in figure 3.13 of section 3.5.2 for the six enriched semi-coaxial detectors used in the Phase I data analysis. The location of the seven γ-lines used for energy calibration within the energy spectrum are indicated as grey lines and labelled at the top of the plot.

Calibration measurements can be only achieved by accessing the detectors via the main CF360 "cluster" flange mounted on top of the cryostat in the clean room. The flange along with a DN630 shutter acts as resealable closure to prevent the contamination of the cryostat's interior with environmental impurities and is moreover used when deploying the detector strings from the attached glove box into the liquid argon. Practically this procedure is accomplished by three electro-mechanical, vacuum-tight systems affixed directly on top of the cluster flange which store the ^{228}Th sources and can be individually decoupled and lowered through the neck of the cryostat. A technical drawing of the final apparatus with the three units of the source insertion system (SIS) for a view from top is given in figure 3.12. The substriptions in red denote the location of the sources (here S1, S2 and S3, respectively) and the four detector strings deployed during Phase I. Also visible are the connections for the tubes of the 3-string (left) and 1-string (right) lock to the cluster flange. Some of the most relevant general properties of the ^{228}Th sources, like their original activity, installation date or average distance to the closest detector stings, are further listed in table 3.5. Besides the mechanical parts, also a specially developed control software for status monitoring is on hand [Tar12].

Source	Original activity [kBq]	Date of measurement [yyyy-mm-dd]	Date of installation [yyyy-mm-dd]	Distance to string [mm]
S1	25	2010-04-09	2011-06-20	130 (S1) 178 (S2)
S2	17.7	2010-04-30	2011-06-20	135 (S3)
S3	26.5	2010-02-01	2010-11-08	138 (S4)

Table 3.5: List of the three ^{228}Th calibration sources installed in GERDA along with their original activities and distances to the closest detector strings.

To guarantee a background contribution resulting from the calibration sources that is negligible during the physics data taking of the experiment, additional tantalum absorbers with a height of 60 mm and a diameter of 32 mm are employed as

shielding. In [Fro12] Monte Carlo simulations have been pursued in attempting to educe the γ background from the sources when being shielded and located in their "parking position" at the very top of the cryostat, approximately 5 m above the array of Ge-diodes. The resulting estimation lies well within the requirements of GERDA Phase II and yielded a value of $4.3\pm0.1(\text{stat})\pm0.1(\text{syst})\cdot10^{-5}\,\text{cts}/(\text{keV}\cdot\text{kg}\cdot\text{yr})$.

3.5 Run configurations

In total a number of 14 semi-coaxial $^{\text{enr}}$Ge and $^{\text{nat}}$Ge detectors were placed at disposal for operation in the GERDA experiment with the enriched ones being provided by the HdM ($\text{ANG}1-5$) and the IGEX ($\text{RG}1-3$) collaborations. Out of the six diodes made of natural germanium supplied from the GENIUS-TF experiment, only three have been measured in the underground setup during Phase I. Additionally five more crystals of new BEGe type from a set of 30 diodes originally produced for Phase II have already been used for parts of the first experimental phase. A list of all the detectors deployed in GERDA down to the present day is compiled in tables 3.2 and 3.3. The next sections are intended to give a short overview of the changing run configurations, including the different installed detectors and arrangement of strings in the GERDA cryostat.

Channel mapping by DAQ	Run number and date of start					
	$1-13$ Jul 2010	$14-15$ Jun 2011	$16-19$ Jul 2011	$20-23$ Aug 2011	$24-32$ Nov 2011	$35-46$ Jul 2012
0	GTF45	RG1	RG1	RG1	ANG1	ANG1
1	GTF32	ANG4	ANG4	ANG4	ANG2	ANG2
2	GTF122	RG2	RG2	RG2	ANG3	ANG3
3			GTF32	GTF32	ANG4	ANG4
4			GTF45	GTF45	ANG5	ANG5
5			GTF112	GTF112	RG1	RG1
6				GTF110	RG2	RG2
7				GTF42	RG3	RG3
8					GTF112	GTF112
9					GTF45	GD32B
10					GTF32	GD32C
11						GD32D
12						GD35B
13						GD35C

Table 3.6: List of all run configurations since the beginning of the commissioning up to the end of Phase I of the GERDA experiment. Thereby the detectors are sorted according to their channel ID mapping in the DAQ system. Concerning the last two columns, runs with number 25 or higher are already considered for the physics data of Phase I.

3.5.1   First steps: The Commissioning Runs

Starting from June 2009 a string equipped with three of the non-enriched GTF detectors has been deployed for the first GERDA commissioning run. As previously reported in section 3.2.5, the first taken background data revealed an unexpected energy line at 1525 keV, which originates from the consequent decay chain ^{42}Ar$\to^{42}$K$\to^{42}$Ca in the LAr and represents the full energy peak of the latter decay. Assuming this radiation process to occur in close vicinity to the detector surface, the maximal released electron energy of 3525 keV is high enough to significantly contribute to the background near the $Q_{\beta\beta}$-value at 2039 keV and thus spoils the scrutiny of the existence of the $0\nu\beta\beta$-decay. Subsequent runs with varying setups have been performed to investigate possible methods to reduce the ^{42}K induced background, It was found that the contributions can be mitigated most efficiently, if a mini-shroud made of thin copper is installed around the detectors (already shown in picture 3.9c) when explaining the mounting procedure). Further investigations also included different polarities that were applied to the shroud to either attract or repel the ^{42}K ions created in the decay of ^{42}Ar or string positions within the cryostat to scan the environment for possible located sources of contamination.

The next Runs 14+15 were dedicated to the commissioning of the first enriched coaxial detectors and allowed to draw new inferences (e.g for possible improvements) from the taken data. A picture of the corresponding diodes, namely the RG1, ANG4 and RG2, can be found in figure 3.9b).

In the following the piecewise implemention of an increasing number of germanium diodes was aspired. Lastly the GERDA Run 20 was recorded using a total of 8 detectors conglomerated of 3 enriched and 5 further GTF crystals of natural isotopic composition. To accomplish the increased amount of detectors, the hitherto 1-string arm was expanded by a second string lock with a two-fold string array on the opposite side of the cryostat port (confer with figure 3.12). Details of the several run configurations and their chronological development until the end of Phase I are assembled in table 3.6 along with the channel ID mapping for each detector as recorded by the DAQ.

3.5.2   Final detector array for Phase I

Officially Phase I of the GERDA experiment was launched contemporaneous with the data acquisition of Run 25, where in total 11 crystals, three of natural and eight of enriched ^{76}Ge composition, have been employed. This increased amount of detectors could only be managed by supplementary complementing the two-fold string arm, used since Run 20 (confer with previous section 3.5.1), to a three-fold string array. The 1-string arm on the contrary remained unaltered. A detailed run configuration along with the channel mapping in the DAQ is shown in the second last column of table 3.6. Out of these initially eight enriched detectors, two, the ANG1 and RG3, developed an unstable performance (high leakage currents) early after the

beginning of the data taking and were thus not considered for the Phase I data-set. However, for some time they have been further used as veto to reject multi-site events. Accordingly the total mass available for physics analysis amounts to 14.6 kg with an average enrichment in ^{76}Ge of about 86 % (see table 3.2). A measurement taken with the ^{228}Th sources in January 2012 during Run 28 in figure 3.13 for the remaining six enriched semi-coaxial detectors the present work is focussed on. All peaks are described well by a Gaussian and an additional error function to account for the background. When fitting the γ-line at 2614 keV, values between 4.2 keV and 5.3 keV, that can be translated to a mass weighted average of 4.5 keV at $Q_{\beta\beta}$ [Ack13], have been obtained for the $FWHM$.

String position	Detectors of Phase I			
	3-string			1-string
	S2	S3	S4	S1
top	GTF112	RG1	ANG3	GD32B
				GD32C
middle	ANG2	ANG4	ANG5	GD32D
bottom	ANG1	RG2	RG3	GD35B
				GD35C

Table 3.7: String assignment of the enriched semi-coaxial detectors during the GERDA measurements lasting from November 2011 to May 2013. In July 2012 five more crystals of BEGe geometry have been employed later on in the course of data taking and operated for only part of the Phase I run time.

With Run 33 the 1-string arm, housing the two GTF45 and GTF32 detectors of natural germanium composition, was removed to clear space for 5 enriched BEGe
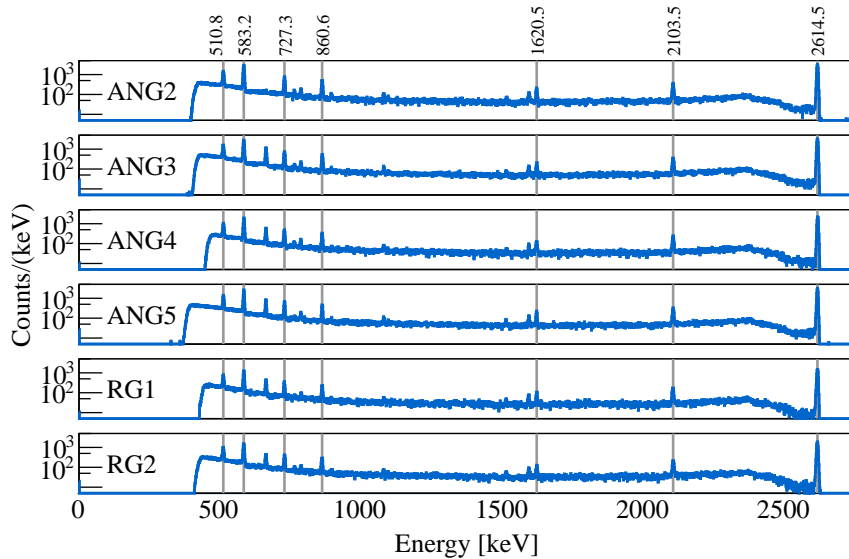
Figure 3.13: Energy spectra of calibration measurement with ^{228}Th sources taken in January 2012 during Run 28 for the six semi-coaxial germanium detectors used for physics data. Two diodes (ANG1 and RG3) are not accounted for analysis due to high leakage currents. The seven most prominent γ-lines resulting from the subsequent decays of ^{208}Tl or ^{212}Bi and availed of for the energy calibration, are marked with gray lines as well as labelled according to their energies.

detectors which have been installed and operated for data taking since Run 35 (see last column of table 3.6). One of the BEGe detectors, namely the GD35C at the bottommost position, also showed in the following an unstable behaviour (with respect to the energy calibration) and has no longer been used. Further details of the string configuration are collected in table 3.7 and visualized in figure 3.14. Since March 2013 the RG2 had to be operated below its full depletion voltage and was additionally omitted, but still further operated to suppress multi-site events. Due to temperature-induced instabilities, a fraction of 5 % of the data had to be discarded as well. As a result, the total exposure considered for the analysis of Phase I data that has been collected until May 2013 amounts to 21.6 kg·yr of enriched germanium detector mass that effectively yields 215.2±7.6 mol of ^{76}Ge within the active volume.
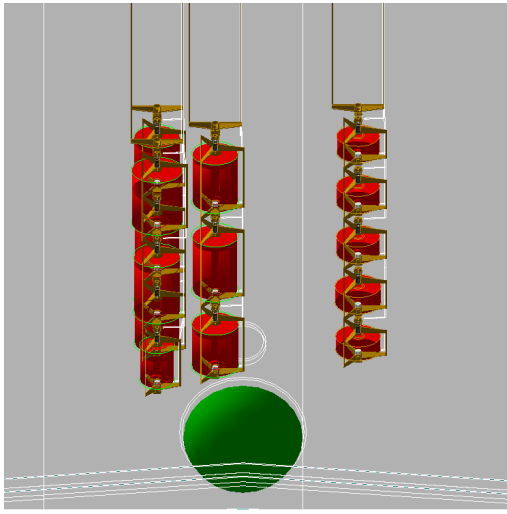
Figure 3.14: Schematic drawing of the Phase I setup, whereas the 1-string (right) housing the five detectors of BEGe configuration was only inserted for parts of the Phase I data taking. All other semi-coaxial detectors were mounted at the 3-string (left). Both string arms have been operated at different heights with the 1-string arm being slightly lifted to a higher position. Visual output obtained with graphic viewer "OpenGLImmediateX" provided by the GEANT4 software. (The green structure at the bottom margin signifies one of the PMTs used for the muon-veto.)

3.5.3   Future Perspective: Phase II

A future second phase, Phase II, is planned to start in May 2014 and is currently in preparation. Several changes in the setup will be provided, like ~ 25 further (in total ~ 30) custom-made BEGe diodes of enriched germanium that will be additionally deployed to exceed the overall exposure, a whole new lock-system to handle the increased number of detectors and an enhanced electronics hardware optimized in terms of the challenging experimental demands. To further reduce the background by another order of magnitude to the required level of 10^{-3} cts/(keV·kg·yr) an improved support structure and signal/high voltage contacting mechanism [Bod15] for the crystals consisting of not only purer but also less material has been developed. Supplementary a LAr scintillation veto instrumented with photomultipliers will be installed close to the germanium array within the cryostat of the GERDA experiment [Weg14]. The detected light can then be used in anticoincidence with the germanium crystals to effectively suppress those background events that also deposit energy in the liquid argon. This technique was investigated earlier in a dedicated test facil-

ity, named LArGe, and has proven to show an impressive and stable background reduction performance [Hei11].

Regarding all these precautions in combination with a refined and enhanced pulse shape analysis, a sensitivity on the half-life $T_{1/2}^{0\nu}$ for the neutrinloess double β-decay in ^{76}Ge of $\sim 2 \cdot 10^{26}$ yr, corresponding to a scan of the effective neutrino mass $|m_{\beta\beta}|$ down to the ~ 10 meV range, is aspired.

3.6 GERDA Phase I physics data

In neutrinoless double β-decay experiments the main focus lies on the possible presence of a peak at the corresponding $Q_{\beta\beta}$-value of the decay (for ^{76}Ge it is 2039 keV). All other parts of the energy spectrum are instead considered as background, which can not only effectively deteriorate the detection efficiency on the hypothetical $0\nu\beta\beta$-signal, but also have to be well understood before being able to draw unambiguous conclusions out of the spectral shape. Therefore in [Ago13c][Bec14][Hem14] the distribution of the physics data has been carefully investigated by means of Monte Carlo simulations to determine and evaluate the various background contributions. With also considering constraints set on the basis of material screenings or observed prominent structures in the spectral shape, a background model has been developed that describes the measured spectrum in a wide energy region with high accuracy. Both, the experimental observations as well as the theoretical expectations, are intended to be discussed in the upcoming section along with the resulting predictions on the sensitivity of the Phase I of the GERDA experiment.

3.6.1 Experimental energy spectrum

Figure 3.15 compares the overall energy spectrum acquired during the whole Phase I data taking for the two detector types of enriched semi-coaxial (top) and BEGe (bottom) geometry in the energy range up to 6000 keV. Several salient features can be identified:

- At energies below roughly 500 keV the spectra are dominated by the cosmogenic decay of ^{39}Ar. Because of differences in detector geometries as well as $n+$ layer thicknesses, the particular spectral shape varies largely for the semi-coaxial and BEGe type diodes.

- The subsequent energy region between 500 and 1500 keV exhibits a predominant continuous spectrum caused by the neutrino-accompanied double β-decay.

- A number of γ-lines, resulting from a contamination with different radioactive isotopes, can be identified. Along the whole spectrum characteristic energy peaks attributed to the decays of ^{40}K, ^{42}K, ^{208}Tl and ^{214}Bi, to a smaller extend also particular lines from ^{60}Co, ^{214}Pb and ^{228}Ac, are visible. All prominent

features can be correctly reconstructed at the expected energies within their statistical uncertainty. By means of the most prominent line at 1524.6 keV, resulting from ^{42}K, an exposure weighted average $FWHM$ energy resolution of 4.5 keV for the semi-coaxial and 3.1 keV for the BEGe detectors is found. Hence for physics data, the interpolated values of the $FWHM$ at $Q_{\beta\beta}$ for the two different detector types are determined to 4.8 ± 0.2 keV and 3.2 ± 0.2 keV, respectively, which occurs to be about 10 % larger compared with the corresponding resolutions obtained from calibration measurements [Ago13a]. This broadening is assumed to be caused by fluctuations of the energy scale between two calibration runs.

- For higher energies, several close-by, peak-like distributions appear at 4.7 MeV, 5.4 MeV and 5.9 MeV due to α-decays of ^{226}Ra, ^{222}Rn and ^{218}Po in the vicinity of the detectors. The by far most prominent structure however results from the corresponding decay of ^{210}Po with a maximum energy of 5.3 keV. Because of the short ranges of α particles in absorber materials (as explained in section 3.2.2) the only possible origins of this radiation can be identified on the $p+$ surface or groove of the detector as well as in the close-by LAr.

Marked as green shaded area is the region of interest (ROI) with the energy interval ΔE ranging from 1930 to 2190 keV used for the determination of the background index BI and the $0\nu\beta\beta$ analysis. Two windows at $2099-2109$ keV and $2114-2124$ keV
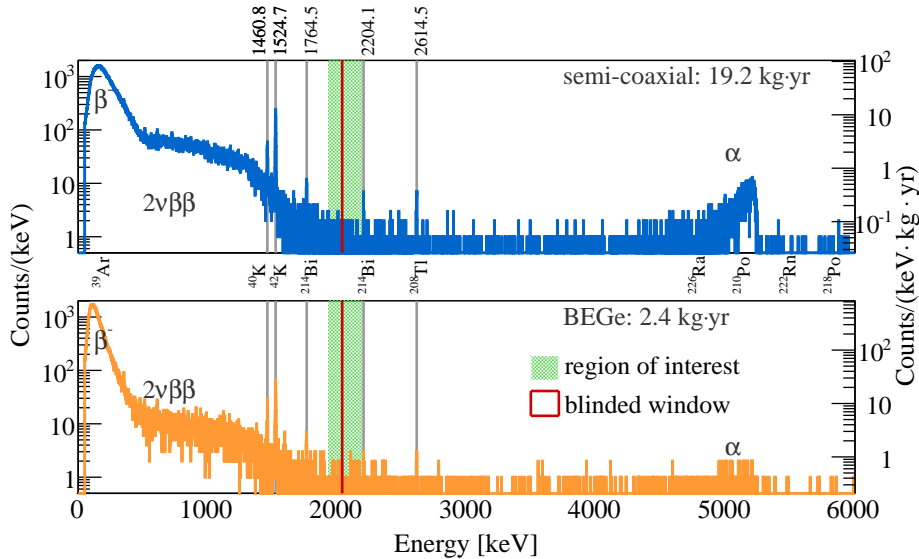
Figure 3.15: Energy spectra taken during whole Phase I with all the enriched semi-coaxial (top) and BEGe (bottom) detectors being summed up, corresponding to a total exposure of 19.2 kg·yr or 2.4 kg·yr, respectively. The ROI of 230 keV width, from which the background index BI is determined, is represented by the green shaded area, the vertical red line indicates the blinding region of $Q_{\beta\beta} \pm 5$ keV. Additionally some the most prominent γ-lines are marked with gray lines.

are removed from the ROI owing to known γ-lines resulting from ^{208}Tl and ^{214}Bi contaminations, respectively. To avoid bias in the signal search a small region of 10 keV for semi-coaxial and 8 keV for BEGe detectors centered around $Q_{\beta\beta}$ has been blinded (red solid line) for the whole progress of the analysis techniques. In case of the coaxial geometry, this results in a net width of 230 keV for the evaluation of the background.

As different detectors experience different surroundings, for instance during their fabrication or storing before commissioning, and because the experimental conditions do change, depending on what is intended to be investigated, their energy spectra and hence their background might vary (between single diodes as well as over time). A careful selection of data sets thus can effectively optimize the result.

Concerning the storage, the enriched semi-coaxial detectors share the same history, since they all have been kept underground after their deployment in the HdM or IGEX experiments, showing therefore a low intrinsic activity. But with continual operations regarding the source insertion system (SIS) during Run 34 and the subsequent deployment of the five enriched BEGes at the beginning of Run 35, the experimental setup, however, changed during the ongoing data taking of Phase I. In succeeding measurements a correlated increase of the BI could be observed, while apart from the time period of Run $34 - 35$, right before and after the insertion of the BEGes in July 2012, the rate in the ROI has always been stable within uncertainties.

Set	Exposure $M_{\text{det}} \cdot t$ [kg·yr]	Events in ROI [cts]	BI $\left[\dfrac{10^{-3}\text{cts}}{\text{keV·kg·yr}} \right]$	δE [keV]	efficiency ε
Golden	17.9	76	18 ± 2	4.8	0.688 ± 0.031
Silver	1.3	19	63^{+16}_{-14}	4.8	0.688 ± 0.031
BEGe	2.4	23	42^{+10}_{-8}	3.2	0.720 ± 0.018

Table 3.8: Parameter list for the three Phase I data sets. The total exposure, the number of events within the ROI, the BI, energy resolution and the efficiency are given [Ago13a].

For further analysis of the background intensity and the $0\nu\beta\beta$-signal, the Phase I run time is therefore divided into three different subsets with similar characteristics based on the detector type as well as the BI evaluated in the energy region close to $Q_{\beta\beta}$. Accordingly data from the BEGe detectors form one set, whereas a second subset, hereinafter known as the "golden" data set, includes the major part of the data from the semi-coaxial detectors except the two Runs 34+35 with higher background levels when the SIS has been changed and BEGe detectors were inserted; in the following this short, intermediate period is referred to as the "silver" data set. Table 3.8 lists the number of background events and the corresponding background indices along with the total exposures for the three data sets. Also given is the respective efficiency

$$\varepsilon = f_{76} f_{\text{av}} \varepsilon_{\text{det}} , \tag{3.20}$$

which accounts for the fraction f_{76} of ^{76}Ge atoms (reported in tables 3.2 and 3.3), the active volume fraction f_{av} and the probability ε_{det} that a $0\nu\beta\beta$-decay occurring in the

active volume of a detector also deposits its entire released energy, thus contributing to the full energy peak at $Q_{\beta\beta}$. For the latter Monte Carlo simulations deliver 0.92 for semi-coaxial and 0.90 for BEGe detectors. If an additional pulse shape analysis is applied to the data, another fourth factor $\varepsilon_{\mathrm{PSD}}$, stating the signal acceptance of the method, has to be considered.

3.6.2   Composition of backgound

For the GERDA background model explained in [Ago13c][Bec14][Hem14] all background components, that were either identified in the energy spectra (see figure 3.15) or known to be present in the close vicinity of the diodes because of previous screening measurements, have been simulated with the MAGE framework based on GEANT4. Other potential sources lacking any direct evidence of existence, are instead not further considered in the analysis though. Also contributions arising from the cryostat or the water tank have been disregarded, as it has been shown that they contribute with a negligible small value, less than $10^{-4}\,\mathrm{cts}/(\mathrm{keV\cdot kg\cdot yr})$, to the background index BI [Bar09c]. The GERDA setup, the Phase I detectors along with the specific dimensions (as reported in tables 3.2 and 3.3) and their arrangement into the four strings are correctly implemented in the simulation software.

Decay	Source	Location
$2\nu\beta\beta$	^{76}Ge	detector volume
β	^{42}K	homogeneous in LAr, $n+$ surface, $p+$ surface
β, γ	^{214}Bi	detector assembly, radon shroud, mini-shroud,
	^{214}Pb	$n+$ surface, $p+$ surface, LAr close to $p+$ surface
γ	^{40}K	detector assembly
	^{208}Tl	detector assembly,
	^{212}Bi	radon shroud, heat exchanger
	^{60}Co	detector volume, detector assembly
	^{228}Ac	detector assembly, radon shroud
α	^{210}Po	
	^{226}Ra	$p+$ surface
	^{222}Rn	LAr in bore hole

Table 3.9: Source and location of the simulated background components. For the $p+$ dead layers different thicknesses up to 1000 nm in steps of 100 nm were assumed. The ^{226}Ra (^{222}Rn) decay comprises a decay chain with the isotopes ^{226}Ra, ^{222}Rn, ^{218}Po and ^{214}Po (^{222}Rn, ^{218}Po and ^{214}Po) [Ago13c].

Since energy spectra from sources with rather equal distances in the same order of magnitude to the detectors also exhibit quite similar shapes, e.g for γ radiation in terms of the ratio between peak intensity and Compton continuum, the various origins of contamination that are represented by the diverse components of the experimental setup can hardly be unraveled. Instead simulations of representative source locations, like in the detector assembly (meaning the support structure), the mini-shroud, the radon shroud and the heat exchanger at the cryostat neck have been performed to account for possible sources at close-by, medium and far distances. Additionally other parts of the experiment, as the detector volume itself, the $p+$ (with varying thicknesses) and $n+$ surface of the diode or an homogeneous

distribution inside the LAr, have been considered as well. All simulations conducted for the different $2\nu\beta\beta$, β, γ or α decay modes (considered isotopes: ^{40}K, ^{42}K, ^{60}Co, ^{208}Tl, ^{210}Po, ^{212}Bi, ^{214}Bi, ^{214}Pb, ^{228}Ac, ^{222}Rn, ^{226}Ra) and positions are collected in table 3.9. Finally the obtained energy spectra have been folded for each detector with a Gaussian distribution of the energy dependant $FWHM = \sqrt{a^2 + b^2 \cdot E}$ as extracted from the experimental data.

A global model that describes the background in a wide energy region in astonishing agreement with the measurement, was attained by fitting the different simulated contributions of table 3.9 to the experimental energy spectra using a Bayesian fit. For the specific calculations the Bayesian Analysis Toolkit BAT [Cal09] has been applied. Therein the posterior probability of the model and its parameters when fitting binned distributions is defined as

$$P(\boldsymbol{\lambda}|\boldsymbol{n}) = \frac{P(\boldsymbol{n}|\boldsymbol{\lambda})P_0(\boldsymbol{\lambda})}{\int P(\boldsymbol{n}|\boldsymbol{\lambda})P_0(\boldsymbol{\lambda})\mathrm{d}\boldsymbol{\lambda}} \qquad (3.21)$$

with $P_0(\boldsymbol{\lambda})$ representing the prior probability of the parameters and $P(\boldsymbol{n}|\boldsymbol{\lambda})$ being the likelihood written as the product of the probability of the data for a given model in each bin

$$P(\boldsymbol{n}|\boldsymbol{\lambda}) = \prod_i P(n_i|\lambda_i) = \prod_i \frac{e^{-\lambda_i}\lambda_i^{n_i}}{n_i!} \; . \qquad (3.22)$$

Here n_i denotes the observed number of events and λ_i the expected number of events in the i-th bin, respectively. For different data sets (of sufficient statistics) from Phase I, namely the "golden" and "BEGe" set, a *minimum fit* with only taking a minimal amount of well motivated close background origins into account, as well as a *maximum fit* with additional sources from medium and far distances, have been carried out in the energy range from $570\,\mathrm{keV}$ to $7500\,\mathrm{keV}$ with a $30\,\mathrm{keV}$ binning. The analysis hereby considers parts of the Phase I data including all measurements acquired until March 2013 with the end of Run 43, corresponding to an exposure of $16.7\,\mathrm{kg{\cdot}yr}$ for the six enriched semi-coaxial and $1.8\,\mathrm{kg{\cdot}yr}$ for the four BEGe detectors.
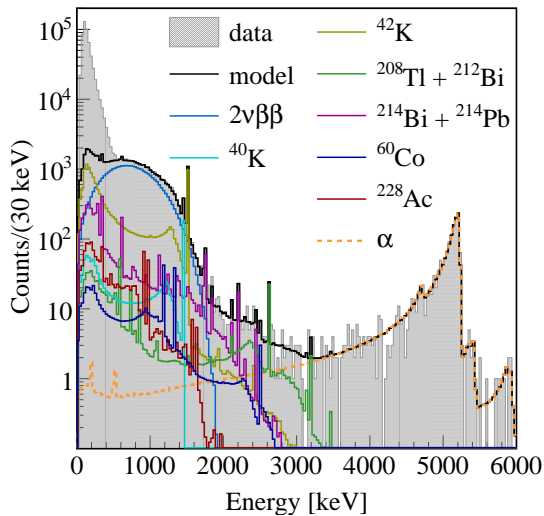
Figure 3.16: Background decomposition for the "golden" data set with the six working semi-coaxial germanium detectors according to the best fit minimum model. The gray shaded area represents the experimental energy spectrum measured until March 2013 with an exposure of $16.7\,\mathrm{kg{\cdot}yr}$, the lines in different colours the $2\nu\beta\beta$, β, α or γ contributions of the respective isotopes and the black solid line the total sum of all background sources. By courtesy of Neslihan Becerici-Schmidt, who provided access to the simulation spectra and fit results.

As a result both models allow to describe the experimental data sets very well within reasonable statistical fluctuations while only showing some minor differences. This is basically due to strong correlations present between the several background sources from different distances, which could not be distinguished in the maximum fit. However, it was found in compliance with the two models that the predominant fraction of the background originates from close sources, especially from the $n+$ and $p+$ surfaces, explaining the - all in all - rather equivalent fit results. Figure 3.16 shows the minimum model fit retrieved for the "golden" data set with semi-coaxial germanium detectors of Phase I. The measured data is depicted as gray shaded area, the various considered contributions as lines of different colours and the total sum as a black solid line. For the region of interest between 1930 keV and 2130 keV the GERDA background model predicts an approximately flat energy distribution composed of β-rays from ^{42}K and ^{214}Bi, Compton events of γ-rays from ^{208}Tl and degraded α events. Also an expectation for the background index in the blinded energy window around $Q_{\beta\beta}$ could be derived and yields, when for example applying the minimum fit model, mean values of $BI_{\text{golden}} = 18.5 \times 10^{-3}$ cts/(keV·kg·yr) for the "golden" data set of the semi-coaxial detectors and $BI_{\text{BEGe}} = 38.1 \times 10^{-3}$ cts/(keV·kg·yr) for the BEGe diodes, respectively.

3.6.3 Physics reach and motivation for PSD

By availing the predicted background index for the blinded region close to the $Q_{\beta\beta}$-value of the double β-decay, several assumptions on the experimental sensitivity can be pursued for a given total exposure $M_{\text{det}} \cdot t$ and efficiency ε. Lets discuss the following hypothetical scenario for the by far predominant "golden" data set of the six working enriched semi-coaxial detectors, where after unblinding an event number of N_{obs} within the since then non-accessible window at $Q_{\beta\beta} \pm 5$ keV is observed.

Using the theoretical predictions on background index BI_{golden} derived by Monte Carlo simulations, that converts (if no further pulse shape analysis is applied to the data yielding $\varepsilon_{\text{PSD}} = 1$) in an average number of $N_{\text{bkg}} = 3.09$ cts for the expected background events within the blinded 10 keV energy window, the 90%C.L. confidence intervals on the value $N_{\text{obs}} = 0, 1, 2, ...$ have been inferred by conducting the Feldman-Cousins approach as reported in [Fel98]. Anyhow, by knowing the boundaries of the confidence belt, also the expected corresponding upper limit on the half-life at (90%C.L.) can be calculated with equation 2.53 via

$$T^{0\nu}_{1/2}(90\%\text{C.L.}) > \frac{\ln 2 \cdot N_{\text{Avg}}}{N_{\text{obs}}(90\%\text{C.L.}) \cdot m_{\text{mol}}} \; \varepsilon \cdot M_{\text{det}} \cdot t \qquad (3.23)$$

when applying the values for the total exposure, the efficiency (both given in table 3.8) and the molar mass $m_{\text{mol}} = 75.6$ g of the enriched detectors, which enter the formula as well. The obtained results of these computations can be found in table 3.10 along with the respective probabilities for detecting N_{obs} events when assuming a Poisson distribution. For reasons of clarity, hereby only cases with a probability > 0.0001 are listed.

Ultimately the sensitivity, defined as the average upper limit on the half-life that would be attained by an ensemble of experiments with the expected background N_{bkgd} and no true signal, can be concluded to 1.49×10^{25} yr. Anyways, in almost 64.4% of all possible outcomes of this example case the upper 90%C.L. limit is turning out to be worse than $T^{0\nu}_{1/2} > 2.0 \times 10^{25}$ yr and thus not sufficient enough to refute the Heidelberg-Moscow claim of the observation for the $0\nu\beta\beta$-signal.

But when analyzing the shape of the detector signals with the aim to reject background events, this situation can be turned to good account though. To investigate the actual impact on the experimental sensitivity, two different approaches have been assumed, where in a first ansatz (i) the signal acceptance of the PSD technique is kept quite high at $\varepsilon_{PSD} = 0.9$ resulting in a moderate background suppression of 50% with on average $N_{bkgd} = 1.66$ remaining background events in the region around $Q_{\beta\beta} \pm 5$ keV. In a competing strategy (ii) the background rejection is drastically en-

Number of observed signals N_{obs}	Without pulse shape analysis $\varepsilon_{PSD} = 1$ $BI = BI_{golden}$ $N_{bkg}(Q_{\beta\beta} \pm 5 \text{ keV}) = 3.09$			With pulse shape analysis $\varepsilon_{PSD} = 0.9 \ (0.7)$ $BI = BI_{golden} \times 0.5 \ (0.2)$ $N_{bkg}(Q_{\beta\beta} \pm 5 \text{ keV}) = 1.66 \ (0.62)$			
	Probability	Upper limit	$T^{0\nu}_{1/2}$ [10^{25} yr]	Probability		Upper limit	$T^{0\nu}_{1/2}$ [10^{25} yr]
0	0.0365	0.82	8.24	0.1909	(0.5157)	1.24 (1.80)	4.92 (2.63)
1	0.1207	1.70	3.99	0.3162	(0.3415)	2.78 (3.69)	2.19 (1.28)
2	0.1999	2.77	2.44	0.2617	(0.1131)	4.25 (5.24)	1.44 (0.91)
3	0.2207	4.12	1.64	0.1445	(0.0250)	5.76 (6.76)	1.06 (0.70)
4	0.1827	5.27	1.28	0.0598	(0.0041)	6.92 (7.92)	0.88 (0.60)
5	0.1210	6.67	1.10	0.0198	(0.0005)	8.24 (9.26)	0.74 (0.51)
6	0.0668	8.15	0.83	0.0055	(0.0001)	9.81 (10.79)	0.62 (0.44)
7	0.0316	9.20	0.74	0.0013		10.86	0.56
8	0.0131	10.66	0.64	0.0003		12.32	0.46
9	0.0048	11.98	0.57	0.0001		13.64	0.45
10	0.0016	13.18	0.51				
11	0.0005	14.49	0.47				
12	0.0001	15.51	0.44				

Table 3.10: Results from Feldman-Cousins calculations [Fel98] on the upper 90%C.L. limit for the Poisson signal mean in case of $N_{obs} = 0, 1, 2, \dots$ observed events and a known mean background of N_{bkg}. As example case here the "golden" data set of the enriched semi-coaxial detectors is considered. Also listed is the Poisson probability of a particular outcome and the corresponding upper 90%C.L. limit on the half-life $T^{0\nu}_{1/2}$ of the $0\nu\beta\beta$-decay. Three different scenarios are assumed: no PSD with $\varepsilon_{PSD} = 1$ and $BI = BI_{golden}$, (i) moderate PSD with $\varepsilon_{PSD} = 0.9$ and $BI = BI_{golden} \times 0.5$ as well as (ii) strong PSD with $\varepsilon_{PSD} = 0.7$ and $BI = BI_{golden} \times 0.2$.

hanced yielding a survival fraction of 20 % leaving only $N_{\mathrm{bkgd}} = 0.62$ residual counts in the blinded energy window at the expense of a decreased signal acceptance of $\varepsilon_{\mathrm{PSD}} = 0.7$. For both cases the outputs received from the calculations are likewise collected in table 3.10.

With respect to a data analysis without using any pulse shape discrimination cut, a significant increase of the sensitivity is observed. The average upper 90%C.L. limit on the half-life thereby improves for option (i) by about 10 % to 1.64×10^{25} yr and for option (ii) by about 7 % to 1.59×10^{25} yr. Obviously the version with a higher signal efficiency and less background reduction holds the better performance and is more favourable. Another important side-effect is the shift of the probability distribution in terms of the expected half-life to the advantage of the experiment. Again alternative (i) seems to be the more benefiting choice showing only a residual fraction of 49.3 % of all possible outcomes with a limit worse than $T_{1/2}^{0\nu}(90\%\mathrm{C.L.}) > 2.0 \times 10^{25}$ yr, which is an actual improvement by 23.5 % if compared to an analysis without pulse shape considerations. In the above discussion only conservative conjectures have been made; still in some individual cases the implication of studies on the topology of events can actually acquire a huge relevance for the final result of the experiment.

In the preceding sections the field of pulse shape discrimination (PSD) and its importance have been stressed repeatedly. Also it was shortly mentioned that such an analysis based on the ratio of the maximum amplitude A of the current pulse over the energy E, is already in place for the diodes of BEGe type and has been proven to be a simple and very effective PSD method [Ago11a][Bud09][Ago13b]. The $0\nu\beta\beta$-signal acceptance at $Q_{\beta\beta}$ after applying a fixed cut on the single A/E parameter is thereby determined to $\varepsilon_{\mathrm{PSD}} = 0.92 \pm 0.02$ using events in the double escape peak (DEP) of the 2615 keV γ-ray from the calibration data with the ^{228}Th sources and cross-checked with the $2\nu\beta\beta$-decays of ^{76}Ge as well as MC simulations. Background events at this energy range are, on the contrary, efficiently suppressed, exhibiting a survival fraction of only 20 %.

Since the major part of the Phase I measurements results from the "golden" data set, also a working and reliable pulse shape analysis technique for the semi-coaxial crystals with sufficient potential is crucially needed for the success of the GERDA experiment to either determine the actual value or to set a new upper limit on the half-life of the neutrinoless double β-decay in ^{76}Ge. But their detector geometry differs extremely from that of the BEGe diodes and hence shows different electric field distributions with the corresponding weighting profiles, where electrons and holes both contribute to the signal formation. As a consequence pulses in the bulk volume exhibit a variety of different shapes and the A/E parameter by itself is not a useful variable for coaxial detectors. This work is therefore dedicated to the development of an effective analysis algorithm for this particular detector geometry, as will be discussed throughout chapter 4, and its verification in terms of reliability or performance on the basis of several consistency checks with physical data in chapter 5 as well as by means of Monte Carlo simulations in chapter 6.

4. Pulse shape analysis of semi-coaxial detectors

As shown in chapter 3, the occurrence of background events resulting from closeby radioactive sources could be significantly mitigated by operating the germanium detector array naked in a low-mass support structure and submersed in liquid argon instead of in a customary massive vacuum cryostat. In combination with the application of prescreened, purified material for the construction of the setup, the shielding based on several layers consisting of LAr, ultra-pure copper and an enormous water tank as well as the carefully chosen experimental site located deep underground, where the surrounding rocks act as an effective absorber against cosmic rays, enabled to establish a very low background level that is an order of magnitude lower with respect to any previous experiment.

Additionally advanced software tools provide access to off-line data analysis routines for a constant monitoring of the experimental performance in terms of energy resolution and stability. It has been proven that a carefull postprocessing and tracking of the data quality can reduce non-physical events due to different origins like cross-talk, electromagnetic noise, discharges or pile-ups. In a further powerful background suppression method, true physical events that pass this preceding quality cuts are excluded from the analysis if they come in coincidence within a $8\,\mu$s time period of a valid detection signal from the muon-veto system or if they cause a simultaneous energy deposition in more than one HPGe detector. Thus by this simple software related applications the sensitivity of the scrutiny for the neutrinoless $0\nu\beta\beta$-decay is effectively enhanced without employing any complicated, cost-intensive hardware components.

But with remaining background indices of $(18 \pm 2) \cdot 10^{-3}\,\text{cts}/(\text{keV·kg·yr})$ for the "golden" and $(63^{+16}_{-14}) \cdot 10^{-3}\,\text{cts}/(\text{keV·kg·yr})$ for the "silver" data set of the enriched semi-coaxial diodes, there is still some room left to improve the sensitivity of the GERDA experiment by means of an elaborated pulse shape analysis technique that yields an increased background reduction. In this chapter the development and application of *multivariate analysis* (MVA) techniques, which are integrated in the TMVA package [Hoe07][Vos07] described in the first section 4.1, to data obtained during Phase I is discussed. The chosen *Artificial Neural Network* (ANN) method, as the classifier with the best performance, can be applied for a powerfull separation of so-called *single site* events (SSE) that deposit energy similar to the hypothetical $0\nu\beta\beta$-signal within a small volume of the detector, from those of *multi-site* topology (MSE) with the energy being deposited at several locations, like typical background from e.g. photons interacting via multiple Compton scattering.

Beyond the first presented performance of the ANN-based pulse shape analysis discrimination (PSD) technique, in [Ago13d], this work focuses on a thorough systematic study of the input parameters and the classification potential after their integration in the multivariate analysis program (section 4.2), before in the next

section 4.3 the training results of the different implemented MVA methods are evaluated. Finally section 4.4 and 4.5 present detailed systematic tests with respect to performance and log term stability using data from calibration and physics runs.

4.1   TMVA - Toolkit for Multivariate Data Analysis

The software package Toolkit for Multivariate Analysis (TMVA) is an open source product[1] and provides a generic scheme where a large variety of sophisticated multivariate classification techniques can be trained, evaluated and tested in parallel. Since they all experience their training and testing on the same independent data sets, meaningfull comparisons between the various methods can be drawn for a particular scope of usage with a given problem. MVA classification algorithms are thereby not only commonly utilized within their originally intended field of application, high-energy physics (HEP), but also play a fundamental role in a wide area of today's natural science, sociology or even commercial applications (e.g. image analysis, financial movements, ...) and will be in case of the analysis presented within the framework of this thesis consequently deployed - for the first time ever - with the aim to scrutiny the neutrinoless double β-decay. In doing so, impeding events induced by any source but the signal of interest is desired to be rejected and thus the classification is performed in respect of the two different categories "signal" and "background".

However the framework consists of object-oriented implementations in C++/ ROOT source code for each of the offered discrimination techniques, which are, as of version 4.1.2 (the one used in this work):

- Rectangular cut optimization

- Projective likelihood estimation

- Multi-dimensional likelihood estimation (PDE range-search, k-NN)

- linear and nonlinear discriminant analysis (H-Matrix, Fisher, FDA)

- Artificial Neural Networks (three different implementations)

- Support Vector Machine

- Boosted/Bagged Decision Trees and

- Predictive learning via rule ensembles.

Although all the above mentioned methods differ e.g. in terms of their response to (non-)linear correlations and vulnerability to overtraining owing to too many

---

[1]TMVA is distributed either separately via `http://tmva.sourceforge.net` or as part of the ROOT package [Bru08].

variables with too few classification power, they still commonly rely on an advancement from one-dimensional cut-based discrimination patterns towards multivariate supervised learning techniques that make use of user-supplied data sets with known event classification. Hereby the data can be either provided in form of ROOT trees or ASCII text files. Both data processing frameworks developed for the GERDA experiment do offer the one or the other format and are therefore suitable for an implemention into the TMVA framework. For a deeper discussion of the used software package for multivariate data analysis the reader may be referred to [Hoe07], nontheless the following section 4.1.1 is intended too very briefly describe the basic working principles and advantages of the various implemented classifiers according to the quoted reference. At this point it should be mentioned however that, depending on the underlying problem, all algorithms require at least some minor specific adjustment to access the maximum classification performance. This of course also includes an individual optimization of the preprocessing (section 4.1.2) and training procedures for the user-supplied data sample sets (section 4.1.3).

4.1.1   Implemented classifiers

Rectangular Cut optimization is the most commonly used and by far simplest technique for separating two event types from a mixed sample. Hereby the discrimination is achieved by an ensemble of rectangular cuts on the input variables, where - in contrast to all other classifiers - only a binary respone (signal or background) is returned. TMVA additionally offers an optimization that maximizes the background rejection for a given signal efficiency by using multivariate parameter fits (Monte Carlo sampling or a Genetic Algorithm are both available).

Projective likelihood estimation consists of constructing a model out of one dimensional probability density functions (PDFs) that reproduces the input variables for the training sample the best. For a given event i, the likelihood $\mathcal{L}_{S(B)}(i)$ for being of signal (S) or background (B) type is obtained by multiplying the corresponding normalized probability densities $p_{S(B),k}(x_k(i))$ of all $k = 1, ..., n_{\text{var}}$ input variables

$$\mathcal{L}_{S(B)}(i) = \prod_{k=1}^{n_{\text{var}}} p_{S(B),k}(x_k(i)) \qquad \text{with} \int_{-\infty}^{+\infty} p_{S(B),k}(x_k)\mathrm{d}x_k = 1, \ \forall k \ . \qquad (4.1)$$

The unknown parametric form of the PDFs is empirically derived from the histogrammed variable distributions in the training data with non-parametric functions as fitted polynomial splines or by utilizing an unbinned kernel density estimator. Further scaling by the sum of the signal and background likelihood then yields the response value $y_{\mathcal{L}}(i) = \mathcal{L}_S(i)/(\mathcal{L}_S(i) + \mathcal{L}_B(i))$.

Multi-dimensional likelihood estimation generalizes of the preceding projective likelihood classifier to n_{var} dimensions, where n_{var} again denotes the used number of input variables. In the PDE Range Search, or in short PDE-RS, the estimation for an observed event i from the training sample is deduced by counting

the (normalized) number $n_{S(B)}(i,V)$ of sourrounding signal and background events within a defined volume V. The final classification $y_{\text{PDE}-\text{RS}}(i,V)$ is then conducted according to the majority of the nearest training events via the ratio

$$y_{\text{PDE}-\text{RS}}(i,V) = \frac{1}{1 + (n_B(i,V)/N_B) \cdot (N_S/n_S(i,V))} \, , \qquad (4.2)$$

where $N_{S(B)}$ represents the total number of signal or background events in the whole data training set.

Similar to the PDE-RS, the second multi-dimensional k-Nearest Neighbour (k-NN) approach, as well compares a given event to reference data of the training set and searches for a fixed number of adjacent events with closest distances (see figure 4.1 for an example classification with two of the n_{var} discriminating input variables x_k, $k = 1, .., n_{\text{var}}$). As a probability density estimator (PDE) then again acts the fraction of signal or background events in the vicinity. For both options the influence of each reference event can be additionally weighted with respect to their distance by applying a number of offered kernel functions.
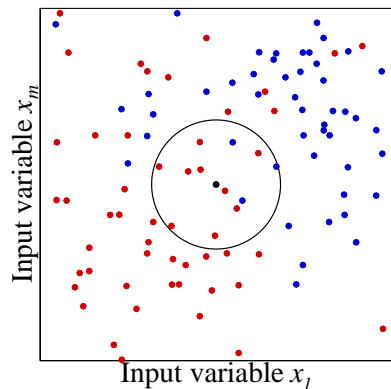
Figure 4.1: Working principle of the k-Nearest Neighbour algorithm for two of the n_{var} discriminating input variables x_k with $k = 1, .., n_{\text{var}}$. The plot represents a projection upon the two-dimensional coordinate planes, where the filled red and blue circles denote either signal or background events. In this particular example, the k-NN method searches for the 12 points in the *nearest neighbourhood* (black hollow circle) with the closest distance to the query event i, shown as black filled circle.

Linear and non-linear discriminant analysis: In the linear standard method of Fisher discriminants event classification is obtained by determining a hyperplane in the input variable phase space such that the projection of their output classes upon the corresponding axis results in the best possible separation of signal and background from each other, whereas events of the same topology are collected in a close vicinity. Mathematically the discrimination of events is based on the overall sample means $\overline{x}_k$ and class-related sample means $\overline{x}_{S(B),k}$ of each input variable $k = 1, ..., n_{\text{var}}$ as well as the total covariance matrix C of the sample that can be partitioned into a sum of a within-class matrix $\mathcal{W}_{kl} = \sum \langle x_{S(B),k} - \overline{x}_{S(B),k} \rangle \langle x_{S(B),l} - \overline{x}_{S(B),l} \rangle = C_{S,kl} + C_{B,kl}$ and a between-class matrix $\mathcal{B}_{kl} = \frac{1}{2} \sum (\overline{x}_{S(B),k} - \overline{x}_k)(\overline{x}_{S(B),l} - \overline{x}_l)$ - each of them describing the distribution of the events with respect to the means of their own class or the overall sample means. The response of the Fisher algorithm for event i is then given by

$$y_{\text{Fisher}}(i) = F_0 + \sum_{k=1}^{n_{\text{var}}} F_k x_k(i) \qquad (4.3)$$

with the *Fisher coefficients*

$$F_k = \frac{N_S N_B}{N_S + N_B} \sum_{l=1}^{n_{\text{var}}} \mathcal{W}_{kl}^{-1}(\overline{x}_{S,l} - \overline{x}_{B,l}) \,, \tag{4.4}$$

the number $N_{S(B)}$ of the signal or background events in the training sample and the offset F_0 shifting the sample mean $\overline{y}_{\text{Fisher}}$ to zero.

Alternatively the H-Matrix method computes for each event i a multivariate signal(background) $\chi_{S(B)}^2(i)$ estimator using the corresponding sample means $\overline{x}_{S(B)}$ and the inverse covariance matrix $C_{S(B)}^{-1}$ (also called *H-Matrix*)

$$\chi_{S(B)}^2(I) = \sum_{k,l=1}^{n_{\text{var}}} (x_k - \overline{x}_{S(B),k}) C_{S(B),kl}^{-1}(x_l - \overline{x}_{S(B),l}) \,. \tag{4.5}$$

From this $y_{\text{H}}(i) = (\chi_B^2(i) - \chi_S^2(i))/(\chi_S^2(i) + \chi_B^2(i))$ is adduced as classification parameter.

An intermediate solution designed for only partially non-linear or relatively simple problems is offered with the Function Discriminant Analysis (FDA), where any desired function with adjustable parameters is fitted to the training sample data, requiring the function value to be as close as possible to '1' for signal or '0' for background events.

Artificial neural networks (ANN) represent any simulated combination of connected nodes, also called neurons, with each generating a certain output response according to a particular (non-linear) function at a given set of weighted input parameters. Thus for a particular event i a neural network can be regarded as a mapping from a multi-dimensional space of $k = 1, ..., n_{\text{var}}$ input variables $x_k(i)$ onto a final one-dimensional response value $y_{ANN}(i)$. Thereby the performance of an ANN is defined by the specific arrangement of the neurons, the weights assigned to the inter-neuron-connections and by the response resulting from the overall neuron response function ρ.

In principle artificial neural networks consisting of n neurons exhibit a maximum of n^2 possible connections. However in case of *multi-layer perceptrons*, as one conceivable realization of an ANN, this complexity is reduced by arranging the neurons in layers with the only allowed connections being from a given layer to the following one in forward direction without cycles or loops. The resulting layout scheme then consists of a first *input* layer composed of n_{var} neurons with $k = 1, ..., n_{\text{var}}$ input variables, a terminating *output* layer that holds the response value y_{ANN} and a variable number of intermediate so-called *hidden* layers. An example of such an feed-forward architecture is shown in figure 4.2 for a multilayer perceptron with two hidden layers. In fact all three implementations in TMVA concerning neural networks are of this type and offer a configurable user-defined number of layers between input and output as well as neurons within each of these layers.

The neuron response function ρ transforms the input signals with weights $w_{ij}^{(l-1)}$ from the incoming $i = 1, ..., n$ connections of the j-th neuron in layer number l
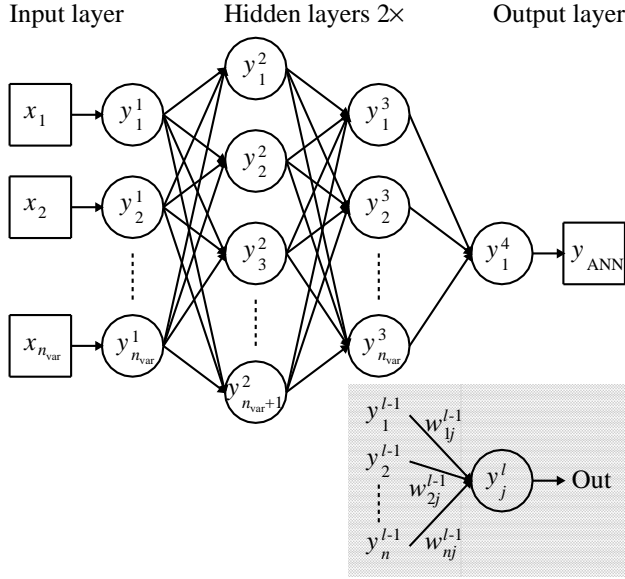
Figure 4.2: Multilayer perceptron with an input layer that consists of a number of n_{var} input variables and an output layer given by one neuron that yields the response value y_{ANN}. Exemplarily the middle part of the here shown feed-forwarded neural network structure is constructed by two hidden layers each holding $n_{\mathrm{var}}+1$ or n_{var} neurons. The gray shaded inset at the right bottom depicts the j-th neuron y_j^l in layer l with n input connections that carry a weight of $w_{ij}^{(l-1)}$.

into the neuron output $y_j^{(l)}$ (see gray shaded inset on the bottom right in figure 4.2). Ultimately ρ can be often divided into a first $\mathcal{R}^n \mapsto \mathcal{R}$ *synapse function* κ and a second $\mathcal{R} \mapsto \mathcal{R}$ *neuron activation function* α. Within TMVA the latter are implemented optionally in the following forms

$$\kappa : (y_1^{(l)}, ..., y_n^{(l)} | w_{0j}^{(l)}, ..., w_{nj}^{(l)}) \rightarrow \begin{cases} w_{0j}^{(l)} + \sum_{i=1}^n y_i^{(l)} w_{ij}^{(l)} & \text{Sum} \\ w_{0j}^{(l)} + \sum_{i=1}^n (y_i^{(l)} w_{ij}^{(l)})^2 & \text{Sum of squares} \\ w_{0j}^{(l)} + \sum_{i=1}^n |y_i^{(l)} w_{ij}^{(l)}| & \text{Sum of absolutes} \end{cases} \quad (4.6)$$

and

$$\alpha : x \rightarrow \begin{cases} x & \text{Linear} \\ e^{-x^2/2} & \text{Radial} \\ 1/(1 + e^{-kx}) & \text{Sigmoid} \\ (e^x - e^{-x})/(e^x + e^{-x}) & \text{Tanh} \end{cases} . \quad (4.7)$$

Hence, for a given arrangement of nodes the training of a neural network is performed by optimizing the interconnecting weights and α, κ functions such that the discrimination power between events of background or signal topology is maximized. By way of example, the output of an ANN consisting of, for the sake of simplicity, only a single hidden layer with a hyperbolic tangent activation function $\alpha^{(1)}$ and an output layer represented by a linear activation function $\alpha^{(2)}$ results in the classifier response

$$y_{\mathrm{ANN}} = \sum_{j=1}^{n_{\mathrm{h}}} \tanh\left(\sum_{i=1}^{n_{\mathrm{var}}} x_i w_{ij}^{(1)}\right) \cdot w_{j1}^{(2)} , \quad (4.8)$$

if a simple sum is applied for the synapse function κ. Here n_{var} and n_{h} specify the number of neurons in the input and the hidden layer, respectively, Further the

weight $w_{ij}^{(1)}$ accounts for the connections between the i-th input-layer neuron and the j-th hidden-layer neuron and subsequently $w_{j1}^{(2)}$ for the connection between the j-th hidden-layer neuron and the final output neuron.

Support Vector Machine as a non-linear discrimination algorithm aligns a hyperplane in a transformed variable space that separates signal and background data and relies only on a minimal subset of all training events (*support vectors*) in close vicinity. In order to define a non-linear metric in the variable space, several (Polynomial, Gaussian and Sigmoidal) kernel functions are on hand.

Boosted/bagged decision trees (BDT) are binary structured classifiers where at each branching consecutive split decisions (passed/failed) are performed on one single discriminating input parameter at a time. As depicted in figure 4.3 the phase space of the training sample is hereby continuously divided according to cut on the variable with the maximum separation power for the given node until a final so-called leaf node is reached that classifies an event i as either signal-like or background-like, depending on the majority of training events that end up in it.
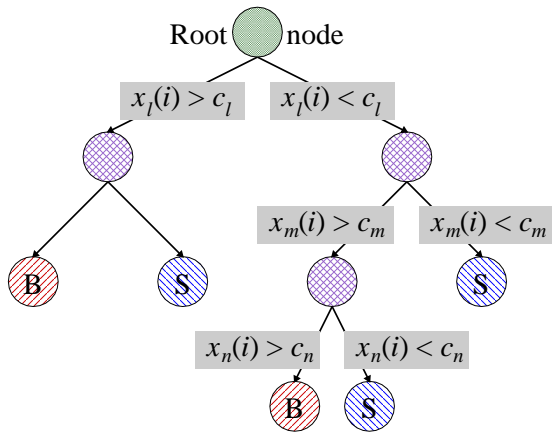
Figure 4.3: Schematic view of a decision tree. Starting from the root node (green) the i-th event of the data, described by the parameter set $x_k(i)$ with $k = 1, ..., n_{var}$ discriminating input variables, passes a sequence of binary split criterions c_k. Thereby at each node the parameter that results in the best separation power between the two event classes is used, until the branch reaches a *leaf node* that is either classified as signal "S" or background "B".

Since single decision trees tend to suffer from low statistics, the procedure is often extended to a *forest* of decision trees by the concept of 'boosting' with the advantage of an enhanced performance and a higher stability in respect of fluctuations. All individual trees are derived from the very same training data set by reweighting the events. Hereby in the most popular algorithm implemented in TMVA, the *adaptive boost* (AdaBoost), events that have been misclassified during the building of the last $(n-1)$-th decision tree are allocated a higher event weight $\alpha_n = (1 - err_{n-1})/err_{n-1}$ correlated to the misclassification rate err_{n-1} in all leaf nodes, for the training of the following n-th tree. As opposed to performing boosting with the aim to construct an ensemble of decision trees, bagging represents a resampling technique that randomly draws events out of the parent sample to construct different training samples.

Predictive learning via rule ensembles (Rule-Fit) makes use of an ensemble of so-called rules, each defined by series of cuts, that can be for example easily extracted from every node (except the root node) of the above mentioned decision trees. When applied on a given discriminating input argument, the return value of

a rule is non-zero only if the whole sequence of cuts is satisfied. The classification function $y_{\text{Rule}-\text{Fit}}(i)$, as response of the Rule-Fit algorithm, is composed as linear combination of the rule ensembles with additional coefficients (rule weights) that maximizes the separation performance for signal and background events.

4.1.2 Preanalysis and -processing

The interaction between the user-dependent input and the automatized TMVA classification machinery consists at the beginning of a first preanalysis and -processing of the data. In the preanalysis the linear correlation coefficients and an interim ranking (later superseded by a classifier-specific version) of the input variables are derived.

In addition also a preprocessing can be applied on the training/testing events prior to forwarding them to a multivariate method. Besides the normalization of the input variables, two possible transformations are offered: decorrelation via the square-root of the covariance matrix or via a principal component decomposition. For both of them the decorrelation only succeeds for linearly correlated and Gaussian distributed parameters. Eliminating linear correlations from the data samples can enhance the separation power of some classifiers that do not take variable correlations into account. For strongly non-linear problems, it is instead likely that the performance becomes even worse with linear correlation and the appropriate methods without any prior decorrelation should be applied. Thus all multivariate analysis methods can be in principle distinguished into two different types with one intrinsically considering non-linear correlations between input variables in the classification (as for example ANN and BDT) and the other doing not (presented by the Likelihood-, Fisher- and cuts-related methods). It is therefore expected that the different algorithms show very different performances when applied for a certain purpose. Ultimatively, there is no specific answer to the question what classifier should be optimally used for a given set of (non-)correlated input parameters. However, as a transparent and easy graspable guide, an assembly of several relevant properties of the MVA methods, such as for instance their performance behaviour with respect to the degree of correlation between the supplied variables, is provided in table 4.1.

4.1.3 Training, testing and evaluation

After the preprocessing for each classifier a dedicated weight file in XML format that contains the performed transformations is created when the training has converged. Reading the weight files also provides all the information needed for the later application of the trained classifier on the data of unknown composition. Hereby the events pass through the corresponding decorrelation schemes with which the original training data has been transformed.

However, once the training has been finished, the emphasis is put on the extraction of the achieved performances and the results from the different classifiers become subject of evaluation aspects. One important issue is, for instance, the ranking of

the variables according to their classification power. By only determining and excluding weakly-separating input parameters a significant gain in the robustness and performance for the methods can be attained already. But also the classifiers tend to be less sensitive for overtraining which occurs within a machine learning problem when too many parameters of a model dependent algorithm have to be adjusted to too few data points. Consequently, the various offered multivariate methods exhibit a different predisposition for overtraining. Linear discriminants, like for example Fischer or H-Matrix, can hardly suffer from overtraining, where on the contrary boosted decision trees are easily overtrained without the appropriate measures of precaution due to their large number of nodes. As a problematic outcome, overtraining causes a deceptive increase of the classification capability - if measured in the training sample over the objectively acquirable one that can be ascertained with an independent test sample. In order to detect this effect and to measure the actual impact it is convenient to compare the classification distributions obtained from training and test samples for eventual discrepancies. Despite their robustness on overtraining or less classifying variables often the speed of the algorithm during the training procedure or application on data of unknown composition is as well of crucial importance (especially if the computing is slowed down due to a high number of discriminating parameters feeded into the program). The classification properties of both aspects are also compiled in table 4.1 in order to give a complete but brief and strongly simplified overview of the respective advantages and drawbacks inhered by the different formalisms.

After all, the preferable algorithm to be used for a certain purpose highly depends on the problem on hand, but can be easily estimated for the aim of this work to improve the sensitivity of the GERDA experiment when analyzing the back-

Criteria		Classifier									
		Cuts	Likeli-hood	PDE-RS	k-NN	H-Matrix	Fisher	ANN	SVM	BDT	Rule-Fit
Performance	No or linear correlations	o o	o o o	o o	o o	o o	o o o	o o o	o o	o o	o o o
	Non-linear correlations	o	o	o o o	o o o	o	o	o o o	o o o	o o o	o o o
Speed	Training	o	o o o	o o o	o o o	o o o	o o o	o o	o	o	o o
	Response	o o o	o o o	o	o o	o o o	o o o	o o o	o o	o o	o o o
Robustness	Overtraining	o o o	o o	o o	o o	o o o	o o o	o o	o o o	o	o o
	Weak variables	o o o	o o	o	o	o o o	o o o	o o	o o	o o o	o o

Table 4.1: Collection of different classifiers properties concerning the performance in case of no, linear or non-linear correlations between the feeded input variables, the speed of the training procedure or application of the deduced algorithm on the data of unknown composition and robustness in terms of overtraining and weakly discriminating parameters. The circles represent the attributed degrees "good" = o o o, "fair" = o o and "bad" = o (adopted from [Hoe07][Vos07]).

ground rejection as a function of the signal efficiency (as will be done in subsection 4.3.2). This and many other control plots, as the MVA-output distributions of the training/test samples, variable distributions or correlation matrices, will be provided in the following sections for the specific application of the TMVA package on the experimental data of GERDA Phase I.

4.2 Adaption to the GERDA Experiment

In order to success fully adapt the open-source TMVA software discussed in the last section 4.1 several issues have to be thoroughly considered, like for instance the proper choice of meaningful (in the sense of discrimination power) input variables, the provision of training or test samples which represent a realistic proxy for signal-like or background-like events and, finally, the carefull splitting of the overall data into several distinct sets for reasons of changes in the setup or different boundary conditions (e.g. BEGe and semi-coaxial detector geometry). These facets are intended to elucidated in the subsequent three subsections 4.2.1, 4.2.2 and 4.2.3.

4.2.1 Input variables

Since all the recorded information on an event occurring within the bulk volume of the enriched semi-coaxial detectors of the GERDA experiment is contained in the charge trace digitized by the FADC, it is reasonable to also use these samples as input variables for the multivariate data processing. Naturally the "high-frequency-short-window" option with a sampling rate of 100 MHz and a length of $4\,\mu s$ is preferable to the alternative "low-frequency-big-window" alternative with 25 MHz and $160\,\mu s$ for the pulse shape analysis. If considering the electrical field distribution of the semi-coaxial detector geometry, where electron and holes both contribute to the charge collection with the result that huge differences can arise even at the very beginning or end of the pulse depending on the carrier drift, a restriction to only parts (low, middle or top) of the leading edge is hardly feasible and most certainly results in an significant deterioration of the selection performance. To not lose any discrimination power, it is further aspired to utilize the entire pulse or, to be exact, the whole rising part of the sampled trace in the MVA analysis. Therefore several steps are performed to prepare the corresponding samples of the trace before forwarding them as input parameters to the TMVA framework:

- At the beginning, a baseline subtraction is applied on the complete trace length using the information as mean or RMS of the samples obtained from the first $20\,\mu s$ before the trigger. In case that there is a slope in the baseline, as caused due to pile-up, the event is declined. As already mentioned in section 3.3 this effect is induced by a high detection rate and thus this selection effects practically only calibration data that are used for the training or testing samples.

- In the next step the pulse is slightly smoothed with a moving window averaging of 80 ns integration time corresponding to 8 samples. The purpose of this procedure is to reduce the noise and therefore also a possible later effect of the energy dependent signal-to-noise ratio on the discrimination pattern of the multivariate analysis tools. With averaging over a number of 8 samples, a fair compromise between an efficient noise reduction and only a small sacrifice on information was chosen.

- To further remove the energy dependence, the maximum pulse height, that is directly correlated to the energy deposited within the active volume of the detector (see section 3.3), is normalized to one.

- Finally, the times t when the pulse reaches $1, 3, 5, ..., 99\,\%$ of the full height are determined for a step size of $2\,\%$. Hereby in particular the time position where the pulse height yields a value of $A_1 = 0.5$, equivalent to $50\,\%$ of the maximum amplitude, serves as reference and is set to zero: $t(A_1 = 0.5) = 0$. In order to increase the precision of the rise time determination, which is strongly limited owing to the $100\,\text{MHz}$ sampling frequency, a (linear) interpolation is applied between two bins when determining the corresponding time points.

An example for the selection of the input parameters is depicted in figure 4.4 for two pulses representing single site (SSE) and multi site (MSE) candidate events (blue and red solid lines) measured with the ANG4 detector in a calibration phase during Run 28 (after applying the MWA). The reference time $t_{\text{SSE,MSE}}(A_1 = 0.5) = 0$ at $50\,\%$ of the maximum pulse amplitude is marked by the respective fine dotted lines. Additionally shown is the determination of the input parameters feed into the TMVA algorithm for the pulse height $A_2 = 0.2$ at $20\,\%$ of the pulse amplitude with the corresponding times $t_{\text{SSE}}(A_2)$ (blue dashed line) and $t_{\text{MSE}}(A_2)$ (red dashed line). The thus resulting 50 timing informations at the different heigths of each charge pulse are used as input for the multivariate data analysis.
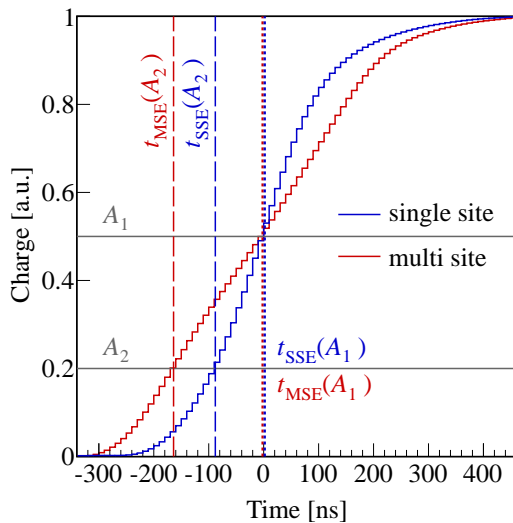
Figure 4.4: Physics data pulses obtained with the ANG4 detector in a calibration measurement during Run 28 for SSE (blue solid line) and MSE (red solid line) event candidates (after applying a mowing windo average of 80 ns). Given by fine dotted lines is the reference time $t_{\text{SSE,MSE}}(A_1 = 0.5)$ at $50\,\%$ of the maximum pulse amplitude. Also shown is the determination of the input parameters for the TMVA algorithm at a pulse height of $A_2 = 0.2$ with the respective times $t_{\text{SSE}}(A_2)$ (blue dashed line) and $t_{\text{MSE}}(A_2)$ (red dashed line).

4.2.2   Selection of training/testing samples

Common to all investigated multivariate pattern recognition programs provided by the TMVA software is the use of calibration data, approximately taken once per week to train the algorithm. The spectrum obtained from calibration measurements with ^{228}Th sources (see section 3.4) contains a full energy peak (FEP) at 2614.5 keV from the ^{208}Tl decay as part of the thorium decay chain. Associated to this energy line is the double escape peak (DEP) at 1592.5 keV that comprises (apart from some almost negligible bremsstrahlungs) exclusively events of single site topology, while the single escape peak (SEP) at 2103.5 keV and the full energy peaks (FEP) - the second one present in the spectrum at 1620.7 keV originates from the decay of ^{212}Bi as another channel of the thorium chain - are dominantly MSE.
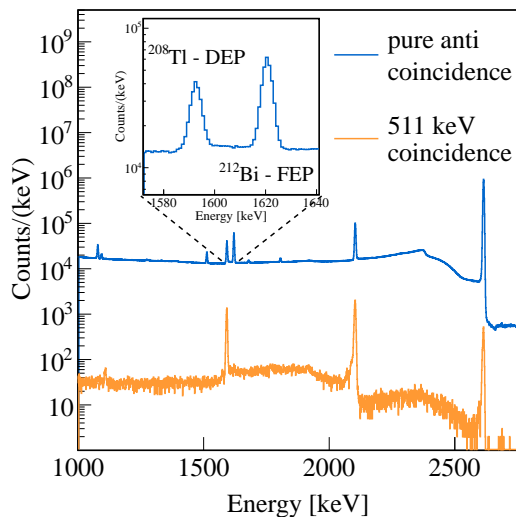
Figure 4.5: Energy spectrum of the combined six enriched semi-coaxial germanium diodes and 70 individual calibration runs taken during GERDA Phase I with an applied anti-coincidence cut (blue line). The DEP of the 208Tl decay at 1592.5 keV and the FEP of the ^{212}Bi decay at 1620.7 keV used as training samples for the MVA are both revisualized strongly enhanced in the inset on the top margin. Also shown is the spectrum of events that are measured in coincidence with an energy deposition of 511 keV in a second detector (orange).

An example spectrum in the energy range from 1000 keV to 2750 keV is given in figure 4.5, where all calibration runs performed during GERDA Phase I - in total a number of 70 individual data sets - are summed up for the six enriched semi-coaxial germanium diodes after applying an anti-coincidence cut (blue line). The γ-lines discussed above are altogether clearly visible as the four most prominent peak structures with the energetically highest line, the FEP of ^{208}Tl, being at the right margin of the histogram.

With respect to the direct application as multivariate training and/or testing samples, the ^{208}Tl DEP events within the interval 1592.5 keV $\pm$ 1·$FWHM$ serve as the only available proxy for SSE and such being the case as signal data set, whereas multi site events of the adjacent full energy line of ^{212}Bi in the equivalent interval around 1620.7 keV are selected as background data set. Both peaks are revisualized enhanced in the small inset on top of figure 4.5. The choice of the peaks in close vicinity i.a. also accounts for a possible impact of the singal-to-noise ratio on the classification output, despite the adopted counter measures as averaging or normalizing. However it should be reminded of the one problematic disadvantage coming along with the non-eludable DEP, which is that the distribution

of the associated events is not exactly homogeneous inside the detector bulk volume as it is for $0\nu\beta\beta$-decays. This is because the two escaping 511 keV photons result in the events locations being predominantly situated at the corners.

Another noteworthy critical issue arising with the choice of the singal and background event classes is, that both samples are not perfectly pure but rather a mixture of SSE and MSE due to the Compton events under the energy lines. A possible strategy to encounter this Compton induced background was found by applying a coincidence cut, where only events are kept that deposit simultaneously an energy of 511 keV corresponding to the rest mass of an electron in a second detector of the germanium array. The resulting spectrum is plotted in figure 4.5 as well (orange histogram). Obviously events contained in the double and single escape peak are effectively isolated, while effectively suppressing all other γ-lines and the Compton continuum. On average the improvement for the signal-to-background ratio S/B yields a factor of ≈ 6 for the DEP and ≈ 10 for the SEP (as new proxy in barter for the rejected FEP of ^{212}Bi). Besides the acceptable drawback of utilizing signal and background samples from then distant peaks for the training, which may introduce an energy dependency in the multivariate analysis, this "electron-triggering" procedure only allows very small (for some detectors even too small) training samples sizes and is therefore declined. Dedicated investigations on that issue finally revealed that based on a such reduced amount of samples the classification methods become not only less performing but necessarily also more proned to overtraining. A list of the resulting event number per data set is stated in table 4.2 for each detector channel.

But events evoked by Compton scattering of γ-rays also bear exciting opportunities since they contain a large fraction of SSE that spans a wide energy range. They are thus suitable for characterizing the PSD methods, especially their energy dependencies. Likewise the neutrinoless variant of the double β-decay, the $2\nu\beta\beta$-decay is homogeneously distributed and hence also allows a cross check of the of the pulse shape analysis in terms of the signal detection efficiency. Both consistency checks are - among others - presented in the succeeding chapter 5.

4.2.3   Splitting of Phase I data into several sets

Similar to the case of the $0\nu\beta\beta$ analysis or determination of the background index BI, where the data was splitted into a so-called "golden" and "silver" sample (already mentioned in section 3.6.1), for the development of the multivariate PSD techniques the Phase I measuremens have been - again - grouped in several, to be more precise three, different intervals with the aim to obtain the optimal results from the TMVA classification algorithms. This splitting does thereby of course account for the training/testing phases with supplied samples of known composition from the 70 calibration runs as well as for the subsequent application on the data of unknown composition. As for the pulse shape analysis presented in this thesis, the separation of the measurements into different subsets sharing the same characteristics involves two different motives:

- **Change in the setup configuration:** With the insertion of the BEGe diodes at the beginning of July 2012 and some preceding modifications regarding the SIS, the detector assembly as well some electronics have been significantly altered. In a following short period of measurements several changes in the behaviour of the germanium crystals could be identified, including an increased level of background events and, as for the BEGe's only, a so far unobserved time dependent shift of the A/E pulse shape parameter [Ago13d].

- **Different length of calibration runs:** The duration of the (bi-)weekly calibrations, performed to monitor the energy resolution and performance stability of the germanium detectors, varies over the total time span of the GERDA Phase I data taking. Since the combined individual calibration measurements are intended to serve as input sample for the training of the event recognition methods, this would yield in a higher weighting or importance of single data sets or time intervals recorded with more statistics.

Figure 4.6 compares the number of events within the regions $\pm 1 \cdot FWHM$ around the DEP of ^{208}Tl at 1592.5 keV (blue) and FEP of ^{212}Bi at 1620.7 keV (red), used as classification samples for the multivariate data analysis, of each calibration run as a function of time. For all of the shown six semi-coaxial detectors, the chronological sequence is defined by a higher event number level in the first half of the overall time span - that peaks at the beginning of July owing to intensified characterization measurements for the recently deployed BEGe detectors - if compared with the remaining second part of Phase I. Also marked is the resultant separation applied to the three data-sets into a first, second and third part of similar behaviour (black arrows and labeling). The first period with on average longer calibration measurements extends from the start of data taking to July 2012, where the detector array as well as several more hardware components have been changed (pI), the second period (pII) lasts for the four weeks after the modifications and the third period (pIII) represents the rest of Phase I with in general shorter calibration runs. Different from the other detectors, for RG2 the second period spans until November 2012 when its operating voltage was reduced. By this splitting pattern a fair compromise between isolating data-set of different boundary conditions and accumulating still sufficient statistics for the training process of the algorithms could be preserved (for each period at least ≈ 4500 events are available per detector and event class).

In table 4.2 the event numbers of the signal- and background-like proxy samples are summarized for the three periods pI, II+III if a pure anticoincidence cut is applied and for the unsplitted data-set in case of a coincidence cut where an additional energy amount of 511 keV is deposited in a second detector. Due to a stronger intensity of the 1620.7 keV FEP of ^{212}Bi as proxy for MSEs compared to the 1592.57 keV DEP of ^{208}Tl of predominantly SSEs, the size of the background samples is systematically higher for all data-sets. Potential variations in the event numbers with respect to the single detectors (especially for the RG1+2 diodes with a shift to smaller values) on the contrary arise - among other things - because of the different crystal dimensions and

positions within the array, which do have naturally an impact on the anticoincidence performance. Further also the relative distances of the three ^{228}Th calibration with respect to the germanium detectors do have a significant effect on the measured event rate (as will be discussed in section 6.2).
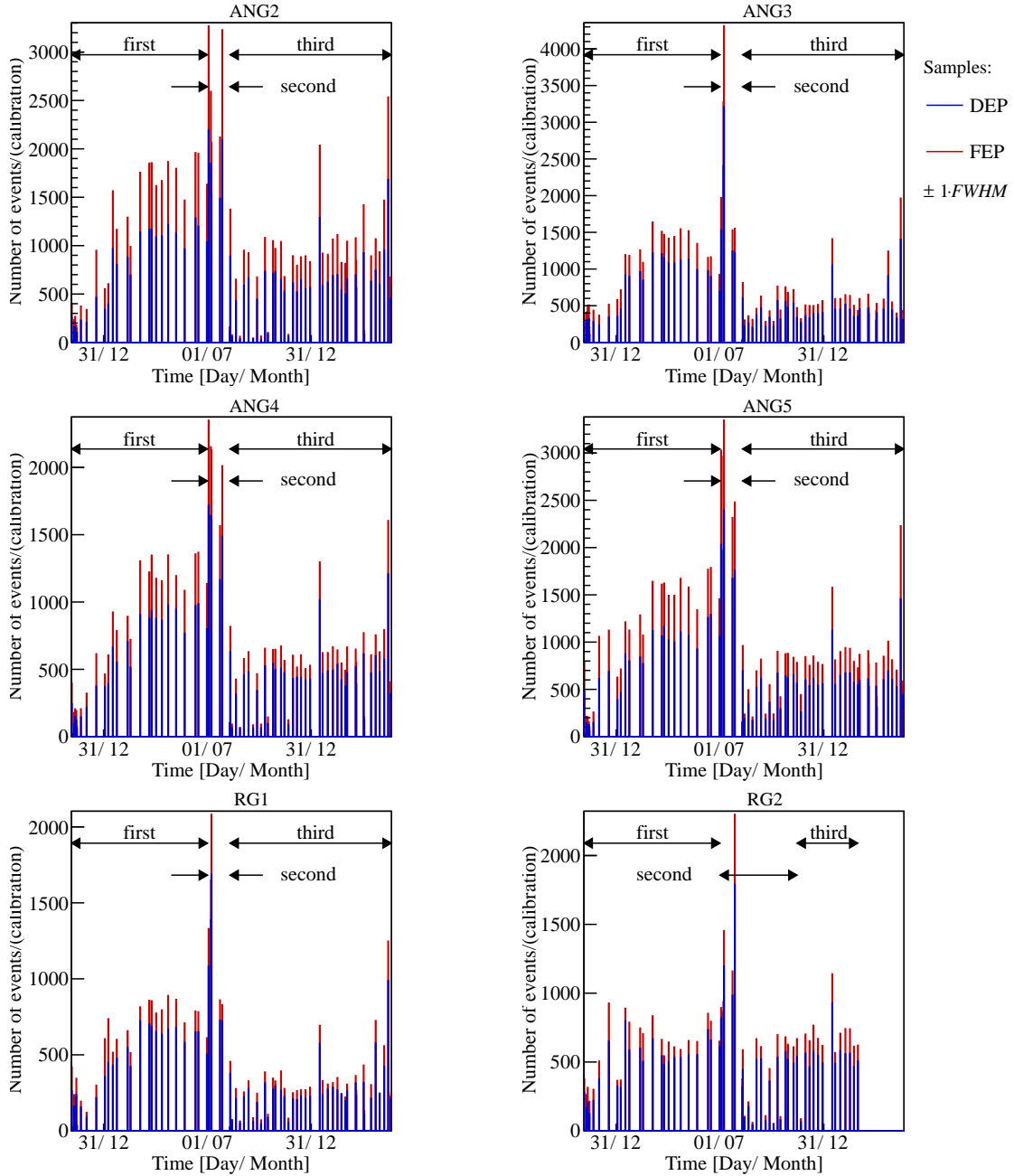

Figure 4.6: Number of events within the energy intervals $\pm 1 \cdot FWHM$ around the DEP of the ^{208}Tl decay (blue) and FEP of the ^{212}Bi decay (red) for each single calibration run of the PhaseI data taking as a function of time (here: separately for the six semi-coaxial detectors). The splitting of the data into three individual sets is denoted by black arrows.

Detector	Training sample	Number of events in data set			
		pI	pII	pIII	All + 511 keV coincidence
ANG2	signal	21465	7184	17198	2034
	background	32535	10262	25700	3548
ANG3	signal	20919	8675	19332	1307
	background	27217	10816	25502	1954
ANG4	signal	16472	6019	18668	1772
	background	22961	7971	23201	3103
ANG5	signal	20967	7739	23503	1980
	background	29705	10733	31404	3366
RG1	signal	12523	4403	11041	1255
	background	15761	5585	13319	2088
RG2	signal	13351	10216	7873	294
	background	15771	12486	9758	510

Table 4.2: Event numbers of signal or background training samples of the multivariate pulse shape analysis for the three different data-sets and detectors. For each detector, event class and subset a statistic of at least ≈ 4500 examples is collected. Also the numbers for a scenario with combined data-sets and an applied 511 keV coincidence cut are listed.

4.3   Evaluation of training/testing results

4.3.1   Properties of the input variables

As already mentioned during the discussion of the TMVA pattern recognition software in section 4.1, the supplied input variables will much likely show a more or less pronounced separation potential into either signal or background for a given event. This characteristic can be directly reflected in a difference of importance or ranking of the various parameters - here times t in units of [%] when the charge pulse has reached a certain percentage of its maximum amplitude - for the construction of the classification boundaries of the offered algorithms. Also relevant for the success or
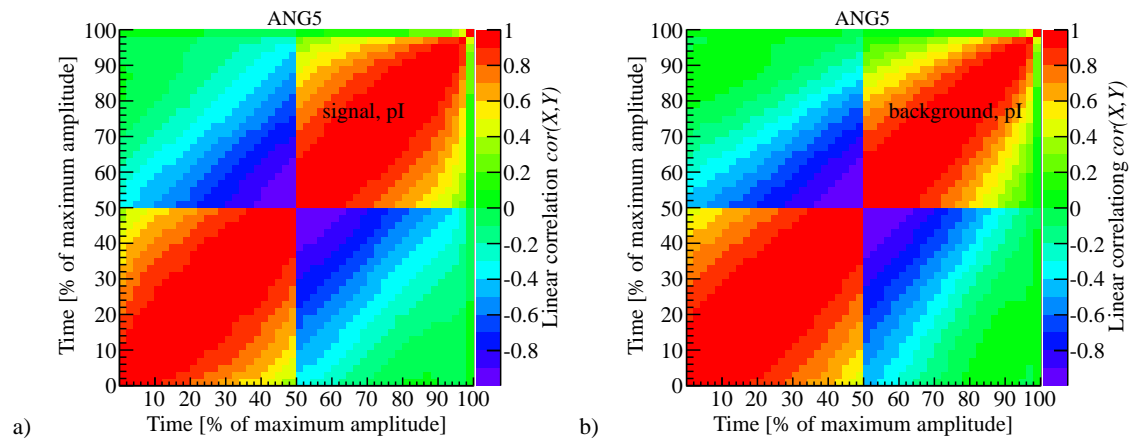
Figure 4.7: Linear correlation coefficients between the $n_{\mathrm{var}} = 50$ input variables used for the **a)** signal and **b)** background training samples of the ANG5 detector in period pI.

failure of a particular classifier is the correlation strength and nature (linear or non-linear) present among the different discriminating variables, which can engender a significantly degraded performance for some methods, as for example the projective likelihood or any Linear Discriminant Analysis (LDA). Both issues are intended to be investigated in the following.

Usually the correlation $cor(X, Y)$ between two random input parameters X, Y with means $\overline{X}$, $\overline{Y}$ and variances $\sigma(X)$, $\sigma(Y)$ is measured by

$$cor(X, Y) = \frac{cov(X, Y)}{\sqrt{\sigma(X)\sigma(Y)}} = \begin{cases} 1 & \text{exact linear with positive slope} \\ 0 & \text{no linear relation} \\ -1 & \text{exact linear with negative slope} \end{cases} \tag{4.9}$$

with the covariance

$$cov(X, Y) = \sum_{i=1}^{n_{\text{var}}} (X_i - \overline{X})(Y_i - \overline{Y}) . \tag{4.10}$$

Per definition the coefficient $cor(X, Y)$ is symmetric in X and Y and lies between an interval of $[-1, 1]$ that quantifies a linear relationship. While zero holds for entirely independent variables, the converse is in general not true though, since non-functional or functional relations of higher orders may be not, or only barely, accounted for in the value of $cor(X, Y)$.

Method unspecific ranking	Time [% of maximum amplitude]					
	ANG2	ANG3	ANG4	ANG5	RG1	RG2
	pI, pII, pIII	pI, pII, pIII	pI, pII, pIII	pI, pII, pIII	pI, pII, pIII	pI, pII, pIII
1	1, 1, 1	85, 87, 87	85, 87, 87	87, 87, 85	85, 87, 87	91, 93, 95
2	3, 3, 3	87, 89, 89	83, 89, 85	85, 89, 87	83, 89, 85	93, 91, 93
3	91, 5, 5	83, 85, 85	87, 85, 89	83, 85, 89	81, 85, 89	89, 89, 1
4	5, 7, 7	81, 83, 83	81, 83, 83	81, 83, 83	87, 83, 83	87, 95, 91
5	93, 95, 95	79, 81, 81	87, 81, 81	89, 81, 81	79, 81, 81	85, 87, 3
6	89, 97, 9	89, 1, 3	89, 91, 81	79, 91, 79	77, 1, 79	95, 85, 89
7	7, 9, 93	1, 3, 1	77, 79, 79	77, 79, 91	89, 91, 91	83, 83, 5
8	87, 93, 97	77, 5, 79	1, 77, 1	75, 77, 77	75, 3, 77	81, 81, 87
9	9, 91, 11	3, 79, 5	3, 75, 77	91, 75, 75	1, 5, 75	79, 1, 7
10	85, 11, 91	75, 7, 7	75, 3, 3	73, 73, 73	3, 79, 1	77, 79, 9
⋮	⋮	⋮	⋮	⋮	⋮	⋮
46	37, 53, 67	95, 49, 45	47, 55, 27	33, 35, 37	95, 53, 45	41, 41, 35
47	53, 49, 57	97, 93, 93	49, 49, 29	95, 39, 41	49, 45, 47	33, 35, 37
48	55, 55, 55	51, 95, 95	95, 51, 39	35, 37, 39	97, 95, 95	35, 39, 39
49	97, 51, 65	99, 97, 97	97, 97, 97	97, 97, 97	99, 97, 97	97, 97, 97
50	99, 99, 99	49, 99, 99	99, 99, 99	99, 99, 99	51, 99, 99	99, 99, 99

Table 4.3: Method unspecific ranking of the $n_{\text{var}} = 50$ input variables (here: time values at different heights of the pulse amplitude) for the six semi-coaxial detectors and three data subsets pI, pII, pIII. Only the ten best and five worst ranked parameters are listed.

Figure 4.7 displays the corresponding computation outcome according to equation 4.9 of the correlation among the $n_{var} = 50$ input parameters used in this thesis for the a) signal and b) background training samples. Due to a general similarity in the correlation matrices of the different detectors or data subsets, here the results
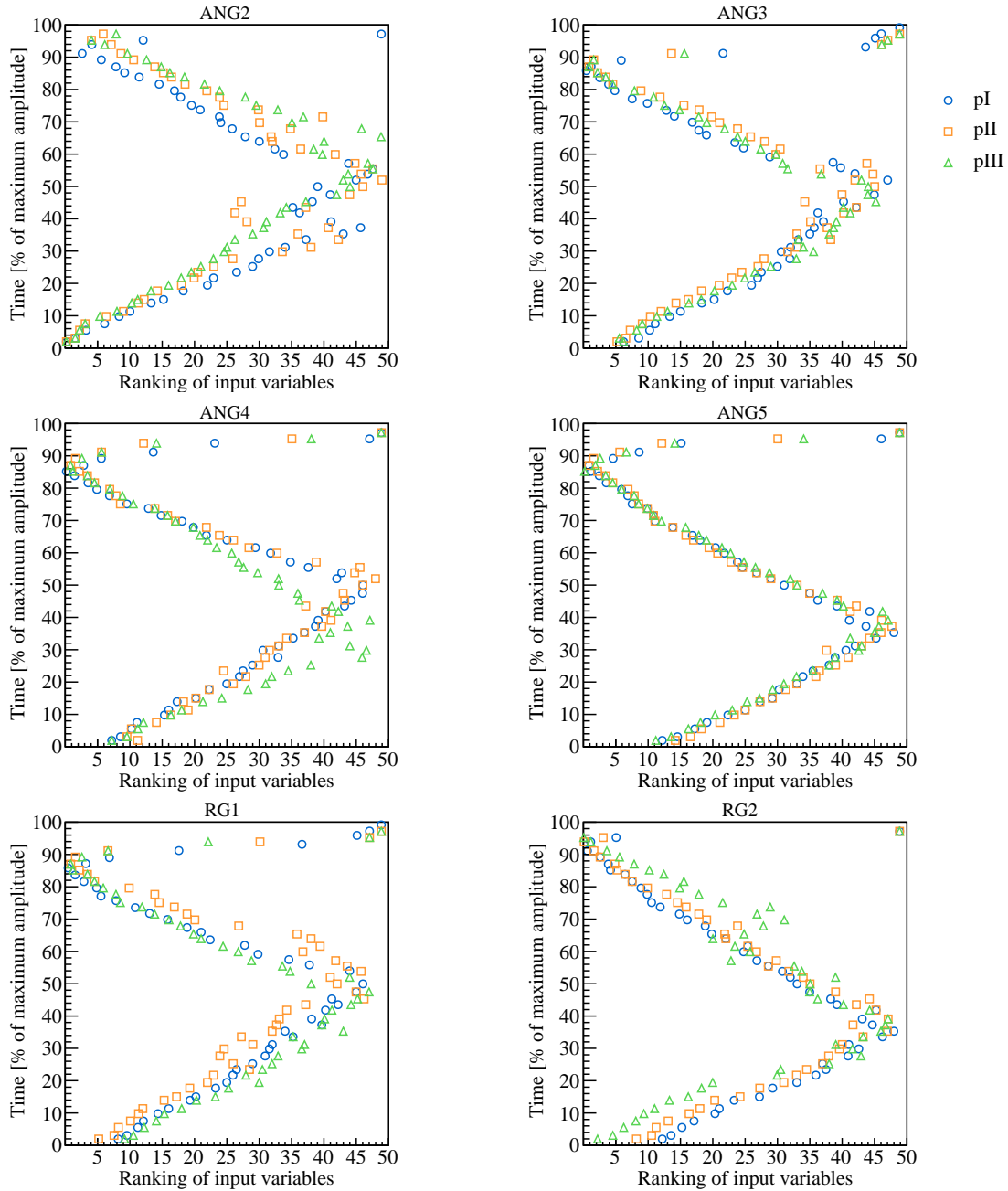
Figure 4.8: Method unspecific variable ranking of the input variables. The discriminating time values at different heights of the charge pulse are plotted as a function of their separation potential in signal- or background-like events. Further the three different data-sets are marked with hollow blue circles (pI), orange rectangles (pII) and green triangles (pIII).

are exemplarily shown for the ANG5 and the first period pI only. Unsurprisingly adjacent times $t(A)$ at almost the same heights A feature a rather strong (linear) dependence, whereas far-distant variables, each from the very beginning or ending of the leading edge of the charge pulse, seem to be almost non-linearly correlated or even completely decoupled. However, to make an unambiguous statement about the effect on the different classifier algorithms that may suffer from non-linear relationships between the discriminating parameters, it is crucial to also inspect the analogous scatter plots with respect to their separation performance.

During the preanalysis and training/testing procedure the TMVA classification package provides access to rankings - either of general, method unspecific or algorithm-based nature - referring to the variable discrimination power between signal and background. The analogous calculations of the first preliminary ranking are collected in table 4.3 for the six semi-coaxial detectors and three different subsets pI, pII+pIII. For reasons of clarity only values for the 10 most and 5 least important variables are stated. Further a visual impression of the variable importance is given in figure 4.8, where the different input parameters are depicted as a function of their ranking. The data-sets are thereby represented by hollow blue circles (pI), orange rectangles (pII) and green triangles (pIII), respectively.

In consistence with all detectors, clearly those time values at very low or very high amplitude, corresponding to regions around the starting and close to the ending point of the pulse rising structure, are assigned the best ranking positions. On the contrary, input variables located in vicinity to the middle part of the rising flank at, roughly 50 % of the maximum amplitude, are significantly less relevant for the classification decision. Such a behaviour makes insofar intuitively perfectly sense, as the reference point $t(A = 0.5) = 0$ was chosen to lie exactly in this region that
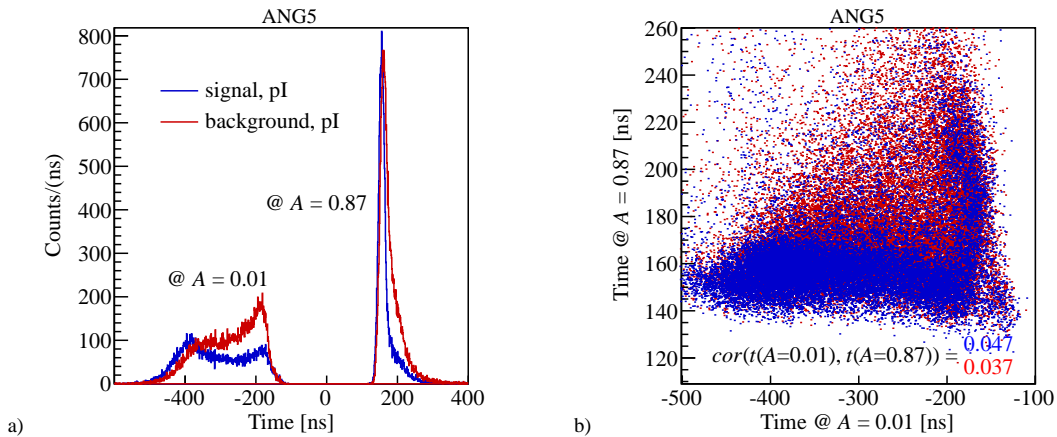
Figure 4.9: a) Time distribution when passing the 1 % (@ A=0.01) and 87 % (@ A=0.87) pulse height for ^{228}Th calibration events with energies in the interval $\pm 1 \cdot FWHM$ centered around the 1592.5 keV DEP (blue solid line) or 1620.7 keV FEP (red solid line) and **b)** corresponding scatter plot of the two input variables with the same color code. Values are exemplarily shown for the ANG5 detector and period pI only.

is therefore naturally expected to contain very little information. For the different data-sets slight variances for the weakly-classifying parameters with shifts to times that correspond to higher or lower pulse heights, but no general systematic effects can be observed. Solely the ANG5 germanium detector exhibits an remarkably stable behaviour over time.

Figure 4.9 a) shows, as an example of the separation power, the distribution for the two event classes signal and background of the semi-coaxial ANG5 diode from ^{228}Th calibration measurements of period pI with energies in the interval $\pm 1 \cdot FWHM$ centered around the 1592.5 keV DEP (blue solid line) and 1620.7 keV FEP (red solid line). Exemplarily those input variables from the bottom or top of the rising edge of the highest importance/ranking with times at 1 % and 87 % pulse height (see table 4.3) are presented. Additionally the corresponding scatter plot (with the same color code: blue for SSE-like and red for MSE-like) is given in figure 4.9 b) on the right side. The respective correlation coefficients can be derived
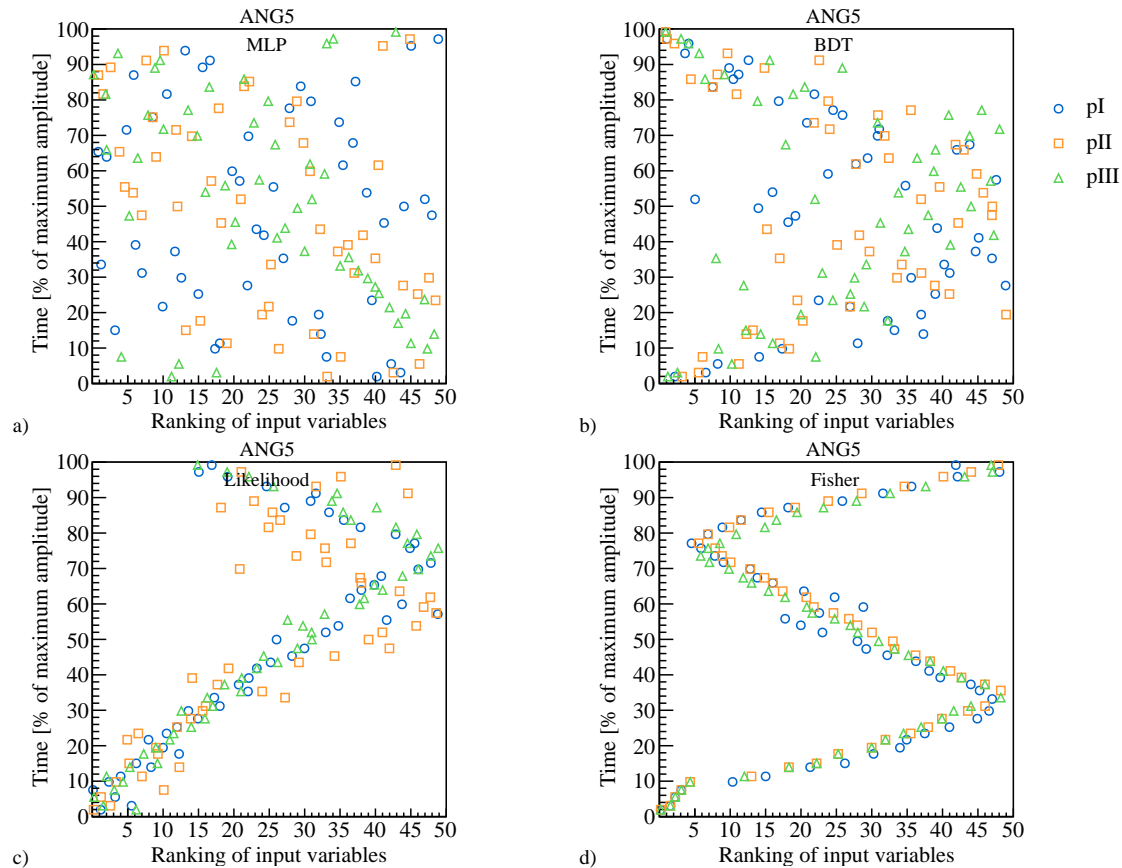
Figure 4.10: Method specific variable ranking of the input variables for four different multivariate classification methods: **a)** multilayer perceptron (MLP), **b)** boosted/bagged decision trees, **c)** Likelihood estimator and **d)** Fisher discriminant. Exemplarily the ANG5 detector is shown, where the three different data-sets are - similar to figure 4.8 - indicated by hollow blue circles (pI), orange rectangles (pII) and green triangles (pIII).

to $cor(t(A = 0.01), (t(A = 0.87)) = 0.047$ for the signal and $= 0.037$ for the background training sample. Thus the input parameters are neither linearly correlated (or at most marginally), nor independent. Much rather the distribution is based on a non-functional relationship and it is therefore assumed that the training with different classifier methods, which suffer more or less under a degraded separation performance in case of non-linear input variables, may exhibit strongly varying results on, for instance, the classification power, event response distribution or ranking of the time input parameters. The former two issues will be soon discussed in the upcoming subsections 4.3.2 and 4.3.4 dealing with the resulting relations between background suppression versus signal efficiency as well as the risk of overtraining for the single classifiers.

As for the latter assumption concerning the importance of the various time values being dependent on the investigated pattern recognition algorithm, a method specific ranking can be accessed by the training output of the TMVA analysis package. The determined relations between time parameters and selection power are depicted in figure 4.10 for four of the multivariate classification techniques - namely the a) multilayer perceptron as special case of a neural network (MLP), the b) boosted/bagged decision tree (BDT), the c) likelihood and the d) Fisher algorithm - provided by the open source program. Again the combination of the ANG5 along with period pI is adduced as a reference for the comparison. The corresponding input variable importance I_i with $i = 1, ..., n_{\text{var}} = 50$ of the four depicted methods has been thereby derived according to the following rules:

- In case of the MLP neural network structure a method specific ranking is implemented that uses the sum over the squared weights $w_{ij}^{(1)}$ of the connections between the n_{var} variable's neurons in the input layer and the n_{h}-dimensional first hidden layer

$$I_i = \overline{x}_i^2 \sum_{j=1}^{n_{\text{h}}} \left(w_{ij}^{(1)} \right)^2 , \qquad (4.11)$$

  where $\overline{x}_i$ denotes the sample mean of the i-th parameter.

- The importance I_i is calculated within the BDT algorithm by counting how often a classification parameter i occurs for the splitting of the decision tree nodes during the growing of the forest. At each child node also a weighting according to the squared separation gain and the number of the containing events is applied [Bre84].

- For the likelihood method, the ranking of a certain variable i is determined by comparing the separation ability of the full n_{var}-dimensional variable set with the discrimination power obtained by removing the i-th variable from the sample.

- The working principle of the Fisher discriminant analysis is based on simultaneously maximizing the between-class dispersion, while minimizing the within-class separation. Hence a suitable measure of the discrimination power of a

variable is given by the diagonal quantity $\mathcal{B}_{kk}/\mathcal{C}_{kk}$, where $\mathcal{B}_{kl}$ represents the between-class matrix and $\mathcal{C}_{kl}$ the within-class matrix from section 4.1.1.

It somehow appears for several of the other methods - such as cut-based analysis, PDE-RS, K-NN, H-Matrix or FDA - that the multivariate processing instead does not provide any ranking informations at all. However, from figure 4.10 that covers four of the investigated algorithms a clearly disparate behaviour is visible. The last Fisher classifier d) shown at the lower right of the figure, as representative for those methods that are strongly susceptible to non-linearly correlated input variables, features a distribution of the time parameters at different pulse height as a function of the importance I_i where - again - very low and relatively high values are ranked the best. In general the pattern closely resembles the previously discussed ranking for the method unspecific case. On the contrary the relationship between the input values and their ranking of first feed-forward artificial neural network algorithm a) displayed at the upper left of the figure, does reflect a complete different picture. No systematic ordering can be observed and all discrimination input parameters are equally contributing to the classification decision. The two remaining estimators, the c) likelihood as well as the b) decision tree method, serve as intermediate examples for which somehow the strict structure seems to be piecewise smoothed down towards a random dispersion of the time parameters.

4.3.2   Background rejection vs. signal efficiency

After the training with the input variables, the classifiers are subjected to evaluation with the aim to figure out their performances. Thereby the training and the subsequent testing of the attained classification rules is performed on statistically independent data samples to ensure an unbiased validation. Per default in the TMVA software program the user supplied background or signal data sets containing the discriminating parameters is divided in half such that one obtains equal samples sizes for the train- and test-procedure. Given the fact of the relatively large number of input variables used in the pulse shape analysis presented in this work, it is reasonable to retain a sufficient amount of events for the training sequence though, in order to mitigate against the effect of overtraining (for more details see next section 4.3.4). Hence, the fraction was altered such that the data sample is cutted in parts of $\frac{2}{3}$ (for training) and $\frac{1}{3}$ (for testing), which is considered to represent a good compromise between unrestrained pattern recognition process (no lack of statistics) and still gaining a meaningful statement when comparing with the test set.

With the aim to ease the choice of the optimal classifier to be used for a specific problem, it is extremely adjuvant to compute and display the respective background rejection as a function of the signal efficiency derived from a cut on the output of the different multivariate algorithms. This kind of depiction belongs to the class of so-called *Receiver Operating Characteristic* (ROC) diagrams that show in their standard form the true positive rate on the vertical axis versus the false positive rate of a sequence of different possible cut positions.

Figure 4.11 illustrates the corresponding smooth ROC curves for the six semi-coaxial detectors and the eight classifier results of period pI that feature the best performances. Here the horizontal axis is slightly different form the standard notation (signal efficiency = 1−false positive rate) and accordingly the north-east corner
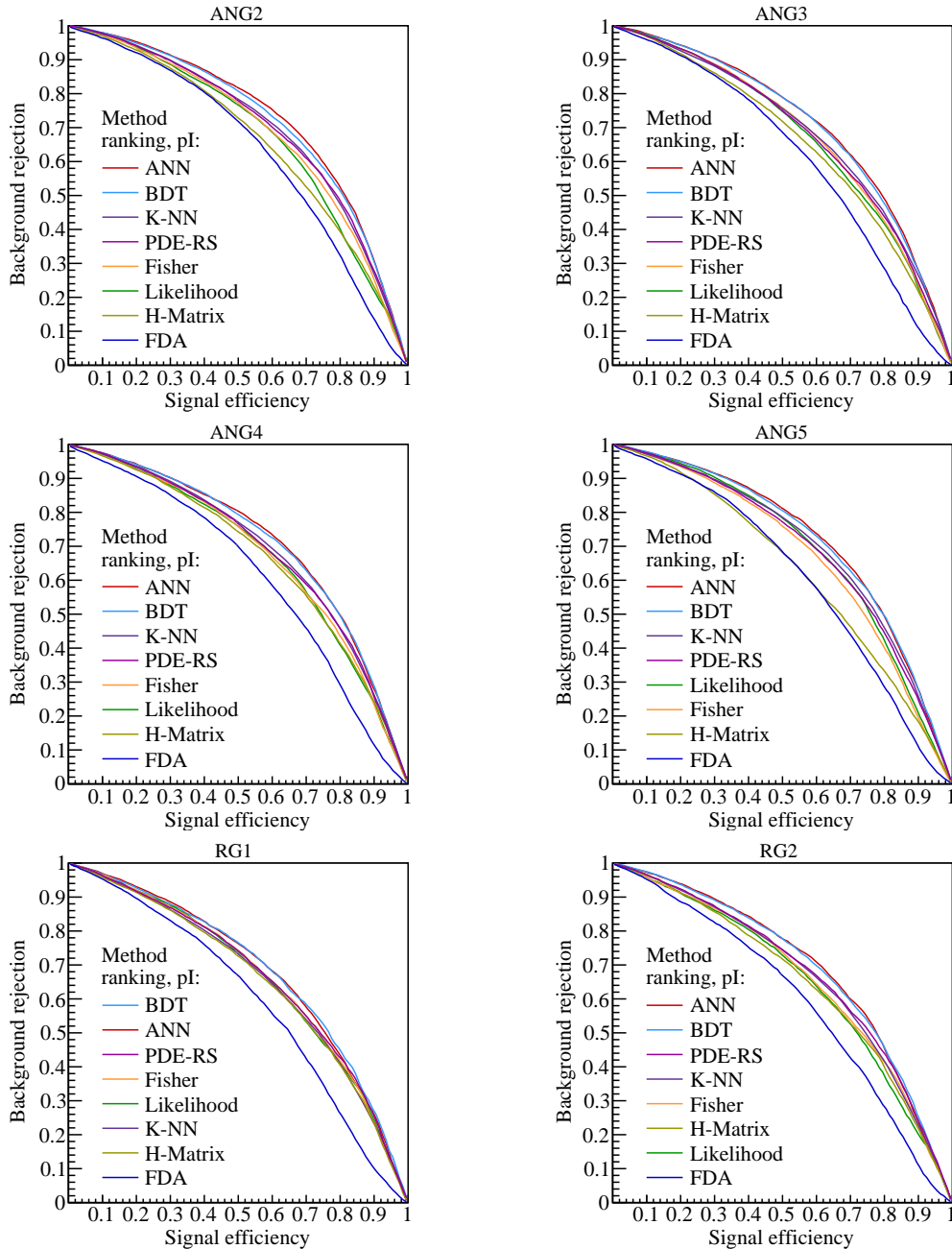

Figure 4.11: Background rejection as a function of the signal efficiency obtained by cutting on the different multivariate analysis outputs from the training for the events of the test sample. The corresponding results for the six semi-coaxial detectors and the first period pI are displayed along with the ranking of the classifiers according to their performance.

is the place to be. Thus a suitable quantity to conduce a meaningful descending order of the classification capacity is the net area of the background rejection versus signal efficiency function (the larger the area the better the overall potential). As can be seen in consistence for all detectors, the artificial neural network (ANN) and boosted/bagged decision tree (BDT) algorithms yield the highest suppression power for events of background-like topology, while simultaneously retaining those originating from the signal sample with a slight preference for the method based on multilayer perceptrons. Systematically all other six multivariate techniques, like projective likelihood or the multi-dimensional likelihood estimation (k-NN + PDE range search) and (non-)linear discriminant analysis (H-Matrix, Fisher + FDA), perform considerably less. Classifier methods not shown in figure 4.11 have been neglected either due to an distinctly worse discrimination ability - that accounts for rectangular cut optimization and predictive learning via rule ensembles - or because of an highly unstable behaviour - as it is the case for the support vector machine algorithm. For both cases the origin of the insufficient classifier outcome may be owing to a general working principle that simply does not reflect the requirements of the given problem

| Period | Method ranking from top (= best) to bottom (= worst) | | | | | |
	ANG2	ANG3	ANG4	ANG5	RG1	RG2
pI	ANN BDT k-NN PDE-RS Fisher Likelihood H-Matrix FDA	ANN BDT k-NN PDE-RS Fisher Likelihood H-Matrix FDA	ANN BDT k-NN PDE-RS Fisher Likelihood H-Matrix FDA	ANN BDT k-NN PDE-RS Likelihood Fisher H-Matrix FDA	BDT ANN PDE-RS Fisher Likelihood k-NN H-Matrix FDA	ANN BDT PDE-RS k-NN Fisher H-Matrix Likelihood FDA
pII	ANN BDT k-NN PDE-RS Fisher Likelihood H-Matrix FDA	ANN BDT k-NN Likelihood PDE-RS Fisher H-Matrix FDA	BDT ANN k-NN PDE-RS Fisher Likelihood H-Matrix FDA	ANN BDT k-NN PDE-RS Likelihood Fisher H-Matrix FDA	BDT ANN k-NN PDE-RS Likelihood H-Matrix Fisher FDA	ANN BDT PDE-RS k-NN Likelihood H-Matrix FDA Fisher
pIII	BDT ANN PDE-RS k-NN Fisher Likelihood H-Matrix FDA	ANN BDT k-NN Fisher PDE-RS Likelihood H-Matrix FDA	ANN BDT k-NN PDE-RS Fisher Likelihood H-Matrix FDA	ANN BDT k-NN PDE-RS Likelihood Fisher H-Matrix FDA	ANN BDT k-NN PDE-RS Fisher H-Matrix Likelihood FDA	ANN BDT PDE-RS Fisher H-Matrix k-NN Likelihood FDA

Table 4.4: Ranking of the different classifier algorithms according to the net area of the background rejection versus signal efficiency function for the semi-caxial germanium detectors and all three data periods pI, pII and pIII of GERDA Phase I.

as well as a not elaborate enough tuning of the algorithms during the adaption or a general inconsistency in to the GERDA Phase I data (as will be discussed in theu pcoming subsection 4.3.3).

An overview on all three periods pI, pII and pIII of the data subsets is given in table 4.4, where the methods are ranked from top (= best performance) to bottom (= worst performance) for each of the six investigated detectors. Also for the two other data-sets, the ANN and BDT estimators do again yield the best results, even the ranking of the remaining algorithms shows, in general, huge similarities for all three periods with only some minor changes in a few individual cases.

4.3.3 Selection and setting of classifier

Due to the systematic success of the artificial neural network being predominantly the top ranked classifier in terms of background rejection as a function signal efficiency across all evaluated semi-coaxial germanium diodes and data-sets of GERDA Phase I it was chosen to be the pulse shape discrimination method used for the $0\nu\beta\beta$-analysis. As another benefit a quite similar multilayer perceptron approach, based on a slightly different adaption to the GERDA experiment, has already emerged to represent a powerfull method for an active background suppression in [Vol12] within an independent investigation, but was somehow not further pursued for the final studies on the Phase I physics data. Even already within the Heidelberg-Moscow experiment, the ANN algorithm has been as well studied and yielded consistently very promising results back then [Maj99].

In case of the different multivariate algorithms provided by the TMVA package, also several tuning options are on hand allowing to adapt the method in the context of a particular problem of interest. For most of the decision algorithms presented in this section, the proposed default values tested and optimized by the TMVA software developers already guaranteed a fast training process (even when applying the high number of $n_{\mathrm{var}} = 50$ input variables) and yielded in general a stable classifier response. Moreover, individual changes in the setting of the multivariate methods usually did not result in significant improvements on the discrimination performance. The used booking options of the neural network architecture that turned out to perform the best on the GERDA data are specified in the following:

- From the three neural network implementations available in TMVA, the so-called TMlpANN algorithm is selected due to its superiour performance. (This particular method interfaces the ROOT class `TMultiLayerPerceptron`).

- The number of training cycles was chosen to be 200, which represents a good compromise that allows not only an adequate processing time consume but also on the other hand a sufficient number of epochs to achieve a stable training result.

- The event fraction in the training tree used for cross validation is set to $\frac{1}{3}$.

- For the multilayer perceptron architecture with an input layer of n_{var} neurons corresponding to the 50 input variables and a single output neuron holding the classifier response value, two additional interjacent hidden layers, each with a number of n_{var} and $n_{\mathrm{var}} - 1$ nodes, were specified. This constitutes a fair tradeoff between a sufficient precision that increases with the amount of neurons or hidden layers and an acceptable demand on computing power/time.

- In the course of the learning process for each of the supplied N training events $\boldsymbol{x}_{\mathrm{a}} = (x_1, ..., x_{n_{\mathrm{var}}})_{\mathrm{a}}$, for a $= 1, ..., N$, the neural network response $y_{\mathrm{ANN,a}}$ is calculated and compared with the known output $\hat{y}_{\mathrm{a}} \in \{0, 1\}$ (where 0 signifies background events and 1 likewise signal events). Accordingly an *error function* E, as a measure for the agreement of the ANN qualifier value with the desired one, is defined by

$$E(\boldsymbol{x}_1, ..., \boldsymbol{x}_N | \boldsymbol{w}) = \sum_{\mathrm{a}=1}^{N} E_{\mathrm{a}}(\boldsymbol{x}_{\mathrm{a}} | \boldsymbol{w}) = \sum_{\mathrm{a}=1}^{N} \frac{1}{2} (y_{\mathrm{ANN,a}} - \hat{y}_{\mathrm{a}})^2 , \qquad (4.12)$$

with $\boldsymbol{w}$ representing the ensemble of adjustable weights in the multilayer perceptron. In the analysis presented in this work, the so-called *Broyden-Fletcher-Goldfarb-Shannon* (BFGS) learning algorithm that specifically relies on the second derivative of the error function E was used to optimize the classification performance of the neural network [Bro70][Fle70][Gol70][Sch70]. One benefit arising with this BFGS method is the reduced number of iterations within the training procedure, whereby the computing time per iteration is directly proportional to the squared number of synapses.

4.3.4   Classifier response and overtraining

When training a specific machine learning algorithm with user supplied data of known event class, it is of crucial importance to also carefully check for and - in the event of detection - eliminate any kind of overtraining. During the building of a classification pattern of a multivariate algorithm overtraining occurs if the handled problem has too few degrees of freedom due to too many model parameters of a method that have to be adjusted to too few data points. The susceptibility for such kind of "mistraining" therefore also highly depends on the used MVA technique. As has already been summarized in table 4.1 Fisher and H-Matrix - or any *linear* - discriminant does hardly suffer from overtraining, whereas BDTs are easily affective to be at least partially overtrained without adopting the appropriate counter measures (e.g. pruning/cutting down the large number of insignificant nodes within the tree that do not add any or only little information on the final decision rules). For the case of multilayer perceptrons the convergence of the error estimator between the training and test sample, freezing the training procedure after the minimum value has been passed.

In general overtraining results in a seeming increase of the classification power, if measured on the training sample, and to an effective decrease in the performance

when comparing with an independent test sample. Thus, a convenient strategy to
recognize overtraining and estimate its effect on the classification result, is to make
a comparison between the discrimination sensitivity derived from the training and
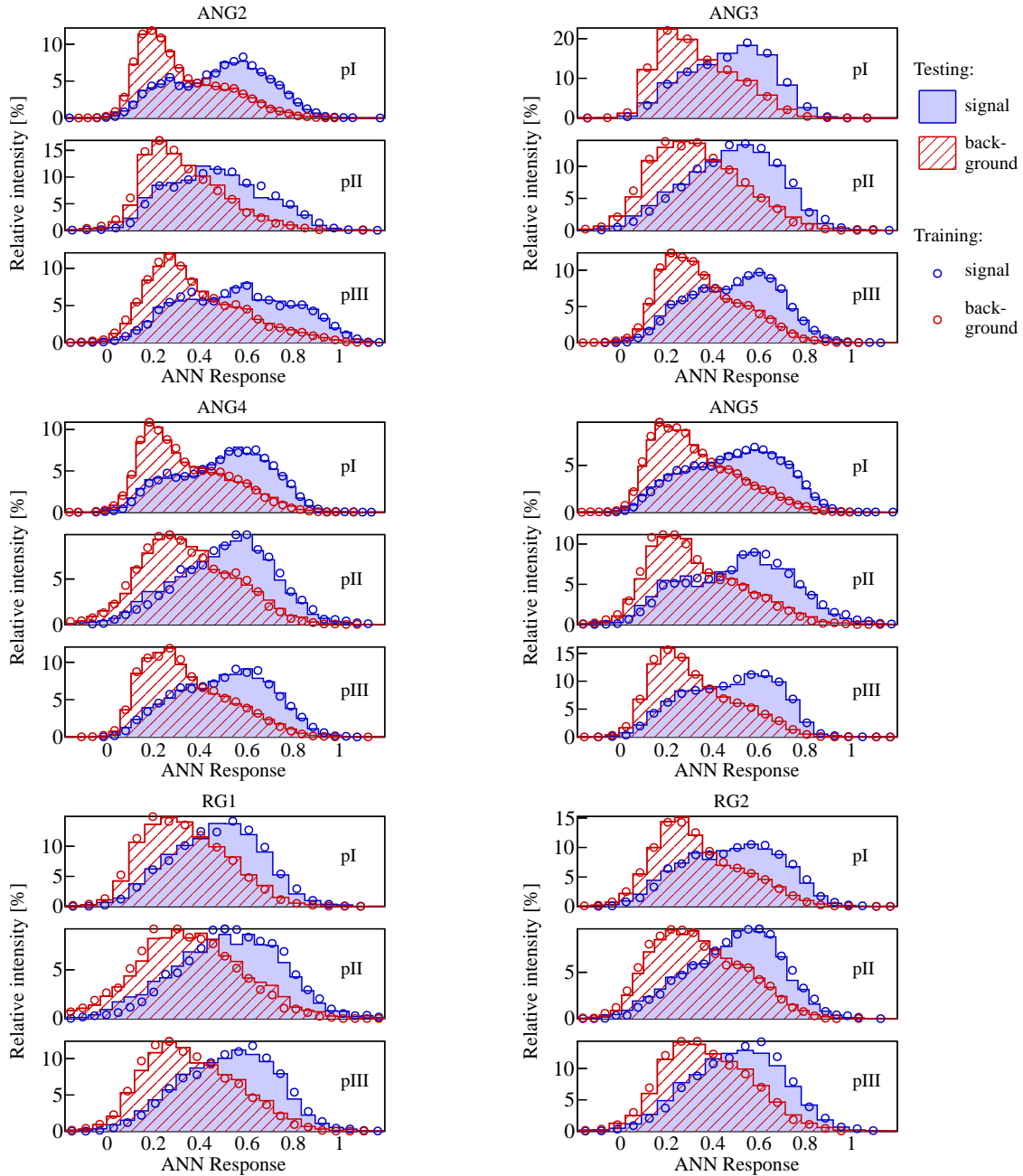test sets. Such a test on the artificial neural network has been performed for each of

Figure 4.12: Artificial neural network output distributions of the supplied signal (blue)
and background (red) events for all six semi-coaxial detectors and data periods pI, pII and
pIII. Results from the training procedure are displayed as hollow circles, whereas dispersions
with filled and hatched area originate from the testing sample.

the semi-coaxial detectors and data periods of Phase I and is depicted in figure 4.12. Shown with filled and hatched area are the ANN classifier response distributions based on the test sample, whereas hollow circles represent the corresponding dispersion from the training sample. Further those events originating from the supplied signal or background data-sets are displayed in blue and red color, respectively. By convention the data are assigned to a discriminating qualifier such that signal-like events accumulate at large (≈ 1) and background-like events on the contrary at small (≈ 0) classifier output values. Ultimately two things can be concluded from figure 4.12 on the classifier output distributions:

- No overtraining is observed. This accounts for each single germanium diode, in particular the RG1+2 detectors that feature systematically lower data statistics, as well as all three data periods with pII being by far the shortest one.

- In terms of the general shape or even the absolute qualifier value, the response of the artificial neural network on the GERDA Phase I data is in close agreement for all six semi-coaxial crystals and periods pI, pII and pIII.

Both points abet the assumption that the training based on the multilayer perceptron algorithms results in a reliable and overall consistent classification performance.

When cutting on the output and keeping only those events that are compareably larger, the requirement selects a set from the overall signal and background samples with efficiencies or rejectons that increase/decrease with the respective cut position. The associated relations between the background suppressions and signal efficiencies has already been shown in figure 4.11 for the eight best performing classifiers.

4.4 Application to calibration data

As has already been mentioned, calibration data from the GERDA experiment have been used for the training of the multivariate analysis algorithms, where two distinct energy intervals of 1592.5 keV $\pm 1 \cdot FWHM$ around the DEP from the ^{208}Tl decay and 1620.7 keV $\pm 1 \cdot FWHM$ around the FEP from the ^{212}Bi decay serve as proxy for a signal- and background-like event topology. A clear, albeit not complete, separation with a partial overlap of the sample types could be achieved. To confirm the robustness of the ANN classification with respect to different observational properties, as for example energy and time stability, or to quantify the actual impact of the discrimination performance on a data-set of mixed event type, in this section an application of the trained multilayer perceptron on the whole energy range of the calibration data is aspired.

4.4.1   Energy dependency

Figure 4.13 displays the resulting qualifier distribution from the Compton continuum composed of a mixture of single site + multi site events at different energies, which

can be conveniently compared to estimate a possible energy dependence of the selection. Here the corresponding neural network response of six different energy regions (1375, 1550, 1845, 1955, 2155 and 2300 $\pm$ 25 keV) is shown for the first data time interval pI and all semi-coaxial germanium diodes (at the respective upper half of the
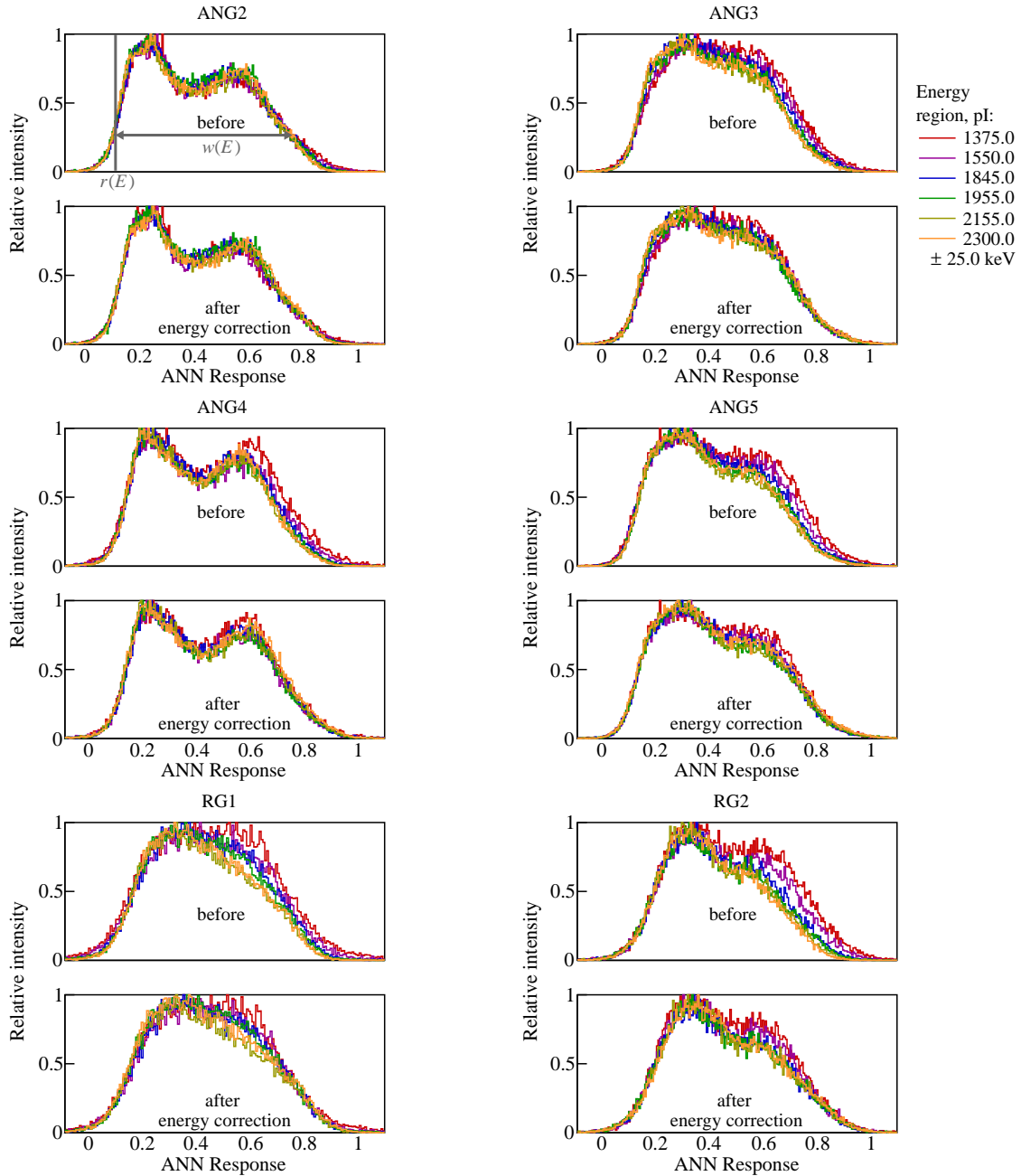
Figure 4.13: ANN response distributions resulting from Compton events at six different energy regions for the semi-coaxial detectors and period pI of Phase I (without (upper half) and with (lower half) applied energy correction). In case of the ANG2 also the quantities important for the empirically derived energy correction are marked.

figure). A corresponding depiction for the two remaining data periods can be found in the appendix B.1.1. For most detectors, except the ANG2, a systematic drift of variable intensity is visible. In particular the right falling edge of the dispersion is continuously shifted to lower qualifier values for increasing energies. The by far largest variation - about twice as big than for any other diode - is thereby featured by the RG2 (assumably owing to the also poorest energy resolution attributed to the very same detector).

In general such a behaviour can be easily explained by a fraction within the Compton events of signal-like topology that drastically declines for an increasing energy (e.g. due to energy dependent bremsstrahlung effects, to only name one possible reason). Hence, the higher the energy interval of the considered slice is chosen, the less important the share of SSEs associated with larger ANN response values would appear, resulting in a seeming drift to the left - as observed. Anyhow, by means of detailed Monte Carlo simulation (MCS) efforts (as will be presented in chapter 6) revealing the percentual amount of single site events to remain almost constant with the energy (see figure 6.10), it was principally shown that this is actually not the case though - suggesting the presence of a general, yet unresolved energy dependency.

Consistently this dependency also emerges for all three data periods pI, pII and pIII and implies that a systematic energy adjustment is required. Thus an energy dependent empirical correction of the qualifier according to

$$\text{ANN Respone}(E) = r(E) + (\text{ANN Respone} - r(E)) \cdot \frac{w(E@\text{DEP})}{w(E)} \qquad (4.13)$$

has been deduced and retroactively applied on the classifier response. Hereby the quantities $r(E)$ and $w(E)$ (both indicated in figure 4.13 for the ANG2) denote the energy dependent ANN response value at the leading edge and width of the distribution at a particular height, which was set to a fixed value of 25 % of the maximum amplitude. For the calculations the interpolated values at the position of the double escape peak (DEP) with energy 1592.5 keV have been used as reference points, respectively. The finally adjusted ANN output is additionally plotted in figure 4.13 (lower half). As can be seen a steady energy correction of sufficient performance could be successfully accomplished for each single detector.

4.4.2   Fixing of PSD cut parameter

Figure 4.14 a) shows a scatter plot of the corrected qualifier value inferred from the artificial neural network classifier versus the energy for an overall region that spans from 1000 keV to 2750 keV. Since a remarkably similar behaviour is observed for each of the different data-sets combinations of detector and time interval, here exemplarily only data for the ANG2 and period pI are presented for reasons of clarity and comprehensibility. Anyhow, a detailed overview of all detectors and periods pI, pII+pIII is still be given in the appendix B.1.2. Clearly the ANN response

distribution peaks for the double escape peak (DEP) with events of mainly single site topology at higher qualifier values, while for full energy peak (FEP) events at 1620.7 keV and 2614.5 keV or single escape peak (SEP) events at 2103.5 keV of predominantly multi site character the intensity is deflected to lower values.

The qualifier threshold for the pulse shape cut is determined for each detector and each period individually and fixed such that 90 % of the events located in the DEP are kept. For the statistical uncertainty universal values of $\pm 2\,\%$ for the periods pI+III and $\pm 3\,\%$ for the shortest period pII with lower statistics have been derived (a detailed description of the performed error computation, that will be hereinafter also used troughout this whole thesis, can be found in the appendix A). In case of ANG2 the resulting position of the cut at an response value of 0.354 is marked in figure 4.14 a) as grey solid line, for all other detectors and data periods the concluded cut values vary between 0.314 and 0.410. A complete list of the derived qualifier thresholds is given - among other pulse shape suppression properties - in table 4.5.

Figure 4.14 b) shows a ^{228}Th calibration spectrum with (green) and without (red) pulse shape selection corresponding to a projection of the scatter plot in figure 4.14 a) for the ANG2 and pI on the energy axis. Analogous plots for the other data intervals and detectors are additionally depicted in the appendix B.1.3. For the analysis of the ANN classifier suppression performance on background-like events, the survival fraction of MSE in the SEP at 2103.5 keV and FEP at 2614.5 keV are studied when applying the discrimination threshold derived from the neural network on the calibration spectrum. Thereby the survival is explicitly defined as the fraction of the peak content remaining after the PSD cut, i.e. the Compton events under the γ-line are subtracted by scaling linearly the event counts from energy regions below and above the peak. Table 4.5 states the corresponding fractions for the different
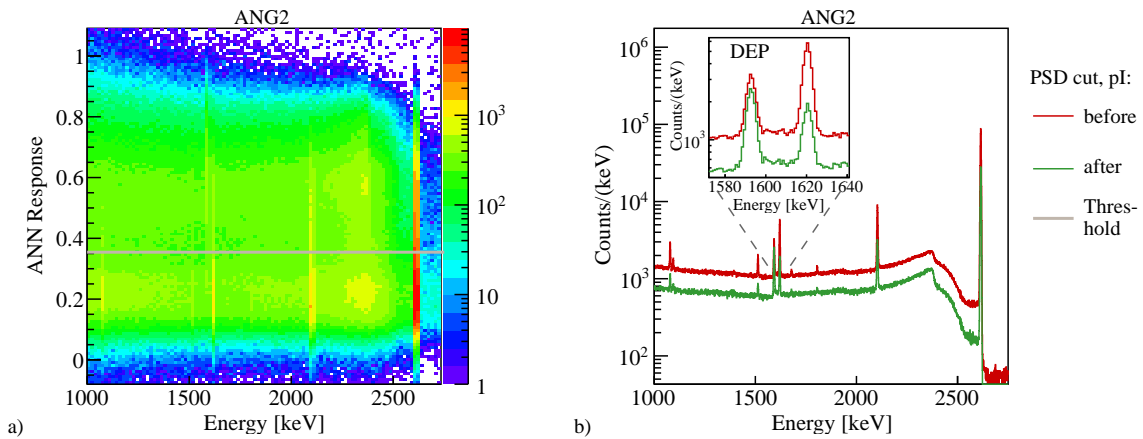
Figure 4.14: a) ANN classifier response versus energy for ^{228}Th calibration events of ANG2 and period pI. The gray solid line at 0.354 illustrates the position where 90 % of the DEP events are retained. **b)** Corresponding ^{228}Th calibration spectrum with (green) or without (red) a PSD cut for the ANG2 and pI, where (as defined by the gray line of the left figure) the cut is fixed for a survival fraction of 90 % in the DEP (see inset).

detectors and periods as they are calculated based on his method. Obviously roughly 65 % from those events of multi site topology can be effectively rejected, while still keeping 90 % of the DEP intensity that serves as proxy for the $0\nu\beta\beta$-signal efficiency. The last column concerning the calibration data additionally lists the number of events in the region $\pm 25\,\mathrm{keV}$ centered around the $Q_{\beta\beta}$-value of ^{76}Ge where for ^{228}Th calibration measurements only a Compton continuum of mixed MSE and SSE type without any γ-line is present.

Detector	Period	ANN threshold	Calibration data			Background data		
			SEP	FEP	@$Q_{\beta\beta}$	$2\nu\beta\beta$	^{42}K	ROI
ANG2	pI	0.354	32.0 ± 0.5	31.6 ± 0.1	56.2	69.0 ± 0.9	27 ± 6	3/5
	pII	0.316	48.0 ± 0.8	40.1 ± 0.1	62.8	—	—	0/1
	pIII	0.314	45.9 ± 0.4	39.5 ± 0.1	62.1	72.3 ± 0.7	40 ± 5	5/8
ANG3	pI	0.359	34.8 ± 0.5	35.7 ± 0.1	60.0	80.3 ± 0.6	51 ± 6	8/11
	pII	0.382	36.9 ± 0.8	38.0 ± 0.1	58.3	—	—	2/3
	pIII	0.356	38.1 ± 0.5	44.1 ± 0.1	62.1	79.7 ± 0.5	44 ± 6	4/6
ANG4	pI	0.345	35.9 ± 0.6	37.1 ± 0.1	59.3	80.9 ± 0.7	46 ± 7	2/2
	pII	0.390	33 ± 1	38.5 ± 0.1	58.1	—	—	0/1
	pIII	0.376	34.8 ± 0.5	35.0 ± 0.1	58.3	83.0 ± 0.5	44 ± 6	2/4
ANG5	pI	0.351	30.2 ± 0.5	33.9 ± 0.1	58.7	77.3 ± 0.8	42 ± 7	2/11
	pII	0.382	28.7 ± 0.8	29.7 ± 0.1	52.5	—	—	1/2
	pIII	0.361	33.6 ± 0.5	36.7 ± 0.1	59.4	78.1 ± 0.6	31 ± 4	6/16
RG1	pI	0.362	40.5 ± 0.7	35.9 ± 0.1	59.6	77.3 ± 0.8	47 ± 7	2/5
	pII	0.365	45 ± 1	47.4 ± 0.2	61.2	—	—	2/3
	pIII	0.397	37.4 ± 0.7	39.0 ± 0.1	58.0	77.5 ± 0.6	41 ± 8	2/4
RG2	pI	0.392	34.1 ± 0.7	39.1 ± 0.1	56.6	82.5 ± 0.6	50 ± 7	11/12
	pII	0.410	31.2 ± 0.8	33.5 ± 0.1	54.9	74 ± 1	37 ± 11	3/3
	pIII	0.357	46.9 ± 0.9	44.1 ± 0.1	62.6	76 ± 1	58 ± 8	2/2

Table 4.5: Cut threshold as well as survival fractions of the neural network pulse shape discrimination along with the statistical errors (as explained in the appendix A) in units of [%] for different event classes and detectors (under the condition of keeping 90 % of the DEP events. Values for calibration and physics data from the three periods pI, pII and pIII are listed. The SEP at 2103.5 keV, FEP at 2614.5 keV from the calibration measurements and the ^{42}K γ-line, that signifies the 1524.7 keV full energy peak present in the background runs, serve as event candidates of multi site topology. Due to the statistics of the physics data being quite small in the middle period pII, the latter number is not always stated. The denotation "$2\nu\beta\beta$" names the energy interval between 1000 keV and 1400 keV, which predominantly consists of single site events originated by the neutrino-accompanied double β-decay. Calculated statistical errors for the survival fraction of the region at ± 25 keV centered around $Q_{\beta\beta}$ of mixed event type are usually smaller than 0.1 %. The last column lists event counts of the physics data before and after the PSD cut within the ROI of 230 keV width around the hypothetical $0\nu\beta\beta$-signal.

4.4.3 Time dependency

As discussed in section 4.2.3, the training was performed for the three periods pI, pII and pIII individually by combining all calibration data that lie within the corresponding time intervals. However, the derived pulse shape discrimination rules can then also be applied to every single calibration in order to look for possible drifts
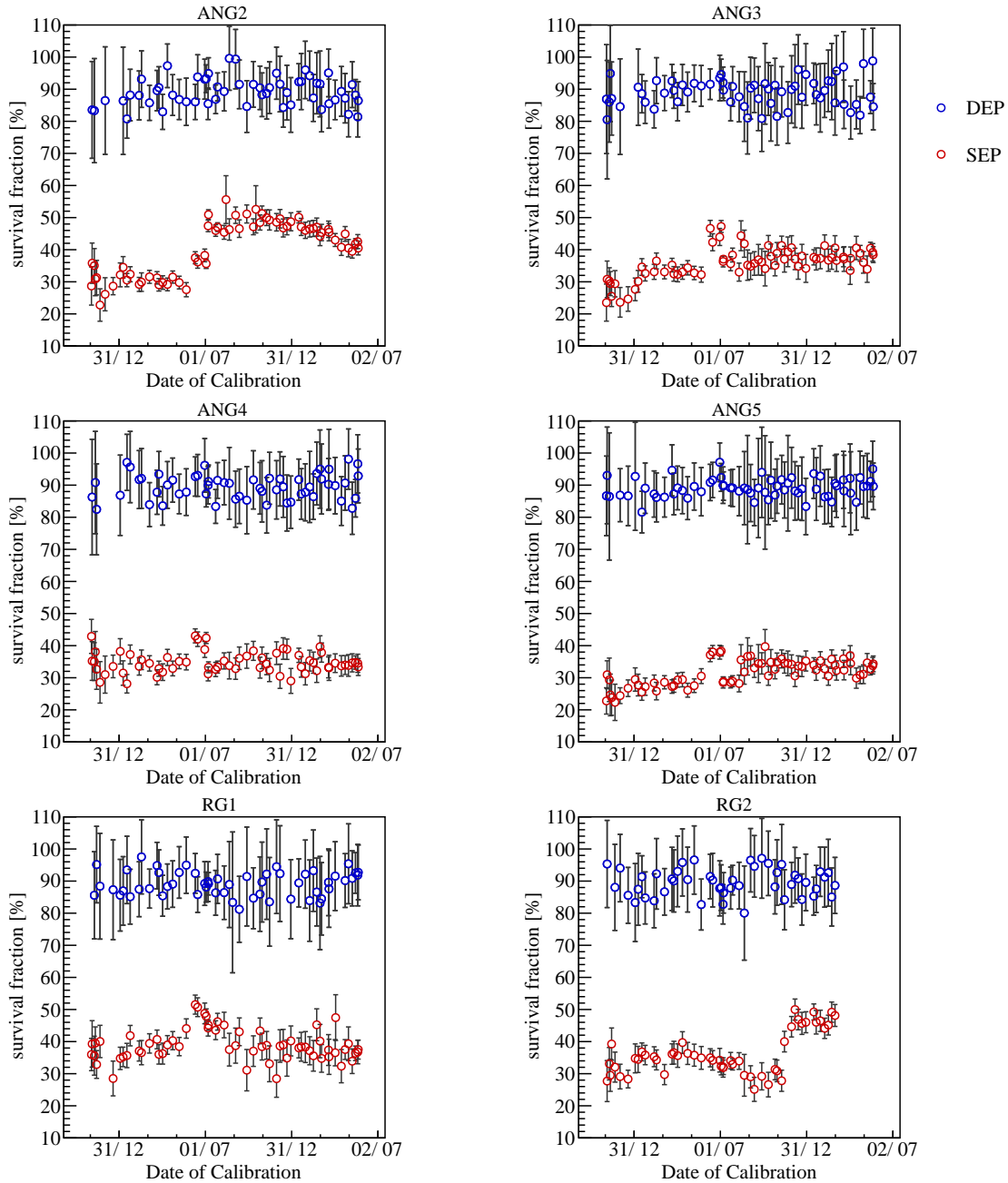

Figure 4.15: Survival fractions of the double escape peak (blue hollow circles) and the single escape peak (red hollow circles) for individual calibrations of the entire Phase I.

in time. Figure 4.15 compares the double escape peak survival fraction (blue hollow circles) for the entire Phase I time span from November 2011 to May 2013 and all six semi-coaxial germanium detectors. Significantly shorter calibration runs with rather poor statistics are thereby excluded. As can be seen, all plots show a stable performance in time within statistical uncertainties at a value of roughly 90 %. Also depicted are the equivalent entries (red hollow circles) for events with energies around the single escape peak position. In contrast to the time independent survival fraction of the DEP, for several detectors (e.g. ANG2) the rejection of MSE is instead not stable. Especially visible is the deterioration starting in July 2012 right after the commissioning of the new BEGe detector type. This time behaviour is attributed to different changes in the GERDA setup (BEGe insertion or modification of the source insertion system). Also remarkable is a further change of the SEP survival fraction at the end of 2012 for the RG2 detector that is related to a decreased operational voltage.

4.5   Application to blinded background data

The consistent behaviour of the pulse shape discrimination on the calibration measurements, where preferably those events of multi site character in the single escape and full energy peaks are cutted, while 90 % of the single site events within the
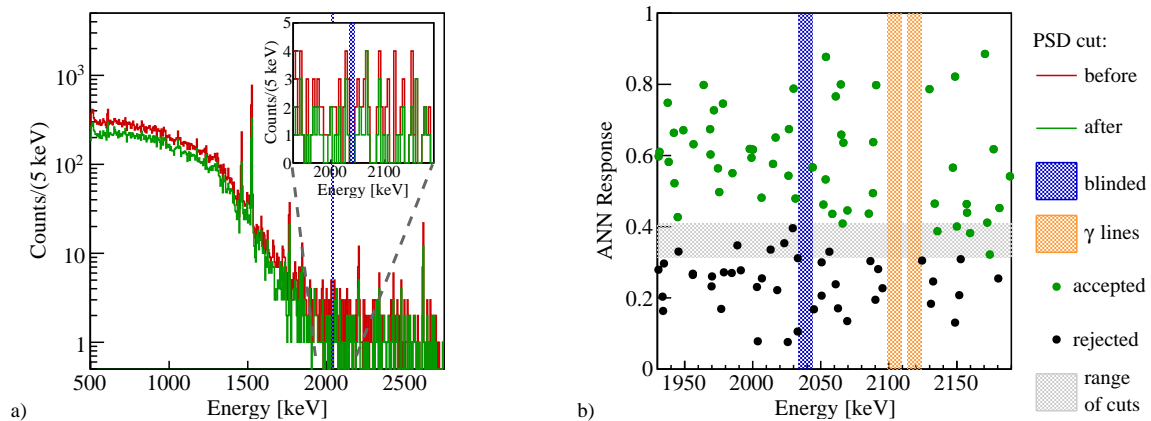
Figure 4.16: a) Energy spectrum of the combined physical data from the semi coaxial germanium detectors with (green) and without (red) neural network PSD selection, whereas the region of interest (ROI) between 1930 keV and 2190 keV is shown enhanced in the small inset at the upper right of the figure. The blinded energy window around $Q_{\beta\beta}$ that ranges from 2034 keV up to 2044 keV is indicated as blue shaded area. **b)** Scatter plot of the neural network qualifier value for events with energies within the ROI close to $Q_{\beta\beta}$. Events rejected by the ANN cut are marked with black dots and those that are accepted with the green equivalent. The range of the classifier threshold is given as gray shaded region. Further intervals not considered in the analysis owing to two γ peaks at 2103.5 keV and 2119 keV are denoted with orange shaded areas.

double escape peak are on the contrary kept, is one key aspect for the analysis of the neural network classification performance. To check whether the ANN discrimination pattern further confirms its robustness on the physics data used for the $0\nu\beta\beta$-analysis, qualifier thresholds for the different detectors and time intervals have been subsequently applied on the GERDA Phase I background data.

Figure 4.16 a) illustrates the energy spectrum of all semi-coaxial germanium detectors summed up before (red) and after (green) the ANN selection. For energies up to 1400 keV the distribution is dominated to a great extend by events of single site character resulting from the neutrino accompanied $2\nu\beta\beta$-decay of the ^{76}Ge detector material. Also visible is the full energy peak at 1524.7 keV of basically multi site topology originated by the ^{42}K ions in the surrounding liquid argon as, albeit already migrated by an enclosing copper-made mini-shroud (see section 3.2.5 or 3.5.1), the most prominent line of the spectrum. Table 4.5 lists the survival fractions for both event types of (i) mainly signal-like nature in the $2\nu\beta\beta$-part of the energy spectrum between 1000 keV to 1400 keV and (ii) background-like class from the FEP γ-line of the potassium isotope ^{42}K. Similar to the application on the calibration measurements also for the physics data an effective suppression of MSE in the energy peak can be achieved, while still retaining the majority of the SSE from the $2\nu\beta\beta$ dispersion. A closer, systematical study on the survival fraction of the two neutrino spectrum and its consistency with the predictions from the background model for the enriched semi-coaxial detectors of Phase I presented in section 3.6.2 and [Ago13c][Bec14] will be postponed to the next chapter in 5.2 as one of several investigated crosschecks based on the experimental data in the context of the classifier reliability. Also shown in the figure as blue shaded area is the blinded ± 5 keV energy window at 2039 keV and the adjacent region of interest (ROI) around $Q_{\beta\beta}$ that spans from 1930 keV to 2190 keV (small inset at the upper left). The last column of table 4.5 states the number of events in this very same ROI energy interval with a total width of 230 keV after subtracting the blinded energy window $2034 - 2044$ keV and two regions $2099 - 2109$ keV (SEP of ^{208}Tl) and $2114 - 2124$ keV (γ-line from ^{214}Bi) with and without the cut derived from the artificial neural network algorithm. Hereby about 45 % of the events are classified as background.

The distribution of the qualifier for all events in the 230 keV window around $Q_{\beta\beta}$ - minus the blinded energy interval and the two excluded peak regions with 10 keV each - added up for all semi-coaxial crystals is shown in figure 4.16 b). Events that are rejected by the ANN qualifier threshold are marked as black dots and those that are accepted as green dots. Also regions not considered in the analysis due to γ-lines or the blinding procedure are indicated by blue and orange shaded areas. The range of variety in the classifier cuts determined for a 90 % survival fraction of the DEP events from the calibration spectrum is further signified with the gray shaded interval.

5. Systematic studies using GERDA data

The consistent description of the neural network based pulse shape discrimination, developed as an efficient background suppression technique for the semi-coaxial germanium detectors of GERDA Phase I, is one basic prerequisite for the $0\nu\beta\beta$-analysis of the physics data. Since the multivariate supervised learning method is supplied with training data that covers the calibration measurements performed every one or two weeks, a confirmation whether the ANN algorithm exhibits an equivalent pattern recognition performance on the physics data from the background runs is still due. Naturally only in case of a validation of its robustness on both data sources an application of the classifier selection rules for the data identification is justified. Hence throughout this chapter the performance of the ANN classification in terms of different observational properties are investigated, as for example the specific response distributions of events with predominantly multi site or single site topology from calibration and background data in the first section 5.1.

On the other hand, for the pulse shape analysis presented in this thesis the survival fraction of the ^{208}Tl double escape peak at an energy of 1592.5 keV from the calibration spectra serves as efficiency for $0\nu\beta\beta$-events. However, it is commonly known that for these DEP events the energy deposition within the detector material is not homogeneously distributed as the probability for the two 511 keV photons to escape is larger close to the mantle and especially in the edges of the top and bottom side of the cylindrical diode geometry. Therefore it is indeed conceivable that the artificial neural network estimator is possibly rather finding those events at the outer surface instead of selecting the desired SSE ones or at least a partial volume dependent discrimination is introduced. In doing so, the DEP survival fraction would not be a relyable measure for the efficiency of the ANN cut on the $0\nu\beta\beta$-decay, which is occurring homogeneously inside the whole detector bulk.

As another candidate of also single site nature *and* an additional homogeneous distribution in the enriched germanium, $2\nu\beta\beta$ events from the physics data bear an exciting opportunity. Hence a comparison between their pulse shape selection efficiency and the preset fraction of 90 % survival rate in the DEP, as will be drawn in detail in section 5.2, represents a powerfull test.

Interestingly, events at the Compton edge of the 2614.5 keV full energy peak of ^{208}Tl, featuring a distribution in the detector volume similar to the double escape peak, can be as well deployed as a further SSE rich sample for a supplementary consistency check on the classifier stability in a wide energy range. Thereby the considered energy interval for the Compton events spans from $2300 - 2400$ keV and is insofar higher than $Q_{\beta\beta}$. Accordingly, comparing the survival fraction of the SSE-like part of the distribution with that of 90 % for the DEP located below $Q_{\beta\beta}$ allows to scrutinize for an energy dependence of the PSD efficiency (see section 5.3).
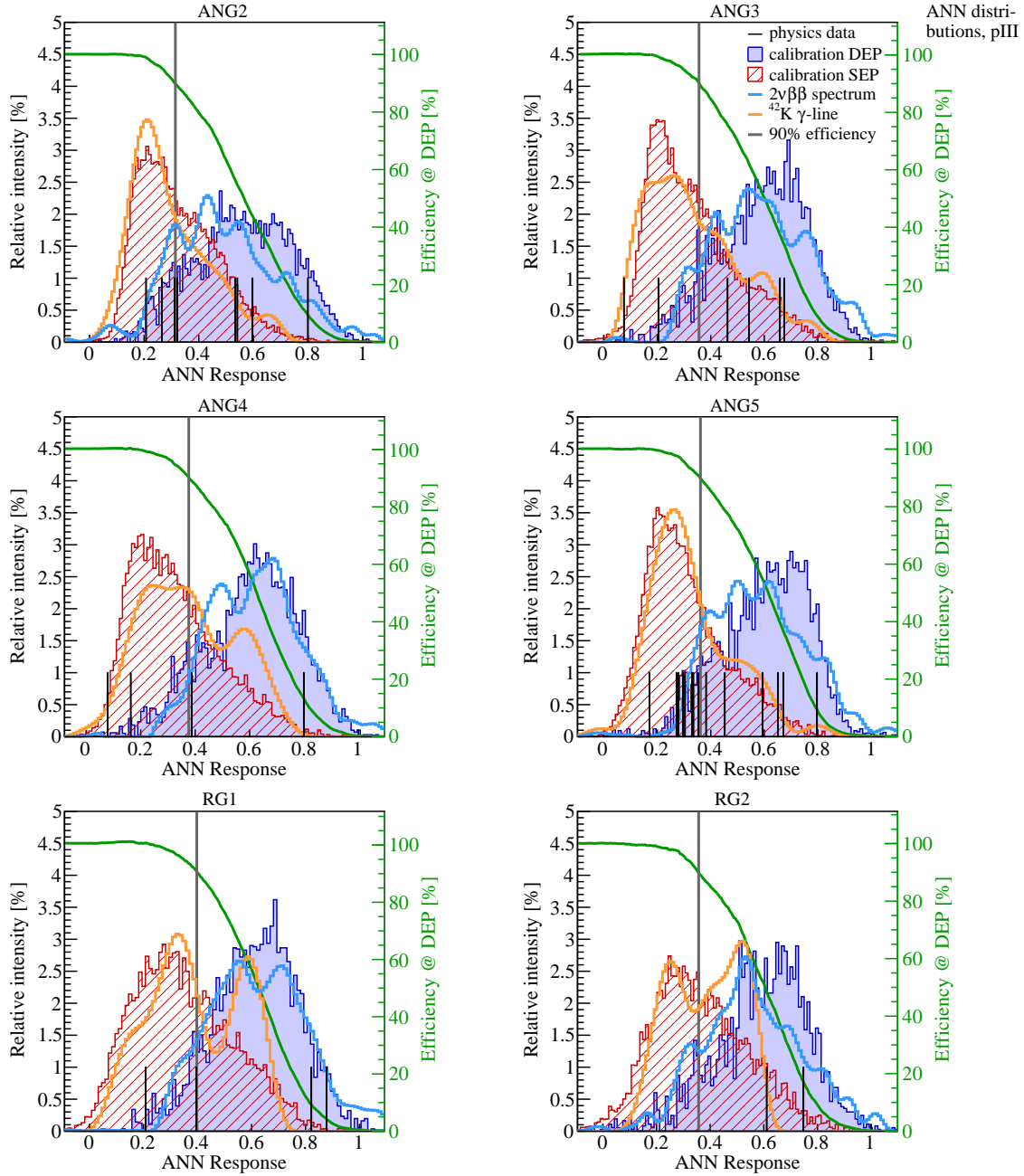
Figure 5.1: ANN response for the semi-coaxial diodes of period pIII. Distributions of the ^{228}Th calibration events of the DEP (blue filled area) and SEP (red hatched area) are shown along with the survival fraction in the double escape peak versus the cut position (green), where the grey vertical line marks the threshold corresponding to a rate of 90 %. Contributions from the Compton continuum are subtracted statistically using events in energy side bands. Also displayed are the qualifier values of physics data events from the 230 keV window around $Q_{\beta\beta}$ (black), the 1524.7 keV FEP of ^{42}K (orange) as well as the interval $1000 - 1400$ keV dominated by the $2\nu\beta\beta$-decay with subtracted MSE part (cyan).

In section 5.4 another approach, where a new ^{56}Co source has been inserted into the GERDA experiment in order to perform the corresponding calibration measurements and to verify or falsify a possible energy dependence of the multilayer perceptron selection efficiency, is presented. The valuable advantage coming with the respective cobalt spectrum originates in several DEPs - 3 of them in vicinity to the hypothetical $0\nu\beta\beta$-signal - and high number of SEP as well as FEP γ-lines.

Apart from the neural network analysis presented in this work, two further pulse shape algorithms based on very different techniques have been developed and are conveniently used as independent cross checks in section 5.5. As will be addressed, it turned out that both of the competing methods - one is a likelihood classification, the other a PSD identification by means of the pulse asymmetry - identify in good agreement with the ANN approach a very similar set of events as either signal- or background-like.

5.1 Classifier response distributions

Like already explained in the last chapter 4, the neural network pulse shape analysis for the semi-coaxial GERDA Phase I detectors relies on the so-called "supervised learning" method. Therefore the algorithm is trained with user supplied data samples of known classification data - here events that occur in the ^{208}Tl DEP at 1592.5 keV and the ^{212}Bi FEP at 1620.7 keV from the various individual calibration measurements. Hence, it should be implicitly examined if the multivariate classifier also shows the same selection performance or in other terms output dispersions for the physics data used in the $0\nu\beta\beta$-analysis.

Figure 5.1 displays the ANN response of the DEP (blue filled area) and SEP (red hatched area) events for the semi-coaxial detectors obtained from calibration runs taken during the third period pIII. For both peaks the distributions from the subjacent Compton continuum has been priorly subtracted statistically using events in the energy side bands. (Please note, that owing to this procedure negative entries - especially for bins which contain only few statistics, i.e. with regard to the DEP distribution in the region of low neural network qualifier values - may occur.) Obviously an efficient separation between these two representatives of the multi site and single site event class could be achieved.

Furthermore also qualifier outputs for different samples from physics data taking, like on the one hand $2\nu\beta\beta$ events in the energy interval between 1000 keV to 1400 keV of the spectrum (cyan) and on the other hand those located in the FEP γ-line of ^{42}K at 1524.7 keV (orange), are depicted. To ease the cognoscibility, a slight smoothing has been applied to both curves that come along with relatively poor statistics. Hereby the events from the latter full energy peak attributed to the isotope ^{42}K are of predominantly multi site character and when comparing the shape with the SEP dispersion, as an MSE equivalent from the calibration data, a quite well agreement can be determined. This stands in contrast to the A/E parameter used for the

pulse shape method particularly designed for the BEGe detector geometry for which, however, distinct but not yet completely understood differences in the single escape and full energy peak output distributions have been perceived though.

In case of the former event type from the $1000 - 1400\,\text{keV}$ region, that originates to a large extend due to the neutrino-accompanied double β-decay and consists thus of mostly SSE character, the same picture is observed - thereby the less dominant MSE part has been priorly subtracted corresponding to the predictions given by the GERDA background model in [Ago13c][Bec14] (see also the next section 5.2 for more details about the exact percentual numbers on the multi site event/single site event composition) by using the SEP sample as a proxy for background-like events. Also their distribution exhibits a large accordance with the one for the ^{208}Tl calibration DEP events of signal-like topology. It is therefore reasonable to assume the same classifier response behaviour for the two data sources from calibration as well as background measurements and so an application of the ANN cut on the physics data is ultimately justifiable.

Also shown in the figure is the qualifier response on events in the region of interest represented by a $230\,\text{keV}$ window around $Q_{\beta\beta}$ (black) and the neural network threshold determined according to a $90\,\%$ survival fraction in the double escape peak (grey vertical line). Additionally the green curve illustrates the DEP survival rate in units of [%] as a function of the cut position (right scale). Equivalent plots concerning the other two data periods pI and pII can be conveniently found in section B.2.1 of the appendix.

5.2   Survival fraction at $2\nu\beta\beta$ region

The survival fraction of those events resulting from the homogeneously distributed $2\nu\beta\beta$-decay is well suited for a comparison of the single site and explicitly the $0\nu\beta\beta$ efficiency of the neural network pulse shape discrimination. In order to not only exclude the γ-line at energies of $1460.8\,\text{keV}$ and $1524.7\,\text{keV}$ originated by the decay of the isotopes ^{40}K and ^{42}K, respectively, but to also avoid multi site events from above the Compton edge attributed to the ^{42}K potassium FEP, the considered range has been chosen to extend between $1000 - 1300\,\text{keV}$. For lower energy regions it is instead assumed that the electronic noise may deteriorate or at least distort the discrimination between SSE and MSE noticeably. According to the spectral decomposition derived within the GERDA background model from references [Ago13c][Bec14] and shortly presented in section 3.6.2 of this thesis, in this particular interval the data set is composed by fraction of $f_{2\nu\beta\beta} = 0.76 \pm 0.01$ from $2\nu\beta\beta$-decays.

The remaining $24\,\%$ however are Compton events that predominantly arise either from the $1460.8\,\text{keV}$ or $1524.7\,\text{keV}$ γ-lines owing to ^{40}K- and ^{42}K-decays or from ^{214}Bi with the accordingly ensued Compton continuum. Hence, in order to estimate the suppression of the events not coming from $2\nu\beta\beta$-decays, it is a good approximation to deploy the pulse shape survival fraction $\varepsilon_{\text{Compton}}$ from the corresponding Compton

region of the calibration data. For those intervals of distinct energy lines within the calibration spectrum, i.e. at 1078.6 keV from ^{212}Bi and 1093.9 keV from ^{208}Tl, the energy dependent survival fraction is additionally required to be interpolated from the side bands to the respective left and right of the peak.
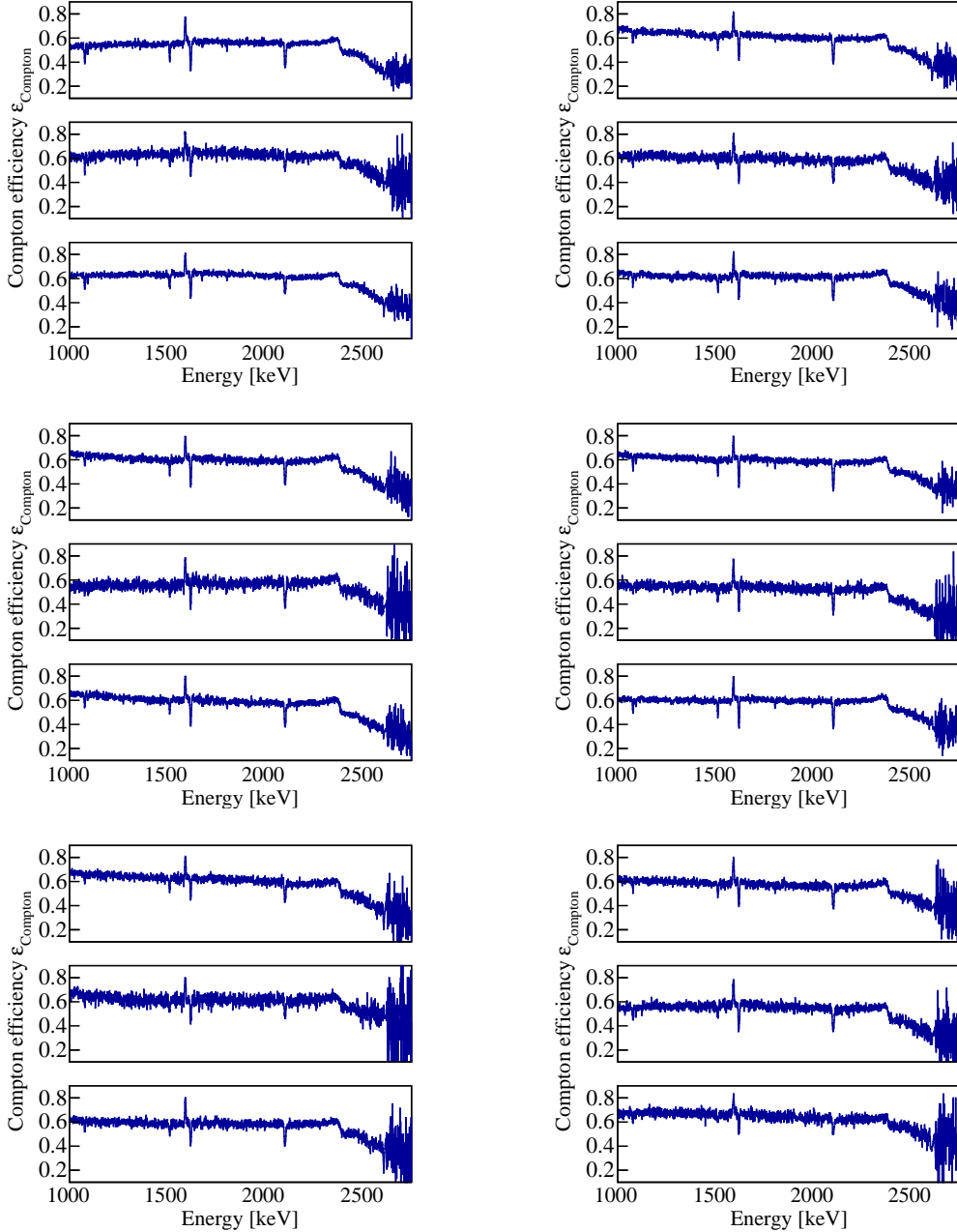

Figure 5.2: Survival rate of the ^{228}Th calibration data as a function of energy after applying the artificial neural network selection for all semi-coaxial detectors and time periods pI, pII, pIII. Hereby for each bin the ratio of the content before to after the ANN cut has been computed.

Figure 5.2 histograms the Compton efficiency derived from the artificial neural network algorithm with a fixed survival fraction of 90 % in the DEP, as a function of energy for all semi-coaxial germanium diodes and time periods pI, pII+pIII. Hereby for each bin the ratio of the content before to after the ANN cut has been computed. As can be seen, typical values for $\epsilon_{\mathrm{Compton}}$ range between 0.5 to 0.7 for the different detectors and are in most cases slightly higher if compared with the numbers quoted in table 4.5 for a $\pm 25\,\mathrm{keV}$ window around $Q_{\beta\beta}$ due to a small energy dependence. Also visible is the correspondent, opposing sensitivity of the developed pulse shape discrimination on the various γ-lines containing almost exclusively events of multi site (low efficiency) or single site (high efficiency) type, which have not yet been disentangled from the energy dependent efficiency curve and again emphasize the consistency of the ANN method.
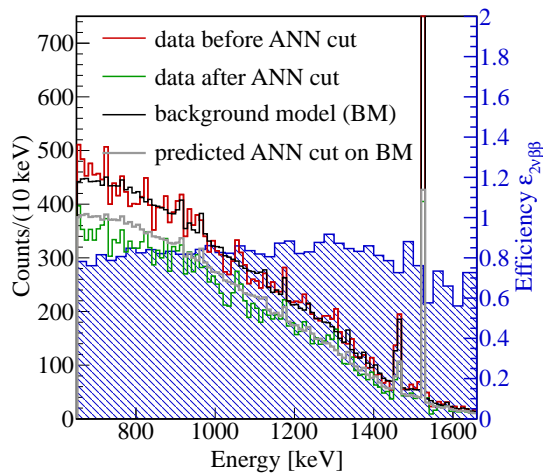
Figure 5.3: Multivariate artificial neural network selection on the physics data for the combined semi-coaxial detectors (before the cut in red and after the cut in green) and the expected effect on the GERDA Phase I background model predicted in [Ago13c][Bec14] (black and gray). Overlayed is also the extracted pulse shape discrimination efficiency $\varepsilon_{2\nu\beta\beta}$ for $2\nu\beta\beta$ events (blue hatched histogram with right side scale).

Figure 5.3 shows the physics data for the combined semi-coaxial detectors from November 2011 up to March 2013 of the "golden" subset (red) overlayed with the appendant background model (black) derived in [Ago13c][Bec14]. Further depicted are the same distributions after applying the PSD cut (in green for the data and in gray for the model). Concerning the background model, the predominant $2\nu\beta\beta$-fraction is scaled by the DEP survival rate of 0.9 while the rest is adjusted according to $\varepsilon_{\mathrm{Compton}}$ taken from the $^{228}\mathrm{Th}$ calibration data for each detector as well as time period and weighted by the respective exposures. Note that both pairs of histograms agree roughly in the energy range from $1000\,\mathrm{keV}$ to $1300\,\mathrm{keV}$. This observation can be quantitatively confirmed when calculation the $2\nu\beta\beta$ PSD efficiency using

$$\varepsilon_{\mathrm{data}} = f_{2\nu\beta\beta} \cdot \varepsilon_{2\nu\beta\beta} + (1 - f_{2\nu\beta\beta}) \cdot \varepsilon_{\mathrm{Compton}} \,. \tag{5.1}$$

The distribution of the resulting efficiency of $2\nu\beta\beta$ events is also illustrated as blue hatched histogram in figure 5.3. The average value for the survival rate in the range of $1000 - 1300\,\mathrm{keV}$ has been determined to $\varepsilon_{2\nu\beta\beta} = 0.85 \pm 0.02$, where the error is mainly dominated by the systematic uncertainty of the Compton efficiency. To estimate this effect, a fluctuation of the central value by 10 %, as the typical absolute variation of $\varepsilon_{\mathrm{Compton}}$ between $1000\,\mathrm{keV}$ and $2000\,\mathrm{keV}$, is assumed.

As a result, the obtained efficiency $\varepsilon_{2\nu\beta\beta}$ exhibits a value close to the DEP survival fraction of $\varepsilon_{DEP} = 0.9$. This strongly supports the assumption that there are no significant systematic effects related to the differences of the DEP and $2\nu\beta\beta$ event distribution within the detector volumes.

5.3   Survival fraction at Compton edge

^{228}Th calibration events at the Compton edge (CE) from the 2614.5 keV full energy peak of the ^{208}Tl-decay, i.e. in the region close to 2380 keV, are enhanced in events of single site topology and distributed similar to those from the associated double escape peak of thallium in the detector. Ultimately, the qualifier distribution for these CE events can be roughly approximated as a linear combination of the DEP dispersion and the one from multiple Compton scattered γ-ray events (MCS) of multi site character. In particular events with an energy larger than the Compton edge, for instance in an interval reaching from 2420 kev to 2460 keV, consists nearly entirely of MCS. To allow a meaningful comparison, the total event counts of both distributions in the qualifier region starting from zero up to the maximum of the multi Compton scattered dispersion are used for normalization. Figure 5.4 presents the two corresponding normalized CE (magenta) and MCS (red) curves along with the classifier output from the calibration DEP (blue filled area) for all semi-coaxial detectors of the first data period pI. Hereby the former specifically contains events that occur within an energy window of (2350 ± 25) keV.

Period	Survival fraction of "MCS subtracted" CE [%]					
	ANG2	ANG3	ANG4	ANG5	RG1	RG2
pI	90 ± 6	89 ± 6	92 ± 5	91 ± 6	90 ± 7	90 ± 7
pII	89 ± 8	91 ± 6	90 ± 7	87 ± 8	89 ± 8	86 ± 7
pIII	90 ± 6	92 ± 5	89 ± 6	92 ± 5	88 ± 6	93 ± 6

Table 5.1: Survival fractions for the SSE part of the Compton edge (CE) obtained by subtraction of the multi Compton scattered (MCS) distribution.

Further the resulting distribution after subtraction of the multi Compton scattered part (cyan) is shown in the figure as well (as observed already for the DEP curve, some bins do have entries ≤ 0 owing to statistical fluctuations). Note that this "MCS subtracted" Compton edge curve yields a quite acceptable agreement with the ANN response dispersion of the double escape peak. This statement also accounts for the remaining data intervals pII and pIII as can be ascertained with the respective plots provided in the appendix B.2.2. The vertical gray line additionally marks the cut threshold derived for the pulse shape discrimination under the condition of keeping 90 % of the DEP events and serves as orientation to estimate the classifier efficiency for the remodeled SSE part of the CE. Therefore the survival fraction is explicitly defined as the part above the selection cut. Its value has been determined for each of the six single detectors and three time periods, as listed in table 5.1, and varies between 0.86 and 0.93 with statistical errors in the range of $0.05 - 0.08$.
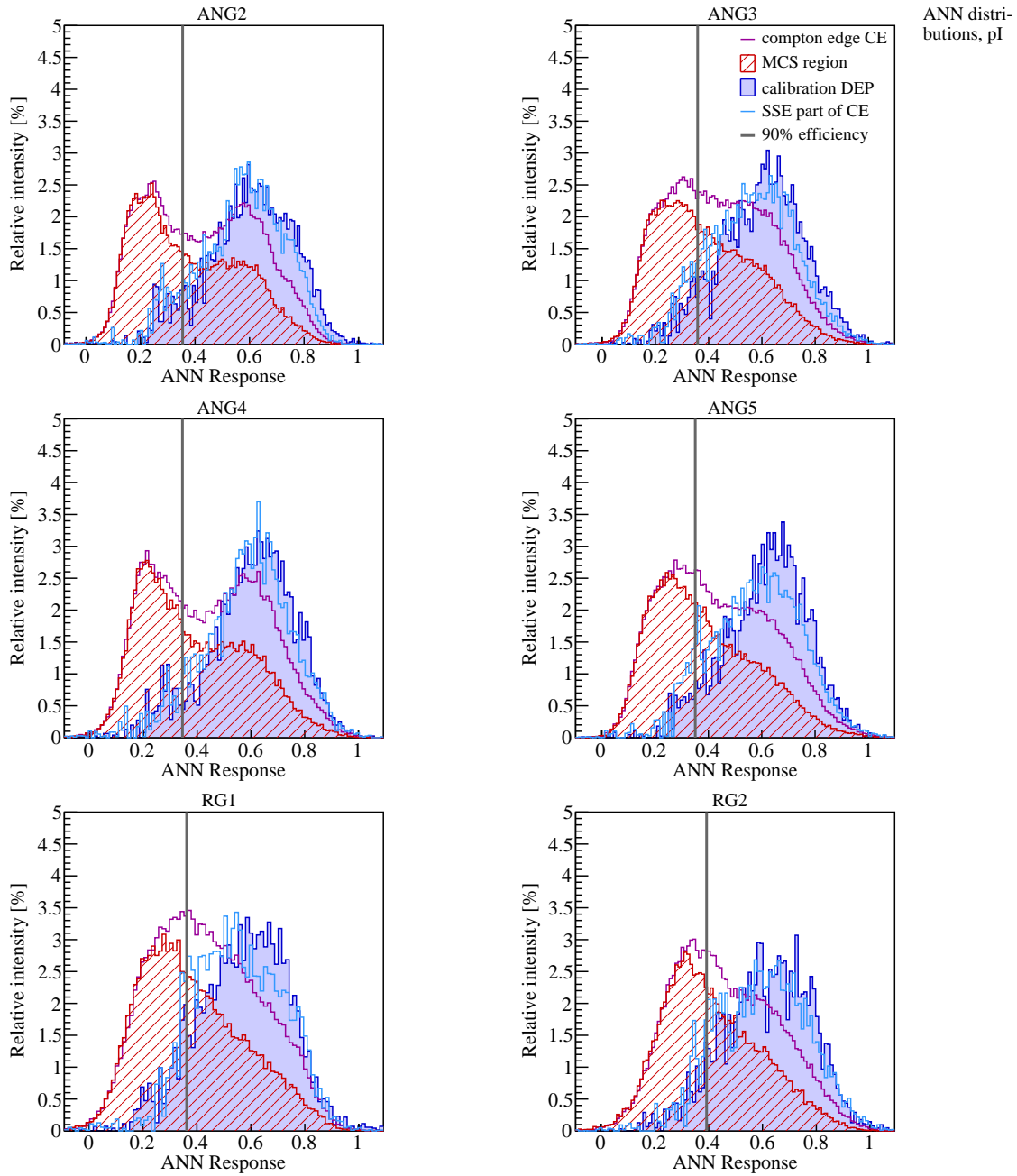
Figure 5.4: Neural network qualifier distributions for events at the Compton edge (magenta) as a linear combination of "multi Compton scattered" (red hatched area) and DEP (blue filled area) dispersions. Also shown is the Compton edge after subtraction of the MSC part consisting of purely multi site events (cyan). For the comparison, the qualifier interval from zero up to the maximum of the MCS distribution is used to normalize the curves. In general a good agreement of the resulting SSE part with the double escape peak dispersion is observed. The respective ANN threshold according to a 90 % efficiency in the DEP is emphasized as vertical gray line as well.

Consequently, no systematic shift relative to the double escape peak survival rate of 0.90, for example due to an energy dependence of the efficiency, is visible. When alternatively using SEP events instead of the multi Compton scattered ones as proxy for with the aim to model the multi site event contribution, consistent values are obtained.

5.4 Measurements with ^{56}Co calibration source

After the cessation of the Phase I data taking up to Run 46 in May 2013 and a sequencing roughly one-month-long Run 47 including 4 additional calibration measurements with the three ^{228}Th sources, the GERDA setup was drastically changed in the beginning of 2013. In principle two major operations have been performed: on the one side the 5 detectors of BEGe type hosted by the 1-string arm were removed from the germanium crystal array, while on the other side a new ^{56}Co calibration source with an activity of about 3 kBq was inserted in the S2 position of the SIS (see section 3.4). Subsequently throughout the next Run 48 special calibration measurements with the cobalt source being in close vicinity to the semi-coaxial detector array were taken.

The main advantage of such a ^{56}Co spectrum is motivated by the increased number of γ-lines with respect to an equivalent measurement utilizing ^{228}Th, where in principle up to almost 50 different peaks can be recognized - among them also two, in terms of event statistics, usable double escape peaks at energies of 1576 keV and 2231 keV rather close to $Q_{\beta\beta}$. Further there are two additional, but weaker, DEP at 2180 keV and 2251 keV. A study of the survival fractions for the respective γ-lines distributed over the whole energy range and in particular a comparison of the DEPs at different energy regions, one in vicinity to the hypothetical $0\nu\beta\beta$-signal at 2039 keV, would thus allow to scrutiny a possible energy dependency of the neural network discrimination cut.

Therefore in subsection 5.4.1 the ANN classifier is first trained again with a now extended data set consisting of pIII, the last period of the Phase I data taking, and Run 47 performed right before the ^{56}Co calibration measurement. This is done to test whether the GERDA data pass through any kind of changes concerning the behaviour towards the qualifier response. Primarily the stability of the efficiency for the DEP of ^{208}Tl within the transition between pIII and the four calibration measurements of Run 47 is validated in order to decide if it is reasonable to also classify the cobalt sample using the very same recognition rules obtained by the training on the extended data set.

In case of confirmation not only the classification pattern, but also the cut threshold derived according to a 90 % survival fraction of the double escape peak from the thorium spectra can be applied on the ^{56}Co data, as will be shown in subsection 5.4.2. Subsequently subsection 5.4.3 finally discusses the resulting efficiency rates of the most prominent SEP, FEP and DEP energy lines of the cobalt spectrum

and its implication on the systematic uncertainty of the ANN estimator. At this point, however, the reader is reminded that the following approach only involves five out of the originally six enriched semi-coaxial GERDA Phase I detectors, as RG2 had to be operated below its full depletion voltage since March 2013 and is thus disqualified for any further analysis.

5.4.1   Training and evaluation of extended ^{228}Th calibration data-set

Common to the procedure described in the last chapter 4, the neural network training has been again performed with events occurring within $\pm 1 \cdot FWHM$ around the ^{208}Tl DEP at 1592.5 keV and the ^{212}Bi FEP at 1620.7 keV as input samples of known event classification, meaning either background- or signal-like. In difference to previous computations, for this specific application the combined ^{228}Th calibration runs from the last period of Phase I *plus* Run 47 are intended to be deployed though.

Figure 5.5 a) illustrates the resulting scatter plot of the qualifier output as a function of the energy within the interval $1000 - 2750$ keV after application of the trained pattern recognition rules on this extended calibration data set pIII + Run 47. Exemplarily here only the RG1 detector is shown, but as usual an extention to all other semi-coaxial crystals is provided in the appendix B.2.3. The corresponding cut threshold for an efficiency $\varepsilon_{\mathrm{DEP}} = 0.9$ of the thallium DEP is further emphasized as horizontal gray line.

A projection of this scatter plot for the RG1 on the energy axis yields the corresponding one-dimensional energy spectrum shown in figure 5.5 b) for the two possibilities with (green) and without (red) pulse shape selection cut. The small inset at the top left depicts a blow-up of the close-by DEP and FEP double peak structure
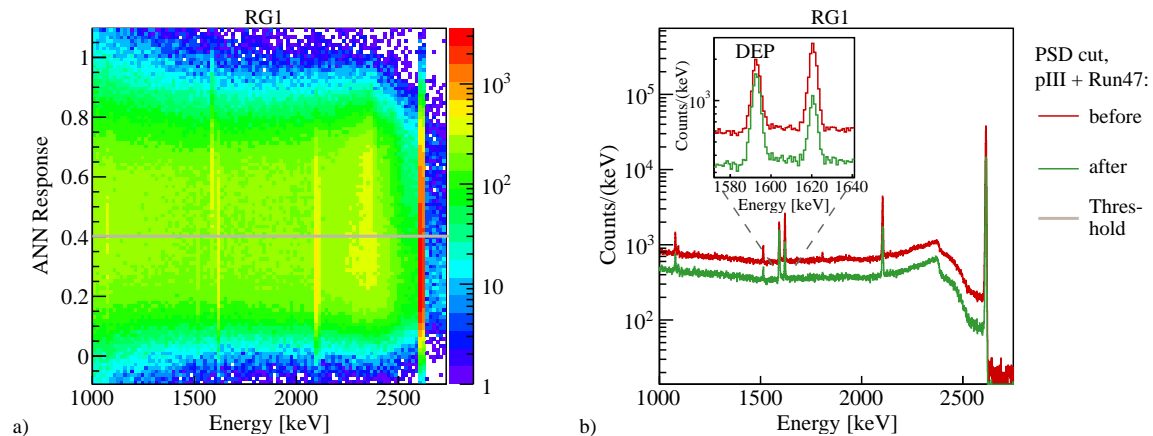
Figure 5.5: a) ANN classifier response versus energy for ^{228}Th calibration data of RG1 and period pIII + Run 47. The horizontal gray line signifies the cut position where 90 % of the DEP events are sustained. **b)** Corresponding projected ^{228}Th calibration spectrum before (red) and after (green) application of the pulse shape discrimination with a 90 % survival rate of the DEP (as can be ascertained by the small inset at the top left).

around approximately 1600 keV. For an overview of all five semi-coaxial that still worked during the relevant time period of pIII and Run 47 the reader is advised to have recourse to the appendix B.2.4.

Table 5.2 summarizes the most important classifier properties, like the cut parameter position as well as the survival fractions along with the statistical uncertainties (in units of [%]) in case of the SEP at 2103.5 keV and the FEP at 2614.5 keV or in the ± 25 keV region centered around the $Q_{\beta\beta}$-value, for the final time span pIII of Phase I combined with the new Run 47. (The error estimation been prosecued as specified in the appendix A.) In general no sizeable discrepancies between the extended data sample and the third period pIII only are observed (compare with table 4.5 from section 4.4.2 about the application of the PSD on Phase I data), which implies that the Run 47 data exhibits a similar behaviour concerning the classification algorithm.

Detector	ANN threshold	^{228}Th calibration data		
		SEP	FEP	@$Q_{\beta\beta}$
ANG2	0.316	47.9 ± 0.4	45.2 ± 0.1	64.0
ANG3	0.354	39.1 ± 0.5	41.6 ± 0.1	61.9
ANG4	0.385	34.8 ± 0.5	37.2 ± 0.1	59.3
ANG5	0.368	32.1 ± 0.4	37.5 ± 0.1	59.1
RG1	0.401	36.6 ± 0.7	37.2 ± 0.1	56.5

Table 5.2: Position of the ANN classifier cut threshold along with the resulting survival fractions in units of [%] for the ^{228}Th calibration SEP/FEP of ^{208}Tl and a ± 25 keV window around $Q_{\beta\beta}$ - when retaining 90 % of the DEP events - from data collected during pIII + Run 47.

By applying the derived pulse shape selection on every single calibration measurement, the time dependency of the DEP efficiency and specifically a conceivable drift after the end of Phase I, during the four calibration measurements of the following Run 47, can be easily scrutinized (similar to what has already presented in section 4.4.3 for the entire Phase I measurements). Figure 5.6 opposes the respect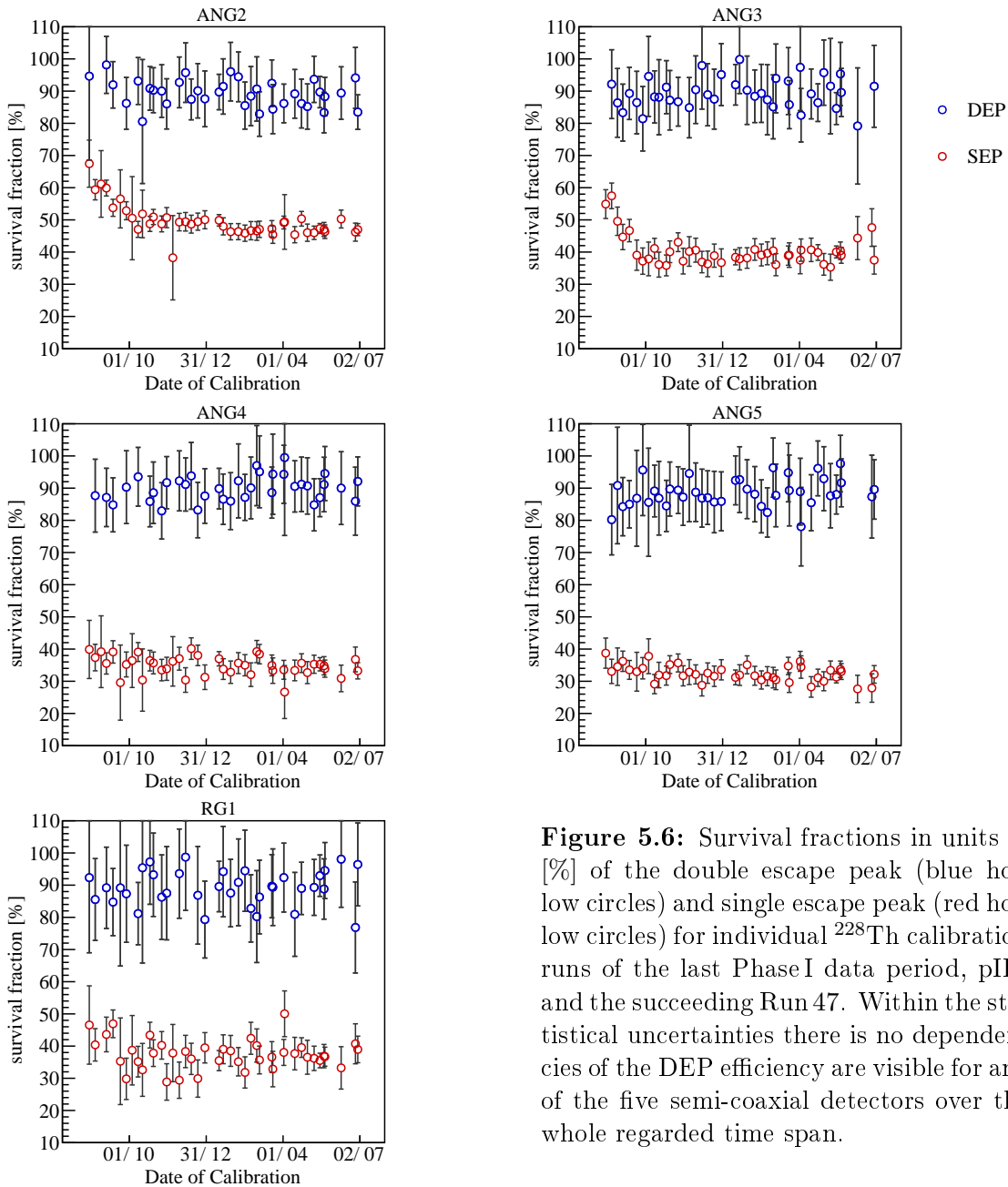ive survival fractions for the double escape peak (blue hollow circles) and single escape peak (red hollow circles) as a function of time, including the final "official" data interval pIII used for the $0\nu\beta\beta$-analysis together with Run 47. Hereby the plot is shown for all remaining five enriched semi-coaxial germanium detectors, where for all of them no evidence of any kind of time dependencies of the ANN classifier on the DEP efficiency can be observed within the given statistical uncertainties.

Thus it is consequently assumed that there are no considerable changes in the data quality in terms of the response on the multivariate selection algorithm during the chronological sequence of the GERDA data taking until the end of Run 47 that i.e. also marks the beginning of the cobalt calibration measurements with the freshly inserted new ^{56}Co source. Hence in the following pulse shape analysis on the cobalt data the classification pattern as well as cut threshold derived for each detector according to a 90 % survival rate of the DEP from the thorium spectra will be justifiably applied on the ^{56}Co data.

5.4.2 Application of PSD cut to ^{56}Co calibration data

Transferring the very same, unaltered recognition rules from the training on the ^{228}Th event sample to the data set obtained with the cobalt calibration source creates the scatter plot of the ANN qualifier response versus energy depicted in figure 5.7 a) for the RG1 detector only. Equivalent plots of the remaining germanium diodes, which however all show very similar distributions, can be found additionally in the appendix B.2.5 though. Thereby the most striking feature of the ^{56}Co measurement - the huge number of γ-lines allocated over the whole $1000 - 2750\,\mathrm{keV}$ wide energy

Figure 5.6: Survival fractions in units of [%] of the double escape peak (blue hollow circles) and single escape peak (red hollow circles) for individual ^{228}Th calibration runs of the last Phase I data period, pIII, and the succeeding Run 47. Within the statistical uncertainties there is no dependencies of the DEP efficiency are visible for any of the five semi-coaxial detectors over the whole regarded time span.

range - is already revealed by the color code of the two-dimensional histogram, where the predominant energy peaks with higher event density are illustrated in red shades. Further the gray horizontal line highlights the PSD cut threshold fixed with the aid of the ^{228}Th calibration data discussed in the last subsection according to retain 90 % of the DEP events.

The corresponding projection on the energy axis results in the cobalt energy spectrum of the RG1 presented in figure 5.7 b) for the two options of "before" (red) and "after" (green) the application of the pulse shape discrimination cut (marked in the left figure) on the qualifier output. Again the most obvious token of the spectral dispersion is given by the various monoenergetic spikes. Apparently both double escape peaks at energies of 1576 keV and 2231 keV, albeit being the ones of larger statistics out of the in total four DEPs provided by the cobalt spectrum, rather seem to be representants of less prominent energy lines and are therefore expected to carry a quite high statistical error.

5.4.3 Survival fraction of γ-lines

For the ^{56}Co analysis the survival rate of the different energy peaks of the spectrum is studied. Hereby the survival is explicitly defined as the fraction of the γ-line content remaining after the neural network cut derived from previous thorium calibration runs taken during period pIII + Run 47. In particular the peaks are fitted by a Gaussian folded with a linear slope and a sigmoid function, both accounting for the background consisting of Compton events, each to determine the respective intensities. Using the alternative counting method in order to derive the line content, while
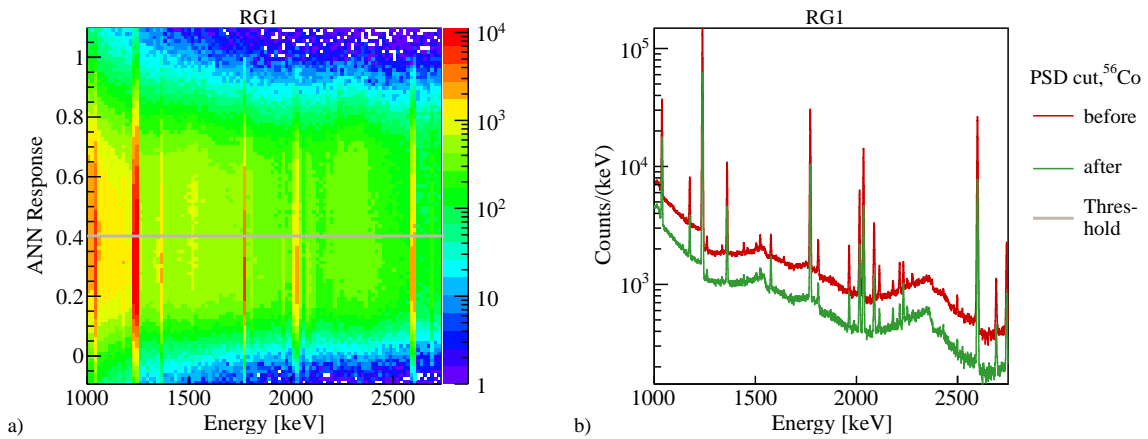
Figure 5.7: a) Neural network qualifier output as a function of energy for ^{56}Co calibration data taken during Run 48 for the RG1 detector. The cut position on the ANN response, where a fraction of 90 % of the DEP events from the ^{228}Th calibrations of the combined third period pIII of Phase I and Run 47 are kept, is marked by the gray horizontal line. **b)** Respective one-dimensional ^{56}Co spectrum after the projection on the energy axis for the two options of "with" (green) and "without" (red) pulse shape selection cut.

excluding those events that originate from the underlying Compton continuum by subtracting linearly scaled event numbers from energy regions below and above the peak position (as presented in subsection 4.4.2 for a first evaluation of the developed ANN pulse shape), is instead regarded as a less favourable procedure for the given data sample though. This is mostly due to two reasons: First of all the robustness of the calculation is strongly constrained by the statistics, which is for some of the γ-lines quite - if not even too - poor. On the second matter, the ^{56}Co spectrum consists in parts of a row of close-by accumulated peaks, such that a subtraction of Compton induced events with the aid of energy side bands to the left or right of the peak vicinity, as proxy for the background continuum, can not be accomplished any more. Hence, computing the efficiency of the ANN estimator on the various γ-lines based on a parameter fitting algorithm is considered as the more relyable approach.

Table 5.3 states the finally extracted survival fractions (in units of [%]) for the 16 most prominent γ-peaks of the ^{56}Co calibration spectrum and different detectors. Apart from the double escape peak, the list as well includes lines of full energy peak and single escape peak type, all randomly distributed over the whole investigated energy range starting from 1000 keV up to 2750 keV. Furthermore the corresponding survival fractions of the individual γ-lines are plotted in figure 5.8 as function of energy for the five different semi-coaxial detectors to also give a visual impression.

Energy of γ-line [keV]	Type	Survival fraction [%]				
		ANG2	ANG3	ANG4	ANG5	RG1
1037.8	FEP	37.5 ± 0.9	50.2 ± 0.6	43.7 ± 0.5	52.4 ± 0.4	45.2 ± 0.4
1175.1	FEP	39 ± 3	44 ± 2	41 ± 2	44 ± 2	42 ± 1
1238.3	FEP	37.1 ± 0.3	43.3 ± 0.2	38.3 ± 0.2	40.9 ± 0.4	41.5 ± 0.1
1360.2	FEP	36 ± 1	41 ± 1	35.1 ± 0.9	36 ± 1	38.5 ± 0.7
1576.5	DEP	80 ± 13	89 ± 10	87 ± 8	94 ± 11	88 ± 6
1771.4	FEP	35.4 ± 0.5	35.3 ± 0.4	31.0 ± 0.3	30.5 ± 0.4	32.9 ± 0.3
1810.8	FEP	39 ± 6	33 ± 4	30 ± 3	32 ± 4	27 ± 3
1963.7	FEP	35 ± 5	33 ± 3	29 ± 3	30 ± 4	32 ± 2
2015.2	FEP	36 ± 2	35 ± 1	30.1 ± 0.9	29 ± 1	30.7 ± 0.8
2034.8	FEP	34.9 ± 0.8	34.2 ± 0.6	30.6 ± 0.5	29.8 ± 0.5	31.2 ± 0.4
2087.5	SEP	42 ± 3	34 ± 2	29 ± 1	28 ± 2	31 ± 1
2113.1	FEP	41 ± 7	31 ± 5	32 ± 4	33 ± 5	28 ± 4
2212.9	FEP	34 ± 6	32 ± 10	31 ± 4	27 ± 11	30 ± 3
2231.5	DEP	89 ± 15	91 ± 10	87 ± 7	90 ± 10	84 ± 6
2598.5	FEP	34.5 ± 0.5	33.3 ± 0.4	29.9 ± 0.3	29.2 ± 0.3	28.1 ± 0.2
2691.0	SEP	44 ± 4	42 ± 4	38 ± 3	33 ± 3	36 ± 2

Table 5.3: Survival fractions of the neural network pulse shape selection algorithm for the 16 most prominent DEP, SEP and FEP γ-lines of the ^{56}Co calibration spectrum in the energy range of $1000 - 2750$ keV and different detectors.

Applying the neural network selection the diodes evidently exhibit efficiencies between $\varepsilon_{DEP} = 0.80$ and 0.94 for the two usable DEPs that are, when also taking their statistical uncertainties into account, in good agreement with the fixed survival rate of 90 % of the thallium double escape peak from the thorium calibrations. A close-up of both peak structures consisting of predominantly single site events is provided in figure 5.9 a) for the lower-energetic line at 1576 keV and b) for the higher-energetic line at 2231 keV with all five germanium crystals being summed up. Again the spectral distribution is shown in its original form before (red) and after (green) performing the ANN classifier cut.
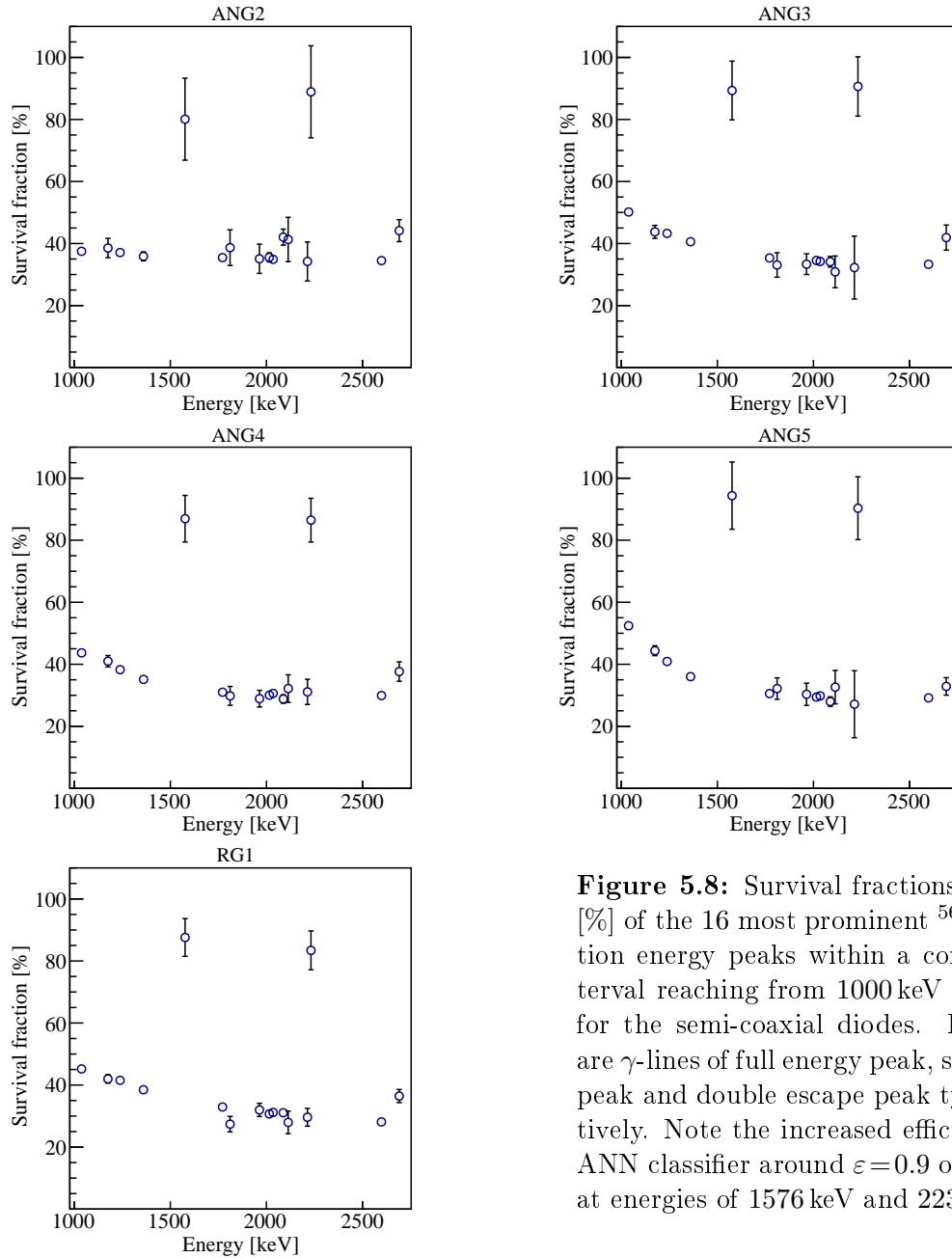
Figure 5.8: Survival fractions in units of [%] of the 16 most prominent ^{56}Co calibration energy peaks within a considered interval reaching from 1000 keV to 2750 keV for the semi-coaxial diodes. Investigated are γ-lines of full energy peak, single escape peak and double escape peak type, respectively. Note the increased efficiency of the ANN classifier around $\varepsilon = 0.9$ on the DEPs at energies of 1576 keV and 2231 keV.

Another crucial issue that is revealed in table 5.3 and can be more particularly observed in figure 5.8 appears as a slight energy dependency of the survival rates for low-energy γ-lines smaller than roughly 1500 keV of mainly multi site character while for higher values no correlations are present at all. This concerns almost every single detector, except ANG2. As already assumed earlier, the pulse shape discrimination is deteriorated towards smaller energy values due to an decreased signal-to-noise ratio.

5.5 Comparison with alternative PSD methods

For the recently finished Phase I of the GERDA experiment two more PSD methods have been independently developed as discussed in [Ago13d]. While the neural network algorithm, as subject of this thesis, is used officially for the $0\nu\beta\beta$-analysis, they instead serve as cross checks for the event selection of the ANN. Eventhough based on very different techniques, it turns out as a matter of fact that all three methods reject a very similar set of events as background. However, no systematic errors for the signal efficiency has been evaluated for both of the concurrent approaches that will be briefly presented in the following.

5.5.1 Likelihood

A second PSD analysis uses the projective likelihood algorithm implemented in TMVA (a short description was given in section 4.1). The training is prosecuted with 8 input variables calculated from the charge pulse trace, where each parameter is given by the sum of four consecutive pulse heights of 10 ns bin width after base-
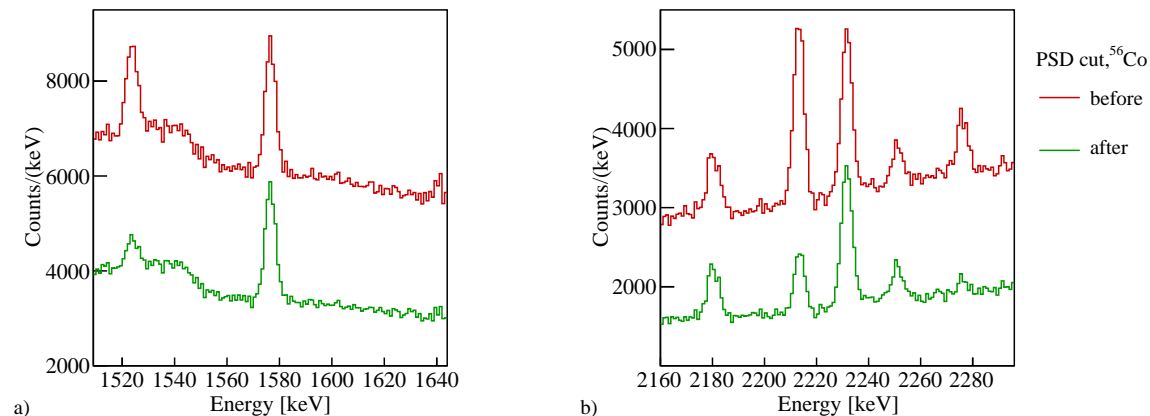
Figure 5.9: Parts of the ^{56}Co calibration spectrum summed up for all semi-coaxial detectors with (green) and without (red) pulse shape discrimination. Energy regions centered around the **a)** low-energetic DEP at 1576 keV and the **b)** high-energetic DEP at 2231 keV are shown, respectively. On the right side also the two additional double escape peaks with lower statistics are visible at adjacent energies of 2180 keV and 2251 keV.

line subtraction and energy normalization. To fix the reference point, the considered pulse is further centered around the time value at which the derivative of the original trace, i.e. the current trace, is maximal.

Unlike the neural network method, the likelihood classifier is trained with a data sample split in only two periods from before (pI) and after (pII) June 2012. As a further different approach - instead of the DEP interval - Compton edge events in the energy region between $2350 - 2370\,\text{keV}$ consisting of a mixture of MSE and SSE are used for the signal-like proxy sample. The background data set is provided by the energy window reaching from $2450\,\text{keV}$ to $2570\,\text{keV}$ that contains almost exclusively multiple Compton scattered photons and hence traces of pure multi site topology.

On the basis of these two training samples a likelihood function $\mathcal{L}_S$ for being of signal event type and $\mathcal{L}_B$ for being of background event type according to equation 4.1 is calculated (see subsection 4.1.1 dedicated to the classifier methods implemented in the TMVA software). The final qualifier response value assigned to a respective event i of unknown classification is then defined by

$$y_{\mathcal{L}}(i) = \frac{\mathcal{L}_S(i)}{\mathcal{L}_S(i) + \mathcal{L}_B(i)} \ . \tag{5.2}$$

Figure 5.10 a) depicts for the ANG3 detector and first half pI of the calibration data a scatter plot of the likelihood qualifier output versus energy. No energy dependencies are considered. The different population densities at either very low or very high classifier values demonstrate the effective separation of the double escape
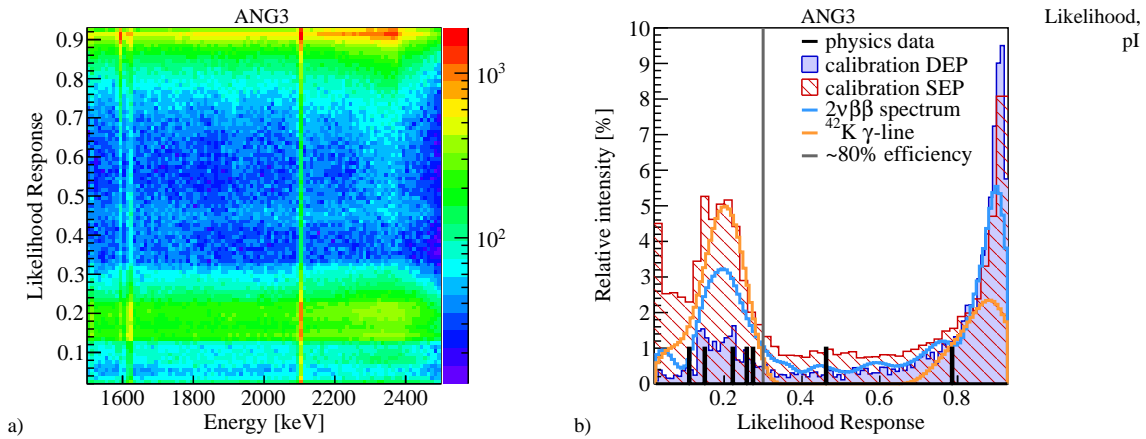
Figure 5.10: a) Likelihood response as a function of energy for the ANG3 detector of the first half pI of the splitted ^{228}Th calibration data set. **b)** Corresponding projected likelihood response for the ^{228}Th calibration DEP (blue filled area) and SEP (red hatched area) with the cut being marked as gray line. The distributions resulting from the Compton continuum are thereby disentangled by statistically subtracting events from the energy side bands. Also shown are qualifier values of the physics data from events in the ROI around $Q_{\beta\beta}$ (black), the ^{42}K γ-line at $1525\,\text{keV}$ (orange) and the $2\nu\beta\beta$-rich interval $1000 - 1400\,\text{keV}$ (cyan). The latter two distributions have been slightly smoothed due to statistical reasons.

peak events at an energy of 1592.5 keV and, for example, the single escape events at an energy of 2103.5 keV. For the cut position a fixed parameter corresponding to about 80 % survival fraction for DEP events is assumed. In particular the value varies slightly for the different detectors and periods pI, pII.

Additionally figure 5.10 b) shows the corresponding projected likelihood response of the first period pI of the ANG3 for different event classes from calibration and background measurements. In general the distribution for physics data from the ^{42}K line (orange) and the SEP dispersion (red hatched area) extracted from the calibration runs, both of MSE character, are in good agreement. Consistently also the events of the $1000 - 1400$ keV energy interval, to a great part originated by $2\nu\beta\beta$-decays, are clearly enhanced in SSE and exhibit, as expected, a distribution similar to that of the DEP events.

Detector	Period	Calibration		Background		
		SEP	@$Q_{\beta\beta}$	$2\nu\beta\beta$	^{42}K	ROI
ANG2	pI	47	57	61	35	1/3
	pII	50	56	57	37	4/10
ANG3	pI	49	58	60	36	2/7
	pII	52	61	64	40	3/11
ANG4	pI	52	60	65	54	2/2
	pII	50	62	71	51	2/5
ANG5	pI	45	57	62	42	0/9
	pII	40	51	61	31	3/20
RG1	pI	50	63	63	59	1/5
	pII	51	62	65	46	2/7
RG2	pI	49	60	70	46	6/8
	pII	51	61	63	50	7/9

Table 5.4: Survival fractions (without statistical errors) in units of [%] and event counts in ROI (last column) of the projective likelihood algorithm for the different detectors and periods pI, pII. The cut is thereby set to retain about 80 % of the DEP events. Numbers are given for calibration and physics (background) data, where Run 33 is discarded, with the meaning of the columns being identical to table 4.5 for the ANN classifier. Values taken from [Ago13d].

Table 5.4 lists for the different semi-coaxial detectors and two periods pI + pII the survival fractions of the SEP and to allow a complete overview also the ones from several other data subsets. A rejection rate of about 65% is achieved for the events within the region of interest (ROI) marked by a 230 keV window around $Q_{\beta\beta}$. Eventual differences in the total event number in the ROI to smaller values, if compared with the corresponding table 4.5 for the neural network classifier, arise for some detectors, since for the likelihood evaluation the whole Run 33 is discarded.

5.5.2   Pulse asymmetry

A third approach uses only two variables as discrimination parameters for the semi-coaxial detectors to select single site events. In chapter 3 it has already been discussed that the A/E parameter alone does not serve as a powerful quantity for a pulse shape selection. But if the amplitude-to-energy ratio is instead combined with the pulse asymmetry defined as

$$A_s = \frac{\sum_{i=0}^{i=n_m} I(i) - \sum_{i=n_m}^{i<200} I(i)}{\sum_{i=n_m}^{i<200} I(i)} \ , \tag{5.3}$$

the event discrimination becomes, however, much more effective though. Hereby $I(i)$ denotes the height of the current pulse, equivalent to the differentiated charge pulse, at time sample i and n_m represents the respective position of the maximum. In total an overall window of 200 samples, corresponding to a time interval of $2\mu s$, around the trigger position at the beginning of the leading edge of the charge trace is analyzed.

To achieve an optimal noise reduction, a moving window averaging based on different integration times of 0 (no filter), 20, 40, 80, 160 and 320 ns for the charge pulse are prosecuted. Afterwards for each shaping time, the two parameters A/E and A_s are derived to compute the empirically derived relation

$$y_{\text{Asym}} = \frac{A}{E} \cdot (c + A_s) \tag{5.4}$$

that exhibits an surprisingly enhanced PSD performance. Since current pulses of SSEs might feature more than only one maximum, the A_s is further shaped with larger integration times to avoid any ambiguities.

The cut threshold is optimized by comparing the DEP survival rate ε_{DEP} from ^{228}Th calibration runs with the fraction of physics data events f_{bkg} from 1700 keV to 2200 keV without the blinded window around $Q_{\beta\beta}$ retained after the PSD selection.
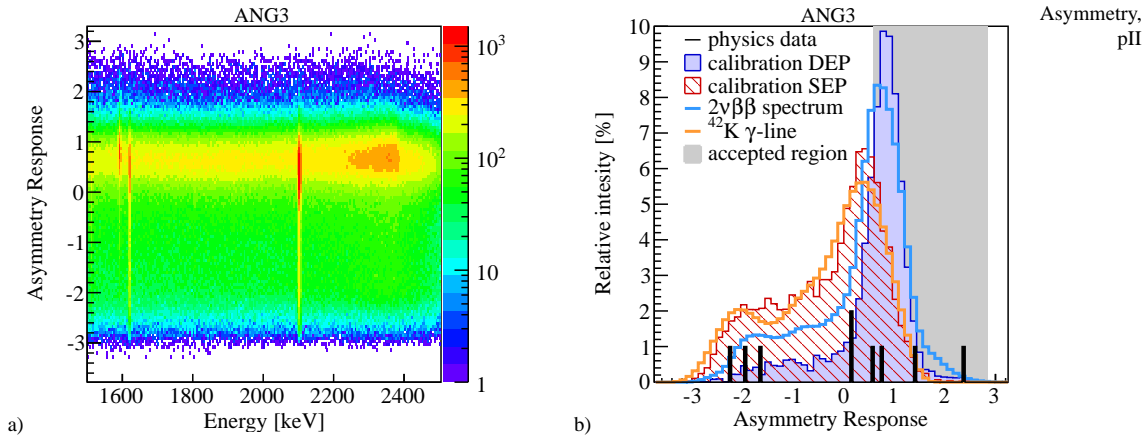
Figure 5.11: a) Asymmetry response versus energy for the ANG3 detector and the second half pII of the splitted ^{228}Th calibration data set. **b)** Corresponding projected qualifier response distributions for the ^{228}Th calibration DEP (blue filled area) and SEP (red hatched area) - with statistically subtracted Compton continuum - as well as the 1525 keV line of ^{42}K (orange) and the energy interval $1000 - 1400$ keV of mostly $2\nu\beta\beta$ events (cyan) from the physics data. The latter two dispersions have been thereby slightly smoothed owing to their small statistics. Also shown are qualifier values of the physics data from events in the ROI around $Q_{\beta\beta}$ (black) and the region accepted by the cut (gray area).

In order to determine the lower cut value, the quantity

$$S = \frac{\varepsilon_{DEP}}{\sqrt{f_{bkg} + 3/N_{\mathrm{bkgd}}}} \, , \tag{5.5}$$

with N_{bkgd} being the total number of background events, is required to be maximized, whereas the upper cut is set to $\approx + 4\sigma$ of the Gaussian width of the DEP qualifier distribution. A scan of all combinations of shaping times and values for c in the interval of $1-4$ is conducted to attain the highest possible value for S. The term $3/Nbkg$ in equation 5.5 is intentionally added to avoid an optimization towards zero background. Using the described optimization procedure then yields DEP survival fractions that very between roughly 70 % and 90 %, depending on the respective detector and time period before (pI) and after (pII) insertion of the BEGes. Moreover, about 75 % of the events in the energy interval $1700 - 2200\,\mathrm{MeV}$ are rejected.

Detector	Period	Calibration		Background		
		DEP	SEP	$2\nu\beta\beta$	^{42}K	ROI
ANG2	pI	69	32	52	28	0/5
	pII	70	40	50	33	4/9
ANG3	pI	90	51	74	55	5/11
	pII	69	22	49	23	4/9
ANG4	pI	78	28	63	41	1/2
	pII	78	45	66	41	1/5
ANG5	pI	81	33	65	39	1/11
	pII	67	16	65	39	1/18
RG1	pI	92	64	78	65	2/5
	pII	69	23	55	38	2/7
RG2	pI	86	38	71	44	4/12
	pII	86	38	65	56	3/5

Table 5.5: Survival fractions (without statistical errors) in units of [%] of the asymmetry based PSD method for the different periods pI, pII and detectors. The rate of the DEP and SEP events from the ^{228}Th calibrations retained after the cut is listed in the third and fourth column. Further numbers + event counts in ROI are given for physics data, equivalent to the last columns of table 4.5 for the ANN classifier and table 5.4 for the likelihood estimator [Ago13d].

All properties of interest, as for instance the survival fractions of events from the DEP and SEP of the ^{228}Th calibration runs or from the ^{42}K γ-line and the $2\nu\beta\beta$-dominated energy region $1000 - 1400\,\mathrm{keV}$ of the physics data, are summarized in table 5.5. The last columns states the number of events within the ROI at $Q_{\beta\beta}$ before and after the asymmetry cut. About 72 % of the events within the region of interest are rejected.

Figure 5.11 a) shows for the ANG3 detector and the second time period, pII, a scatter plot of the asymmetry classifier as a function of the energy. For the presented ^{228}Th calibration data, a separation between the single site events of the DEP and multi site events at the energy of the FEP or SEP can be observed.

Further figure 5.11 b) provides the respective response disperions of the DEP (blue filled area) and SEP (red hatched area) calibration events after statistically subtracting the Compton events below the peaks. Additionally the PSD qualifier

distributions for the physics data in the 230 keV window around $Q_{\beta\beta}$ (black), from the 1525 keV potassium line (cyan) and the interval $1000 - 1400$ keV consisting of predominantly $2\nu\beta\beta$ events (orange) are also overlayed. Finally the grey area signifies the range accepted by the PSD.

It has been observed that the qualifier distribution of physics data within the region of interest (ROI) has a larger spread to higher asymmetry classifier values than the one of events associated with a predominantly multi site character. This is also the reason why events close to $Q_{\beta\beta}$ are actually rejected more efficiently compared to those from typical MSE proxies as the single escape or the full energy peak (see table 5.5). A possible explanation for the anyhow stronger suppression of the background achieved by this particular approach, is deduced by the circumstance that the physics data contain a large fraction of events, which are not of multi site topology, but may arise from for example p+ surface events close to the bore hole. Further affirmative indication regarding this hypothesis is implied by the "maximal" background model of the GERDA experiment [Ago13c] (or see subsection 3.6.2) being also compatible with a significant fraction of p+ events. Finally a dedicated pulse shape simulation performed on that matter has proven the selection to correspond indeed to a volume cut, where preferably those events close to the p+ contact layer and in the center of the detector bulk are removed.

5.5.3   Comparison

When cross checking the event identification of the neural network algorithm with the two other PSD methods on the basis of a likelihood estimator or the pulse asymmetry, respectively, a huge overlap for the three independently cutted data sets can be determined. In fact it is ascertained that each of the event within the region of interest close to $Q_{\beta\beta}$ rejected by the ANN classifier is at least also cutted by one, in almost 95 % of the cases by even both of the competing methods (see figure 5.12). This, however, gives confidence that the pulse shape selection is meaningful.
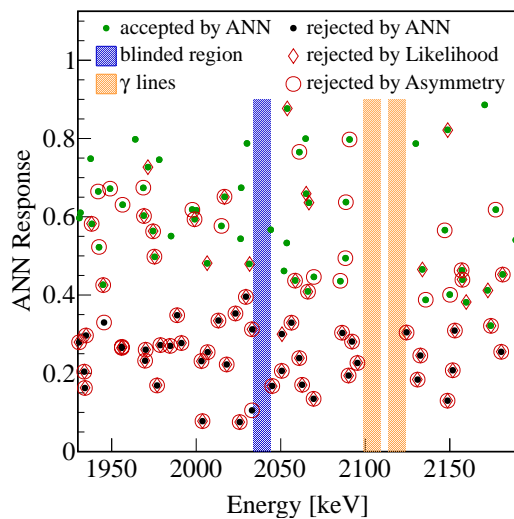
Figure 5.12: Scatter plot of the neural network classifier response for events within the ROI given by a 230 keV energy window close to $Q_{\beta\beta}$ (all semi-coaxial detectors combined). Events accepted by the ANN cut are denoted by green dots and those that are instead rejected by black dots. Further the red circles and diamonds signify events rejected by the likelihood or asymmetry based method, respectively. Intervals not considered in the analysis are marked as blue (blinded region) or orange (two γ-lines at 2103.5 keV and 2119.5 keV) shaded areas.

6. Monte Carlo simulation

Key for the success of a counting experiment for the search of the neutrinoless double β-decay, like the GERDA setup within which the work presented in this thesis has been carried out, is to effectively suppress background that originates from different close-by or far distant radiation sources. This may be either achieved by passive shielding via, in the specific example of the GERDA underground experiment, several surrounding layers of - from the outside to the inside of the setup close to the detector array - rock, water, massive copper plates attached to the cryostat vessel and liquid argon in combination with the usage of only prescreened materials. Other possible methods, based on an active shielding are further provided as muon- and LAr-veto hardware components (see chapter 3).

Previous studies on germanium semiconductors in [Pet93][Ell06][Abt08] have impressively proven, that a carefull data selection by means of pulse shape algorithms can also significantly reduce the obstructive background index resulting in a highly improved experimental sensitivity. Most of these investigations were conducted on the basis of so-called segmented detectors with the outer contact being divided into several isolated areas though, which as a result provide the advantage of an enhanced anti-coincidence cut between the distinct segments. The explicit application of an artificial neural network method, has been - besides this thesis - already considered in [Maj99] and [Vol12] in the past. Thereby both approaches yielded very encouraging results concerning the suppression power for background-like events of multi site topology.

In the course of chapter 4 an independent pulse shape analysis procedure utilizing the ANN algorithm has been developed with special emphasis on its application for GERDA Phase I. Apart from first promising results of the neural network method presented there, further consistency checks have been conducted in the subsequent chapter 5 availing on calibration and physics measurements. However, all efforts made so far were restricted to experimentally obtained data only. Hence, in the present chapter a detailed Monte Carlo simulation (MCS) of the neural network algorithm will be prosecuted in order to explicitly derive its efficiency $\varepsilon_{0\nu\beta\beta}$ on the homogeneously distributed neutrinoless double β-decay.

In doing so, a data subset, suitable for an easy reconstruction of the experimental parameters of relevance within the simulations, is first identified in section 6.1. Since the multivariate classifier is trained with calibration samples, the source position, that describes the measured GERDA data subset the best, has to be determined in a next step throughout section 6.2, before in section 6.3 the thus obtained interaction points of energy deposition within the semi-coaxial detectors can be subsequently used for a detailed pulse shape modelling. Sections 6.4 and 6.5 compare results from the training/testing and the application to the overall calibration spectrum attained from Monte Carlo + Finite Element Method (FEM) computations with those from

the experimental measurements. A conclusion regarding the survival fraction of events arising from the $0\nu\beta\beta$-decay is then given in the following section 6.6, where the trained pattern recognition rules with a cut according to an efficiency of 90 % for the ^{208}Tl DEP are applied on a homogeneously distributed, simulated neutrinoless double β-signal. Finally the last section 6.6.3 is solely dedicated to an estimation of the systematic uncertainties concerning the performed simulation studies (i.e. owing to the source position, electronic response, noise or crystal axis).
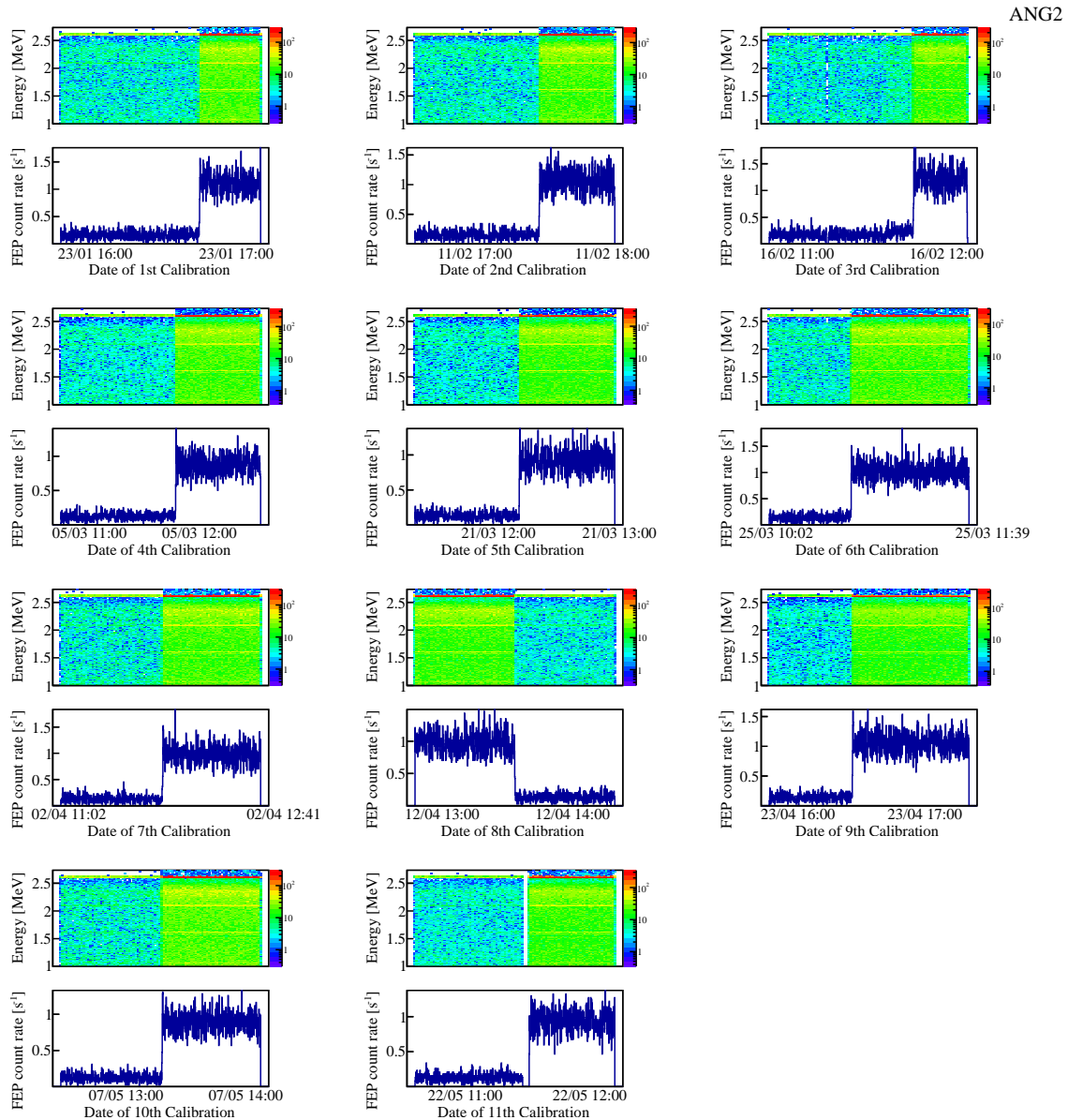
Figure 6.1: Scatter plot of the energy interval $1000 - 2750$ keV versus time for the ANG2 and the 11 calibration measurements between January 23th 2012 within Run 28 and May 22nd 2012 within Run 32 (top half). The lower half depicts the corresponding count rate - after statistically subtracting background events from the energy side bands - in units of $[s^{-1}]$ for the ^{208}Tl FEP at 2614.5 keV (blue). An anti-coincidence cut is applied to the data.

6.1 Choice of data subset

To allow a meaningful comparison of the final simulation results on the artificial neural network performance with the ones obtained from real experimental measurements, a data sample taken within the duration of Phase I is needed that fulfils two important requirements:

- First of all the data subset has to provide enough statistics, such that, during the supervised leaning procedure of the ANN algorithm with the two training samples of either signal- or background-like event class, no overtraining will occur. Thus a combination consisting of several individual calibration measurements is required.

- As a second condition, the data collection has to be comprised of similar experimental parameters for each of the data sets in terms of the detector configuration, the duration of the calibration measurements (to avoid an increased importance of short time intervals with recorded higher statistics) and the ^{228}Th source positions S1, S2 and S3 (see figure 3.12 in section 3.4).

Taking into consideration that the three source positions have been arbitrarily altered for most of the individual runs to equally scan all detectors in the array for an optimal energy calibration, an easily reproducible setup configuration for the Monte Carlo simulations seems highly unlikely.

When perusing the list of the in total 70 performed single calibration runs of Phase I and their particular setup states, the most suitable data subset is, however, found with the 11 consecutive measurements gathered between Run 28 (start: January 24th 2012) and Run 32 (stop: May 22nd 2012) in the course of the first time interval pI of the three periods. (The splitting of the GERDA data into three different subsets pI, pII and pIII has been already discussed and explained in detail throughout subsection 4.2.3).

position	source location according to SIS [mm]			duration [%]
	S1	S2	S3	
1	4950	5500	5500	54
2	5150	5150	5150	46

Table 6.1: Source locations of S1, S2 and S3 for the 11 calibration runs between January 24th 2012 and May 22nd 2012. Values in units of [mm] account for the absolute distance to the respective parking positions.

In particular the considered almost one dozen calibration runs with an average length of roughly $1 - 1\frac{1}{2}$ hours are collected with only two fixed locations for each of the sources S1, S2 and S3 as listed in table 6.1 along with the corresponding percentage share of the total time (last column). The SIS used for the insertion and removal of the thorium sources (priorly addressed in section 3.4) is thereby equipped with a positioning readout system, which traces the absolute spacing to the parking positions in units of [mm]. By that the relative distance of the sources

to one another is known indeed, but the respective distance to the detector array instead still remains to be determined though. Therefore in the next section 6.2 a sequence of comprehensive simulation campaign with varying locations of the tree ^{228}Th calibration sources are impelled to derive their exact position with respect to the 3-string arm deployed with the semi-coaxial germanium diodes.
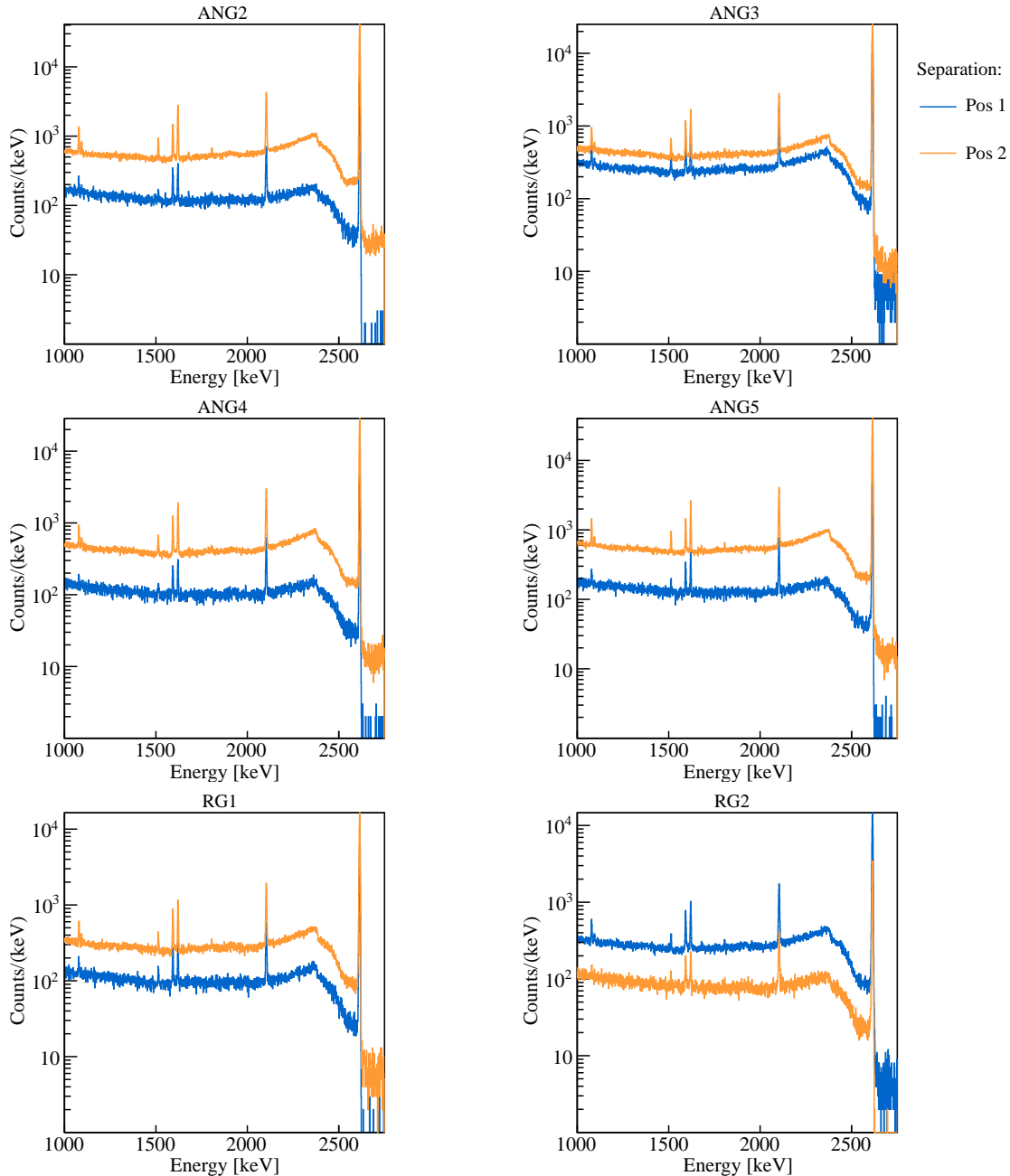
Figure 6.2: Separated energy spectra of the two ^{228}Th source positions 1 (blue) and 2 (orange) from table 6.1 for the combined 11 calibration measurements taken from January 24th 2012 to May 22nd 2012 and the six semi-coaxial germanium detectors.

Figure 6.1 shows for each of the 11 calibration runs (with the setup configuration considered for the Monte Carlo simulation on the ANN classifier) a scatter plot of the energy interval $1000 - 2750$ keV as a function of time (top half). The rearrangement of the source location can be clearly observed by the corresponding change in the population density illustrated by the colour code ranging from blue (low region) to red (high region, i.e. at γ-lines or Compton edge) shades. Here the measured data are presented exemplarily for the ANG2, since this detector apparently exhibits the most distinct variations when altering the positions of S1, S2 and S3. Conveniently the exact time of the source adjustment can be identified by, for example, the count rate within the full energy peak (FEP) of the ^{208}Tl-decay at the energy of 2614.5 keV, as histogrammed in the lower half of figure 6.1 after a statistical subtraction of the background using events in energy side bands to the left and right of the γ-line. Consequently, by tracking the rate of the high energetic peak, also the separate energy spectra can be easily computed for the different source locations.

Figure 6.2 illustrates the, when applying the above described method, disentangled energy spectra of the two positions 1 (blue) and 2 (orange) stated in table 6.1 for the combined 11 calibration runs obtained in Run $28 - 32$ and all six semi-coaxial detectors. For the data quality selection, previously an anti-coincidence cut has been performed. These separated experimental data will be further used in the next section 6.2 to derive the exact source distance to the germanium diode array.

6.2 Determination of source position

In compliance with the procedure applied to the experimental data, also for the pulse shape simulations events located in the 2614.5 keV DEP of ^{208}Tl at 1592.5 keV and from the 1620.7 keV FEP of ^{212}Bi from the thorium calibration data are planned to be provided as signal and background class samples for the ANN training procedure. Since the location for the interaction points of energy deposition within the detectors of the array has a huge impact on the measured charge trace and thus on the outcome of the PSD algorithm, it is of crucial importance to retrospectively identify the relative positions $1+2$ of the three ^{228}Th sources during the taken calibration measurements, which are unfortunately unknown. Therefore a detailed event simulation scan, including all the physical processes involved in the passage of γ-rays or charged particles through matter, was performed using the MAGE framework [Bos11], a software package based on GEANT4 [Ago03][All06]. In doing so, the finally found best fitting source locations and the provided corresponding event interaction points within the germanium crystals due to their radiation can be afterwards ideally used as input coordinates for the subsequent pulse shape simulation (see section 6.3).

6.2.1 Geometry and input parameters for MAGE

For the simulation campaign with variable source position, all parts of the GERDA setup were implemented in the MAGE software code as realistic as possible. This

includes the massive vault of rock sourrounding Hall A of the LNGS underground laboratory in Italy, as the experimental site, and other large scale hardware components, like the outer water tank, inner liquid argon cryostat and the clean room located close-by to the experiment. But also finer geometry structures, e.g. for the cabling or the support holders compounded of several individual parts, are considered. It is commonly known though, that only the cryostat interior and those objects in vicinity to the detectors, will noticeably affect the simulation results.

Figure 6.3 depicts a schematic view of the relevant geometrical parts taken into account when performing the MCS. As already mentioned in subsection 3.5.2, the final GERDA Phase I detector array consists of a three-fold string unit with in total nine semi-coaxial germanium diodes and one further 1-string arm housing two additional detectors. The latter has been removed and redeployed with five BEGe crystals of new geometry type at the beginning of Run 35 in the middle of the Phase I ongoings. Since for the simulations only calibration measurements between Run 28 and Run 32 are of importance, the former setup with an aggregate amount of 11 detectors, of which eight are manufactured of germanium highly enriched in the isotope ^{76}Ge, is considered. Out of these enriched semi-coaxial crystals, six diodes worked stable throughout the Phase I measurements and are thus considered for the final $0\nu\beta\beta$-analysis. For the respective geometrical dimensions of the different detectors within the array, the configuration parameters listed in table 3.2 have been used.
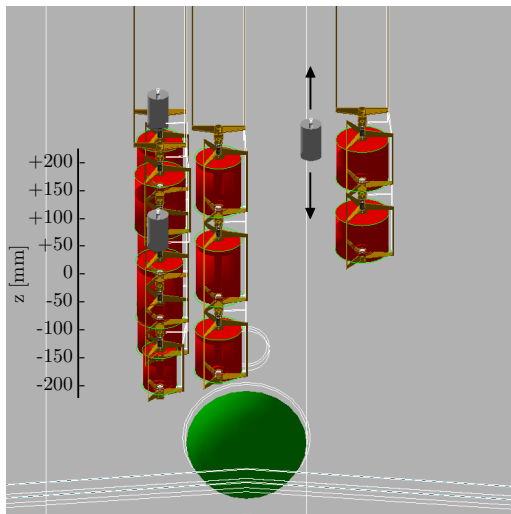
Figure 6.3: Schematic drawing of the 3-string (left) and 1-string (right) array setup of the Phase I measurements as present before the insertion of five new BEGe detectors in Run 35. In total 11 semi-coaxial detectors are deployed, eight enriched in the isotope ^{76}Ge, out of which six are used for the $0\nu\beta\beta$-analysis. Also visible are the simulated three ^{228}Th calibration sources (white color code) on top of their massive thantal absorbers (gray cylinders), here localized all at the same height. Graphical output created with "OpenGLImmediateX" by GEANT4.

Also visible in figure 6.3 are the three ^{228}Th calibration sources, each on top of a thantal absorber with a diameter of 35 mm and a height of 60 mm, here denoted by the gray cylinders, that acts as effective shielding while being lifted up into the parking position, roughly 5.2 m above the detector array. The thorium sources itselves are of only moderate size of around a few millimeters expansion from where the event simulation is homogeneously emanated, respectively. In order to properly conduct the Monte Carlo simulation, several properties concerning the calibration sources, besides their explicit geometries, have been incorporated:

- As is well known, the three sources at S1, S2 and S3 exhibit different radiation activities. Hereby the most recent values obtained before their installation into the GERDA experiment can be found in table 3.5 in units of [kBq] - that also enter the simulations - along with the respective date of the measurement.

- For the two different adjustments of the three sources, a specific relative distance according to 550 mm between the more highly situated S1 and S2=S3 is taken into account for position 1, whereas for position 2 they are instead all set to the same height S1=S2=S3.

- With the change from position 1 to position 2 the source S1 is constantly lowered by a fixed value of 200 mm, vice versa S2 and S3 are lifted by 350 mm.

- The duration of the sources at the two positions 1+2 are weighted pursuant to the experimentally derived numbers stated in the last column of table 6.1.

- To scan all possible source locations, the vertical offsets between S1, S2 + S3 (with the fixed relative distances described above) and the detector structure are varied from far above the upper edge towards the lower edge of the germanium crystal array and beyond in steps of 4 cm. In a reasonable region of roughly 10 cm width, where the event simulations features characteristics close to the experimental measurement, the step size is further reduced to 1 cm and additional computations are performed to collect more statistics. For instance, the explicit example given in figure 6.3 illustrates the corresponding source locations for position 2 with S1=S2=S3 at a height of +220 mm defined within the MaGe internal coordinate system. Also shown in the left margin of the figure is, for reasons of orientation, the scale of the vertical axis.

- For the consecutive decay chain of ^{228}Th only contributions arising from the ^{208}Tl and ^{212}Bi isotopes are simulated, as these represent the only decay channels that emit high energetic γ radiation or electrons being able to reach the detectors.

6.2.2 Comparison of spectral and γ-line intensities

With the aim to select those calibration source positions from the simulations that describe the measurements the best, it is intended in this subsection to compare the spectral shape of the Monte Carlo results with the one from the experimental data. Apparently the count rate of individual γ-lines or the overall energy spectrum, is very sensitive to the location of the thorium radiation origin. Therefore a reasonable way to define the correct relative distance of the three ^{228}Th sources to the detector array can be accessed by the fractional share of particular single germanium diodes of the total event count number of all combined crystals.

In the process of the proposed analysis method the four most prominent line structures at the energies of 1592.5 keV for the ^{208}Tl double escape peak, 1620.7 keV
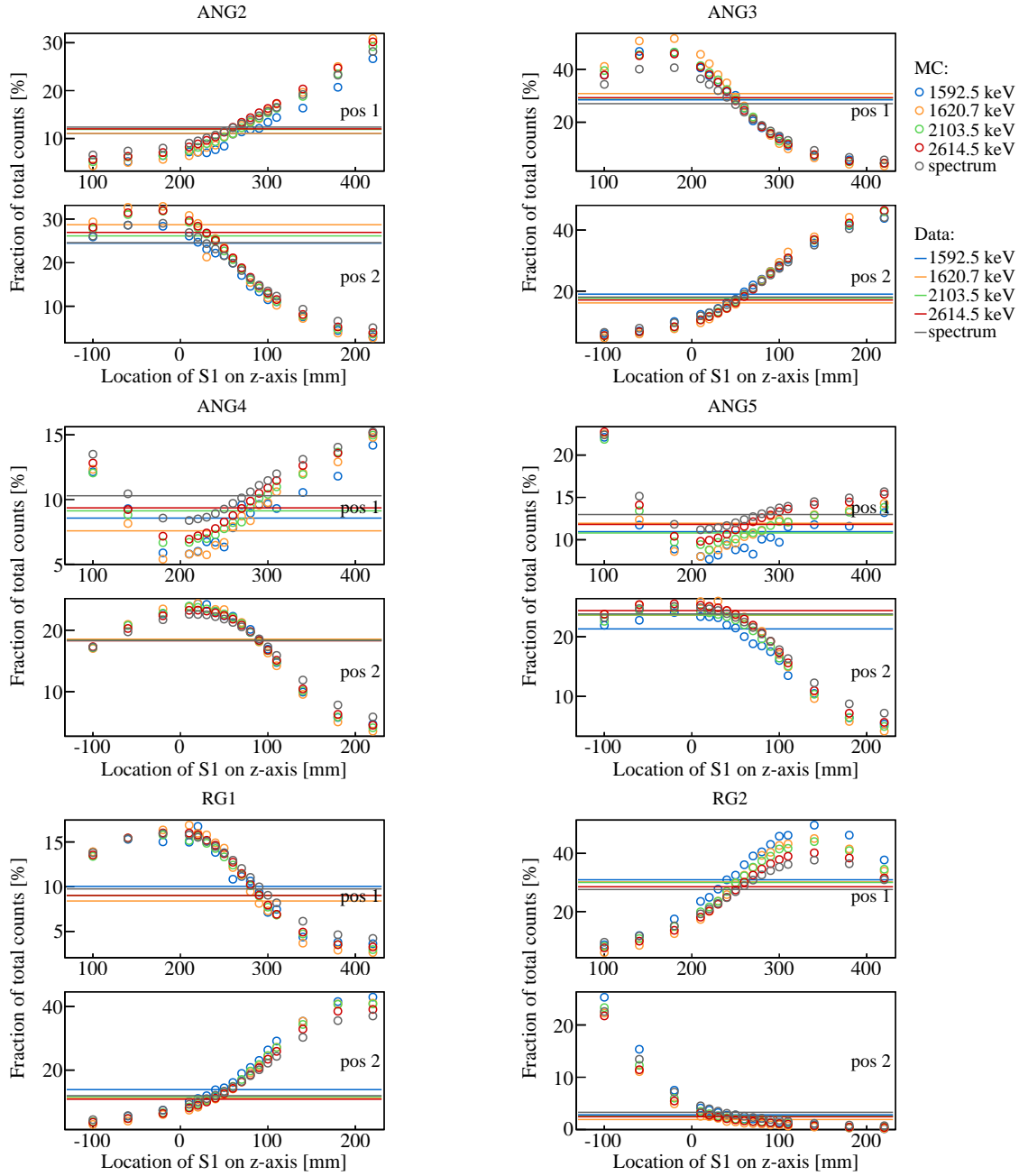
Figure 6.4: Fractional part of the six semi-coaxial detectors on the total event count number from all combined germanium diodes versus the simulated ^{228}Th calibration source position of S1. Both of the two different source locations are depicted, with S2=S3=S1−550 mm for position 1 (upper part) and S1=S2=S3 for position 2 (lower part). Horizontal solid lines denote the respective count ratios from the experimental data for the four predominant γ-lines at the ^{208}Tl DEP (blue), the ^{212}Bi FEP (orange), the ^{208}Tl SEP (green), the ^{208}Tl FEP (red) as well as the spectrum within the energy interval $1000 - 2750$ keV (gray). Hollow circles represent the equivalent values from the Monte Carlo campaign.

for the ^{212}Bi full energy peak, 2103.5 keV for the ^{208}Tl single escape peak and 2614.5 keV for the ^{208}Tl full energy peak as well as the whole spectrum within the interval $1000 - 2750$ keV are investigated separately for the two different positions 1+2. When counting the contents of the monoenergetic γ-lines, the Compton events under the peak are specifically subtracted by scaling linearly the event contributions from energies below and above the peak. Further only the six enriched semi-coaxial detectors that are also considered for the final $0\nu\beta\beta$-analysis of the GERDA experiment are regarded for this studies.

Figure 6.4 contrasts the results for the above suggested computation of the real data and different simulation runs performed with varying source locations for the semi-coaxial detectors of interest as well as the two different positions 1 (upper half) and 2 (lower half). Hereby for each diode the fraction of counts on the total sum over all detectors - that of course amounts by definition to 100 % - is plotted as a function of the calibration source positions. As reference S1 is chosen and its corresponding vertical alignment in z-direction according to the MAGE output is denoted. Whereas the relation S2=S3=S1$-$550 mm applies for the first position, in the second position the sources are all at the same height yielding S1=S2=S3. Values calculated from the experimental measurements are illustrated as horizontal lines given with a colour code that signifies the corresponding numbers attributed to the ^{208}Tl DEP (blue), the ^{212}Bi FEP (orange), the ^{208}Tl SEP (green), the ^{208}Tl FEP (red) and the spectrum (gray). Equivalent results from the simulations are signified instead by hollow circles subjected to the same colour denotation. Prior to all calculations an anti-coincidence selection has been exercised on the data and MCS.

In conformance with all semi-coaxial detectors and both separated data sets owing to a readjustment of the source, the locations that match the data the best can be roughly identified to $S1 = 250$ mm or $S2 = S3 = -300$ mm for position 1 and $S1 = S2 = S3 = 50$ mm for position 2. Some data sets, as for example, the second position of the ANG2+4 or the first position of RG1, do thus also imply slightly different locations shifted to either higher or lower values depending on the considered case. It is assumed though that this minor discrepancies are related to a skewed/twisted orientation of the detector array hosted by the 3-string arm towards the three thorium calibration sources during the Phase I data taking of the GERDA experiment if compared with the simulations. Another conceivable effect explaining this differences may also be introduced due to pile-up rejected events in the experimentally obtained calibration data, which have not (yet) been considered within the simulations since the embedded relative error is considered to be negligible small at the very low %-level. Taking this circumstance into account, the systematic uncertainty of the source position is estimated to be of the order ± 40 mm in vertical direction.

6.2.3 Output used for signal modeling

Figure 6.5 displays for all six semi-coaxial detectors of Phase I considered in the $0\nu\beta\beta$-analysis the simulated ^{228}Th calibration spectrum (blue) appertained to the
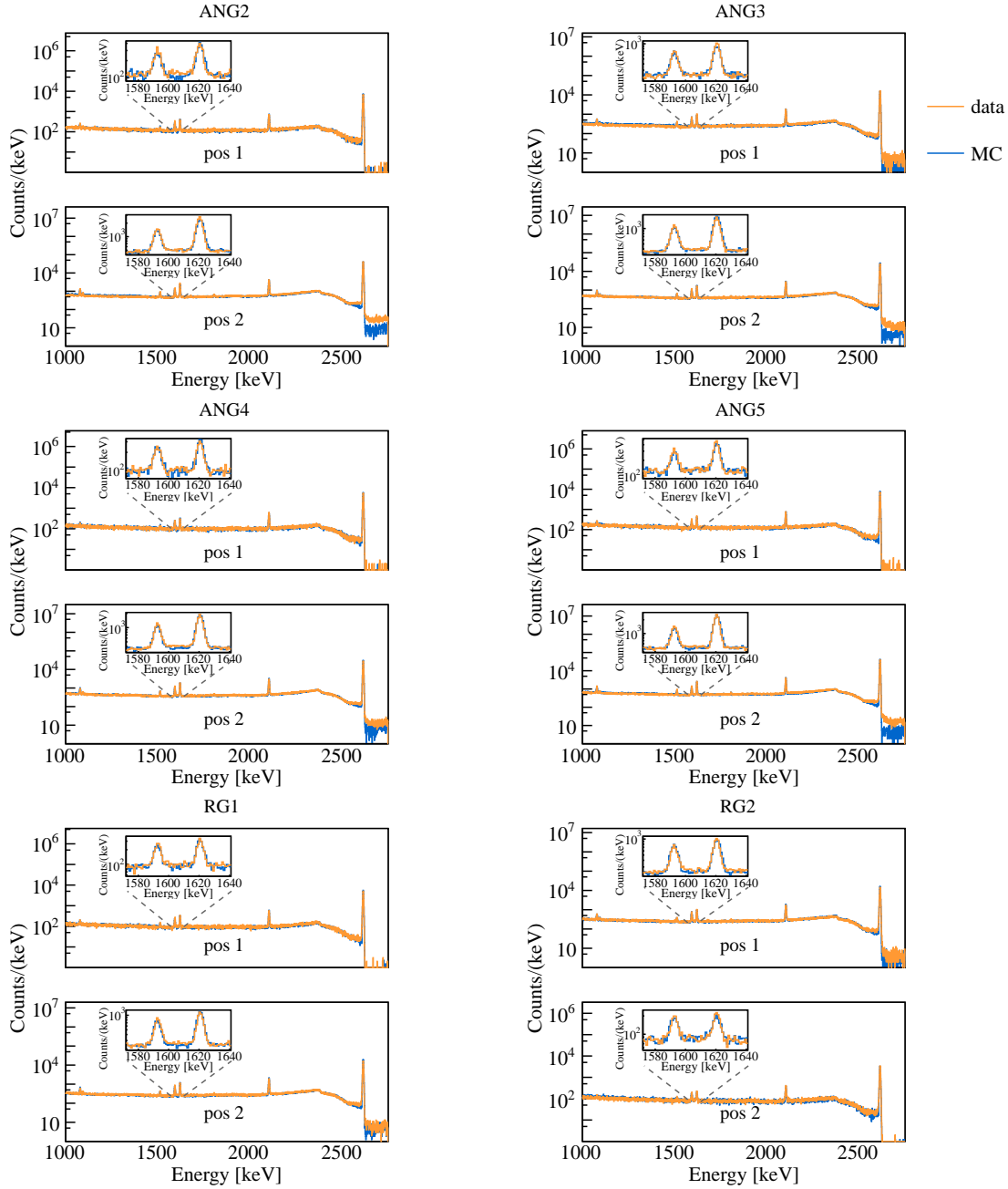
Figure 6.5: ^{228}Th calibration spectrum from measurements taken between January 24th 2012 to May 22nd 2012 (orange) and from Monte Carlo calculations conducted with the most concurring source locations at S1 = 250 mm, S2 = S3 = −300 mm for position 1 and S1 = S2 = S3 = 50 mm for position 2. For all semi-coaxial detectors the simulated spectra have been individually smeared by a Gaussian distribution with an energy dependant $FWHM$ corresponding to the experimental resolution. A small inset on the top left margin shows a close-up of the ^{208}Tl DEP at 1592.5 keV and the ^{212}Bi FEP at 1592.5 keV used as signal and background samples for the training of the ANN classifier, respectively.

set of source locations for S1, S2 + S3 and the two positions 1 + 2, which features the highest conformity with the data (as figured out in the last subsection 6.2.2). Further the corresponding experimental measurement is overlayed (orange). To give a meaningful comparison, the histograms are thereby scaled by means of the total event number in the overall energy range.

With due regard to the fact that the energy spectra received from the Monte Carlo simulations exhibit an infinitely accurate resolution, they have to be additionally smeared with realistic values though for reasons of comparability. For this purpose a Gaussian distribution with an energy dependant $FWHM$ derived for each detector individually from the data obtained between January 24th 2012 to May 22nd 2012 has been folded into the MCS spectra.

In general, for all different diodes and source setups (position 1 is shown in the upper half, position 2 in the lower half of the figure) a good agreement between the two spectral shapes can be observed. This resemblance does not only account for the coarse shape, but also applies in detail for single γ-line structures at different energies. Exemplarily, the small inset on the top left margin depicts a close-up of the energy interval containing the ^{208}Tl double escape peak at 1592.5 keV and the ^{212}Bi full energy peak at 1620.7 keV. Since events from an energy window of $\pm 1 \cdot FWHM$ width centered around these two lines will serve as signal and background training samples for the supervised learning process of the neural network classifier, this particular region and a possible difference between the data and MC is of peculiar interest. Consequently no sizeable discrepancies among the two data sets have been identified. Thus it is assured that the interaction points of energy deposition, also provided by the MaGe software along with the corresponding events within the energy spectra, describe the experimental data very well and can be reasonably used as input for the pulse shape modelling discussed in the next section.
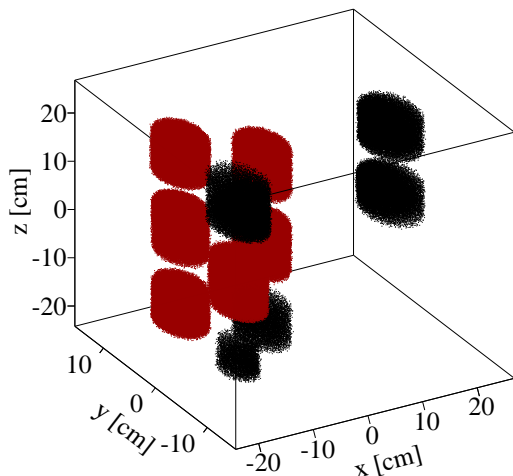
Figure 6.6: Points of energy distribution within the Phase I detector array as present in Run 28 − 32 according to the MaGe output resulting from the Monte Carlo simulation with the optimal ^{228}Th source position, that fits the experimental data the best. Interaction location within the six semi-coaxial diodes considered for the $0\nu\beta\beta$-analysis are illustrated with red dots, black dots signify those interactions taking place in the remaining crystals.

Figure 6.6 hereby visualizes the obtained corresponding interaction locations inside the individual semi-coaxial diodes of the Phase I germanium detector array setup before the insertion of the BEGe crystals in Run 35 for the events simulated with the deduced correct calibration source positions. Energy depositions occurring

within the detectors considered for the final GERDA $0\nu\beta\beta$-analysis (namely ANG2, ANG3, ANG4, ANG5, RG1 and RG2) are emphasized by red dots. Interaction points with energy deposited in one of the other GTF diodes made of natural germanium or those of enriched germanium composition discarded due to an unstable behaviour are instead marked as black dots.

6.3 Pulse shape simulation

This section describes the procedure employed for the pulse shape simulations performed in order to determine the efficiency of the neural network selection developed in this thesis on the $0\nu\beta\beta$-signal. Therefore the found interaction locations inside the germanium detectors as illustrated in figure 6.6 are used as input for a subsequent simulation of the associated pulse shapes. The explicit computation of the electric field inside the Ge crystal, the dynamics of the electron/hole charge carriers generated inside the active detector volume and the induced signals on the electrodes by the charge movement have been conducted with a modified version of the IKP Detector Simulation and Optimization approach, called AGATA Data Library (ADL) package, placed at the disposal in [Bru12] by courtesy of the AGATA Collaboration. Particularly the most recently supplied release 3.0 is utilized.

The ADL software is based on a library programmed in C and provides access to a simulation of the position sensitive detector feedback to γ-ray interactions. In general the source code for the electric field simulation inside the detector volume thereby relies on a Finite Element Method (FEM) to solve the partial differential equations, like for instance the Poisson equation [Akk12]. Conveniently these calculations can be adapted to any user specified detector geometry mapped by an as well variable 3D grid, making the ADL software also a very advantageous tool for other HPGe experiments of different setup construction besides its original purpose of use within the AGATA collaboration.

In GERDA semiconducting germanium detectors of p-type are deployed, where the p-n junction is formed at the border of the roughly $1\,\mathrm{mm}$ thick donor-doped surface mantle, the so-called n+ layer. Typically at applied operational bias voltages, which are usually higher than the detector specific depletion voltages, the inner bulk material is fully depleted of free charges and thus becomes an active volume, while the outer n+ layer or dead-layer mostly retains electrons in the conduction band (anode). On the contrary, the very thin acceptor-doped p+ layer, covering for semi-coaxial detectors the whole surface of the inner bore hole, represents the read-out electrode (cathode). Accordingly the system of equations with the set of boundary conditions, as given by the potentials V_{cathode} and $V_{\mathrm{anode}} = V_{\mathrm{bias}}$ on the conductive electrodes, is defined by:

$$
\begin{aligned}
\nabla^2 \phi(\boldsymbol{r}) &= -\rho(\boldsymbol{r})/\epsilon \\
\phi|_{\mathrm{cathode}} &= V_{\mathrm{cathode}} \\
\phi|_{\mathrm{anode}} &= V_{\mathrm{anode}} \, .
\end{aligned}
\tag{6.1}
$$

Here r denotes the position within the crystal, $\phi(r)$ the electric potential, $\rho(r)$ the charge density distribution proportional to the net p-type impurity distribution in the active volume and ϵ the absolute permitivity of germanium. Further the potential present at the surface surrounding the regarded electrode is given by the quantities $\phi|_{\text{cathode}}$ and $\phi|_{\text{anode}}$, respectively. The results at each point in the given detector volume are then stored in matrices and later on recalled again when generating the time evolution of the position dependent pulse shape response as concluded by the Shockley-Ramo theorem, equation 3.14, and the trajectories of the electrons/holes through the weighting field distribution towards the electrodes. Thereby the movement of charge carriers within the active volume is computed by using the 4-th order Runge Kutta integration method with adaptive stepsize (a detailed explanation of the exact working principle can be looked up online at [Pre95]).

For the specific usage on the GERDA experiment, the ADL software was first adapted, validated and successfully used within the work presented in [Sal15]. As one field of application, elaborate simulations have been accomplished in the context of the HEROICA characterization measurements for the newly commissioned BEGe detector type. It was found that the anticipated simulated pulse shapes describe the behaviour of the experimental data, i.e. A/E cut efficiency or rise time distributions, with sufficient agreement.

6.3.1 Geometry and input parameters for ADL

With the aim to ensure the pulse shape simulations being prosecuted as true to the original as possible, a number of empirically established features and presupposed input parameters from theoretical considerations have been implemented into the signal modelling algorithm, as will be successively addressed in the following list:

- Each of the six enriched semi-coaxial germanium detectors has been added individually to the source code according to the corresponding geometries and dimensions, i.e. in terms of height, diameter, dead layer thicknesses, depth and radius of bore hole or all groove parameters, as collected in table 3.2.

- A grid size of $0.5\,\text{mm}$, which represents a fair compromise between the length of computation time and accuracy of the implemented structures, was chosen. Both, the detector geometry as well as the electrical field calculations are defined and performed over this user-supplied 3-dimensional mash with the given spatial distance between two adjacent vertices, whereas the values for the subsequent charge carrier transportation generating the pulse shapes are interpolated for consecutive points of the rectangular grid.

- As the only unavailable detector parameter, the impurity concentration of the Ge crystal is needed to be derived retroactively from the characteristical behaviour of the single diodes. Therefore a conservative estimation is made by comparing the experimentally measured depletion voltages of the GERDA

Phase I diodes from [Bar09b] with respective simulations performed for varying numbers of impurity concentrations. In particular the lowest possible values for which the detector volume is just about completely depleted are taken as input parameters. A similar procedure has been first proposed in [Gon03] and already successfully deployed multiple times within the GERDA Collaboration [Ago11c][Ago13b].

- Since no further information are available (as already mentioned in the preceding item), a homogeneous impurity concentration is formally - but not necessarily correctly - assumed to be distributed in the germanium, eventhough the program would in principle also allow to import a gradient progression within the volume. It is known that the distribution of space charge across the height and radius of the crystal volume noticeably affects the computation of the electric field and thus the resulting charge trace used for the ANN pulse shape selection algorithm. On that score, it is of basic importance that these data are acquired and considered in more detail in future investigations.

- For the bias voltage $V_{\mathrm{bias}} = V_{\mathrm{anode}}$ applied on the detector anode during the data taking of Phase I, the numbers given in the last column of table 3.2 enter the FEM calculations. On the other hand, for the cathode a value of $V_{\mathrm{cathode}} = 0\,\mathrm{V}$ is assumed.

- The parameters for the charge carrier mobilities are taken from [Bru06a][Bru06b] [Bru06c]. Note that the electron as well as hole velocity anisotropy in HPGe detectors (as deployed in the GERDA experiment) do create significant rise time effects and hence relevant for the support of the neural network pulse shape analysis by dedicated simulations.

- The interaction points as provided from the MAGE Monte Carlo software for the optimal source locations are used as input positions of energy deposition for the pulse shape simulations with the ADL package. Owing to the circumstance that both source codes underlie a different coordinate system, an additional transformation of the 3-dimensional vector positions is performed for reasons of compatibility.

- In case of a multi site event, arising due to several non-localized energy depositions taking place at different position within the active detector volume, the ADL simulation software is capable of processing the trajectories of the different created electron-hole pairs simultaneously. The finally resulting charge pulse of the detector event is then reconstructed by an energy weighted sum over all individual traces corresponding to each of the interaction points.

The general geometry and dimensions of the six semi-coaxial crystal structures integrated into the ADL program are shown along with the corresponding electric field potential simulated with due consideration to the above discussed input conditions in figure 6.7. The provided output contains, likewise to the measured data pulses

used for the PSD, a trace consisting of a number of 400 samples with a total length of $4\,\mu$s. Consequently, each sample accounts for a time interval of $10\,$ns width.
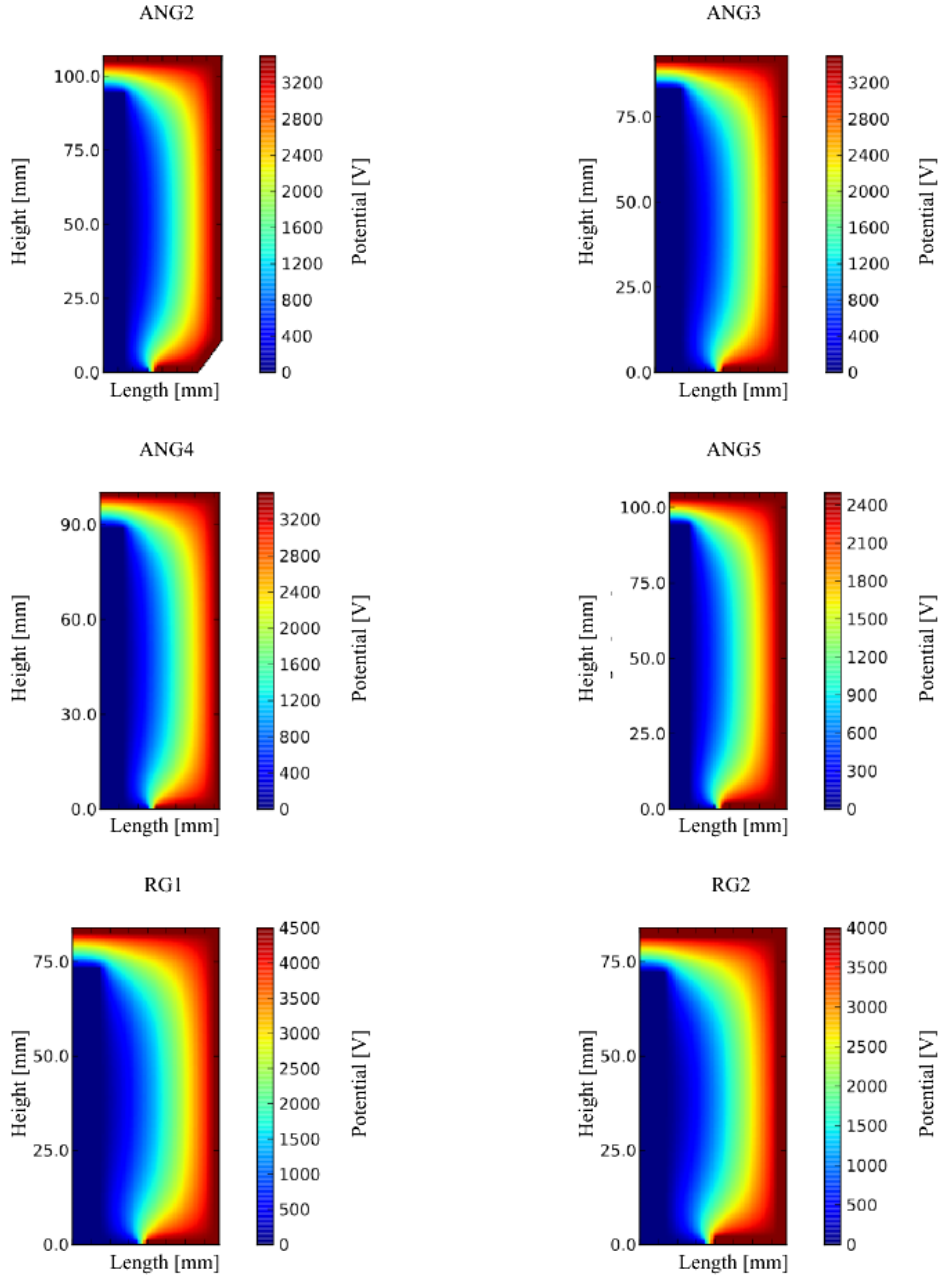
Figure 6.7: Electrical field potential of the GERDA Phase I detectors simulated with the ADL software program [Bru12] (originally developed by the AGATA Collaboration) for a vertical section of one half of the detector passing through the symmetry axis. All six semi-coaxial diodes used for the $0\nu\beta\beta$-analysis presented in [Ago13a] and this thesis are displayed. For the corresponding germanium crystal geometries and applied bias voltages, the values as quoted in table 3.2 are used.

6.3.2   Electronics response

Still the electric field simulation and the thereon based computations of the detector traces, do not take the impact of the read-out electronic hardware, such as the charge sensitive preamplifier, the digital sampling device or even the cabling from the detector array to the FADC-input channels, into account. A prerequisite to be able to compare the simulated charge pulse with the measured ones is, however, to also determine and include this missing electronics response function into the signal modelling. Previous works dealing with a similar issue, concluded empirically that a low-pass filter applied on the raw simulated trace, i.e. in [Ago13b] particularly a three-fold moving average filter of 30 ns is used, already allows to reproduce the effect originated from the electronics in satisfying agreement with the experimental data.

For the analysis presented in this thesis a different, more substantial, approach is anticipated though. For this purpose a comparison of the average charge trace from predominantly single site events of the double escape peak (DEP) occurring within an energy region of $\pm 1 \cdot FWHM$ centered around 1592.5 keV is prosecuted. Therefore the individual traces are first aligned according to their reference point at 50 % height of the maximal amplitude and subsequently summed up. Events attributed to the Compton continuum under the γ-line are further disentangled from the pulse form by subtracting a linearly scaled number of energy weighted traces from regions below and above the peak.

Figure 6.8 (top half) depicts the resulting normalized pulse shapes for the experimental measurements (without any shaping, e.g. by a moving window average filter) taken in Run $28 - 32$ (orange solid line) and the corresponding simulated sample as given by the original output of ADL software (blue solid line). In order to conveniently contrast the two average charge traces with each other, they are further shifted with respect to the beginning of the leading edges. Clearly a for different detectors more or less divergent course of the two curves can be observed especially at the uppermost region close to the end of the leading edge for higher rise times. Systematically, the averaged charge trace obtained from the simulations exhibits a much steeper slope.

In order to derive a general transformation function that can be afterwards also applied on single pulses provided by the ADL program, a Discrete Fourier Transform (DFT) over the whole trace length with 400 samples input has been performed for the averaged data and MC sets. The eventuated distributions are plotted for the frequency range up to 50 MHz in the lower half of figure 6.8 with the same color assignment as used previously. For the experimental measurement the frequency interval above about 10 MHz is exclusively characterized by a white noise, also named Johnson-Nyquist noise, created by the random thermal motion of charge carriers inside an electrical conductor, with a constant power spectral density. By applying the inverse DFT on the ratio of the data and MC contributions and thus converting the waveform from the frequency domain back into the time domain, the wanted
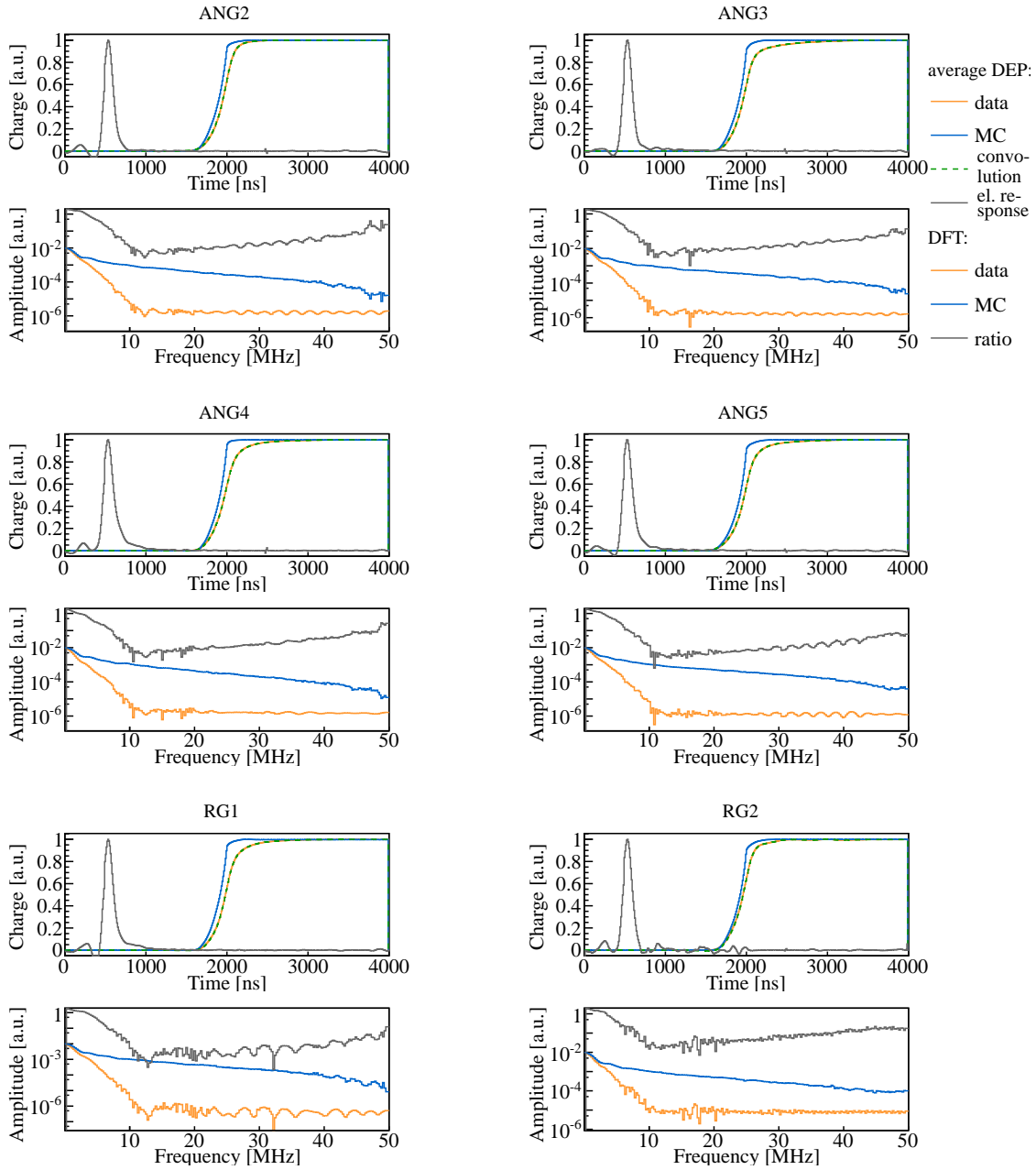
Figure 6.8: Top half: Average charge traces from predominantly SSEs within an energy region of $\pm 1 \cdot FWHM$ centered around the calibration DEP at 1592.5 keV for the data taken in Run $28 - 32$ (orange) and the corresponding performed simulations that do not consider any effects arising from the electronic devices (blue). Also shown are the electronics response (gray) extracted by the Fourier Transform and the resulting pulse form after being convolved with the signals derived from the Monte Carlo calculations (green dashed). **Bottom half**: DFT noise spectrum as a function of frequency for the experimental measurement (orange) and MC (blue), respectively, along with the ratio of these two curves (gray).

electronic response function can be conveniently extracted (both displayed as gray solid lines):

$$\text{electronics response} = \text{inverse DFT of } \frac{\text{DFT(data)}}{\text{DFT(MC)}} \ . \qquad (6.2)$$

Each of the simulated detector signals is consequently convolved with this "unwrapped" response function. The corresponding averaged pulse form is additionally overlayed in the upper part of the figure for the time domain (green dashed line) showing now an astonishing agreement with the trace derived from the experimental data, as desired.

6.3.3 Noise

To reproduce the electronic noise present in the experimental data, that is as well not considered in the preceding simulations with the ADL program, signals are taken from experimentally recorded baselines, i.e. non-triggered charge pulses with 100 MHz sampling frequency and a total length of $16 \cdot 10^3$ entries.

However, the approach of course requires the noise behaviour of the physics and the individual thorium calibration runs - as object of the performed Monte Carlo calculations - to be quite similar in terms of their amplitudes as well as temporal progresses. That this is actually the case can be easily demonstrated by figure 6.9, where the summed up power spectrum of the Fourier transformed charge traces as a function of time is compared for the background data (black) and the (bi-)weekly conducted measurements with closeby ^{228}Th calibration sources (red) for the different semi-coaxial detectors. Here the different data points denote average values taken in steps of 3 hours, which corresponds to the length/time span of the stored single raw data files. The integration interval is thereby chosen to lie between $1 - 10$ MHz, since for this region the by far dominant contributions to the noise spectrum are observed (common to the Discrete Fourier computation presented in figure 6.8 for the averaged charge pulses of the ^{208}Tl double escape peak events from Run $28 - 32$). Higher frequencies do, on the contrary, feature a negligible small constant spectral power density originated by white noise only and are thus not further considered. Apparently for all presented detectors, both data samples resemble each other in significant features, like for instance the time dependency, though the calibration measurements exhibit systematically higher values for the amplitude (especially for the ANG4) that exceed those for the background runs by roughly 20 % at maximum. Also observed is an abrupt and non-periodic recurrently increase of limited duration for the noise power integral showing up simultaneously, but in more of less intensity, for all six semi-coaxial diodes. This effect is attributed to a sharp, strong peak at 2.7 MHz with an unstable temporary nature in the frequency domain of the noise spectrum and, albeit not yet understood though, assumed to be most likely generated during the read-out process.

A critical issue, also necessarily to be included into this considerations, is the significant time instability of the noise behaviour observed throughout the data taking

of GERDA Phase I apart from the already evident detector dependencies. Hence for each germanium crystal a dedicated library of traces from only those physics runs measured between January 24th 2012 to May 22nd 2012, the respective time interval considered for the simulations presented is this chapter, is created.
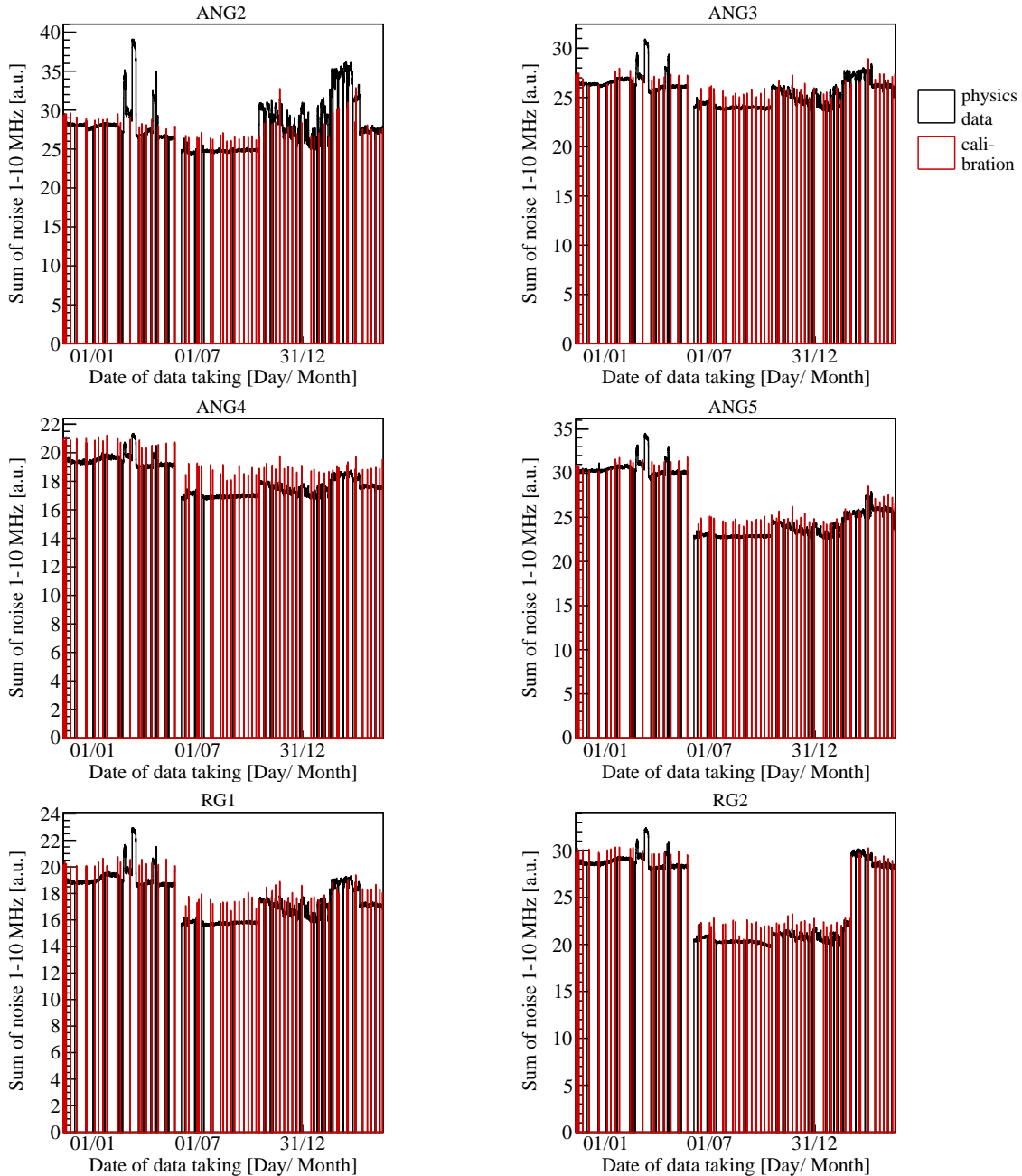

Figure 6.9: Integral between $1 - 10\,\mathrm{MHz}$ of the Fourier transformed charge traces recorded during the constantly ongoing data taking of the physics (black) and the regularly performed short ^{228}Th calibration (red) runs versus the entire Phase I period. Each data point signifies an average value taken for a time span of 3 hours. All six semi-coaxial detectors are shown. By courtesy of Bernhard Schwingenheuer.

To also account for possible crosstalk effects among the different detector channels, only the first half of the overall record length is devoted. This can be regarded as an adequate and effective measure, since the trigger is adjusted in such way, that the rise of the leading edge takes place in the second part of the trace.

Further the amplitude of the noise is normalized according to the experimental signal-to-noise ratio before being added to the simulated event signal with the convolved electronics response (previously derived in the last subsection 6.3.2 from averaged single site events originated in the ^{228}Th double escape peak). The finally generated output of the combined computations with the MaGe and ADL software is an ASCII file of signals similar to those that are experimentally obtained with the digital data acquisition system. Conveniently it is therefore possible to apply the very same analysis tools and ANN selection principles on both of the investigated data sets, experimental as well as simulated, to allow a meaningfull comparison and estimation of the $0\nu\beta\beta$ efficiency.

6.4   Training / testing of the ANN

Common to the event classification procedure presented in chapter 4 as the official pulse shape analysis technique for the GERDA Phase I measurements, the supervised learning of the neural network algorithm with the simulated charge traces and the reference data from Run $28-32$ is also conducted by supplied training/testing samples ideally consisting of signal- as well as background-like topology. Therefore likewise thorium calibration events originating from the ^{208}Tl double escape peak within the interval 1592.5 keV $\pm 1 \cdot FWHM$ as proxy of predominantly single-site character and the ^{212}Bi full energy peak at 1620.7 keV in the equivalent energy range of mainly multi-site nature, respectively, are chosen to serve as example classes.

Detector	Training sample	Number of events	
		data Run $28-32$	MC
ANG2	signal	11943	24101
	background	17801	39411
ANG3	signal	12371	28015
	background	15775	38240
ANG4	signal	9005	24506
	background	12351	38345
ANG5	signal	11057	25602
	background	15481	40226
RG1	signal	6976	18940
	background	8333	26338
RG2	signal	6480	13666
	background	7592	16447

Table 6.2: Event number of signal or background training samples of the multivariate pulse shape analysis for the experimental data taken from January 24th 2012 to May 22nd 2012 (e.g. Runs $28-32$) as well as the simulations performed with the MaGe and ADL software. The corresponding values are listed for all six semi-coaxial detectors. Further the collected statistics is in both cases expected to be sufficient enough to avoid the occurrence of overtraining (compare with table 4.2 for the single periods pI, pII and pIII of GERDA Phase I).

The resulting event numbers of the input samples ultimately used for the training and testing procedure of the six semi-coaxial detectors are summarized in table 6.2 for both, the experimental and simulated, data sets. When comparing the values with those of the three separate periods pI, pII and pIII of Phase I given in table 4.2, it becomes explicit that the statistics for the experimental measurements gathered during Run 28 − 32 is roughly of the same order of magnitude and thus just as sufficient enough to not suffer from any effects originated by overtraining.

For the MC the number of simulated ^{208}Tl and ^{212}Bi decays was chosen such, that the training samples sizes are on average even more than twice as big if compared with the measured data. This amount of processes event computations is assumed to represent a fair compromise between the effective calculation time accumulated by the different process steps accomplished with the MaGe, ADL or TMVA program one the one hand and preventing the occurrence of overtraining due to too less statistics on the other hand.

6.4.1 Event topology and distribution of simulated input samples

Since the event simulation performed with the MaGe software provides detailed information of the interaction points inside the active detector volume, a quantitative description of the different event topologies is facilitated by deploying the spatial distribution of the individual locations of energy deposition as a significant and unambiguous measure.

As has already been mentioned, the main idea of the pulse shape analysis approach used for the Phase I data, is based on the assumption that the time evolution of the charge traces from background events is significantly different to those of signal events. For example, in case of a $0\nu\beta\beta$-decay, as subject of the scrutiny within the GERDA experiment, the two emitted electrons create a charge cloud of only very small expansion (usually in the order of $\sim 1\,\mathrm{mm}$) where its entire energy is deposited. Such localized interactions inside the germanium detector are referred to as single site events (SSE). On the contrary, an incident background radiation originated by closeby naturally present radioactive contaminations, for instance in the detector support structure, the cabling or the surrounding liquid argon, interacts with the active germanium material via various modes of action (like Compton scattering, pair production, photoelectric absorption, etc. as addressed in subsection 3.2.2). This event type is accordingly generated by several separated, non-localized energy depositions and thus called multi site event (MSE).

The resulting differences in the drift paths and time dependent movements of the electron/hole charge carriers is directly conveyed in the final pulse shapes of the above described two event topologies owing to their diverse signal formation processes. These individualities in the time structure of the charge singals can then be directly exploited by the neural network classifier to extract and effective event selection algorithm. So much for the theory the applied pulse shape discrimination relies on.
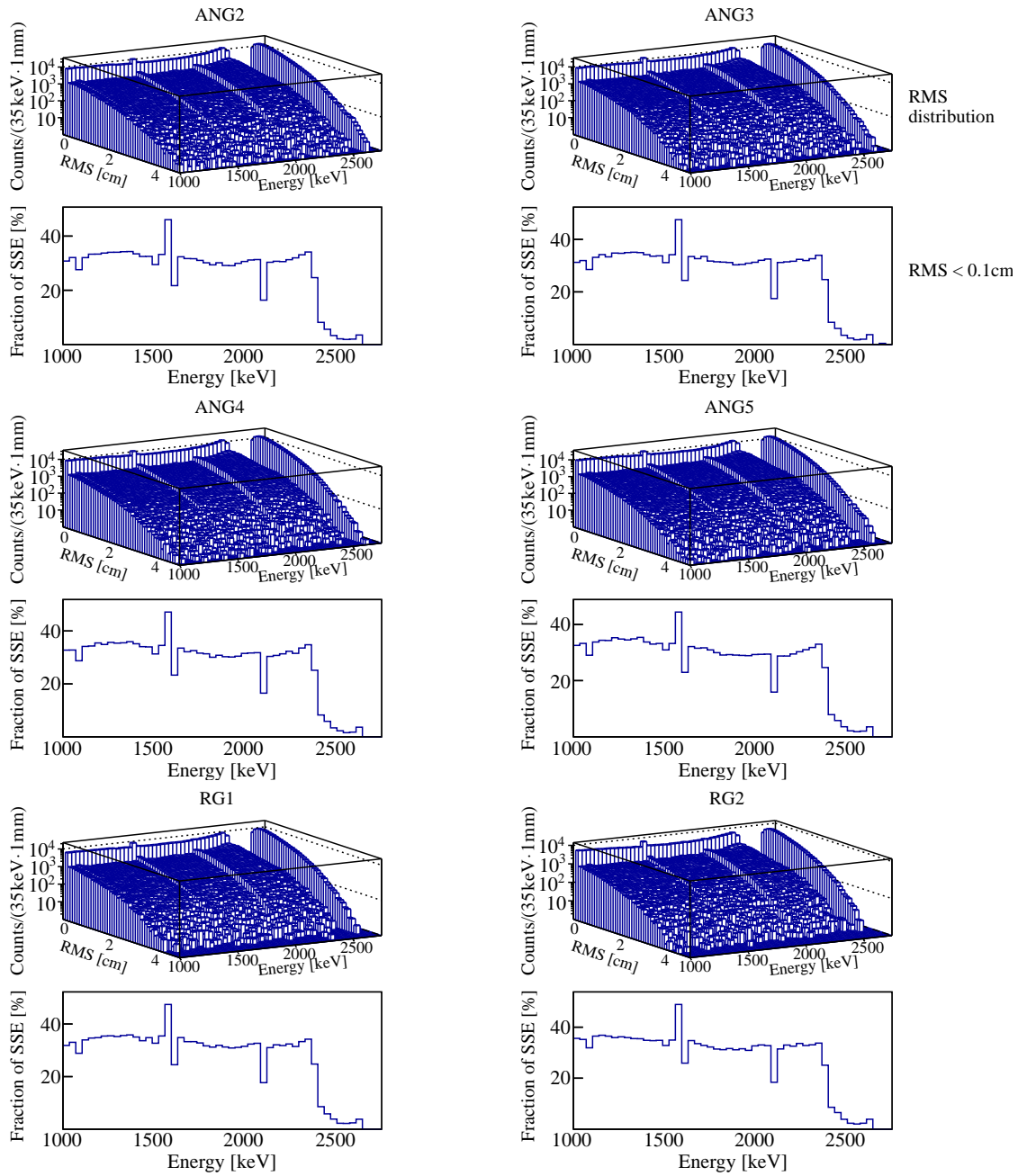
Figure 6.10: Top half: Simulated event distribution as a function of energy from $1000\,\text{keV}$ to $2750\,\text{keV}$ and the energy weighted root-mean-square (RMS) for the various interaction points of energy deposition within the active volume for the six semi-coaxial detectors. Therefore the locations of the three thorium calibration sources that yielded the best agreement with the experimental measurement of Run $28 - 32$ are used. **Bottom half:** Fraction of signal-like SSEs of the total event number in units of [%] as a function of the energy. Hereby the share of single site events in the spectral course is defined by the distribution with RMS $< 1\,\text{mm}$.

To check whether the data samples from the ^{208}Tl DEP at 1592.5 keV and the ^{212}Bi FEP at 1620.7 keV selected for the training of the ANN estimator do actually represent an expressive, veridical sample of signal-like SSEs and background-like MSEs, respectively, the position sensitive information obtained from the simulation of the ^{228}Th calibration spectrum performed with MAGE program can give some revelatory indications.

Figure 6.10 (top half) histograms the frequency of occurrence as a function of energy in the interval $1000 - 2750$ keV and the energy weighted root-mean-square

$$\mathrm{RMS} = \sqrt{\frac{1}{\sum_i E_i} \sum_i \left[(x_i - \overline{x})^2 + (y_i - \overline{y})^2 + (z_i - \overline{z})^2 \right] \cdot E_i} \qquad (6.3)$$

for each event generated by the Monte Carlo calculations. In the above relation the i various interaction points (x_i, y_i, z_i) with energy deposition E_i inside the detector volume are attributed to a barycenter $\boldsymbol{r} = (\overline{x}, \overline{y}, \overline{z})$. Hereby those locations of the three thorium calibration sources that correspond the most to the experimental measurements of Run $28 - 32$ (see subsection 6.2.2) are utilized. From the 3-dimensional depiction, the share of single site events in the spectral course can be easily recognized by the distribution within the first ~ 1 mm on the RMS axis, whereas higher values for the spread of the energy deposits are more likely attributed to a detected multi site event. Interestingly, for the Compton continuum generally a rather constant, almost energy independent, partition of the two event topologies is observed.

However, regions in vicinity to the monoenergetic lines of the ^{228}Th spectrum exhibit a different, less uniform systematics reflecting their dissimilar event composition. This property is, considering the chosen binning and logarithmic scaling of the z-axis, more particularly visible for the $4-5$ most prominent γ-lines. On one side, the double escape peak that serves as signal sample for the supervised classifier learning procedure, features in accordance with the expectations an enhanced fraction of SSE. On the other side, all other predominant peaks - e.g. the adjacent FEP from ^{212}Bi, used as background proxy for the ANN training, and the ^{208}Tl SEP at 2103.5 keV as well as FEP at 2614.5 keV - show a broadened distribution up towards higher values for the RMS and hence a tendency to an increased spread of interaction points with energy deposition, which is in good agreement with the made assumptions where they are of basically MSE nature.

The impression that the monoenergetic γ-lines - apart from the Compton continuum and bremsstrahlung effects - do indeed consist of events of either singe site (for DEP) or multi site (for SEP and FEP) topology, is further supported by the lower half of figure 6.10 illustrating the fraction of signal-like SSEs with RMS ≤ 1 mm of the total event number in units of [%] as a function of the energy. Again the double escape peak at an energy of 1592.5 keV shows a much higher share of events with localized energy deposition, especially if compared to the reduced fraction of the other single escape or full energy peaks composed of predominantly background-like events resulting from non-localized interaction locations inside the detector material. It should be reminded though that the γ-line intensities depend on the bin size of the
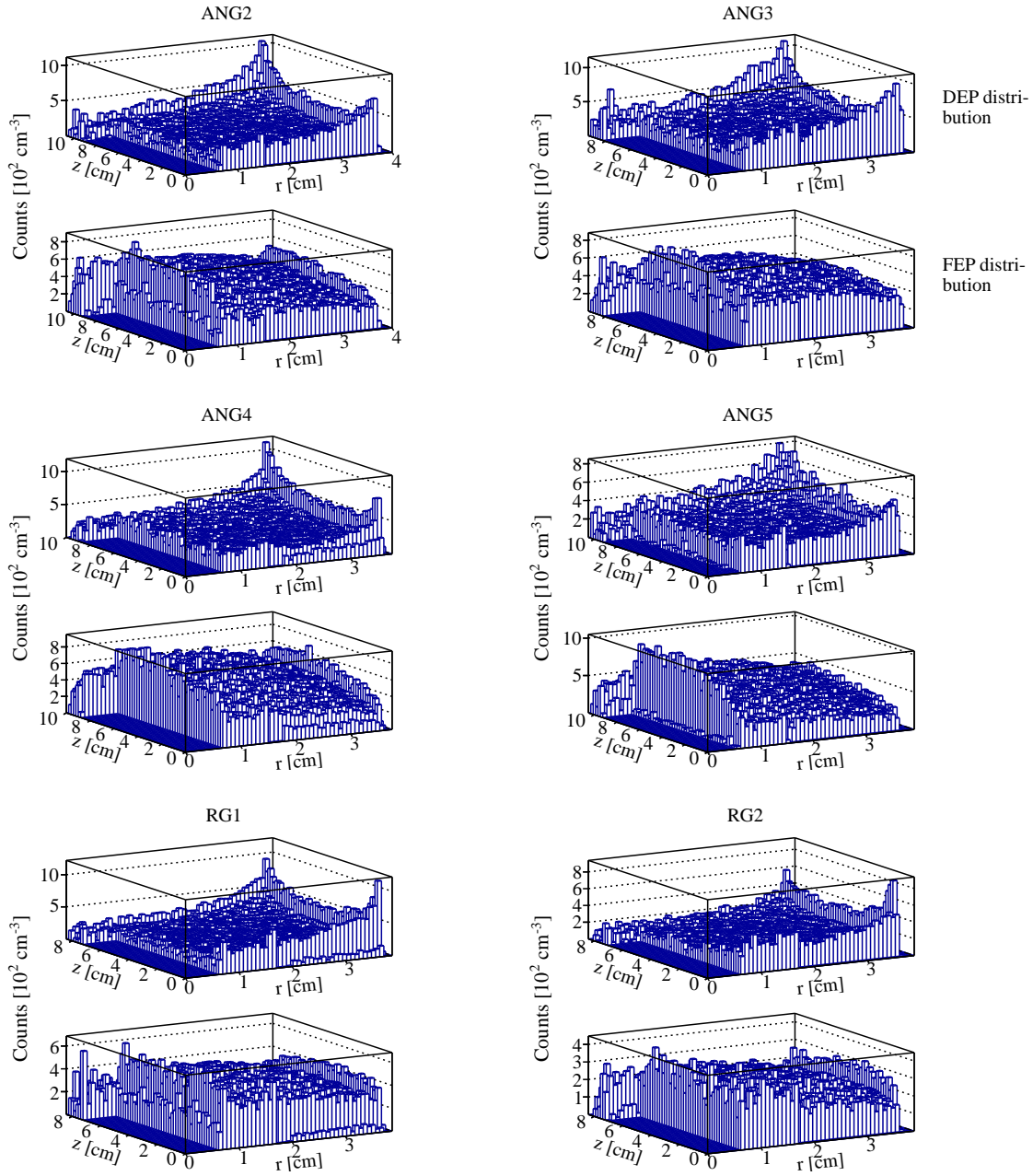
Figure 6.11: Simulated distribution of energy weighted barycenters of interaction points with energy deposition within the six semi-coaxial germanium diodes as a function of the detector height and the radial distance from the center. Both γ-lines used for the training/testing of the artificial neural network classifier, the DEP at 1592.5 keV of ^{208}Tl (top half) and the FEP at 1620.7 keV of ^{212}Bi (bottom half), are shown. Effects from the Compton continuum have been statistically subtracted by linearly scaling events from the energy side bands below and above the peak. The number of counts is further normalized by the volume and hence given in units of [cm^{-3}].

spectrum, which exceeds with a width of 35 keV by far the experimentally achieved resolution (exposure weighted average = 4.8 keV) folded into the Monte Carlo computations, resulting in an alleviation of the peak amplitudes within this particular depiction. Anyhow, the increased amount of SSEs contained within the DEP is also already visible with respect to the Compton continuum assembled of a mixture of single site and multi site events.

Consequently, the conducted Monte Carlo simulations do qualitatively and quantitatively support the pulse shape discrimination approach developed in this thesis and applied for the official $0\nu\beta\beta$-analysis of the GERDA Phase I data. In particular it has been proven, that events originated from the ^{208}Tl double escape peak and the nearby ^{212}Bi full energy peak indeed serve as reasonably proper proxy samples for the signal and background event classes supplied for the training process of the ANN algorithm, though still suffering from an underlying Compton continuum of mixed composition.

At this point it should be also mentioned that the relatively constant and energy independent fraction of single site events characterizing the Compton continuum also implies the validity of the energy correction procedure employed on the neural network classifier output. As previously explained in subsection 4.4.1 most of the detectors featured a systematic drift of the classifier variable intensity for different energy regions. To be more precise, the right falling edge of the ANN response distribution is continuously shifted to lower qualifier values for increasing energies. Apart from a general energy dependency introduced by the multivariate pattern recognition method such a behaviour can be in general also simply accounted for by a SSE share that decreases with the energy. Consistently, the higher the considered slice of the energy interval, the less dominant the part of signal-like events attributed to larger qualifier values would become in the context of the overall Compton dispersion and appear like a drift of the to the left, as observed for the data. Since the Monte Carlo computations revealed the percentual amount of single site events to be nearly constant with energy for all germanium crystals, whereas the experimental data instead revealed an energy dependent behaviour that as well varies from detector to detector, this can not be the case though, making the adapted energy correction a reasonable and compulsive practice.

Another critical issue arising with the choice of the training or testing samples for event classes and that can be easily investigated by means of the data obtained from the Monte Carlo simulations, is that the distribution of the associated signal event class proxy may apparently not be exactly homogeneous inside the detector material, as it is for the $0\nu\beta\beta$-decay under investigation. According to the particle interaction processes in matter, for the DEP used as SSE sample the chance of the two 511 keV photons to escape is larger at the corners. Thus conceivably a volume dependency of the classifier is introduced such that instead of finding single site events, much rather those situated at the outer surface are selected. In order to give a visual cross check the distribution of the energy weighted barycenters of the individual events as retrieved from the MaGe Monte Carlos are shown as a function of the detector

height and the radial distance from the center in figure 6.11 for the two γ-lines used for the supervised learning of the neural network: the DEP at the 1592.5 keV of ^{208}Tl (upper half) and the FEP at the 1620.7 keV of ^{212}Bi (lower half). The corresponding pictures are thereby provided for all six semi-coaxial diodes with the effect from the Compton continuum being disentangled by statistically subtracting events from the energy side bands to the left and right. Further the quantity plotted on the z-axis has been scaled to the volume normalized number of counts in units of [cm^3].

As expected, the DEP events are - eventhough not strikingly different from homogeneity - verily preferably located in vicinity to the outer surface of the detector, since there the annihilation photons have a higher probability to escape from the active volume. On the opposite, events from the FEP tend to have their barycenter being situated in the middle of the detector bulk. Taking these distributions of the deployed training samples into consideration, a volume dependent sensitivity on the event selection by the ANN classifier is assumed to be indeed a critical issue to some extent (for more details on the quantitative outcome see the upcoming section 6.6.2).

6.4.2 Evaluation of results from data and MC

When performing the training of a specific multivariate classification method, or as in the present situation the artificial neural network algorithm, with specifically supplied data samples of known event class, it is peculiarly important to thoughtfully check the result of the supervised learning process for any kind of overtraining. In case of occurrence this effect would lead to a seeming increase of the classification sensitivity over the actually achievable performance and is therefore needed to be avoided.

A potential strategy to detect overtraining is, for example, provided by a simple comparison of the discrimination sensitivity extracted from the training with those obtained from the dedicated test set. Such a test on the ANN is depicted in figure 6.12 for each of the semi-coaxial detectors and sample sets from experimental data taken in Run $28 - 32$ (upper half) as well as Monte Carlo calculations (lower half). Marked with filled and hatched area are the classifier response distributions based on the test sample. Hollow circles instead denote the corresponding dispersion from the training sample. Further events originating from the supplied signal or background samples are illustrated in blue and red color, respectively.

Obviously no overtraining can be observed for any of the enriched germanium crystals. This accounts for the measured data as well as for the conducted simulations. Interestingly it also turns out, that regarding the general shape or even the absolute qualifier value the response of the neural network on the simulated event samples is continually in acceptable agreement with the recorded data from the experiment. All in all the first results on the training/testing phase give grounds to the assumption that the undertaken Monte Carlo approach renders it possible to reflect the properties of the GERDA measurements sufficiently close to reality.

6.5   Application to calibration from data and MC

As discussed in the preceding sections, the training/testing of the multivariate neural network classifier has been conducted with sought out energy intervals from the
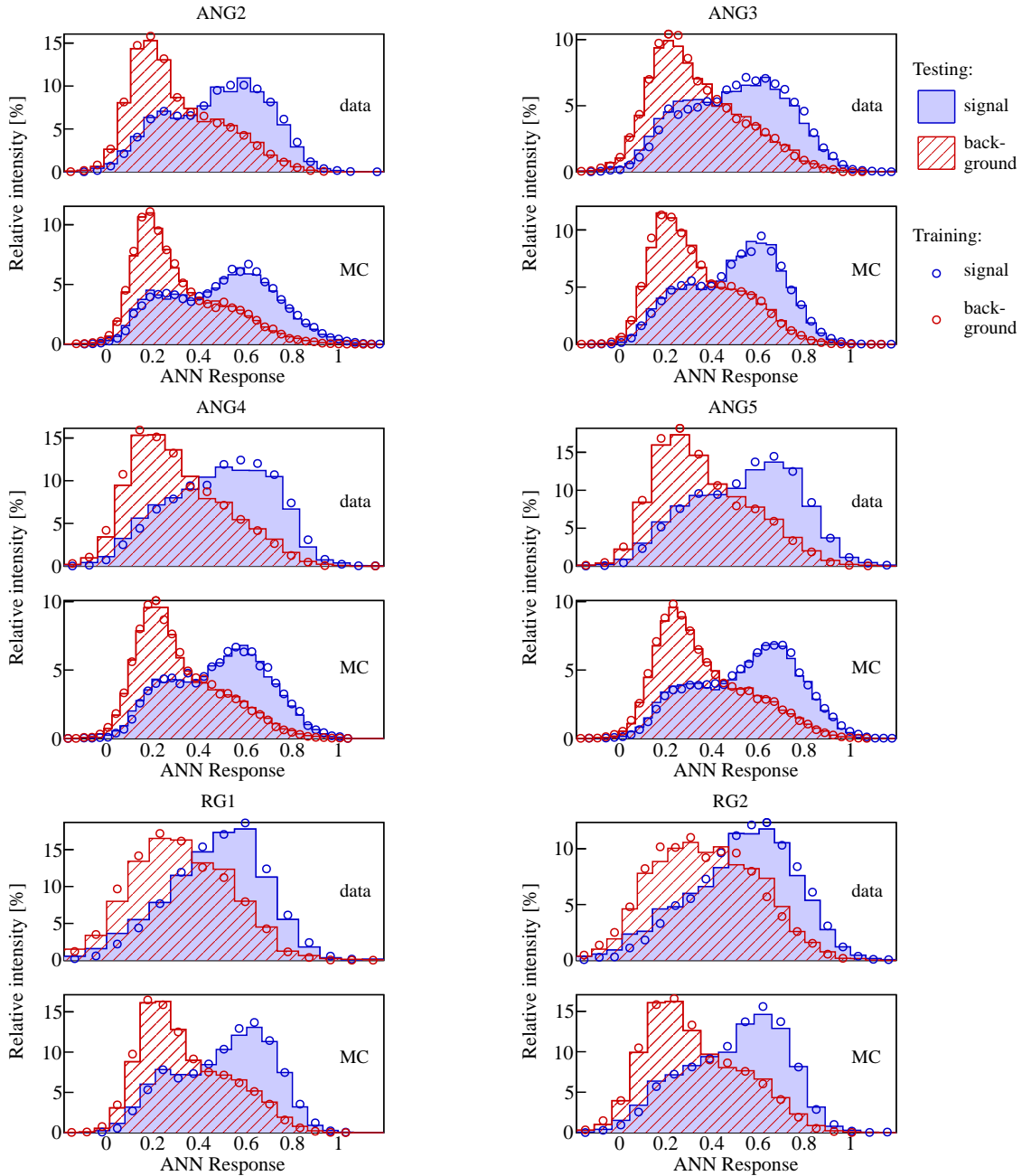

Figure 6.12: ANN response distribution of the signal (blue) and background (red) event class samples for the experimental data from Run $28 - 32$ (upper half) and the simulations (lower half). Results from the training procedure are presented as hollow circles, those that instead engender from the corresponding testing sample set as filled and hatched areas.

^{228}Th calibration sample set of experimental measurements during Run $28-32$ and of Monte Carlo calculations. In particular a $\pm 1 \cdot FWHM$ wide region around the DEP from the ^{208}Tl decay at 1592.5 keV and the FEP from the ^{212}Bi decay at 1620.7 keV is used as event class proxy of signal- and background-like character.

The results of the supervised learning procedure have been presented in the last section, where for both user supplied sample sets, from GERDA data and simulation, surprisingly resembling separation features for the input events of multi site and single site topology could be attained. In a next step, the following section is intended to address the subsequent application on the whole, overall energy interval of the calibration spectrum. To also give a meaningfull statement about the ANN event classification obtained with the simulated calibration set, again a comparison with the results from similarly evaluated experimental data will be drawn.

6.5.1   Energy dependency

Likewise to what has already been done for the evaluation of the GERDA Phase I pulse shape selection in subsection 4.4.1, the energy dependency of the calibration events derived from the Monte Carlo computations and the experimental reference from Run $28-32$ is as well studied.

In case of the data taken between January 24$^{\text{th}}$ 2012 to May 22$^{\text{nd}}$ (in principle a smaller subset of the first period pI of Phase I) the qualifier intensity of the multivariate classifier output is characterized by the very same energy dependency pattern as already determined in previous considerations of the three time intervals pI, pII and pIII of the GERDA measurements. Hereby, again, a drift of the variable distribution, where the falling edge is more and more shifted to smaller response values for increasing energies, is systematically observed for all detectors. The respective depiction can be found in the appendix B.3.1.

Concerning possible energy dependend systematics from Monte Carlo calculations, figure 6.13 (top half) illustrates the generated qualifier distribution from Compton events at six different energy regions 1375, 1550, 1845, 1955, 2155 and 2300 $\pm$ 25 keV and all semi-coaxial germanium diodes. While for the measured data a linear correlation of the ANN response for SSE as a function of energy is empirically well established, simulated calibration events on the other side do not bear the same, consistent description for the various detectors. Some germanium diodes, like ANG2 or RG2, even do not hold any energy dependence at all. Others, in turn, are described by a significant energy dependent response profile, which applies for both, single site and also multi site events, such that the left rising edge is as well more and more shifted to lower qualifier values at higher energies.

Eventhough showing an astonishing resemblance in the general ANN classifier distributions of the measured data, it appears that the simulations conducted with the MAGE and ADL software programs are not capable to reflect the experimentally found energy dependencies. The reasons for that inconsistency could not be resolved up to the present day though. Still, the transformation as defined by equation 4.13

is adapted retroactively on the simulated calibration events of each single detector to correct for the observed energy effect and results in the qualifier dispersions displayed in the bottom half of figure 6.13.
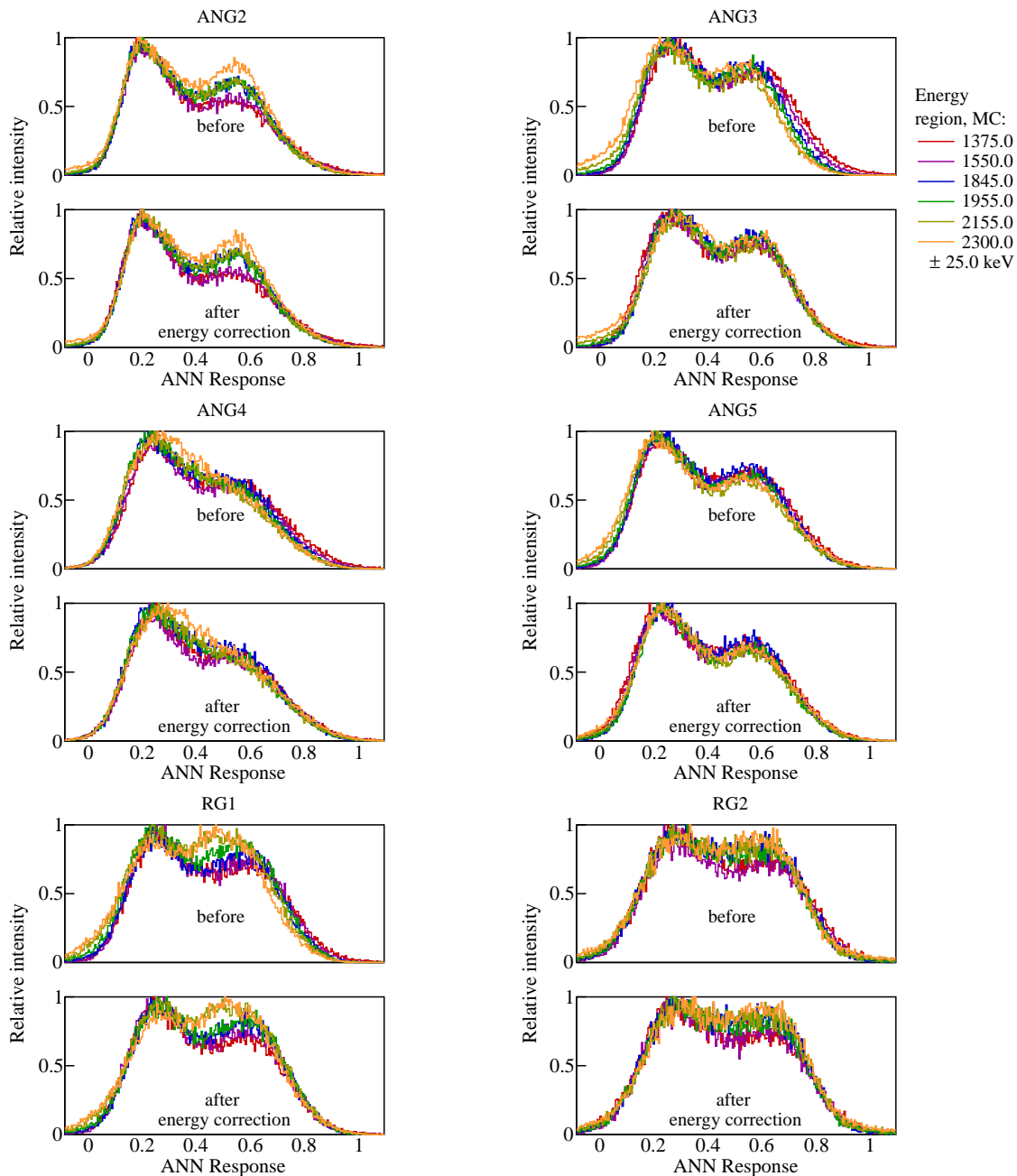

Figure 6.13: Simulated artificial neural network classifier output distributions originated by Compton events at six different energy regions before (upper half) and after (lower half) adaption of the energy correction transformation described by equation 4.13 for the semi-coaxial germanium detectors.

6.5.2   PSD cut parameter and survival fraction

Figures 6.14 a) + c) show a scatter plot of the corrected qualifier value assigned to the ^{228}Th calibration events as derived from the pattern recognition rules of the artificial neural network classifier versus the energy within the interval $1000 - 2750\,\mathrm{keV}$ for the experimental spectrum obtained in Run $28 - 32$ (top half) and the corresponding simulations (bottom half), respectively. Owing to the circumstance that the different semi-coaxial detectors all closely resemble each other in all significant features, here exemplarily only ANG4 is presented. For the sake of completeness, a detailed overview of all germanium crystals is anyhow entered up in the appendix B.3.2 for the measured data and in B.3.4 for the Monte Carlo calculations. Clearly it can be nicely seen, that both sample sets, the simulations along with the experimental
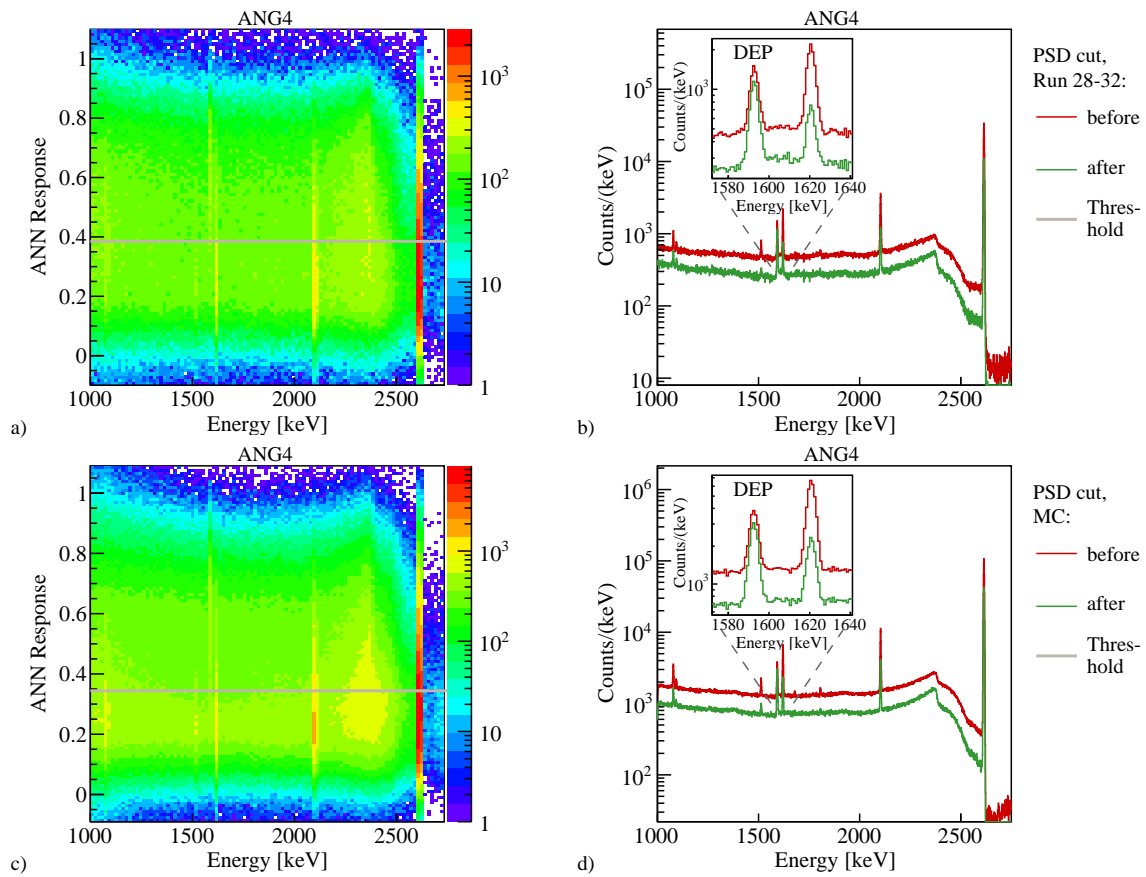
Figure 6.14: Left: ANN classifier response as a function of energy for ^{228}Th calibration events of the ANG4 detector for **a)** the experimental data of Run $28 - 32$ (top half) and **c)** the attendant simulations. The gray solid line denotes in both cases the position where $90\,\%$ of the DEP events are retained. **Right:** Corresponding ^{228}Th calibration spectrum before (green) or after (red) applied PSD cut as defined by the gray line of the left figure, where the cut is fixed for a survival fraction of $90\,\%$ in the DEP (see inset). Again the same diode, ANG4, is shown for the two sample sets attained from **b)** the conducted measurements (top half) and **d)** the performed Monte Carlo calculations (bottom half).

reference data, do for the considered energy region agree well in terms of the general distribution or absolute position of the pulse shape selection output, which peaks, as desired, in each case for the DEP at 1592.5 keV consisting of mostly single site events at higher response values. Whereas for the other γ-lines of predominantly multi site character, like the ^{212}Bi or ^{208}Tl FEPs at 1620.7 keV and 2614.5 keV as well as the thallium SEP at 2103.5 keV, systematically population densities shifted to lower classifier regions are observed.

Further the ANN classifier threshold for the pulse shape discrimination that retains 90 % of those events ascribed to the double escape peak of thorium, used as proxy for the efficiency on the $0\nu\beta\beta$-signal under investigation, is determined for each detector + sample set and additionally marked in figures 6.14 a) + c) as gray horizontal lines. Again remarkably consistent cut values could be identified for the measurements and the corresponding Monte Carlo approach, verifying the precision of the simulations. A list of the computed qualifier thresholds (and other pulse shape suppression properties) is thereby provided in table 6.3.

Detector	sample set	ANN threshold	^{228}Th Calibration			$0\nu\beta\beta$
			SEP	FEP	@$Q_{\beta\beta}$	
ANG2	data	0.359	27.7 ± 0.6	26.8 ± 0.1	52.8	–
	MC	0.336	31.2 ± 0.4	33.2 ± 0.1	54.5	84.1
ANG3	data	0.344	37.1 ± 0.7	37.5 ± 0.1	60.0	–
	MC	0.362	36.0 ± 0.4	33.2 ± 0.1	57.7	82.3
ANG4	data	0.385	30.4 ± 0.7	32.7 ± 0.1	54.5	–
	MC	0.344	33.2 ± 0.4	39.0 ± 0.1	54.5	80.9
ANG5	data	0.369	30.4 ± 0.7	34.0 ± 0.1	57.0	–
	MC	0.356	30.4 ± 0.4	24.3 ± 0.1	52.5	81.2
RG1	data	0.406	36.0 ± 0.9	39.5 ± 0.1	56.6	–
	MC	0.363	36.7 ± 0.5	40.7 ± 0.2	59.8	84.4
RG2	data	0.413	34 ± 1	32.6 ± 0.1	54.2	–
	MC	0.402	31.0 ± 0.6	37.1 ± 0.1	56.7	82.8

Table 6.3: Cut threshold as well as survival fractions of the neural network PSD along with the statistical errors in units of [%], under the condition of retaining 90 % of the ^{208}Tl DEP events, for the six semi coaxial detectors. Values for the ^{228}Th calibration spectrum obtained from experimental data taken in Run $28 - 32$ (equivalent to the time interval from January 24$^{\text{th}}$ 2012 to May 22$^{\text{nd}}$) and from the Monte Carlo simulations discussed in the present chapter are stated. The thallium SEP at 2103.5 keV and FEP at 2614.5 keV, as the two most prominent γ-lines, serve as event candidates of multi site topology. The two last columns list the survival fraction for the region at ± 25 keV centered around $Q_{\beta\beta}$ of mixed event type as well as for the homogeneously distributed simulated $0\nu\beta\beta$-decay inside the active detector volume, both with calculated statistical errors that are usually much smaller than 0.1 % and therefore not further considered.

Figures 6.14 b) + c) depict each a ^{228}Th calibration spectrum before (green) and after (red) pulse shape selection corresponding to a projection of the scatter plots presented in figures 6.14 a) + c) (left side) for the ANG4 and for the experimental measurement obtained during the time span between January 24th 2012 to May 22nd (top half) and the respective simulations (bottom half) on the energy axis. Please note the roughly two times higher statistics of the with the MAGE and ADL software programs remodelled data. Analogous plots for the other germanium detectors are additionally shown in the appendices B.3.3 for the experimental measurements and B.3.6 for the Monte Carlo computations. Already on a first glance the quite similar suppression performances of the two different sample sets can be assessed.

In a more detailed, quantitative analysis of the ANN classifier selection power on events of either signal- or background-like topology, the survival fraction of MSE in the SEP at 2103.5 keV and FEP at 2614.5 keV are investigated when adapting the neural network based PSD threshold on the calibration spectrum. As usually, the survival is explicitly assumed to be the fraction of the peak content remaining after the ANN selection cut. In particular, the Compton continuum under the γ-line is disentangled by subtracting linearly scaled event counts from energy regions below and above the peak. The obtained results on the corresponding single escape and full energy peak fractions of the different detectors are hereby listed in table 6.3 for the experimental data and the Monte Carlo calculations (again the statistical uncertainties have been calculated according to the procedure presented in the appendix A). Effectively both cases feature very similar suppression factors, where about $60 - 70\%$ of the γ-line events designated to be of multi site character can be effectively rejected under the condition of still keeping 90% of the DEP intensity. In addition the second last column states the survival fraction of those events occurring in the ± 25 keV wide region centered around the $Q_{\beta\beta} = 2039$ keV and thus from the Compton continuum of mixed MSE and SSE type.

6.5.3 Classifier response distributions

The consistent description of the neural network based pulse shape discrimination developed and presented in the framework of this thesis as an efficient background suppression technique by a dedicated Monte Carlo approach aimed for a detailed evaluation of the efficiency $\varepsilon_{0\nu\beta\beta}$ on the hypothetical $0\nu\beta\beta$-signal, is one basic aspect for the validation of the reliability of the multivariate supervised learning method. Hence a direct comparison between the selection performance, or in other words, the classifier response distributions for events with predominantly multi site or single site topology from calibration measurements performed every one or two weeks and those from simulations can give some further indications whether the trained selection rules for the pulse shape identification are justified as a veritable reflection of the actual experimental data.

In order to facilitate such a confrontation of the two different data sets, figure 6.15 displays for all six semi-coaxial detectors the ANN response of the double es-
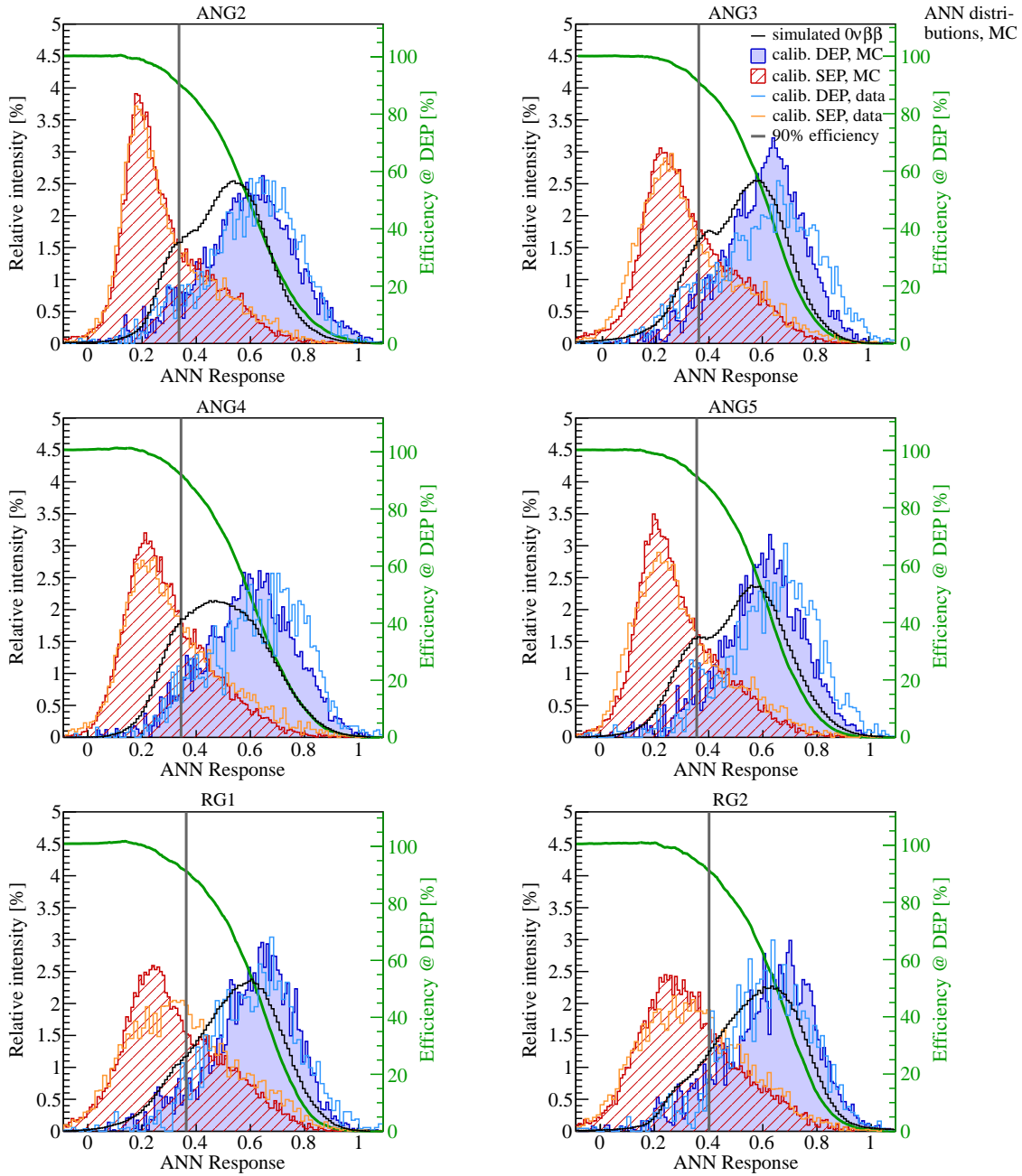
Figure 6.15: ANN response for the six semi-coaxial diodes. Distributions for the ^{228}Th calibration events of the DEP (blue filled area) and SEP (red hatched area) from Monte Carlo calculations are shown along with the survival fraction in the double escape peak versus the cut position (green), where the grey vertical line marks the threshold according to a rate of 90 %. Also displayed are the equivalent γ-line dispersions (orange and cyan) from the experimental data of Run 28 − 32. Hereby contributions from the Compton continuum are subtracted statistically using events in energy side bands. Additionally the simulation output of a homogeneously distributed $0\nu\beta\beta$-signal (see section 6.6) is illustrated (black).

cape peak (blue filled area) and the single escape peak (red hatched area) events extracted from the Monte Carlo calculations together with the overlayed equivalent curves from the combined experimental ^{228}Th calibrations taken during Run $28 - 32$ (cyan and orange) that can be conveniently used as reference. Contributions from the subjacent Compton continuum have been hereby priorly subtracted statistically using events in the energy side bands of the respective γ-line. Obviously the different distributions attributed to the DEP of mostly single site type and the SEP of predominantly multi site character do, with respect to the general shape, intensity as well as absolute classifier output values, agree to a considerable extend with each other. Therefore it appears highly reasonable to assume the simulated neural network response behaviour for the thorium calibration measurements to reproduce the experimentally gained data in reasonable accurateness.

Also shown in figure 6.15 are the DEP survival rate in units of [%] as a function of the cut position (green, right scale) and the explicit neural network threshold determined corresponding to a $90\,\%$ survival fraction in the double escape peak (grey vertical line). Additionally the qualifier dispersion from a simulation of homogeneously distributed $0\nu\beta\beta$-events inside the active detector material in order to estimate the ANN classifier efficiency $\varepsilon_{0\nu\beta\beta}$ on the neutrinoless double β-decay (see the upcoming section 6.6) is illustrated (black).

6.6   Application to $0\nu\beta\beta$-signal from MC

The consistent performance of the pulse shape discrimination on the simulated and experimentally measured ^{228}Th calibrations, where by preference those events of multi site topology in the single escape and full energy peaks are cutted, while $90\,\%$ of the SSEs within the double escape peak are on the contrary retained, has impressively substantiated the validity of the simulation efforts discussed in the present chapter. In the last part of the Monte Carlo study presented in this thesis, the validated PSD is finally applied to simulated $0\nu\beta\beta$-decays of ^{76}Ge distributed inside the detector volume. The primary aim herein is the evaluation of the $0\nu\beta\beta$-signal acceptance by the neural network selection cut along with the corresponding uncertainties.

Therefore another Monte Carlo simulation has been performed, where the ^{76}Ge neutrinoless double β-decays are first generated uniformly in the active detector volume using the Decay0 generator [Pon00] and afterwards propagated with the Geant4 [Ago03][All06] based MaGe framework [Bos11]. In the following steps the obtained interaction points along with the respective amounts of deposited energy are fed into the ADL pulse shape modelling program and subsequently classified with the pattern recognition rules attained from the previous training (as performed in section 6.4) of the ANN method with Monte Carlo calculated sample sets for the signal-like DEP at 1592.5 keV or the background-like FEP at 1620.7 keV from the thorium spectrum. In order to ensure the consecutive processes of the whole pulse shape simulation chain being conducted in conformity with the preceding computations for

the calibration measurements by the three ^{228}Th sources and as close to the real experimental data, the very same assumptions as already mentioned in subsections for the MAGE software as well as for the ADL program do serve again as input parameters for the $0\nu\beta\beta$-signal generation.

The resulting distribution of the artificial neural network response on the simulated neutrinoless double β-decay within the energy range of $Q_{\beta\beta}\pm1\cdot FWHM$ (black) is supplementary superimposed in figure 6.15 upon the other single site DEP and multi site FEP event class dispersins from Monte Carlo calculations and real experimental data of Run $28-32$. It is perceived that the pulse forms pertaining to the $0\nu\beta\beta$-signal are (similar to the DEP dispersions) indeed systematically assigned to higher qualifier values reserved - by definition - for those events of rather signal-like topology. Anyhow, one can also apparently discern clear divergences between the general shapes of the double escape peak, that serves as proxy for SSEs as well as reference to determine the exact position of the PSD cut threshold, and the hypothetical $0\nu\beta\beta$-decay with the latter being slightly shifted to lower regions (indicating an decreased efficiency of the ANN classifier on the neutrinoless signal in relation to the double escape peak).

6.6.1   Efficiency $\varepsilon_{0\nu\beta\beta}$

Figure 6.16 b) depicts the spectral distribution in the reconstructed energy range from $1000\,\text{keV}$ to $2100\,\text{keV}$ of the internal $0\nu\beta\beta$ events before (red) and after (green) the adaption of the ANN-based PSD cut under the condition of keeping $90\,\%$ of the
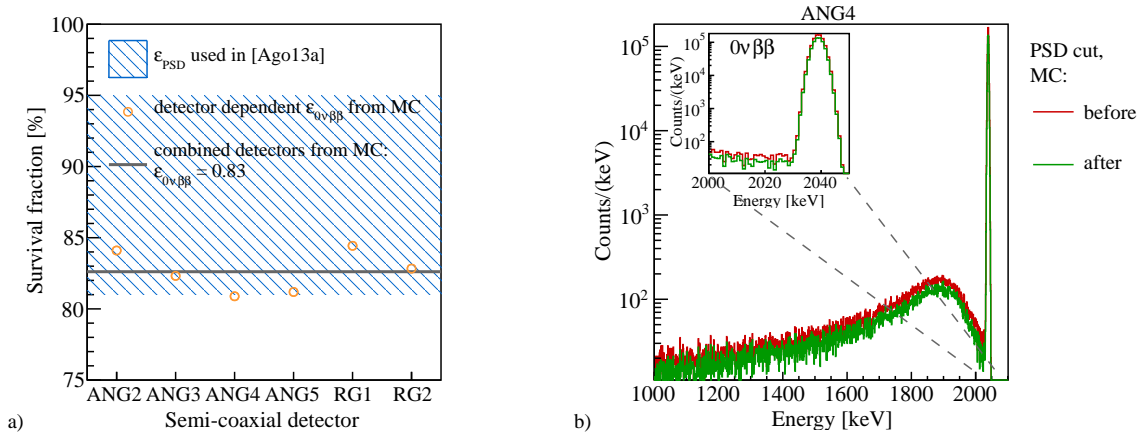
Figure 6.16: a): Simulated survival fraction in units of [%] for the six semi-coaxial germanium diodes along with the interval $\varepsilon_{\text{PSD}} = 90^{+5}_{-9}\,\%$ actually considered in [Ago13a] for the $0\nu\beta\beta$-analysis of GERDA Phase I. The combined average efficiency, weighted according to the active detector mass and enrichment fraction of the ^{76}Ge isotope, is marked as gray horizontal line. **b):** Simulated spectum of the neutrinoless $0\nu\beta\beta$-decay homogeneously distributed inside the semi-coaxial ANG4 detector before (red) and after (green) applying the neural network pulse shape cut. A close-up on the full energy peak at $Q_{\beta\beta}$ in the energy interval $2000-2050\,\text{keV}$ is shown in the small inset on the top left margin.

DEP line intensity. Owing to the resemblance of the spectral distribution observed for each of the different semi-coaxial detectors, here only the simulated data for ANG4 are visualized to give an example. A detailed overview of all detectors is still provided in the appendix B.3.6 for the reader.

As expected, the $0\nu\beta\beta$-spectrum exhibits a sharp peak at $Q_{\beta\beta} = 2039\,\mathrm{keV}$ (see close-up in the small inset at the top left margin). Already from the very first sight it can be identified, that the vast majority of the peak intensity is still retained after the pulse shape cut. A second dominant feature is represented by a tail extending to low energies that occurs due to those events for which a noticeable part of the total energy is either deposited in the dead layer and thus lost outside the active volume or completely escaped from the detector.[1] Regarding the significant chance of the electrons created during the $0\nu\beta\beta$-decay process to also emit a bremsstrahlung photon, naturally not all of the events located in the peak at $Q_{\beta\beta}$ and in the low energy tail are of SSE type. In principle the multi site event contamination for the neutrinoless decay mode is assumed to be in a quite similar order when compared to the one of the double escape peak of ^{208}Tl at $1592.5\,\mathrm{keV}$. However, since the energy of the $0\nu\beta\beta$-signal is distinctly higher with respect to the DEP, consequently the probability for the occurrence of bremsstrahlung and on that note of an multi site event with a non-localized energy deposition is enhanced. Hence, the effect is approximately equivalent to an increase of the spatial extend of the energy deposits as γ-rays from bremsstrahlung of higher energy interact in farther distance to the main interaction site (i.e. the electron-positron pair creation vertex for the DEP or the $0\nu\beta\beta$-decay vertex). This aspect has been already discussed and quantitatively investigated in, for instance, [Bud09][Ago11b]. Accordingly the neural network pulse shape discrimination cut survival probability is - already for that reason - supposed to be slightly lower than the fixed efficiency of $90\,\%$ for the double escape peak and may thus give a reasonable explanation for the $0\nu\beta\beta$-event distribution to be slightly displaced to lower ANN classifier output values in figure 6.15.

However, the resulting survival fractions in units of [%] for the FEP of the $0\nu\beta\beta$-decay of ^{76}Ge at $Q_{\beta\beta}$ after applying the threshold of the neural network cut are summarized in the last column of table 6.3 for each of the single semi-coaxial-detectors. The absolute statistical uncertainties are hereby far below $0.1\,\%$. Additionally figure 6.16 a) gives also a visual impression of the different ANN selection efficiencies on the six individual germanium diodes (orange hollow circles) along with the systematic uncertainty interval $\varepsilon_{\mathrm{PSD}} = 90^{+5}_{-9}\,\%$ of the survival fraction used for the official analysis of the GERDA Phase I results recently published in [Ago13a] (light blue hatched area). The value is thereby estimated on the basis of the specified acceptance rate for events within the DEP and the systematic consistency considerations employed in the preceding chapter 5.

---

[1] The resulting decrease on the signal efficiency is thereby already covered with the quantity $\varepsilon_{\mathrm{det}}$ from equation 3.20 used for the half-life calculation on the neutrinoless double β-decay by means of equation 2.54. Basically it accounts for the probability that a $0\nu\beta\beta$-decay, taking place in the active volume of a detector, actually releases its entire energy in it and therefore contributes to the full energy peak at $Q_{\beta\beta}$.

Systematically the derived values are found to be $5-10\,\%$ below the fixed $90\,\%$ acceptance of the events originated from the double escape peak, which settles the threshold position on the classifier value. This difference can be attributed to various reasons and caused either by the increased appearance of bremsstrahlung in the $0\nu\beta\beta$-signal at $Q_{\beta\beta}$ compared to the DEP at $1592.5\,\mathrm{keV}$ with lower energy (as already discussed) or due to simulation artefacts generated by the adjustments introduced to overcome the deficiencies of the simulations (i.e. positions of ^{228}Th sources, electronic response, noise or impurity concentrations) and possible uncertainties concerning the particle interactions computed within the MAGE Monte Carlo program or the signal formation process of the ADL software. A detailed discussion of the most reasonable contributions to the systematic error is intended to be issued in the concluding subsection 6.6.3 of this chapter. Another conceivable explanation for the deficit in the $0\nu\beta\beta$ survival fraction may be found in a volume dependency of the ANN cut originated by the inhomogeneous DEP event distribution with a slightly preferred arrangement at the outer surface regions of the detector and will be investigated in the next subsection 6.6.2 though.

Further illustrated in figure 6.16 a) is the combined efficiency on the neutrinoless double β-decay from all six semi-coaxial detectors as concluded by the conducted simulations (gray horizontal line). The individual contributions from the germanium crystals are thereby each weighted according to the respectice active masses and enrichment fractions concerning the ^{76}Ge isotope. An average value of $\varepsilon_{0\nu\beta\beta} = 83\,\%$, still located within the anticipated interval for $\varepsilon_{\mathrm{PSD}}$, is obtained. The corresponding statistical error can be derived to a number below $0.2\,\%$ and is therefore not considered in the following analysis since the various systematic uncertainties are found to be by far dominant.

6.6.2   Volume dependency

It is highly instructive to investigate a possible volume effect of the pulse shape selection as one conceivable origin for the loss in the $0\nu\beta\beta$ efficiency in comparison to that of the DEP.

For this purpose figure 6.17 depicts the distribution of the average survival fraction in units of [%] when adapting the ANN cut thresholds listed in table 6.3 (for MC data sample) on the simulated homogeneous neutrinoless double β-signal inside the active volume as a function of the respective height (z-direction) and radius of the individual six semi-coaxial detectors. Bins in the scatter plot which do not contain any information and thus remain unfilled (white) are either attributed to the bore hole or the dead layer on the outer n+ surface of the crystal geometry. Please note that counter-intuitively and very occasionally values inside the bore hole of the detector are still allowed though, since here the disperion of the energy barycenters of individual events are shown. Regions with a relatively low mean acceptance, where the neural network algorithm can not clearly identify SSEs, are signified by violet, blue and green color code, while those areas of high acceptances up to $100\,\%$ are

on the other hand highlighted in red, orange and yellow shades (see color bar with assigned scale at the right axis).

Obviously, a conspicuous volume dependency is present for the applied pulse shape discrimination. In particular those events occurring close to the p+ contact
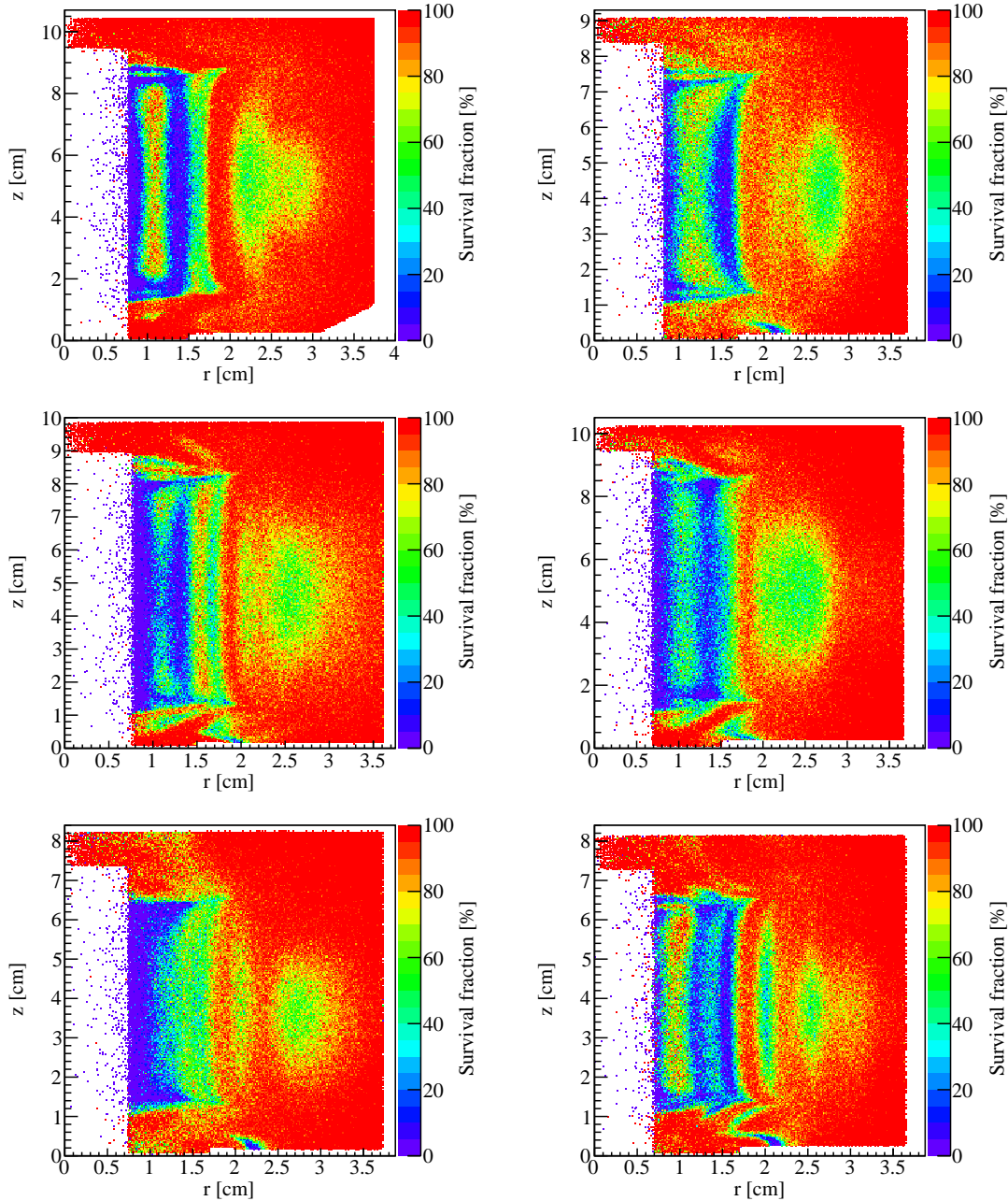

Figure 6.17: Distribution of the survival fraction in units of [%] for a homogeneously simulated $0\nu\beta\beta$-signal inside the active detector volume as function of the height and radius when applying the neural network cuts as listed in table 6.3 (for the MC sample). All six semi-coaxial germanium crystals are shown.

at the inner bore hole of the cylindric geometry of the germanium crystal and to a slightly lower extend in the inner center of the radially projected detector volume are increasingly removed.

One potential argument has already been mentioned before in subsection 6.4.1, where the inhomogeneous distribution of the DEP events used as signal-like proxy sample for the learning process of the ANN, due to a higher probability of annihilation photons to escape from the active volume, has been pointed out. In such case the classifier is eventually trained to select those events in vicinity to the outer surface of the detector instead of the desired SSEs. In [Vol12] this aspect has been explicitly investigated by additionally performing the training of the multivariate classifier with a special sample consisting of intentionally homogeneously distributed DEP events. It was found that the volume effect, albeit being noticeably mitigated, can still not completely suppressed though. Hence, another not yet identified causing for the volume effect is assumed.

At this point it should be also referred to the independently developed and completely alternative PSD method based on the combination of the two input parameters represented by the A/E-value and the pulse asymmetry. An explanation on the corresponding working principle has been priorly given in subsection 5.5.2. Dedicated simulations conducted in order to validate the empirically derived classification algorithm, surprisingly revealed a volume selection of events that is in astonishing accordance with the one retained by the neural network approach presented in this thesis [Ago13d][Sal13]. However, the affected net region is directly related to the overall survival probabilities stated in table 6.3 and responsible for the decreased efficiency on the neutrinoless double β-decay.

6.6.3   Systematic uncertainties

The most reasonable items assumed to have a sizable impact and thus considered as contribution to the systematic uncertainty of the neutrinoless double β-decay efficiency $\varepsilon_{0\nu\beta\beta}$ are intended to summarized in table 6.4 along with the correspondingly deduced absolute numbers. In general the different errors arise, for instance, due to uncertainties in the Monte Carlo simulations regarding either the accuracy of the implemented geometry model for the experimental setup or the precision on the tracking of particles and the particle interaction processes themselves. Other possible reasons engender by virtue of several input parameters entering the simulation chain that were guessed in the consequence of lacking information and therefore may be wrong, whereas in the best case they at least contain some intrinsic errors. In the following it is intended to briefly itemize the predominant contributions:

- For the uncertainty related to the MSC of the interaction points within the detector material by means of the MAGE software two conceivable origins can be identified: (i) a deficient implementation of the experimental geometry within the source code (detector dimensions, material composition or displacements)

and (ii) explicitly the interaction procedure of radiation in matter (see sub-
section 3.2.2) conducted by GEANT4. Both items combined are evaluated to
introduce an absolute error of roughly $\pm 2\%$, where the geometrical share is
considered to be less prominent as the various sizes, shapes or substance of
the different setup components are very well known and carefully integrated
into the program. The second contribution owing to the particle tracking is
extracted from [Ama05][Poo05][Cir10] that have systematically validated the
uncertainty of electromagnetic physics processes supplied by the GEANT4 soft-
ware for γ-rays and $e^{\pm}$ to be at the low-percent level in the energy range
relevant for γ-spectroscopy and the analysis performed with the GERDA data.

- The source position during the data taking of the ^{228}Th calibration runs is one
  further critical, in fact as it tuns out even the most important, issue concerning
  the systematic uncertainties on the neutrinoless double β-decay survival frac-
  tion. Since the neural network is trained with samples from the ^{208}Tl double
  escape peak and the ^{212}Bi full energy peak of the calibration measurements,
  the particular location of S1, S2 + S3 relative to the germanium detector array
  and the resulting event distribution in the active crystal volumes does have an
  incisive effect on the outcome of the learning process and the subsequent appli-
  cation of the selection rules on the $0\nu\beta\beta$-signal. The concreate consequence on
  the absolute number is quantified by repeating the very same analysis with a
  different assumption on the position of the three thorium sources. In particular
  a vertical shift of $\pm 40\,\mathrm{mm}$, equal to the systematic error on the z-position es-
  tablished in subsection 6.2.2 (by a comparison of the γ-line and overall spectral
  intensities), is taken into account. It was thus evaluated that $\varepsilon_{0\nu\beta\beta}$ alternates
  with the uncertainty of $\pm 2\%$.

- As explained in subsection 6.3.2 the computations conducted on the pulse shape
  simulation are not capable to realistically reproduce the implication of the
  electronic devices (cabling, charge sensitive pre-amplifier, etc.) counted among
  the experimental read-out supply on the time formation of the charge trace.
  Hence, in the absence of a better alternative, a feasible but not necessarily
  correct electronics response or transformation function has been generated by
  a comparison of the average single site pulses from the MC and the measured
  data. To estimate the accruing effect, the training and classification of the
  ANN method has been redone with the plain, unchanged simulation output
  from the ADL pulse shape modeling and yielded the absolute contribution to
  the systematic uncertainty of $\pm 1\%$.

- An additional point not integrated in the simulation of the charge signals is
  the electronic noise. In subsection 6.3.3 it has been conveniently reproduced
  by deploying the corresponding experimental baseline traces that are usually
  recorded during the Phase I physics runs. A dedicated Fourier analysis has
  further validated that the obtained information resembles the calibration data
  within detector specific uncertainty bounds of roughly 20% at maximum (see

figure 6.9) and can be therefore still comprehensively used for all sample sets. By performing the simulation and neural network classification on different assumptions for the noise amplitude, this systematics is transferred to a negligible small value of $\pm 0.1\,\%$ for the absolute noise-related uncertainty on the efficiency on the neutrinoless double β-signal.
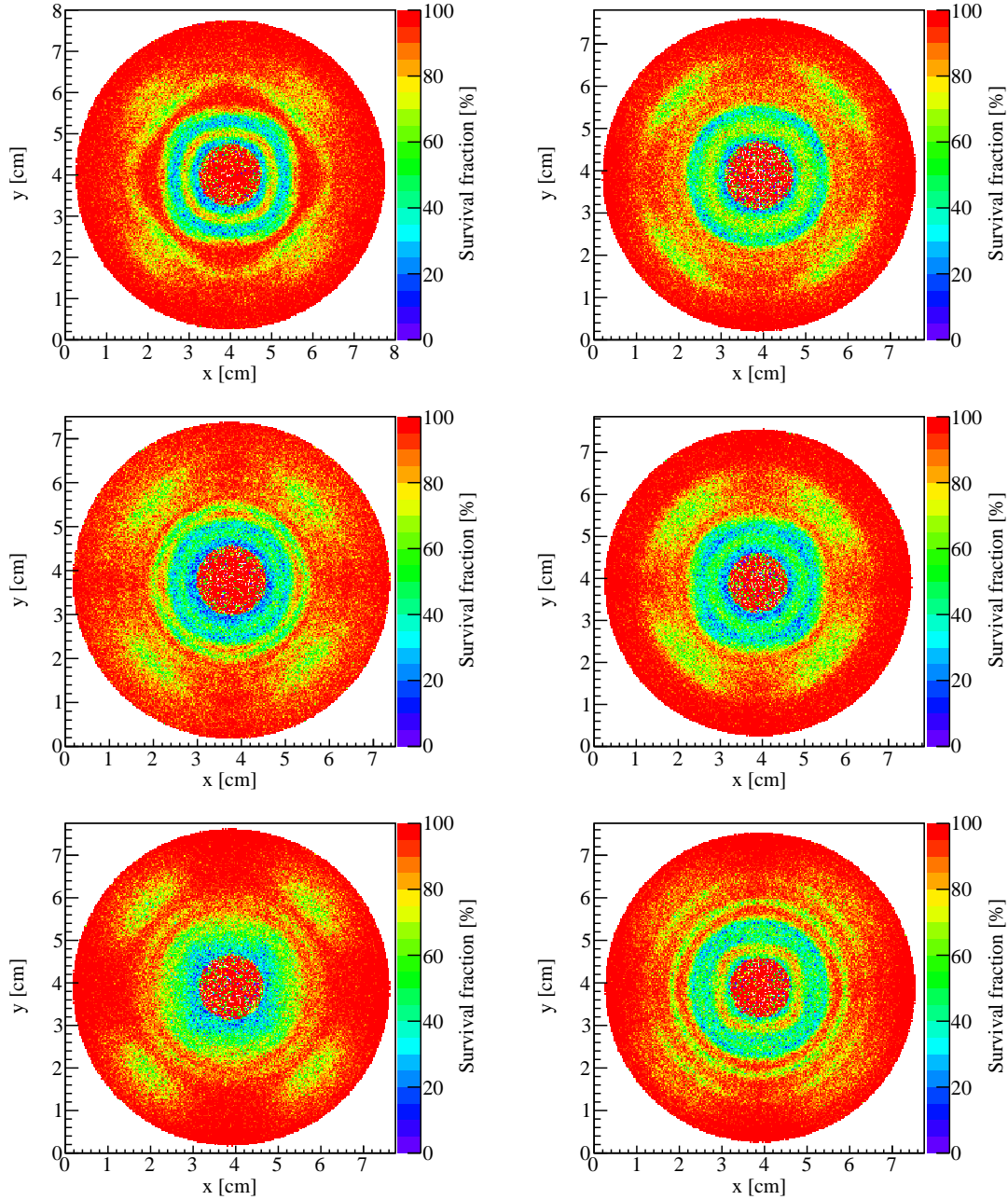

Figure 6.18: Distribution of the survival fraction in units of [%] for a homogeneously simulated 0νββ-signal inside the active detector volume as function of the x- and y-direction for the neural network cuts listed in table 6.3. The resulting data are depicted for a top view on all six semi-coaxial germanium crystals.

- The ADL pulse shape simulation program has been fed with numbers for the impurity concentration of the single diodes which are not known, but retroactively tracked back with the aid of formerly measured voltages for a full depletion of the detector volume from [Bar09b]. Values between $0.6 \cdot 10^{10}$ atoms/cm^3 for the ANG5 with the (by far) smallest depletion voltage of 1000 V and $1.2 \cdot 10^{10}$ atoms/cm^3 for the RG1 with the highest depletion voltage of 4200 V could be iteratively inferred in the course. However, this method is highly inaccurate and an empirically assessed uncertainty of about 20 % on the individual detector impurities remains to be unresolved. In terms of the survival fraction on the neutrinoless double β-decay this can be directly conferred into a systematical error of ± 1 %.

- Besides the volume dependency for the ANN classifier cut already shown in the preceding subsection (see figure 6.17), also a pattern structure that is directly connected to the crystallographic symmetry of the detector material, that apparently influences the signal time structure on a significant level, has been observed. Figure 6.18 illustrates the distribution of the average survival fraction in units of [%] according to the cut thresholds stated in table 6.3 (for MC data sample) on the simulated homogeneous $0\nu\beta\beta$-events inside the active volume as a function of the respective x- and y-directions (top view) of the individual six semi-coaxial detectors. Again the color code covers the optical spectrum from blue up to red shades respectively denoting regions with increasing acceptances on the neutrinoless double β-signal and reveals clearly the symmetry effects related to the structure of the ^{76}Ge crystal lattice. The impact on the classification pattern derived by the multivariate analysis technique during the training and the theron based event selection is studied such that the orientation of the axis is rotated in steps of $15\,^\circ$ within a range of $90\,^\circ$ until the symmetry repeats itself again. This can be easily accomplished within the ADL program by only applying some minor changes. In doing so, for the systematic uncertainty a contribution in the order of ± 1 % could be assigned.

The possible deviations from the mean value $\varepsilon_{0\nu\beta\beta} = 83$ % of the $0\nu\beta\beta$-signal efficiency seen are combined quadratically. Consequently the total systematic uncertainty of the contributions listed above and reported in table 6.4 sums up to ± 3 %.

Item	Systematical uncertainty
Setup geometry & particle tracking	± 2 %
Source position	± 2 %
Electronics response	± 1 %
Noise	± 0.1 %
Impurity concentration	± 1 %
Crystal axis orientation	± 1 %

Table 6.4: Absolute systematic uncertainties on the survival fraction $\varepsilon_{0\nu\beta\beta} = 83$ % of the neutrinoless double β-decay events when applying the ANN pulse shape selection on the simulated data. Here these items expected to introduce the relevant contributions are discussed.

7. Evaluation of the half-live $T_{1/2}^{0\nu}$ in ^{76}Ge

Within Phase I of the GERDA experiment, located at the Laboratori Nazionali del Gran Sasso (LNGS) of INFN in Italy, eight refurbished semi-coaxial detectors from the Heidelberg-Moscow experiment (HdM) [Kla01] and the International Germanium Experiment (IGEX) [Aal02] enriched in the isotope ^{76}Ge have been operated starting from November 2011 until May 2013 with the aim to search for the extremely rare process of the neutrinoless double β-decay with an endpoint energy of $Q_{\beta\beta} = (2039.061 \pm 0.007)$ keV [Mou10]. In the course of data taking also five newly produced detectors of BEGe type have been additionally deployed in July 2012. Two of the semi-coaxial diodes featured soon after the beginning of the measurement a large leakage current and have been discarded though. Also one of the BEGes exhibited an unstable behaviour concerning the energy calibration and has been hence as well excluded from the analysis. Further a fraction of 5 % of the data is not used due to temperature instabilities. Therefore, with the cessation of Phase I, finally a sum of 492.3 live days has been collected and can be directly transferred to a total exposure of 21.6 kg·yr considered for the estimation on the half-live $T_{1/2}^{0\nu}$ of the $0\nu\beta\beta$-decay in the germanium isotope. Hereby the region of interst around $Q_{\beta\beta}$ used for the background estimate entering the analysis spans from 1930 keV to 2190 keV excluding (apart from the blinded window) the intervals (2104 ± 5) keV and (2104 ± 5) keV due to sizable contributions from known γ-lines of ^{208}Tl or ^{214}Bi, respectively. The remaining energy range is (has been), within the framework of this thesis, often referred to as "230 keV window" or ROI (acronym for "region of interest").

To avoid biases in the event selection for the $0\nu\beta\beta$-analysis, a blind analysis, with the interval $Q_{\beta\beta} \pm 5$ keV being hidden until the data handling and all selection cuts are frozen, has been performed. For a more detailed description of the experiment the reader is referred to [Ack13] or chapter 3 of this thesis.

The energy stability performance is thereby monitored with the aid of dedicated calibration runs that have been performed on a (bi-)weekly basis by deploying three ^{228}Th sources of sufficient activity in close distance to the detectors. The deposited energy is retroactively reconstructed offline by a digital filter with semi-Gaussian shaping. From a comparison with the calibration measurements and the known extrapolation on the energy scale, an exposure-weighted average energy resolution ($FWHM$) of the physics data with (4.8 ± 0.2) keV for semi-coaxial detectors and (3.2 ± 0.2) keV for BEGe is expected at $Q_{\beta\beta}$. Thereby the individual resolutions have been stable within 0.1 keV during the entire period of data taking for all detectors.

Data selection

A $0\nu\beta\beta$-decay would in case of occurrence almost always deposit the whole released energy localized in only one detector. Hence solely those events with an energy

deposition in a single germanium crystal are considered, resulting in a background suppression of about 15 % at $Q_{\beta\beta}$ with practically no efficiency loss for the neutrinoless double β-signal. In a second data quality cut all HPGe detector events that happen in coincidence within 8 μs with a signal from the muon-veto are rejected leading to a further background reduction of roughly 7 %. By excluding events that are either preceded or followed by another one within 1 ms in the same detector channel allows to furthermore effectively reject background engendering from the ^{214}Bi-^{214}Po cascade in the ^{222}Rn decay chain and effects less than 1 % of the events close to $Q_{\beta\beta}$. Thereby the dead time owing to the muon-veto and "BiPo" cuts is negligible, considering the low counting rate in the GERDA experiment.

The data are divided into three subsets according to the different background indices (BI), a quantity defined as the number of counts per keV·kg·yr, observed in the ROI around $Q_{\beta\beta}$. In particular a first one covers the whole data collected with the BEGe detectors (2.4 kg·yr exposure), where a second, so-called "silver" subset contains only a short data period from the semi-coaxial germanium crystals of exceptionally high background index at the time when the diodes of BEGe type have been deployed (1.3 kg·yr exposure). The remaining of the semi-coaxial data is collected in a third data set, also denoted as "golden" data set, with the by far highest statistics (17.9 kg·yr exposure).

Background composition

In order to extract a possible neutrinoless double β-process at the $Q_{\beta\beta}$-value or, in case of no event observation, to derive a lower limit on the half-life of the $0\nu\beta\beta$-signal, it is crucial to understand the different contributions observed in the energy spectrum and, by their identification, to develop a strategy for an effective background suppression.

When analyzing the the energy spectrum obtained during GERDA Phase I, several γ-peaks due to ^{40}K and ^{42}K decays as well as the decay chains of ^{226}Ra and ^{228}Th are visible. The spectral shape between the detector dependent trigger threshold of $40 - 100$ keV towards 570 keV is thereby characterized by β-decays of ^{39}Ar, whereas further up between 570 keV and 1700 keV the predominant contribution arises from double β-decays accompanied by neutrino emission ($2\nu\beta\beta$). Higher energy intervals above 3 MeV are, on the contrary, basically determined by α-decays on the p+ layer of the detector (either inner bore hole for semi-coaxial or point-like contact for BEGe geometry) generated from ^{210}Po and to a smaller extend also from the sequential decays of the ^{226}Ra chain. However, around 2 MeV, at the region of interest close to $Q_{\beta\beta}$, a mixture of the above mentioned contributions can be observed (see for instance subsection 3.6.1 on the experimental measurements of Phase I).

A detailed decomposition of the described energy spectrum was done in [Ago13c] (subsection 3.6.2 provides also a brief description of the attained background model) considering physics data recorded until March 2013 that amount to a total exposure of 16.70 kg·yr for the six semi-coaxial detectors and 1.8 kg·yr for the germanium crys-

tals of BEGe type. Hereby the background distribution has been fitted for an energy range of $570 - 7000\,\mathrm{keV}$ to a compositing model consisting of the already mentioned radiative contaminations at different locations, i.e. distances to the germanium diode array. Despite the circumstance that the exact positions of the various contributions can not be disentangled from the available statistics, several other important properties have been ascertained:

- The GERDA Phase I background is engrossed by those sources in vicinity to the detectors or even on the detector surface (mainly α-, β- or ^{42}K-events.)

- It is validated that no peak is expected within the blinded energy window at $Q_{\beta\beta} \pm 5\,\mathrm{keV}$ to originate from any of the conceivable radiative contaminations.

- Also the spectral shape can be in good approximation identified as a constant intensity in the regoin of interest at $Q_{\beta\beta}$.

Pulse shape discrimination

Concerning the general sensitivity of a counting experiment searching for the neutrinoless double β-decay, one important key aspect is the minimization of the background index present close to the Q-value, provided that the $0\nu\beta\beta$-signal efficiency is still kept high. Using an enhanced pulse shape analysis tailored to meet the individual experimental requirements has been repeatedly proven in the field of γ-spectroscopy with HPGe detectors to be an ideally suited method for that purpose.

Assuming that the energy loss of electrons created in the course of the $0\nu\beta\beta$-decay by means of bremsstrahlung is small, the total ionization takes place in localized processes of negligible spatial distance within the detector volume resulting in so-called single site events (SSE). Vice versa, possible background engendering from Compton scattered photons does predominantly exhibit energy depositions at several well separated interaction points and thus yields typically multi site events (MSE). Consequently the time behaviour of the induced current signal on the read-out electrode will differ for the two described event classes, whereby this feature allows for an opportunity to discriminate the obstructive background events. As third event type, surface events, that represent a large fraction of the overall induced background of GERDA Phase I, come along as well with distinct pulse form and are insofar easily distinguishable. A detailed overview on the applied pulse shape selection techniques of the final data analysis is i.a. given in [Ago13d]. Depending on the detector type, two different methods have been developed, thoughtfully validated and fixed before the unblinding of the energy spectra was prosecuted in June 2013.

In case of the BEGe detectors, the ratio of the maximum height A of the current pulse over the deposited energy E serves as an easily graspable, powerful and well understood discrimination parameter. As proxy for the pulse shape of $0\nu\beta\beta$ decays acts the DEP of $2614.5\,\mathrm{keV}$ photons induced by the ^{208}Tl-decay from the calibration data. While for the accepted range of $0.965 < A/E < 1.07$ the signal efficiency is

determined to $(92 \pm 2)\,\%$, a background suppression at $Q_{\beta\beta}$ of more than $80\,\%$ is achieved. A cross check with the corresponding survival fraction of $2\nu\beta\beta$-decays within the energy interval $1000 - 1400\,\text{MeV}$ revealed, in nice accordance with the numbers attained for the double escape peak, a value of $(90 \pm 5)\,\%$.

On the other hand, for the semi-coaxial detector type, the A/E quantity does not represent a useful discriminant for an efficient event selection. This is ascribable to the geometry-specific weighting potential fields with, if compared to the BEGe diodes, a characteristically lower gradient and a hence larger relevant part of volume for the detector signal. As a result a position dependent charge collection and thus pulse shape when moving from the inner p+ surface to the outer n+ surface is engendered, since both charge carriers, electrons and holes, are contributing to the signal formation.

Instead a different approach developed in the framework of this thesis and based on the neural network algorithm TMlpANN provided by the TMVA software package [Hoe07][Vos07], is employed to select single site events. As explained in chapter 4, in particular a feed-forward multi-layer perceptron with two hidden layers of 51 and 50 neurons, respectively, is utilized for which the times where the charge pulses reach $1\,\%$, $3\,\%$, ..., $99\,\%$ of the maximum height act as input variables. The training of the multivariate classifier, that relies on the "supervised learning" method, is conducted with user-supplied signal or background class samples from calibration data containing, on one side, ^{208}Tl DEP events at $1592.5\,\text{keV}$ being conspicuous for their predominantly SSE character and, on the other side, ^{212}Bi FEP events at the $1620.7\,\text{keV}$ of mostly MSE topology. Also the learing process is performed for each detector and three separate time periods of similar conditions individually.

In order to finalize the cut on the classifier output of the neural network, the pulse shape discrimination has been tuned such that a survival fraction of $90\,\%$ for the DEP is retained. The corresponding threshold values on the ANN qualifier have been priorly computed in subsection 4.4.2, where they are also summarized in table 4.5. Hereby the pulse shape selections are especially intended to facilitate the ultimate sensitivity for a $T_{1/2}^{0\nu}$-limit for the neutrinoless double β-decay. As the expected background counts at $Q_{\beta\beta}$ are very few, only a moderate rejection is needed while it is preferred to keep the $0\nu\beta\beta$-efficiency high.

After the introduction of the pulse shape discrimination procedure for the official $0\nu\beta\beta$-analysis, several cross checks based on experimental data from the gathered GERDA Phase I calibration and physics runs - availing on Compton edge (CE) and neutrino-accompanied double β-decay ($2\nu\beta\beta$) events - as well as a complementary measurement with a ^{56}Co source have been subsequently performed throughout chapter 5. Regarding the different deviations from the survival fraction of $90\,\%$ for the DEP seen, the efficiency and overall systematic uncertainty of the ANN classifier on the neutrinoless double β-signal was in summary estimated to $\varepsilon_{\text{PSD}} = 90_{-9}^{+5}\,\%$. Thereupon this value has been used for the determination of the first result on the $0\nu\beta\beta$-decay in ^{76}Ge from the GERDA experiment presented in [Ago13b].

All of the so far performed consistency studies are, however, based on calibration and physics data and thus experimental measurements only. In chapter 6 of this thesis therefore detailed Monte Carlo + Finite Element Method (FEM) calculations have been prosecuted, considering all pivotal conditions of the experiment (as for instance: setup geometry, particle interaction in matter, source position, impurity concentration in the germanium crystal, electronics response, noise or operational voltage). Finally the performed simulation efforts yielded an average efficiency on the hypothetical neutrinoless decay mode of

$$\varepsilon_{0\nu\beta\beta} = (83 \pm 3)\,\% \, ,$$

which is noticeably declined compared to the value for $\varepsilon_{\mathrm{PSD}}$ derived from the experimentally recorded data. The reason has been identified as significant volume dependencies present for the multivariate pattern recognition algorithm - most likely introduced by the DEP events used as signal training sample being inhomogeneously distributed within the active detector region (since the probability for the two $511\,\mathrm{keV}$ photons to escape is larger in the corners). Hence in a conservative approach, hereinafter the second, considerably smaller value $\varepsilon_{0\nu\beta\beta}$ inferred from the simulation computations is ultimately assumed for the efficiency of the neural network method on the $0\nu\beta\beta$-process aimed to be scrutinized.

Results

After the analysis methods discussed above have been finally frozen, the events in the blinded interval around $Q_{\beta\beta} \pm 5\,\mathrm{keV}$ were processed in June 2013.

Set	Exposure $\mathcal{E}$ [kg·yr]	Events in ROI [cts]	BI $\left[\dfrac{10^{-3}\mathrm{cts}}{\mathrm{keV\cdot kg\cdot yr}}\right]$	δE [keV]	efficiency ε	N_{exp}	N_{obs}
			Without pulse shape analysis				
Golden	17.9	76	18 ± 2	4.8	0.688 ± 0.031	3.3	5
Silver	1.3	19	63^{+16}_{-14}	4.8	0.688 ± 0.031	0.8	1
BEGe	2.4	23	42^{+10}_{-8}	3.2	0.720 ± 0.018	1.0	1
			With pulse shape analysis				
Golden	17.9	45	11 ± 2	4.8	0.571 ± 0.032	2.0	2
Silver	1.3	9	30^{+11}_{-9}	4.8	0.517 ± 0.032	0.4	1
BEGe	2.4	3	5^{+4}_{-3}	3.2	0.663 ± 0.022	0.1	0

Table 7.1: List of parameters used for the $0\nu\beta\beta$-analysis. Numbers are stated for the three data sets ("golden", "silver", BEGe") with and without pulse shape discrimination. Hereby $\mathcal{E}$ signifies the exposure, ε the total $0\nu\beta\beta$-decay efficiency and δE the energy resolution ($FWHM$). Additionally the event number observed in the ROI, the corresponding background index BI, and the expected(observed) counts $N_{\mathrm{exp}}(N_{\mathrm{obs}})$ within the blinded region $Q_{\beta\beta} \pm 5\,\mathrm{keV}$ ares shown in the last two columns.

Table 7.1 lists all parameters relevant for the $0\nu\beta\beta$-analysis, i.e. the exposure $\mathcal{E} = M_{\text{det}} \cdot t$, the number of background events in the $230\,\text{keV}$ window as the region of interest (ROI), the background index (BI), the energy resolution δE and the exposure-weighted average efficiency ε of all three subsets with and without pulse shape discrimination (parts of the numbers have already been mentioned earlier in this thesis within table 3.8 of subsection 3.6.1 in the context of a brief introduction to the GERDA experiment). Also stated is the number of events N_{exp} in the inaccessible range of $10\,\text{keV}$ width as expected by the GERDA background model derived by means of Monte Carlo simulations and presented in [Ago13c] along with the experimentally determined counts N_{obs} after the unblinding of the corresponding energy interval.

Furthermore figure 7.1 displays the combined energy spectrum obtained from all enriched HPGe detectors (semi-coaxial + BEGe) before (filled red) and after (filled green) adaption of the neural network or A/E parameter based event selection cuts. The region of interest, i.e. the $230\,\text{keV}$-window with the excluded two intervals of $\pm 5\,\text{keV}$ width from known γ-lines marked by orange shaded areas (lower panel) as well as a more narrow interval zoomed to $Q_{\beta\beta}$ (upper panel) are shown.

Apparently for the combined data set seven events are observed in total in the formerly blinded range $Q_{\beta\beta} \pm 5\,\text{keV}$ if the PSD is disregarded. Table 7.2 reports the details of these events including also the most important results from the pulse shape analysis. Compared to the total number of 5.1 ± 0.5 counts predicted by the background model [Ago13a], no excess of events beyond the expected contribution is seen (see last two columns of table 7.1).
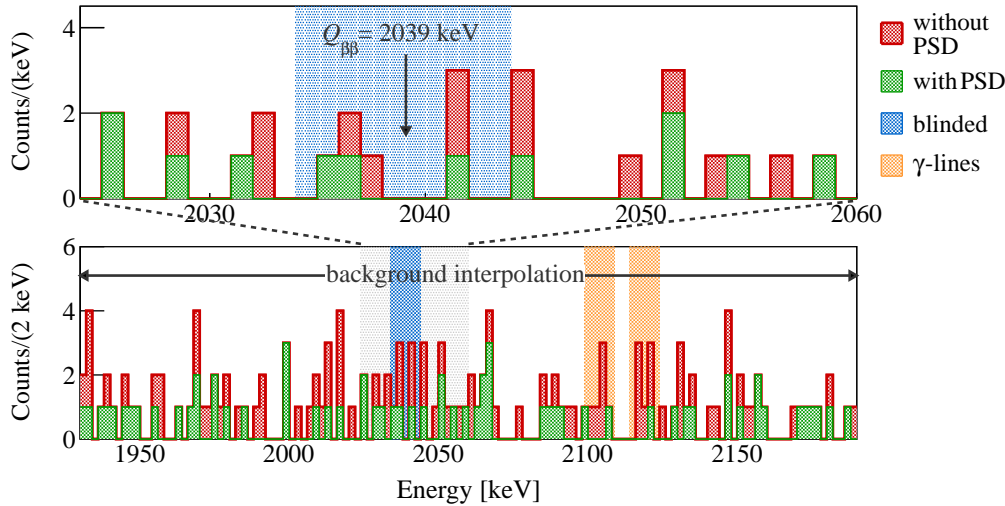
Figure 7.1: Combined energy spectrum from all enriched semi-coaxial and BEGe detectors with (green shaded) and without (red shaded) applied pulse shape discrimination. The region used for the background estimation, namely between $1930\,\text{keV}$ and $2190\,\text{keV}$ excluding the intervals $(2104 \pm 5)\,\text{keV}$ and $(2119 \pm 5)\,\text{keV}$ (both orange shaded) from known γ-lines, (lower half) and a zoom close the FEP of the $0\nu\beta\beta$-decay (upper half) is depicted. The formerly blinded energy range at $Q_{\beta\beta} \pm 5\,\text{keV}$ is illustrated as blue shaded area.

In fact this statement is even further strengthened when additionally applying the pulse shape analysis. After the cut, of the six events from the semi-coaxial detectors, three are classified as SSE, the rest is rejected as background. A cross check with the two alternative discrimination strategies (likelihood and asymmetry) exposed that for five out of the six events the same class identification as either signal or background is yielded by at least one other method. The one event from the BEGe data is as well discarded by the A/E cut and no events remained in the $Q_{\beta\beta} \pm \sigma_{E,k}$ region for this particular subset with $\sigma_{E,k} = \delta E_k/2.35$ being given by the known energy resolution. Hence, the expected background counts and observed number of events are consistent not only for the combined data set but also in all individual subset sets, with or without neural network as well as A/E pulse shape discrimination, such that no indication for a $0\nu\beta\beta$-decay signal and a half-life limit is inferred.

Data set	Detector	Energy [keV]	Date	ANN or A/E response	PSD passed
golden	ANG5	2041.8	18 Nov 2011, 22:52	0.347	no
silver	ANG5	2036.9	23 Jun 2012, 23:02	0.521	yes
golden	RG2	2041.3	16 Dec 2012, 00:09	0.685	yes
BEGe	GD32B	2036.6	28 Dec 2012, 09:50	0.750	no
golden	RG1	2035.5	29 Jan 2013, 03:35	0.696	yes
golden	ANG3	2037.4	02 Mar 2013, 08:08	0.211	no
golden	RG1	2041.7	27 Apr 2013, 22:21	0.368	no

Table 7.2: List of all events within $Q_{\beta\beta} \pm 5\,\text{keV}$. The corresponding cut thresholds of the ANN classifier can be found in table 4.5.

According to equation 2.53, the observed signal count $N_k^{0\nu}$ for each of the three data sets $k = $ "golden", "silver", "BEGe" would (for no verification of a signal) enable to quantify a lower limit on the decay rate, corresponding to the inverse half-life $1/T_{1/2}^{0\nu}$, of the process via the relation:

$$N_k^{0\nu} = \frac{\ln 2 \cdot N_{\text{Avg}} \cdot \mathcal{E}_k \cdot \varepsilon_k}{m_A \cdot T_{1/2}^{0\nu}} \,, \tag{7.1}$$

with N_{Avg} denoting the Avogadro constant. Further $\mathcal{E}_k = M_{\text{det}} \cdot t$ represents the exposure, $m_A = 0.0756\,\text{kg}$ the molar mass of the enriched material and ε_k the efficiency with reference to the individual data subsets. Based on the already stated equation 3.20, the latter quantity is thereby defined as the product of the (set dependent) enrichment fraction f_{76}, the active volume fraction of the detectors f_{av}, the probability ε_{det} of the $0\nu\beta\beta$-events to deposit their entire released energy when occurring in the active volume and - if the pulse shape discrimination is applied on the data - the selection efficiencies ε_{PSD} on the ANN or A/E method discussed above.

As described in [Sch14] the analysis to estimate the $0\nu\beta\beta$-signal strength and a frequentist coverage interval has been conducted corresponding to a profile likelihood approach on the different GERDA Phase I data samples with four free parameters. In doing so, for each of the three subsets the energy spectra have been fitted to a

normalized function $f(E|b_k, 1/T_{1/2}^{0\nu})$, which consists of a constant term b_k attributed to the background as well as a Gaussian peak, with the mean position being centered at $Q_{\beta\beta} \pm 0.2$ keV and a width equal to the standard deviation $\sigma_{E,k} = \delta E_k/2.35$ of the energy resolution δE_k, to also account for a possible $0\nu\beta\beta$-signal. The latter is thereby common to the different data samples. For the background interpolation the 240 keV wide window ranging from a lower energy of 1930 keV up to a maximum value of 2190 keV is used including the now unblindend region around $Q_{\beta\beta}$ but without regarding the intervals (2104 ± 5) keV and (2119 ± 5) keV removed due to known γ-lines arising from the decays of the isotopes ^{208}Tl, ^{214}Bi. Following this assumptions yields the expression:

$$ f(E|b_k, 1/T_{1/2}^{0\nu}) = \frac{1}{240\,\text{keV} \cdot b_k + N_k^{0\nu}} \left(b_k + \frac{N_k^{0\nu}(1/T_{1/2}^{0\nu})}{\sqrt{2\pi} \cdot \sigma_{E,k}} \exp \frac{(E - Q_{\beta\beta})^2}{2\sigma_{E,k}^2} \right) \ , \quad (7.2) $$

where $N_k^{0\nu}(1/T_{1/2}^{0\nu})$ is described by equation 7.1. The (unbinned extended) likelihood $\mathcal{L}$ is then given by

$$ \mathcal{L}(b_k, \varepsilon_k, ..., 1/T_{1/2}^{0\nu}) = \prod_k \frac{\mu_k^{N_k} \cdot e^{-\mu_k}}{N_k!} \prod_{\text{events}} f(E|b_k, 1/T_{1/2}^{0\nu}) $$

$$ \prod_k \left[\frac{1}{\sqrt{2\pi} \cdot \sigma_{\varepsilon,k}} \exp \frac{(\varepsilon_k - \overline{\varepsilon}_k)^2}{2\sigma_{\varepsilon,k}^2} \right] ... \quad (7.3) $$

Hereby the product is calculated over all events with N_k and $\mu_k = \sum_k (b_k \cdot 240\,\text{keV} + N_k^{0\nu})$ signifying each the total number of observed or expected events in the k-th data set, respectively. Concievable systematic errors owing to, for example, the detector parameters or on the resolution, the peak position and all efficiencies have been taken into consideration by additional nuisance parameters in the profile likelihood. The corresponding correction term is in equation 7.3 enclosed by squared brackets and implied for the uncertainty $\sigma_{\varepsilon,k}$ on the efficiency only due to reasons of clarity though, but has been of course also performed in the calculations similarly for all other contributions as well. Correspondingly, the profile likelihood is found to be

$$ \lambda(1/T_{1/2}^{0\nu}) = \frac{\max\limits_{b_k, \varepsilon, ...} \mathcal{L}(b_k, \varepsilon_k, ..., 1/T_{1/2}^{0\nu})}{\max\limits_{\hat{b}_k, \hat{\varepsilon}_k, ..., 1/\hat{T}_{1/2}^{0\nu}} \mathcal{L}(\hat{b}_k, \hat{\varepsilon}_k, ..., 1/\hat{T}_{1/2}^{0\nu})} \ . \quad (7.4) $$

For the likelihood ratio only physically allowed regions have been evaluated, requiring $1/T_{1/2}^{0\nu} \geq 0$ (equatable to $N_k^{0\nu} \geq 0$).

To derive an upper boundary on the (inverse) half-live, an approximation based on the so-called "Wilk theorem" has been conducted. Thereby, according to [Wil38], for high statistics the $-2\ln$ of the ratio of the maximum likelihood can be regarded asymptotically as a χ^2 distribution with p degrees of freedom equal to the difference in dimensionality of the two parameter spaces. Following this approach, the 90 %

coverage limit for one degree of freedom (as it is the case in the above considerations) can be explicitly defined as the $1/T_{1/2}^{0\nu}$ value for which the relation $-2 \cdot \ln \lambda$, with λ being given by the profile likelihood from equation 7.4, fulfils the condition $\chi^2 <$ 2.705, i.e. has changed by a number of 2.705. Further the coverage of this method has been verified using toy Monte Carlo spectra.

With the pulse shape discrimination being applied, the best fit value obtained is $1/T_{1/2}^{0\nu} = 0$ (tantamount to $N^{0\nu} = 0$) emphasizing that no excess above the background has been found. The corresponding 90 % coverage limit for the half-live of the neutrinoless double β-decay on ^{76}Ge could be concluded to

$$T_{1/2}^{0\nu} \ (90\,\%\ \text{C.L.}) > 2.2 \cdot 10^{25}\,\text{yr} \qquad (\text{with PSD})\,, \tag{7.5}$$

which actually marks the world's most stringent value achieved in an $0\nu\beta\beta$-experiment so far.[1] (Please note that the derived value is hereby actually sligtly different to the one previously published in [Ago13a] by the GERDA Collaboration due to another applied fitting algorithm as well as a decreased estimation for the signal efficiency.) If transferred to the number of signal events at $Q_{\beta\beta} \pm 5\,\text{keV}$, this is directly consistent with $N^{0\nu} < 3.2$ counts. Naturally, the quoted limit is weakened due to the uncertainties on the various input parameters (especially the efficiency of $\varepsilon_{\text{PSD}} = 0.83 \pm 0.03$ for the neural network) folded in the final result. However, the effect is found to be very small, since in case of not considering the systematical errors the limit would only improve by roughly 1 %. The respective median sensitivity for the 90 % confidence interval is determined to $2.4 \cdot 10^{25}\,\text{yr}$, given the background levels and the efficiencies collected in table 7.1.

Alternatively, also a Bayesian calculation has been pursued with the same likelihood fit function as well as sampling method for the systematic error estimation. A flat prior in $1/T_{1/2}^{0\nu}$ ranging between 0 and $10^{-24}\,\text{yr}^{-1}$ is assumed and the toolkit BAT is utilized to run the combined analysis on thee different data sets. The evaluated posterior distribution again peaks at $1/T_{1/2}^{0\nu} = 0$ that reverts into the 90 % credible limit of $T_{1/2}^{0\nu} > 1.9 \cdot 10^{25}\text{yr}$ (including folded systematic uncertainties). For the corresponding median sensitivity a value of $2.0 \cdot 10^{25}\,\text{yr}$ is found.

The impact of the pulse shape analysis method developed and presented in the framework of this thesis on the final half-live limit for the $0\nu\beta\beta$-decay from GERDA Phase I, can be easily demonstrated by redoing an frequentist analysis analogous to the one described above, except for simply discounting the ANN selection cut on the semi-coaxial detectors. A result with a significantly decreased 90 % coverage limit of

$$T_{1/2}^{0\nu} \ (90\,\%\ \text{C.L.}) > 1.4 \cdot 10^{25}\,\text{yr} \qquad (\text{without PSD}) \tag{7.6}$$

---

[1]When extending the statistics by further measurements, prosecuted after Phase I and introducing an extra exposure of 1.064 kg·yr, this result can be even strengthened to a new lower boundary on the isotope ^{76}Ge of $T_{1/2}^{0\nu}$ (90 % C.L.) $> 2.3 \cdot 10^{25}\,\text{yr}$. It is worth mentioning though, that this additional data set has not experienced a blinded procedure, making the analysis result potentially biased.

is yielded. Comparing this value with the immensely improved number obtained in equation 7.5 for an applied neural network pattern recognition algorithm, impressively stresses the notably importance of this work.

Comparison to other experiments

To estimate the result on the $T^{0\nu}_{1/2}$-limit obtained within GERDA Phase I in the context of other experiments searching for the $0\nu\beta\beta$-decay of ^{76}Ge, a hypothesis test using the half-life of $1.19^{+0.37}_{-0.23} \cdot 10^{25}$ yr from the by parts of the Heidelberg-Moscow (HdM) Collaboration claimed signal [Kla04] (hypothesis H_1) is performed. When rescaling the corresponding number of counts, GERDA would expect (5.4 ± 1.3) events in the energy interval centered around $Q_{\beta\beta} \pm 2\sigma_{E,k}$ above a background level of (2.0 ± 0.3) after the PSD cuts. This can be compared with the actually detected three events inside the respective energy window, whereby none of them is located in close vicinity to the central position of the neutrinoless double β-decay at $Q_{\beta\beta} \pm \sigma_{E,k}$ though (see tables 7.1 and 7.2).

In a frequentist analysis, 10.000 toy spectra have been generated individually for the "golden", "silver" and "BEGe" data set with Poisson distributed background and signal strengths. Only about $1.9\,\%$ of the best fitted inverse half-life $1/T^{0\nu}_{1/2}$ from the profile likelihood calculations on each of these realizations yielded the experimental result $\sum_k N_k \leq 0$ from GERDA Phase I. Hence the publicated observation of the $0\nu\beta\beta$-decay is strongly refuted with $98.1\,\%$ probability. Instead the limit found by GERDA is consistent with those derived from the HdM [Kla01] (earlier publication, before claim) as well as IGEX [Aal02][Aal04] collaboration, which both also found no indication for a signal, respectively, and sets a new boundary mark in the quest of the neutrinoless double β process related to a possible Majorana nature of the neutrino.

Moreover a Bayesian analysis is as well carried out. Therefore the Bayes factor, defined as the ratio $p(\text{data}|H_1) = p(\text{data}|H_0)$ between the posterior probability of the hypothesis model H_1 with the value of $T^{0\nu}_{1/2}$ from [Kla04] and the opposing hypothesis model H_0, representing the background-only or no-singal assumption supported by the GERDA experiment, has been computed. The factor, including all uncertainties, is ultimately concluded to 0.024 (compare with $p(N^{0\nu} = 0|H_1) = 0.019$ from the profile likelihood analysis above) and thus also clearly disfavours any indication of a peak at $Q_{\beta\beta}$.

At this point it should be mentioned, that the unambiguous, model independent disproof of the claim from 2004 for the discovery of the neutrinoless double β-decay with high probability could not have been accomplished without the employment of the neural network based pulse shape discrimination method on the semi-coaxial detectors developed and presented in the framework of this thesis. After all the result from GERDA Phase I derived without the ANN selection algorithm, is significantly less conclusive, even still compatible with the publication in [Kla04] and thus does not allow for a meaningfull statement on that matter (compare with equation 7.6).

While only those experiments availing themselves of the same isotope do actualy facilitate a model-independent test of the claimed neutrinoless double β-signal in ^{76}Ge, nuclear matrix element (NME) calculations can be used to compare the result obtained within this work to recent limits on the half-lives concluded by means of $\beta\beta$ emitter sources accounted to other elements. The two most stringent boundaries concerning the isotope ^{136}Xe have been thereby provided by the KamLAND-Zen and EXO-200 experiments. As already mentioned in subsection 2.3.4 none of them observed a signal, but instead they found $90\,\%$ confidence level limits of $1.9 \cdot 10^{25}$ yr [Gan13] and $1.6 \cdot 10^{25}$ yr [Aug12] for the half-life, respectively.[2]
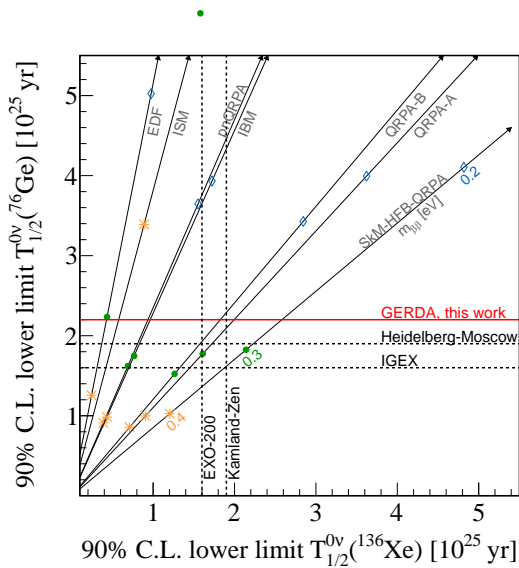
Figure 7.2: Comparison of recent $90\,\%$ C.L. $T^{0\nu}_{1/2}$ limits for ^{76}Ge and ^{136}Xe along with the correlations of the half-lives for selected NME calculations under the assumption of light neutrino exchange. The different regarded methods are taken from [Rod10] (EDF), [Men09] (ISM), [Suh10] (pn-QRPA), [Bar13] (IBM), [Sim13] (QRPA), [Mus13] (SkM-HFB-QRPA) and no axial vector quenching is considered: $g_A = 1.25$. Also shown are the corresponding estimations on the effective neutrino mass $m_{\beta\beta}$ when assuming values of $0.2\,$eV (blue diamonds), $0.3\,$eV (green dots) and $0.4\,$eV (orange stars). Graphics adapted from [Sch14].

Figure 7.2 depicts the different experimental lower limits on $T^{0\nu}_{1/2}$ for ^{76}Ge (value of this work is labeled in red) and ^{136}Xe together with the correlations for a selection of different predictions on the NME, assuming that the exchange of light Majorana neutrinos is the leading mechanism. As can be assured by equation 2.50 in this case, the ratio of the $0\nu\beta\beta$ half-lives is directly proportional to the square of the ratio between the nuclear matrix elements $\mathcal{M}_{0\nu}(^{76}$Ge$)/\mathcal{M}_{0\nu}(^{136}Xe)$. The computations have been thereby already partly reported in subsection 2.3.2 and are here in particular extracted from [Rod10] (EDF), [Men09] (ISM), [Suh10] (pnQRPA), [Bar13] (IBM), [Sim13] (QRPA), [Mus13] (SkM-HFB-QRPA).

Also depicted are the model-dependent estimations on the effective electron neutrino mass $m_{\beta\beta}$ for three different absolute values of $0.2\,$eV (blue diamonds), $0.3\,$eV (green dots) and $0.4\,$eV (orange stars). No axial vector quenching is assumed, i.e. the ratio of the vector and axial-vector coupling constant obeys the standard parameterization $g_A = 1.25$ (for a brief review on that matter see also [Smo10]). Furthermore

---

[2]Only recently, at the time of writing, EXO-200 announced an updated result using an exposure increased by a factor of 3.8 and thus yielding a sensitivity improvement from $0.7 \cdot 10^{25}$ yr with respect to the former publication to now $1.9 \cdot 10^{25}$ yr. However, the derived $90\,\%$ C.L. half-live limit is only $T^{0\nu}_{1/2} > 1.1 \cdot 10^{25}$ yr [Alb14], hence the following discussen is restricted to the previously published value.

the recently reevaluated phase space factor from [Kot12] enter the computations. Conclusively the range for the upper limit on the effective electron neutrino mass $m_{\beta\beta}$ obtained from the analysis of GERDA Phase I data pursued in the framework of this thesis is concluded to $0.3 - 0.5$ eV.

8. Summary and conclusion

In the event of neutrinoless double β-decay ($0\nu\beta\beta$), a process that is theoretically predicted to occur in many extensions of the Standard Model of particle physics, lepton number conservation is violated. Hence a large interest for a quantitative determination of this, if existent, very rare second order decay mode engendered, resulting in a growing number of past, present and future experimental programs in order to solidify the base for advanced theories beyond the known physical explanatory models on particle interactions. Moreover, its detection would directly prove the Majorana nature of at least a part of the neutrino mass and even shed light upon the neutrino mass hierarchy by allowing for an indirect measurement on the absolute scale. By using predictions for the nuclear matrix element (NME), indeed an effective neutrino mass can be evaluated under the assumption of light Majorana neutrino exchange to be the dominating mechanism leading to the process. The experimental signature of the $0\nu\beta\beta$-signal is traceable as a narrow peak at the Q-value of the decay. However, none of the recent attempts have found evidence for such a process - except one. In [Kla04] part of the HdM Collaboration went public claiming the observation for the neutrinoless double β-decay of ^{76}Ge, specifying the corresponding half-live to $T_{1/2}^{0\nu} = 1.19_{-0.23}^{+0.37} \cdot 10^{25}$ yr, which could not be unambiguously scrutinized yet.

The GERDA apparatus located at the Laboratori Nazionali del Gran Sasso (LNGS) of INFN in Italy operates high-purity germanium (HPGe) diodes of mainly semi-coaxial and to a small extend also Broad Energy Germanium (BEGe) type made from isotopically modified material enriched to a fraction of $\approx 86\%$ in ^{76}Ge. Since the same isotope as in [Kla04] is employed, the experiment is ideally suited to confirm or disproof the above mentioned report of discovery in a model independent approach. In a first period of data taking from November 2011 to May 2013 also referred to as "Phase I", a total exposure of 21.6 kg·yr has been collected. Key for the success to either determine a possible neutrinoless double β-process or, in case of no observation, derive a lower limit on the half-life of the signal, is a relyable strategy for an effective background suppression and thus enhancement of the experimental sensitivity.

On that account, in the framework of this thesis a pulse shape selection technique, based on the *Artificial Neural Network* (ANN) method, was introduced and applied to the GERDA Phase I data as an essential part of the official $0\nu\beta\beta$-analysis recently presented in [Ago13a]. The development of the selection algorithm has been pursued with special emphasis on the semi-coaxial HPGe detector type, that constituted with a net exposure of 19.2 kg·yr the by far predominant part of the total statistics. The working principle relies on the time dependence of the detector current pulse that can be utilized to conveniently identify background contributions. Signal-like events related to a $0\nu\beta\beta$-decay deposit their entire released energy within a small, localized

volume if the emitted electrons lose only little energy by bremsstrahlung (single site event, SSE). On the contrary, in background-like events, resulting for instance from photons interacting via multiple Compton scattering, ionization often takes place at several, spatially well separated locations within the detector (multi site event, MSE). Conclusively, the pulse shape will be in general different for these two event classes. To avoid biases in the event selection, a blind analysis has been performed with a $\pm 5\,\text{keV}$ wide energy window centered around $Q_{\beta\beta} = 2039\,\text{keV}$ being kept hidden.

Different multivariate algorithms based on a "supervised learning" method were studied and optimized with regard to yield the best possible selection performance on the GERDA Phase I data. According to the criteria of achieving the most effective background rejection, while retaining a considerably high signal efficiency, an approach consisting of a feed-forward multi-layer perceptron was established. For the training process, the pattern recognition structure has been supported by user-supplied sample sets of known event composition attained from ^{228}Th calibration measurements regularly performed on a (bi-)weekly basis with the aim to track the data quality as well as energy resolution stability of the different germanium crystals. The data was thoughtfully divided into three subsets of similar properties with respect to e.g. the experimental setup configuration or the induced background level close to $Q_{\beta\beta}$ within the physics runs. Hence, the learing procedure was pursued for not only each detector, but also the separate intervals of Phase I individually. Special care has been further laid on investigating the possible occurrence of overtraining and it could be - with the usage of a dedicated test sample set - ascertained that indeed no such effects are present.

In a first step, the event identification performance of the developed estimator was scrutinized by extending the analysis on the overall calibration spectrum and the physics data. Given the graded shielding design and the novel technique of submerging the germanium detectors directly into liquid argon (LAr) applied in GERDA, only very few background counts are expected at $Q_{\beta\beta}$. Consequently, a moderate rejection with still maintaining a high share of the $0\nu\beta\beta$-efficiency, is preferably envisaged. Therefore the cut on the classifier output of the neural network has been fixed by determining the detector specific threshold value where $90\,\%$ of the calibration double escape peak (DEP) events from ^{208}Tl, that are conspicuous for their predominantly SSE character and thus approximately serve as reference for the neutrinoless double β-decay, are kept. An additional inspection in the context of the DEP intensity after application of the ANN cut revealed a stable behaviour in time. It was further estimated that, under this condition for the classifier threshold, on average about $65\,\%$ of those γ-line events of exclusively multi site topology can be effectively rejected. The corresponding effect on the physics data is typically compared in the energy interval used for the $0\nu\beta\beta$-analysis between $1930 - 2190\,\text{keV}$ around $Q_{\beta\beta}$ - with the blinded window as well as the two intervals $2104 \pm 5\,\text{keV}$ (SEP of ^{208}Tl line) and $2119 \pm 5\,\text{keV}$ (^{214}Bi line) being removed - also denoted as region of interest (ROI). Thereon the background identification fraction was quantified to $45\,\%$ resulting in a background index BI of roughly $1 \cdot 10^{-2}\,\text{keV·kg·yr}$, which marks an order of mag-

nitude improvement if compared to predecessor experiments. This unprecedented low background count rate as a prerequisite for the so far as well outstanding sensitivity achieved within the GERDA experiment has been thereby rendered possible especially on account of the PSD selection outlined within this thesis.

As an integral component of this work, also several consistency checks were conducted on the experimental data with special focus on a verification of the developed selection algorithm and an extraction of the systematic uncertainty on the $0\nu\beta\beta$-efficiency. That included, amongst other methods, a comparison of the neural network rules with two independently proposed PSD algorithms based on a likelihood and current pulse asymmetry approach, respectively. Eventhough availing themselves of very different techniques, they were found to identify a remarkably similar set as background: each event in the ROI identified by the ANN qualifier as MSE is at least rejected by one, almost $95\,\%$ of them are refuted by both of the alternative methods. In another essential conjecture made for the pulse shape analysis presented in this dissertation, the calibration DEP from ^{208}Tl was employed as signal proxy for the training epoch of the multivariate classifier. Since the probability of the two $511\,\mathrm{keV}$ photons to escape is larger at the outer surface of the detector volume, the distribution of the double escape peak events is different to the homogeneously occurring neutrinoless decay mode and thus introducing a conceivable volume effect into the PSD algorithm. As a consequence the survival fractions attributed to the DEP and the $0\nu\beta\beta$-signal might differ from each other to a noticeable degree. The quantitative impact has been particularly examined by the SSE-rich energy range $1000 - 1300\,\mathrm{keV}$, which consists according to the GERDA background model in [Ago13b] to $75\,\%$ of homogeneously distributed $2\nu\beta\beta$ events. As a result, the efficiency of the neural network algorithm on the neutrino accompanied double β-decay was evaluated to be $(85 \pm 2)\,\%$. Furthermore an important validation using the Compton edge (CE) region along with multi Compton scattered (MCS) γ-ray events has been conducted allowing for an extraction of a clean SSE distribution at an energy above $Q_{\beta\beta}$. The corresponding survival fraction was hereby determined to range between $(86 - 93)\,\%$ for the different semi-coaxial crystals and data sets and led to the conclusion that no sizable energy dependencies are present. After the cessation of the Phase I measurements, a supplemental calibration spectrum has been taken with a ^{56}Co source providing access to two usable DEPs of sufficient statistics in vicinity to $Q_{\beta\beta}$. Subsequently applying the multivariate selection rules on them, has yielded efficiencies varying from $(80 - 94)\,\%$ depending on the different detector channels and further supports the absence of any energy related effects on the ANN selection cut.

In summary, the above described comprehensive accordance gives reasonable confidence that the identification of background events by the neural network recognition pattern is indeed meaningful. Apart from these complementary studies on experimentally gained measurements only, also a detailed Monte Carlo + Finite Elemente Method (FEM) campaign has been launched, in order to compute the interaction points attributed to energy depositions inside the active detector volume as well as

the corresponding signal traces induced on the read-out electrode by the movement of the charge carriers. The simulations were carried out within the GEANT4 based MAGE and the ADL frameworks incorporating all fundamental configurations of the experimental setup. In virtue of the revealed significant volume dependency, the efficiency of the multivariate ANN method on the $0\nu\beta\beta$-signal has been conservatively concluded to $\varepsilon_{0\nu\beta\beta} = (83 \pm 3)\,\%$ - as inferred from the simulation efforts with the different observed systematic uncertainties being quadratically combined.

Owing to the promising results on the robustness and relyability when being adapted to the GERDA Phase I data or simulation computations, the multivariate classification method presented in the framework of this thesis became the preferred and official PSD algorithm used for the final $0\nu\beta\beta$-analysis of the experiment. After processing the blinded window at $Q_{\beta\beta}$ in total seven events were observed: of the six counts from the semi-coaxial detectors, three were classified as SSE by the neural network selection - which is consistent with expectations, where no excess above a flat background contribution and thus no indication for a $0\nu\beta\beta$-signal is found. A lower half-life limit of

$$T_{1/2}^{0\nu}\ (90\,\%\ \text{C.L.}) > 2.2 \cdot 10^{25}\ \text{yr}$$

for the neutrinoless double β-decay of ^{76}Ge has been established representing the most precise measurement so far. Hereby the derived value sligtly deviates from the one published in [Ago13a] by the GERDA Collaboration owing to a different applied fitting algorithm as well as a decreased estimation for the signal efficiency. Therefore the result does not support the previous discovery publicated in [Kla04], but instead strongly rejects the long-standing claim in a frequentist hypothesis test with about $98.1\,\%$ probability. However, this statement could in particular be accomplished due to the application of the neural network based pulse shape discrimination method developed and presented in the framework of this thesis. Not considering the ANN selection cut in the $0\nu\beta\beta$-analysis, would have instead yielded a drastically decreased $90\,\%$ coverage limit of $T_{1/2}^{0\nu} > 1.4 \cdot 10^{25}\ \text{yr}$ though, which surely does neither allow for a confirmation nor a disproof on the claimed observation.

Assuming the exchange of a light Majorana neutrino as the dominating mechanism of the process, the lower limit on $T_{1/2}^{0\nu}$ can be further adduced to calculate an upper limit on the effective Majorana neutrino mass yielding

$$|m_{\beta\beta}| < 0.3 - 0.5\,\text{eV}\ .$$

Conclusively, the results found by GERDA Phase I call for a further exploration of the neutrinoless double β-decay and the effective Majorana neutrino mass. Therefore a second period of the experiment, GERDA Phase II, is pursued to start commissioning within the present year 2014 aiming for a sensitivity increased by a factor of $\sim$10 corresponding to $T_{1/2}^{0\nu} > 1 - 2 \cdot 10^{26}\ \text{yr}$. As the semi-coaxial detector type is expected to again contribute a notable part of the overall $\beta\beta$-emitter mass, multivariate event discrimination techniques are expected to continuously play a major role in the $0\nu\beta\beta$-analysis.

A. Calculation of statistic uncertainty

The statistical error σ_ε on the γ-line net survival fraction ε remaining after applying the pulse shape discrimination (PSD) cut has been computed according to a counting approach (i.e. no fit of the spectrum is performed).
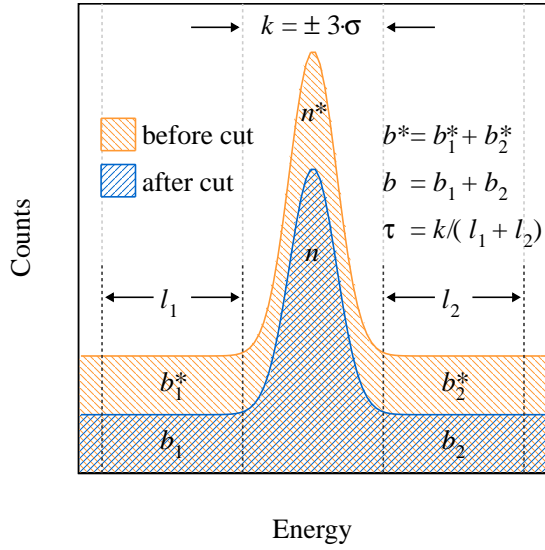

Figure A.1: Schematic depiction to underline the remarks on the calculation of the statistical uncertainty with attached labeling for the used variables. The spectral shapes before and after adaption of the PSD cut are illustrated as hatched orange or hatched blue area, respectively. Further the different ranges signifying the peak regions or the energy side band intervals are each implied by vertical dashed lines. The corresponding widths of the single regions are indicated by black arrows.

As uncorrelated parameters thereby n, denoting the number of events in the peak energy window around $\pm 3 \cdot \sigma$ accepted by the PSD, and n^*, representing the corresponding number of events in the same energy interval rejected by the PSD, have been assumed to perform the calculations. Further the same variables for the "side bands" at either lower or higher energy regions with respect to the γ-line position, used for the subtraction of the Compton continuum, are assigned to $b = b_1 + b_2$ and $b^* = b_1^* + b_2^*$ (see figure A.1, where again the superscript (star sign) implies whether the quantity is approved or refuted by the pulse shape selection). This leads to the following net count in the peak structure after the Compton events have been subducted:

$$
\begin{aligned}
s &= n - \tau \cdot b \, , \\
s_0 &= (n + n^*) - \tau \cdot (b + b^*) \, .
\end{aligned}
\tag{A.1}
$$

Here s_0 and s signify each those event numbers before and after deploying the selection algorithm with τ being the ratio of the energy window widths for $n(n^*) = k = \pm 3 \cdot \sigma$ and $b(b^*) = l_1 + l_2$ (often the interval for the energy side bands is chosen twice as large, such that $\tau = 0.5$). Hence the survival fraction is found to be given by

$$
\varepsilon = \frac{s}{s_0} = \frac{n - \tau \cdot b}{(n + n^*) - \tau \cdot (b + b^*)} \, .
\tag{A.2}
$$

Since for the independent variables no correlations have to be considered, the uncertainty (standard deviation) can be derived by the usual error propagation

$$\sigma_\varepsilon = \sqrt{\left(\frac{\partial\varepsilon}{\partial n}\cdot\Delta n\right)^2 + \left(\frac{\partial\varepsilon}{\partial b}\cdot\Delta b\right)^2 + \left(\frac{\partial\varepsilon}{\partial n^*}\cdot\Delta n^*\right)^2 + \left(\frac{\partial\varepsilon}{\partial b^*}\cdot\Delta b^*\right)^2} \; . \qquad (A.3)$$

When additionally availing oneselves of the so-called "quotient rule" $f' = (u/v)' = (u'\cdot v - u\cdot v')/v^2$ the single partial derivatives in equation A.3 can be easily written as

$$\begin{aligned}
\frac{\partial\varepsilon}{\partial n} &= \frac{s_0 - s}{s_0^2}\\[2mm]
\frac{\partial\varepsilon}{\partial b} &= -\frac{\tau\cdot(s_0 - s)}{s_0^2}\\[2mm]
\frac{\partial\varepsilon}{\partial n'} &= -\frac{s}{s_0^2}\\[2mm]
\frac{\partial\varepsilon}{\partial b'} &= -\frac{\tau\cdot s}{s_0^2} \; .
\end{aligned} \qquad (A.4)$$

Conclusively, the final formula for the statistical error on the survival fraction is then defined by

$$\sigma_\varepsilon = \sqrt{\frac{(s_0 - s)^2\cdot n + \tau^2\cdot(s_0 - s)\cdot b + s^2\cdot n^* + \tau^2\cdot s^2\cdot b^*}{s_0^4}} \; . \qquad (A.5)$$

B. Addendum to figures

B.1 Chapter 4

B.1.1 Energy dependency
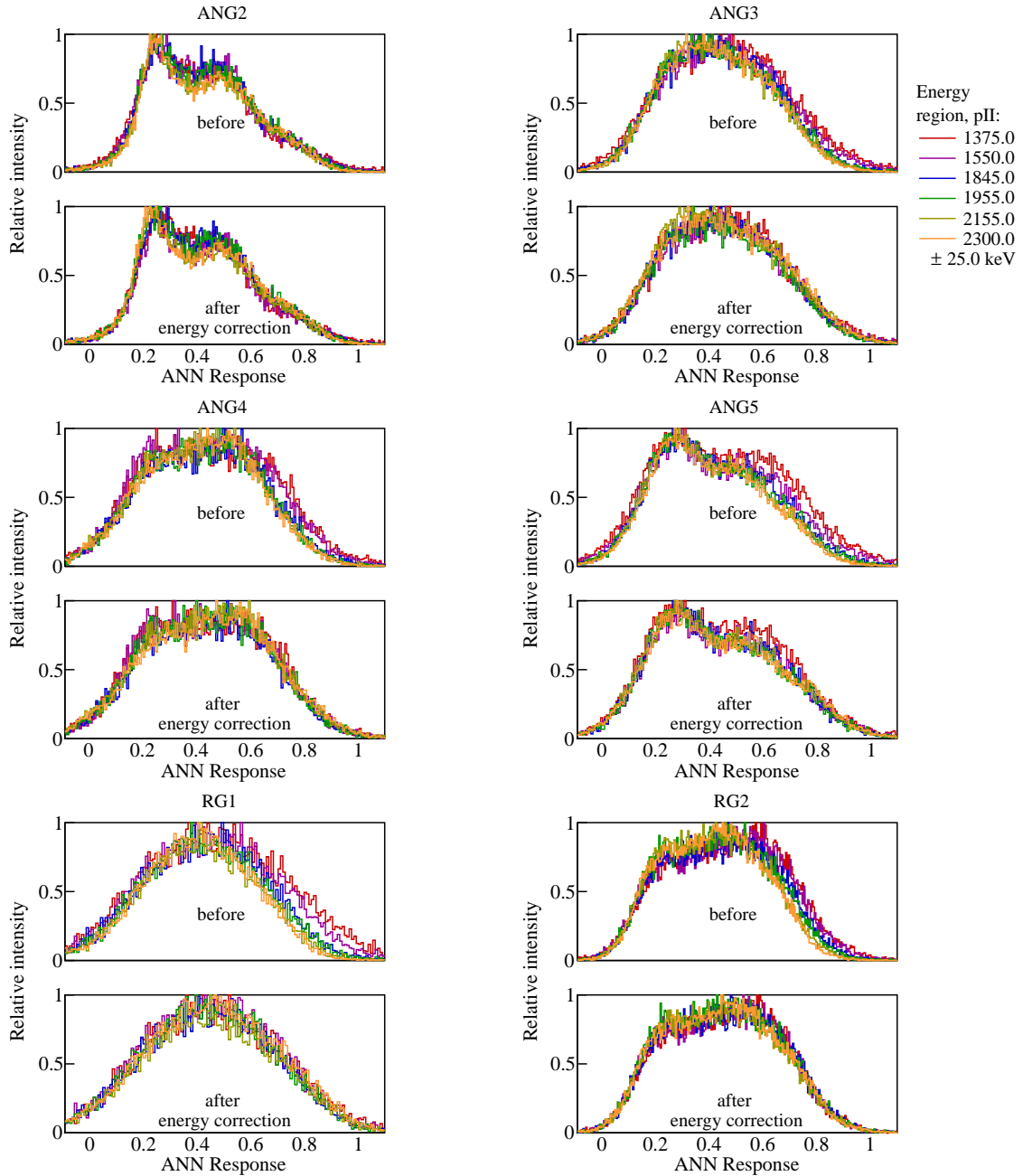
Figure B.1: ANN response for Compton events at six different energy regions without (upper half) and with (lower half) applied energy correction. Distributions are shown for the semi-coaxial detectors and period pII of Phase I data taking.
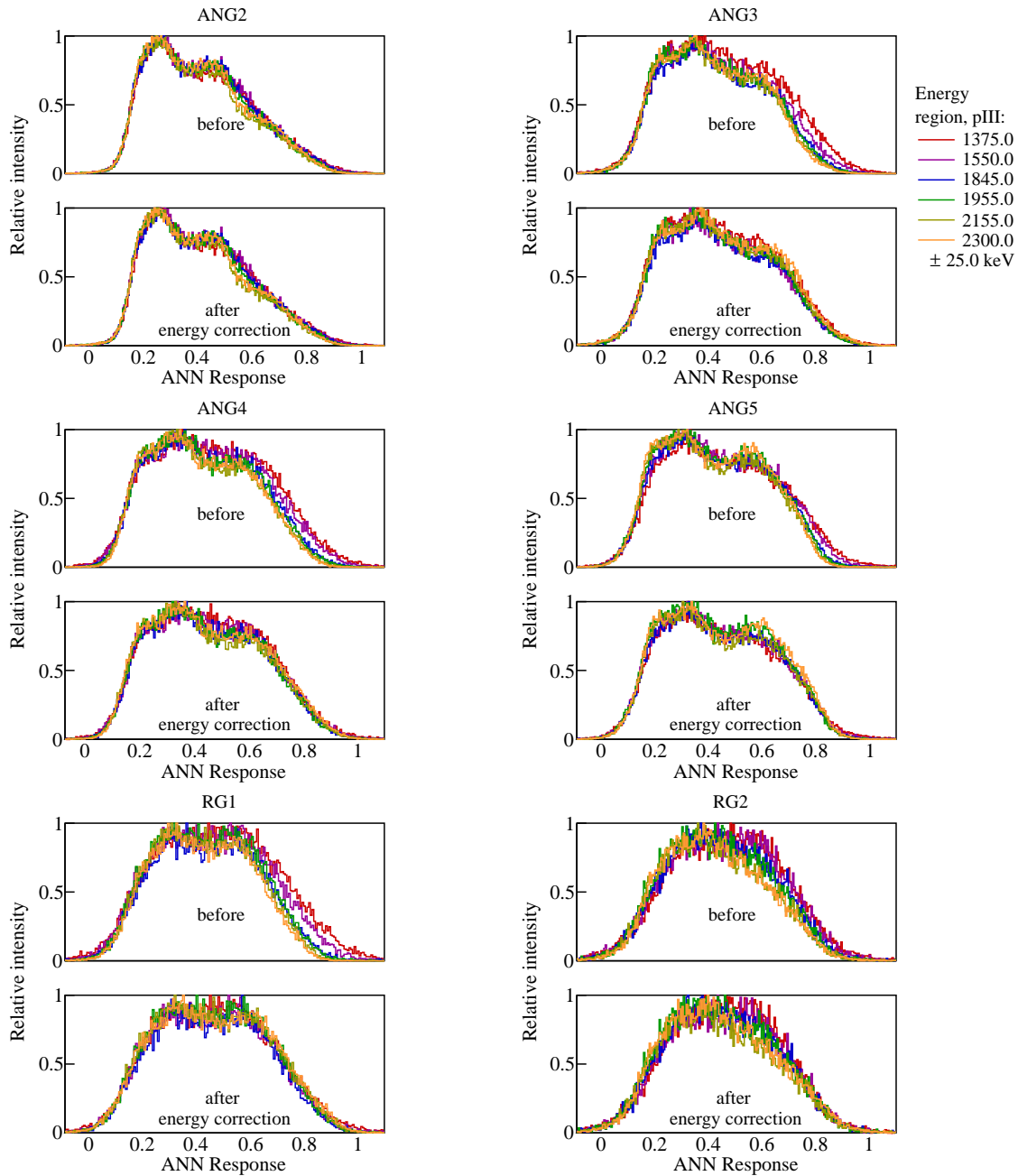
Figure B.2: ANN response for Compton events at six different energy regions without (upper half) and with (lower half) applied energy correction. Distributions are shown for the semi-coaxial detectors and period pIII of Phase I data taking.

B.1.2 ANN Response versus Energy
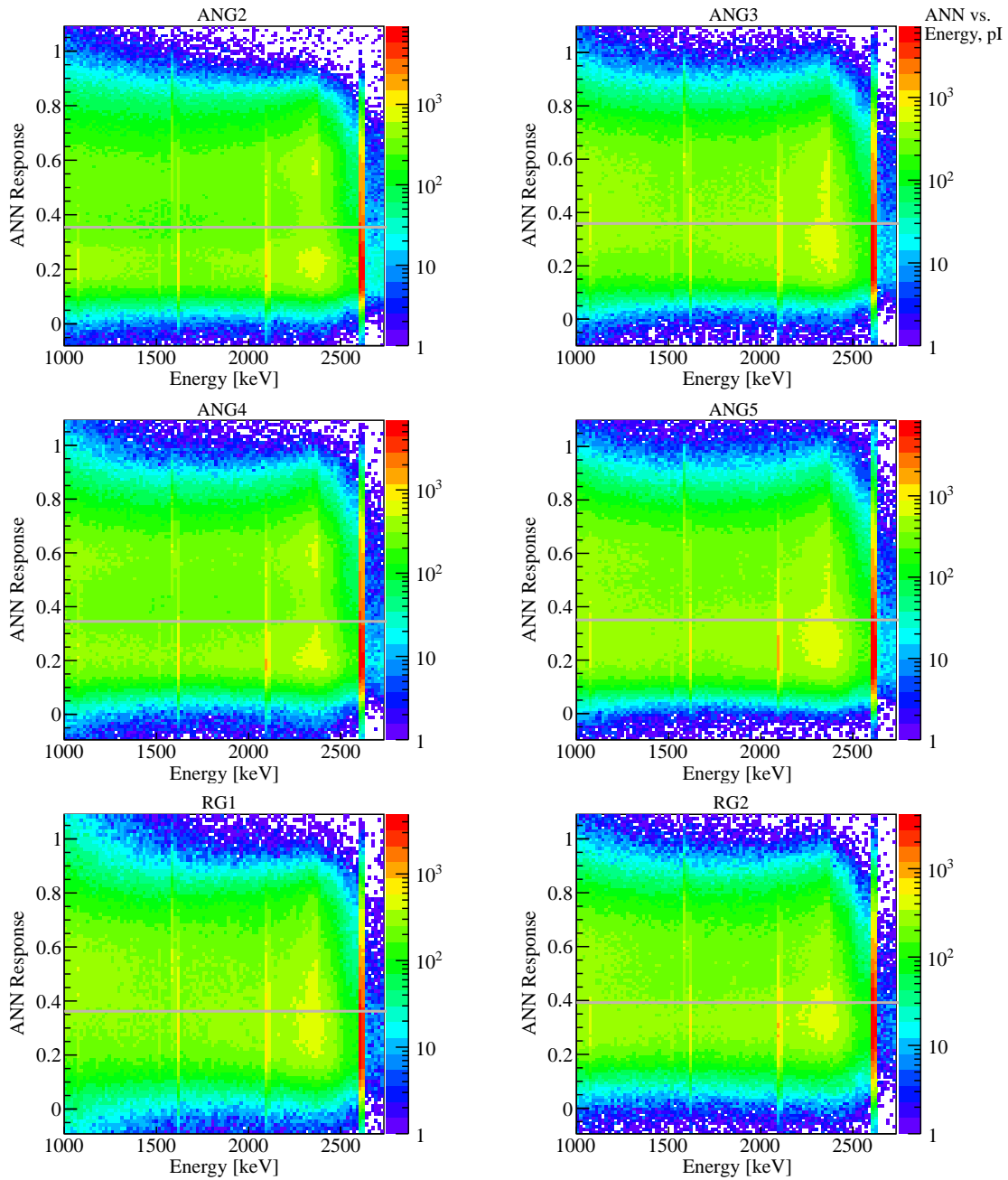
Figure B.3: ANN classifier response versus energy distribution for ^{228}Th calibration events of the semi-coaxial detectors and period pI. The horizontal gray line illustrates the position where 90 % of the DEP events are retained.
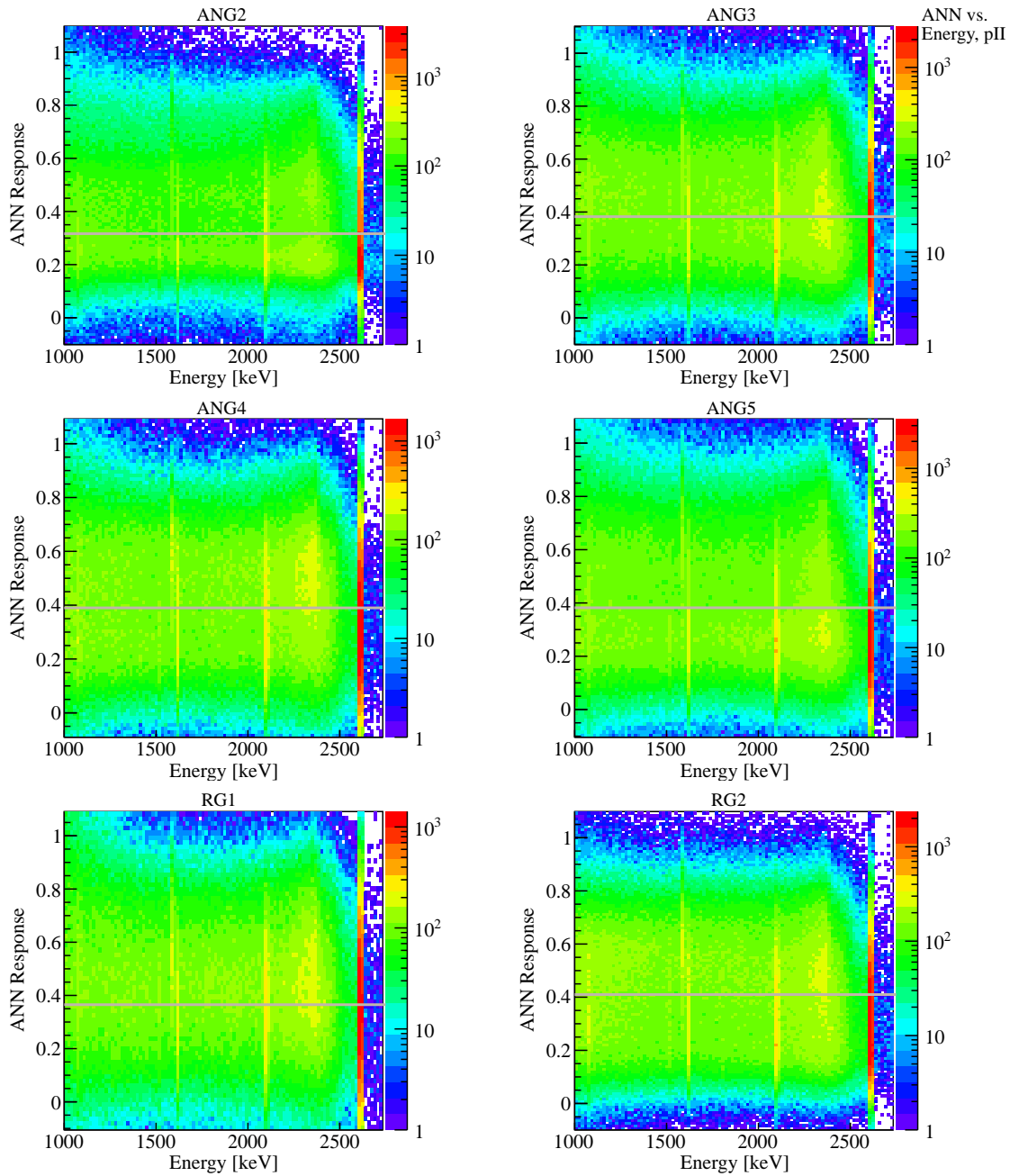
Figure B.4: ANN classifier response versus energy distribution for ^{228}Th calibration events of the semi-coaxial detectors and period pII. The horizontal gray line illustrates the position where 90 % of the DEP events are retained.
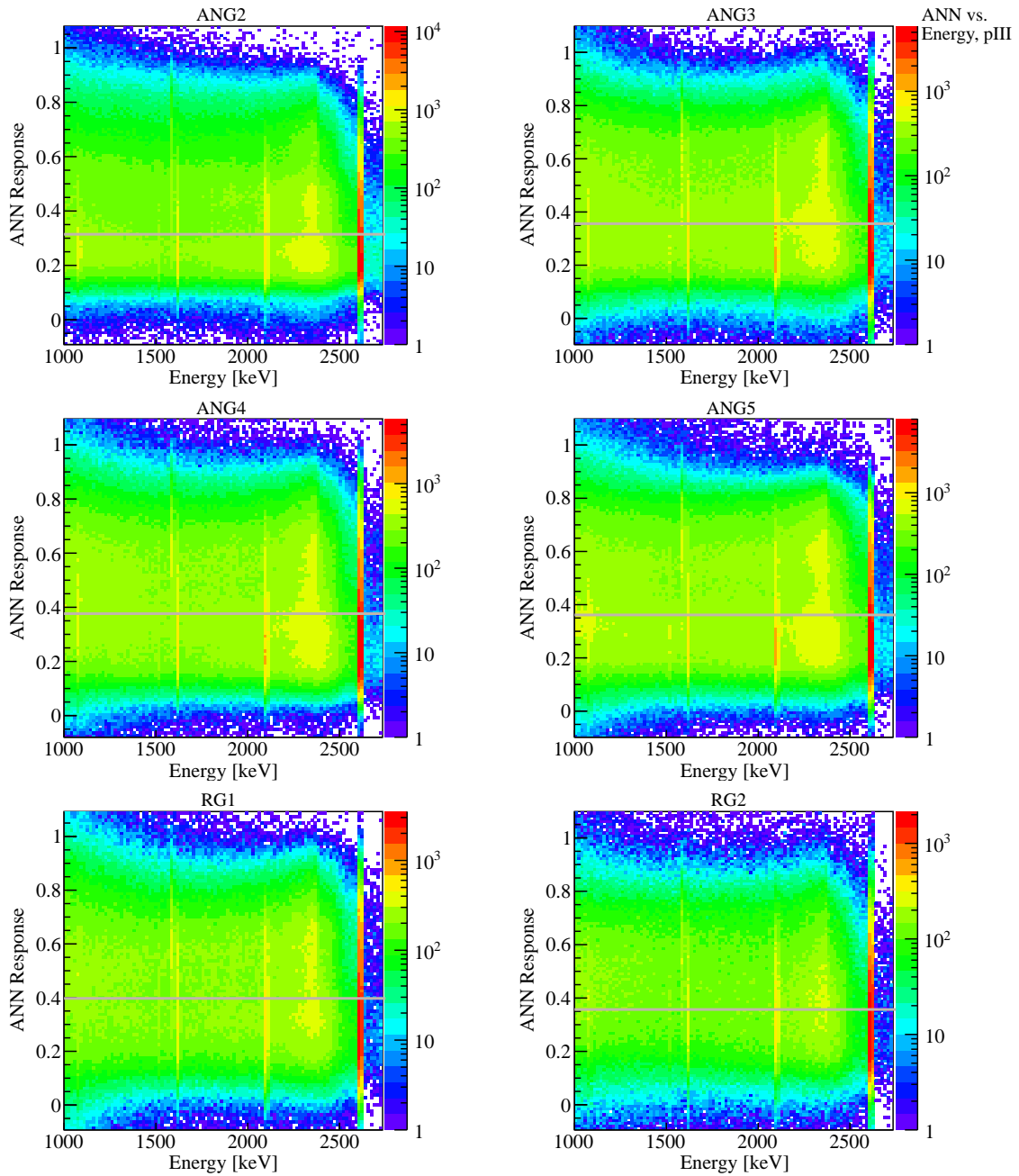
Figure B.5: ANN classifier response versus energy distribution for ^{228}Th calibration events of the semi-coaxial detectors and period pIII. The horizontal gray line illustrates the position where 90 % of the DEP events are retained.

B.1.3   ANN cut on calibration
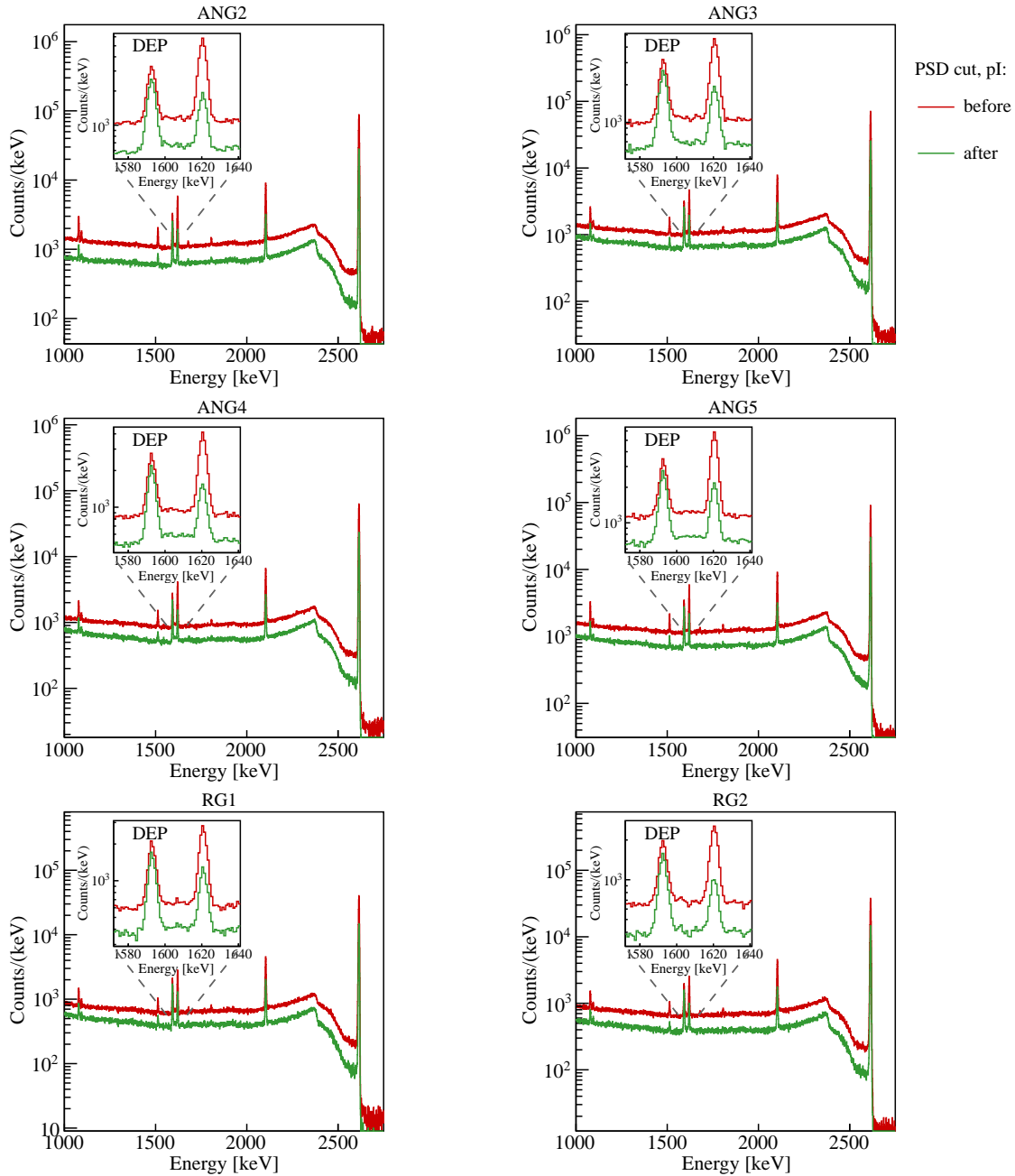
Figure B.6: ^{228}Th calibration spectrum without (red) or with (green) PSD cut for the semi-coaxial detectors and pI of Phase I data taking, where the cut is fixed for a survival fraction of 90 % in the DEP (see inset).
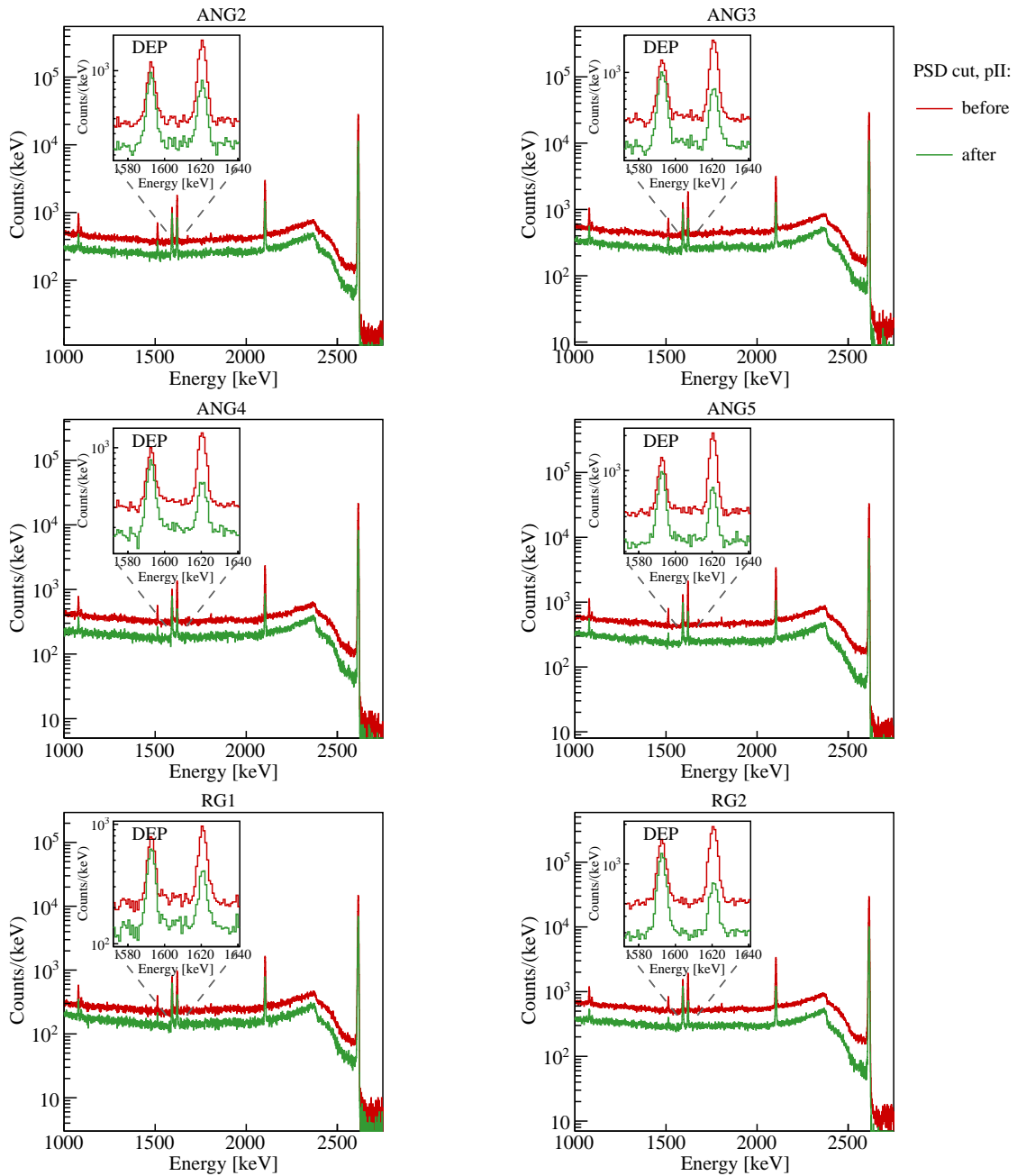
Figure B.7: ^{228}Th calibration spectrum without (red) or with (green) PSD cut for the semi-coaxial detectors and pII of Phase I data taking, where the cut is fixed for a survival fraction of 90 % in the DEP (see inset).
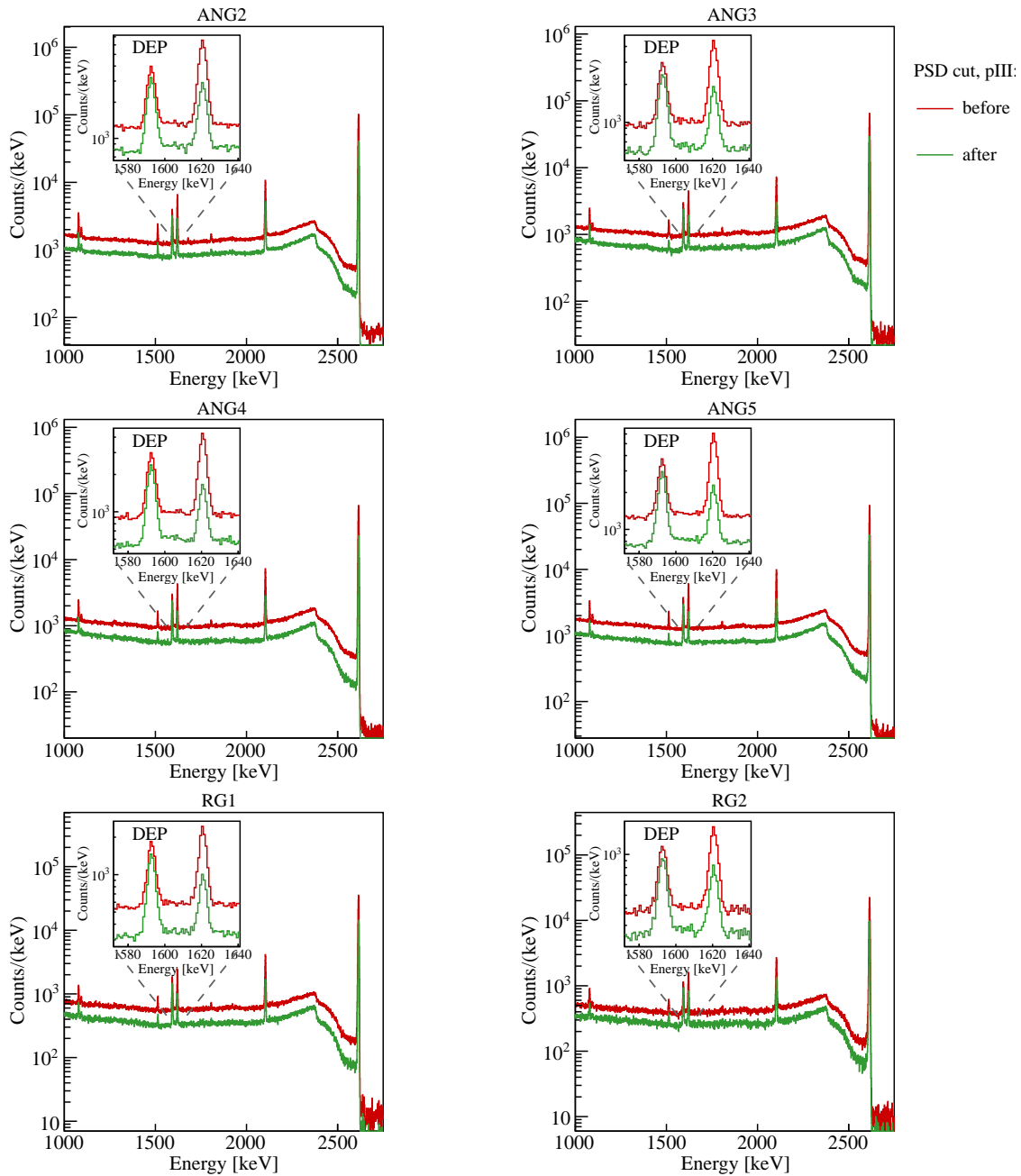
Figure B.8: ^{228}Th calibration spectrum without (red) or with (green) PSD cut for the semi-coaxial detectors and pIII of Phase I data taking, where the cut is fixed for a survival fraction of 90 % in the DEP (see inset).

B.2 Chapter 5

B.2.1 ANN Response distributions
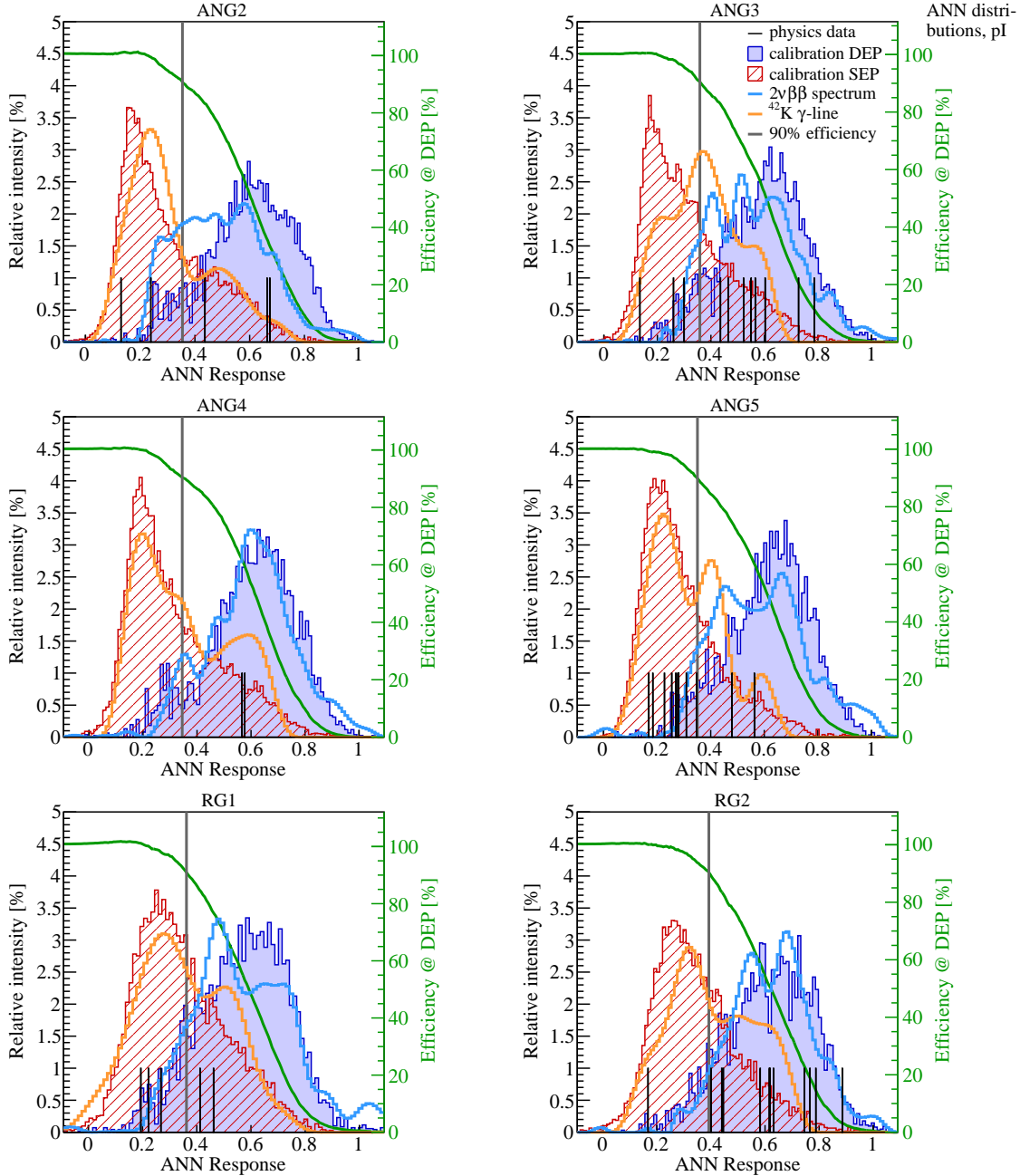
Figure B.9: ANN response distributions for the semi-coaxial detectors of period pI. ^{228}Th calibration events of the DEP (blue filled area) and SEP (red hatched area) are shown along with the survival fraction in the double escape peak versus the cut position (green), where the grey vertical line marks the threshold corresponding to a number of 90 %. Also displayed are the qualifier values of physics data events from the ROI (black), the FEP of ^{42}K (orange) as well as the interval $1000 - 1400$ keV dominated by the $2\nu\beta\beta$-decay (cyan).
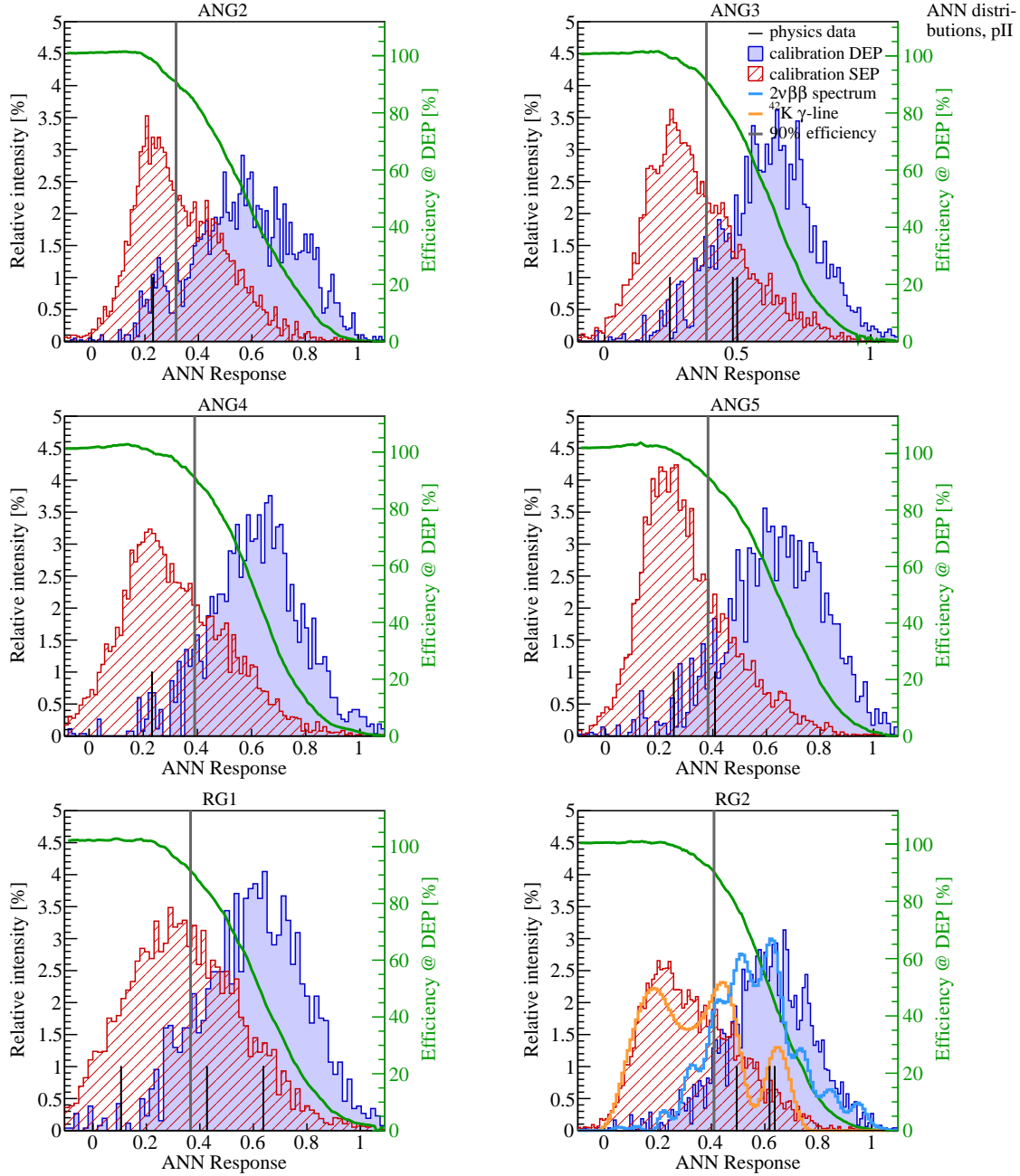
Figure B.10: ANN output distributions for the semi-coaxial detectors of period pII. ^{228}Th calibration events of the DEP (blue filled area) and SEP (red hatched area) are shown along with the survival fraction in the double escape peak versus the cut position (green), where the grey vertical line marks the threshold corresponding to a number of 90 %. Also displayed are the qualifier values of physics data events from the ROI (black), the FEP of ^{42}K (orange) as well as the interval $1000 - 1400$ keV dominated by the $2\nu\beta\beta$-decay (cyan).

B.2.2 Survival fraction at Compton edge
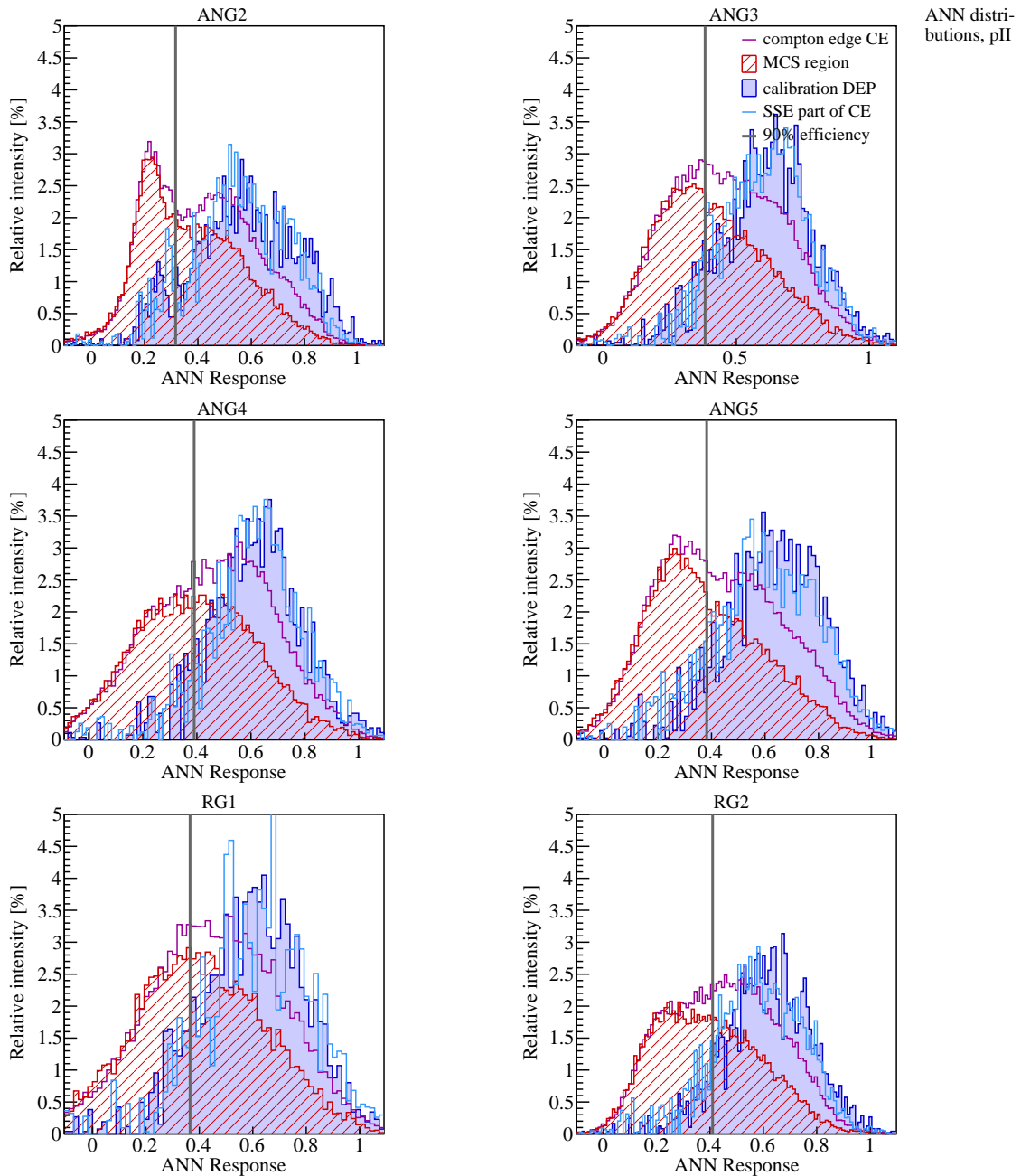
Figure B.11: ANN response for events at the Compton edge (CE, magenta) as a linear combination of "multi Compton scattered" (MCS, red hatched area) and DEP (blue filled area) distributions. Also shown is the CE after subtraction of the MCS part (cyan). The respective ANN threshold according to a 90 % efficiency in the DEP is emphasized as vertical gray line. Data are attributed to period pII.
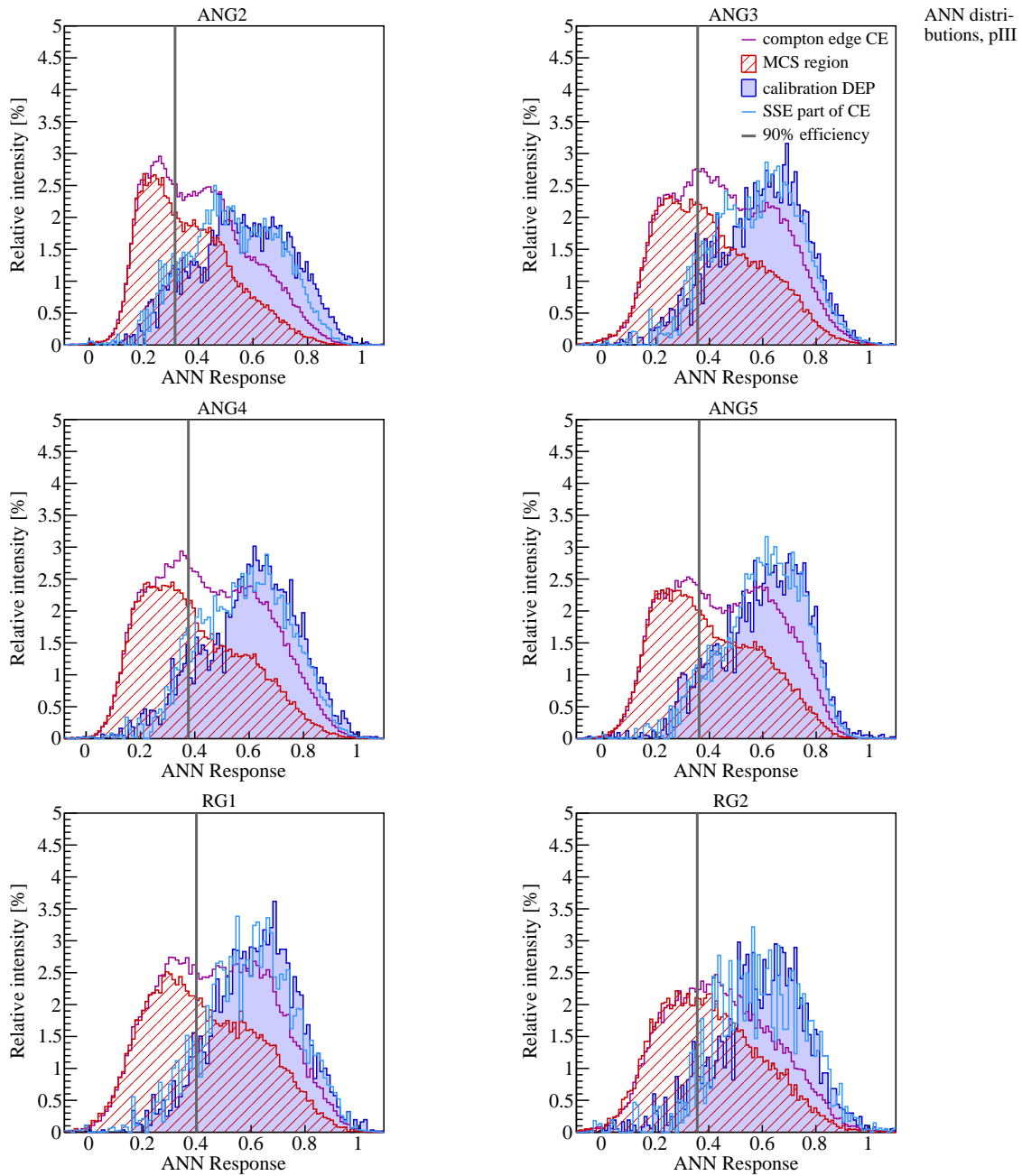
Figure B.12: ANN response for events at the Compton edge (CE, magenta) as a linear combination of "multi Compton scattered" (MCS, red hatched area) and DEP (blue filled area) distributions. Also shown is the CE after subtraction of the MCS part (cyan). The respective ANN threshold according to a 90 % efficiency in the DEP is emphasized as vertical gray line. Data are attributed to period pIII.

B.2.3   ANN Response on calibration versus Energy for pIII + Run 47
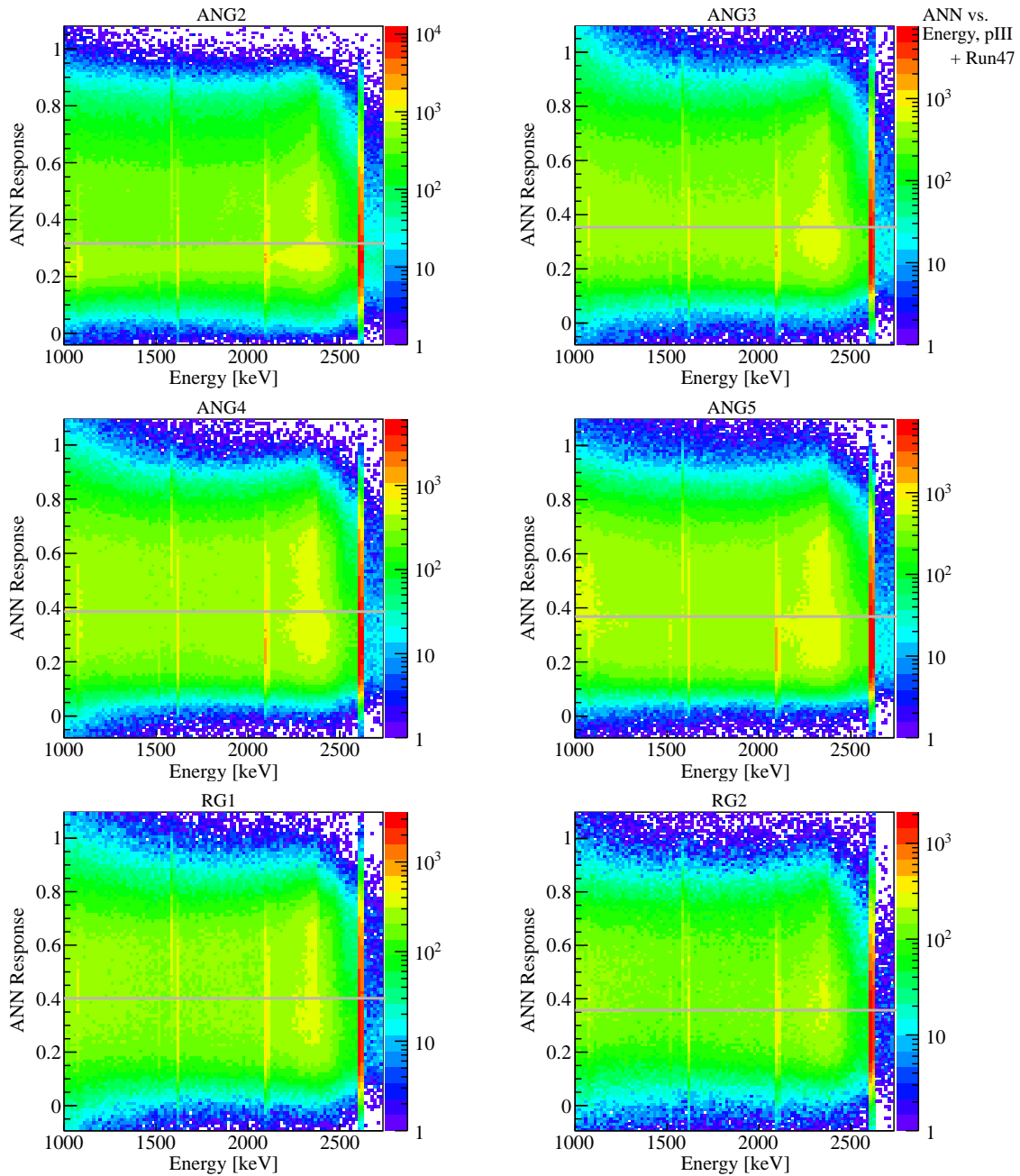
Figure B.13: ANN classifier response versus energy distribution for ^{228}Th calibration events of the semi-coaxial detectors and period pIII + Run 47. The horizontal gray line illustrates the position where 90 % of the DEP events are retained.

B.2.4   ANN cut on calibration for pIII + Run 47
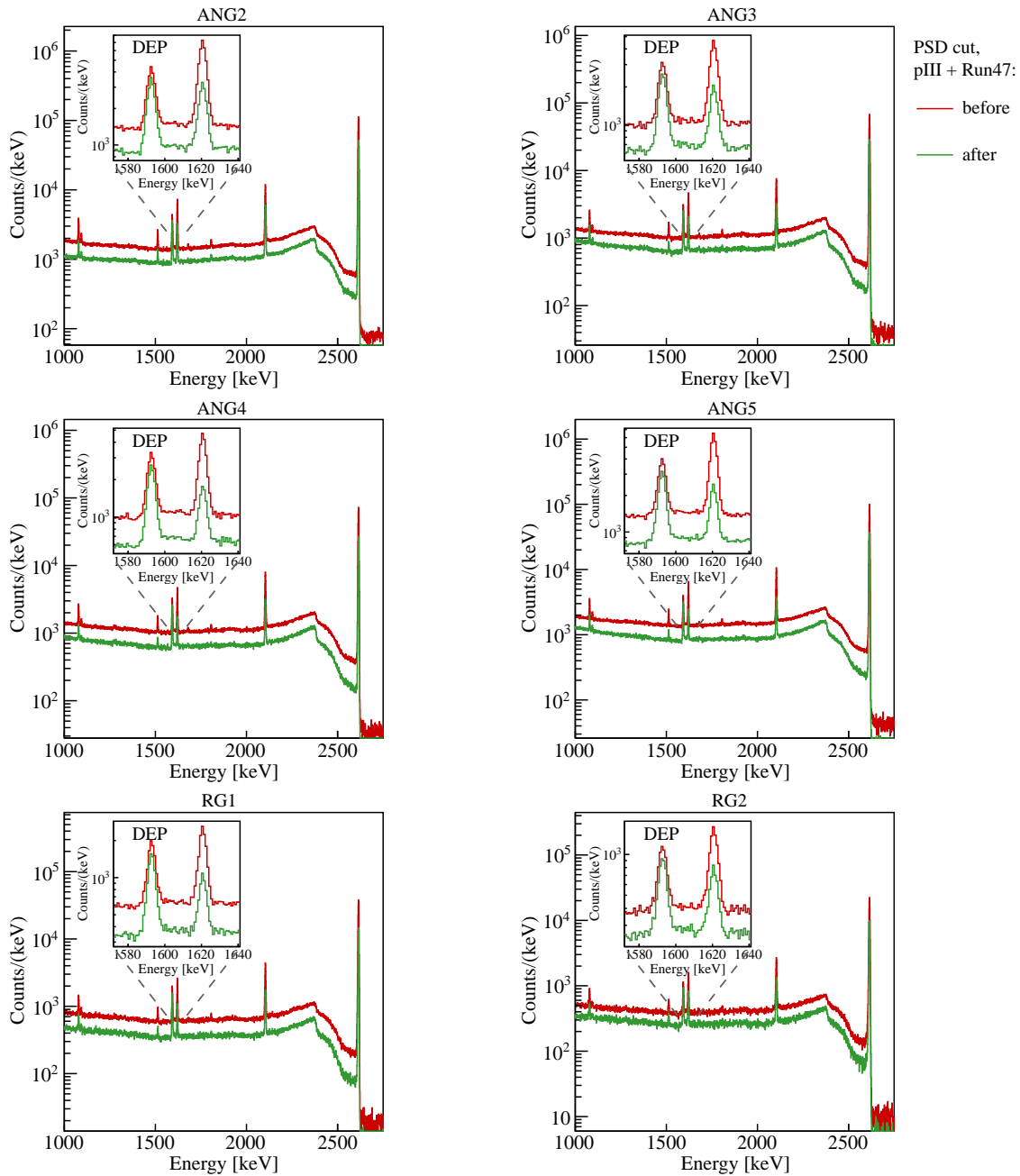
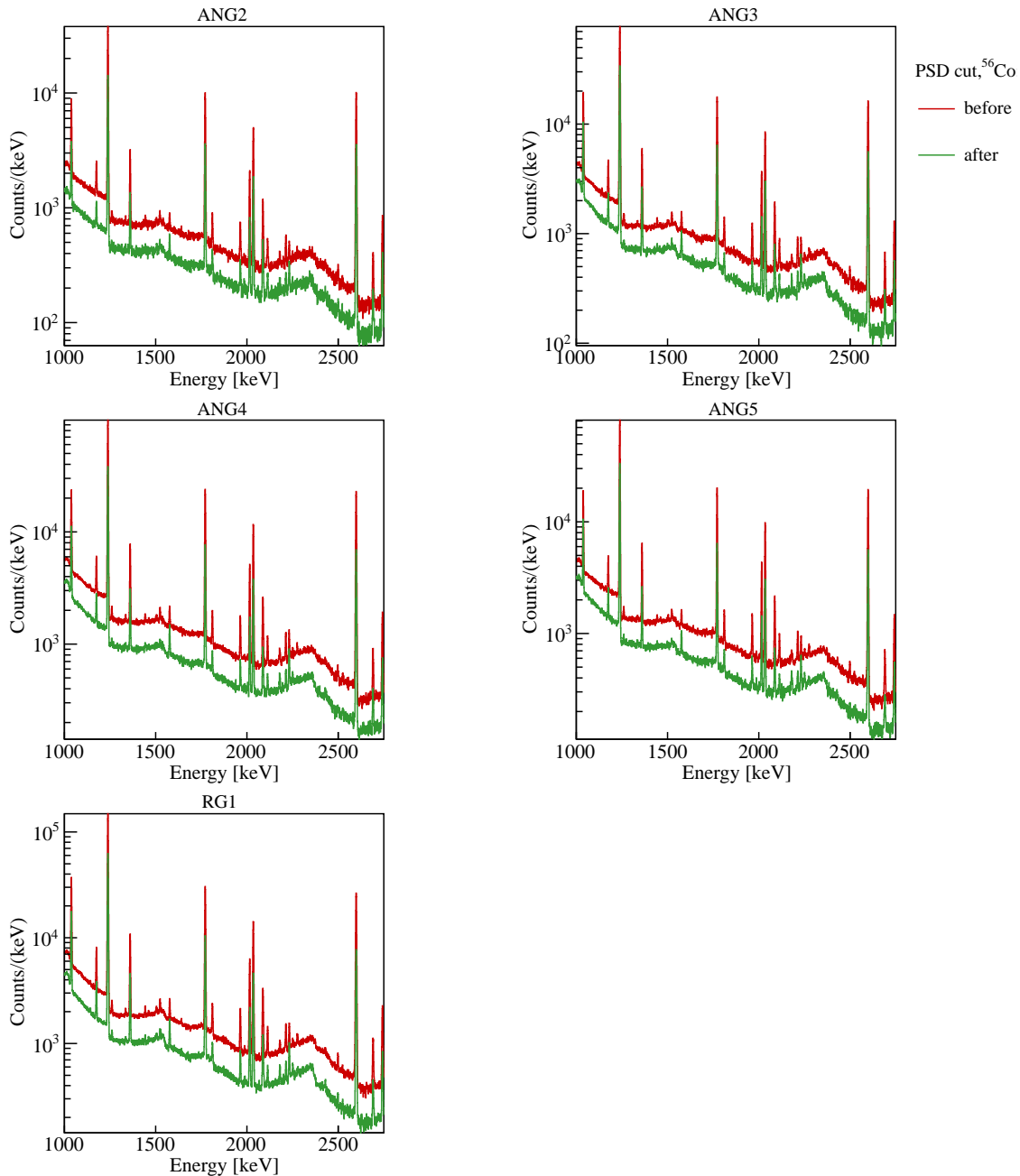**Figure B.14:** ^{228}Th calibration spectrum without (red) or with (green) PSD cut for the semi-coaxial detectors and period pIII + Run 47, where the cut is fixed for a survival fraction of 90 % in the DEP (see inset).

B.2.5   ANN Response on ^{56}Co calibration versus Energy
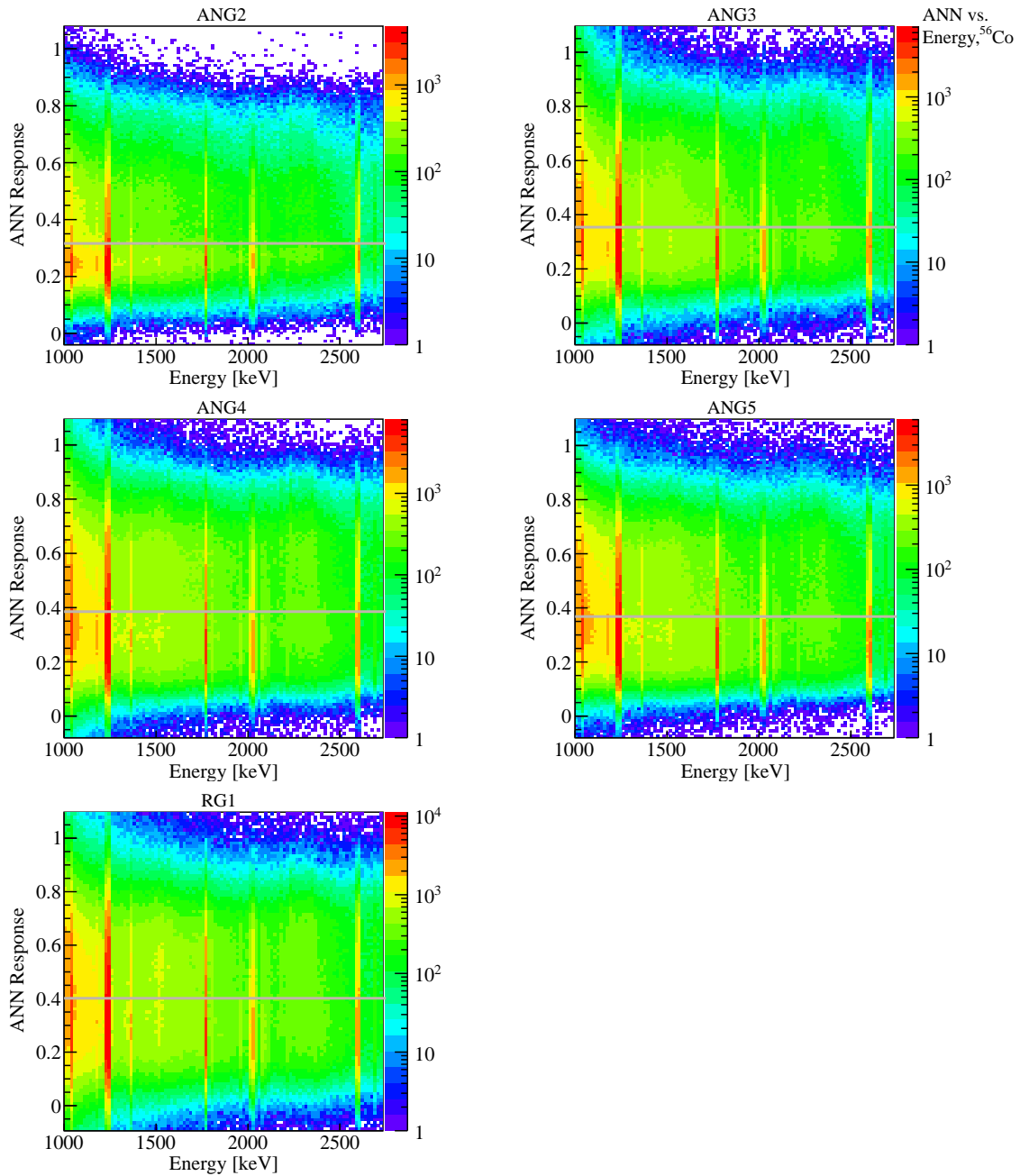
Figure B.15: ANN response versus energy distribution for ^{56}Co calibration events of the semi-coaxial detectors and Run 48. The horizontal gray line illustrates the position where 90 % of the DEP events from the ^{228}Th calibrations of period pIII + Run 47 are retained.

B.2.6   ANN cut on ^{56}Co calibration

Figure B.16: ^{56}Co calibration spectrum without (red) or with (green) PSD cut for the semi-coaxial detectors and Run 48, where the cut is fixed for a survival fraction of 90 % in the DEP from the ^{228}Th calibrations of period pIII + Run 47 (see inset).

B.3 Chapter 6

B.3.1 Energy dependency for data of Run $28 - 32$
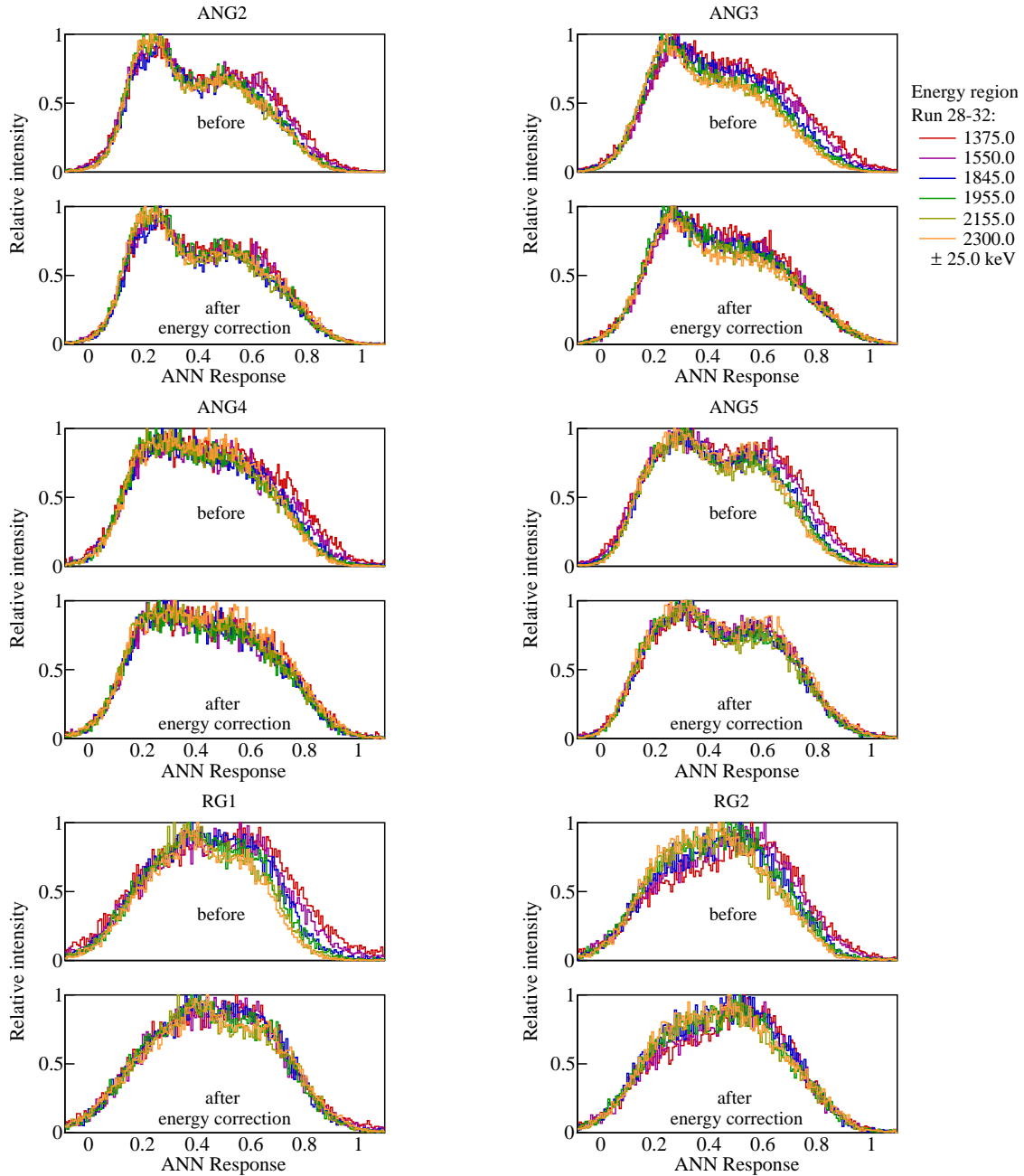
Figure B.17: ANN response for Compton events at six different energy regions without (upper half) and with (lower half) applied energy correction. Distributions are shown for the semi-coaxial detectors and Run $28 - 32$ of Phase I data taking.

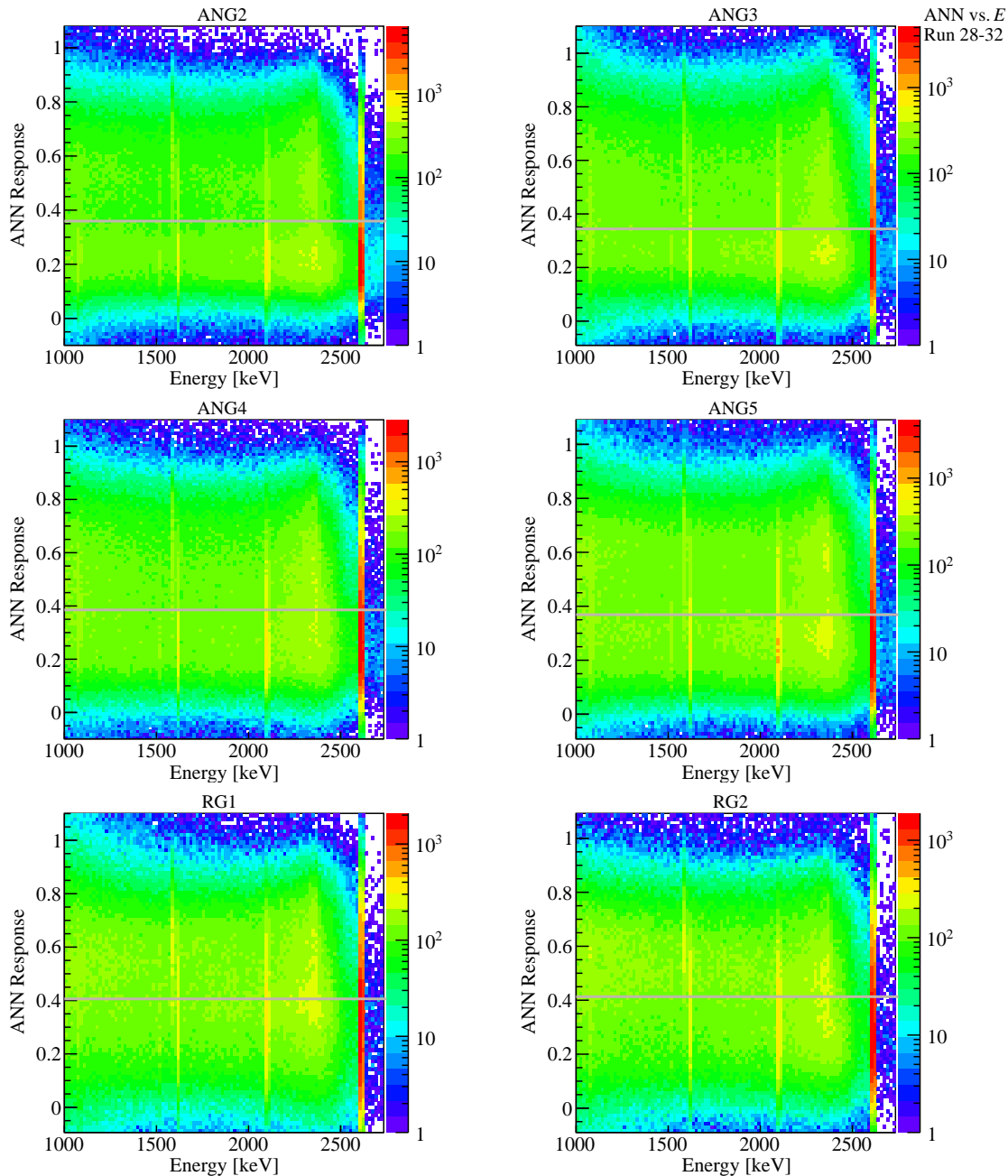## B.3.2   ANN Response versus Energy for Run 28 − 32

Figure B.18: ANN classifier response versus energy distribution for ^{228}Th calibration events of the semi-coaxial detectors and Run 28 − 32. The horizontal gray line illustrates the position where 90 % of the DEP events are retained.
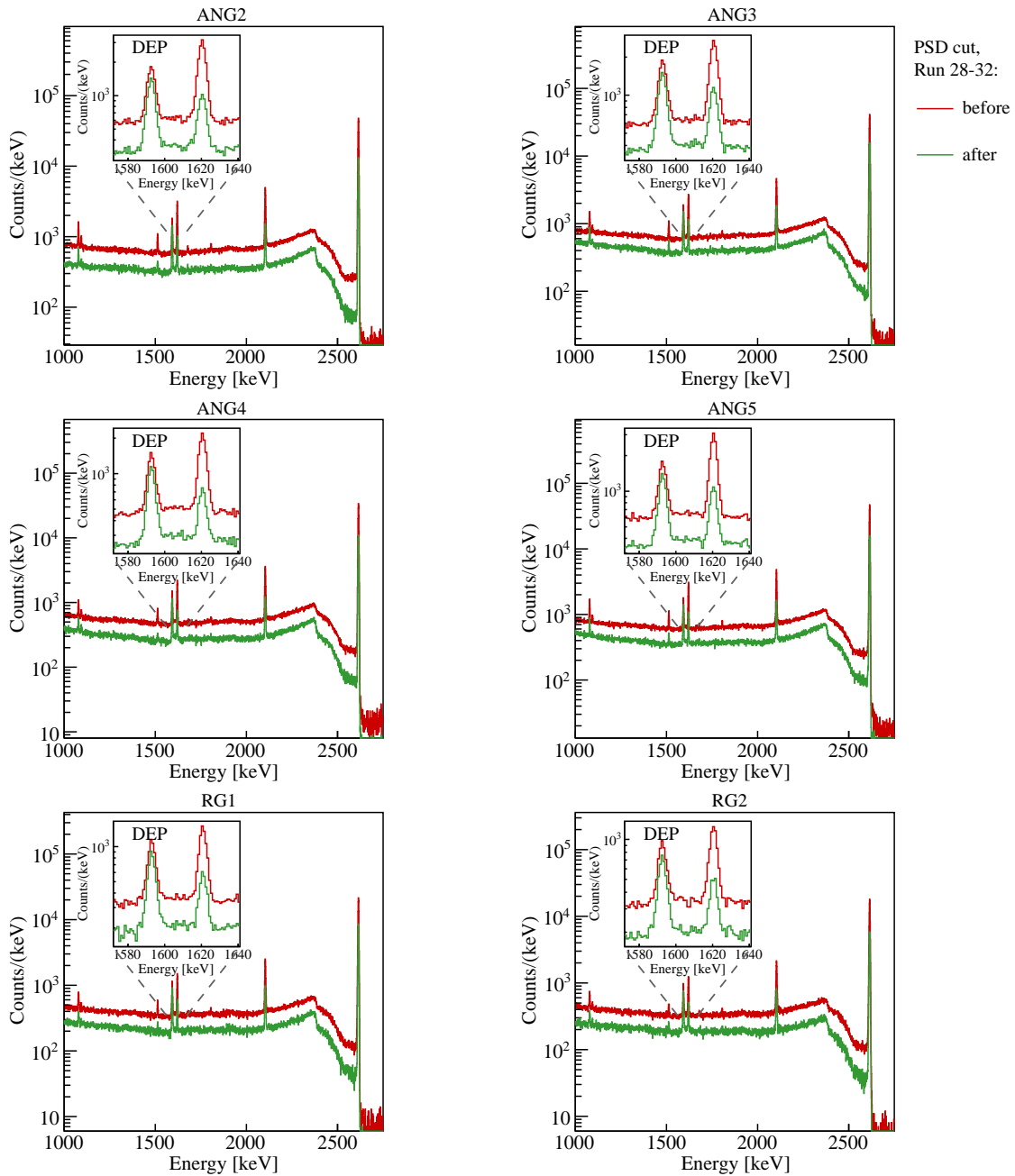
B.3.3   ANN cut on calibration for Run $28 - 32$

Figure B.19: ^{228}Th calibration spectrum without (red) or with (green) PSD cut for the semi-coaxial detectors and Run $28 - 32$, where the cut is fixed for a survival fraction of $90\,\%$ in the DEP (see inset).
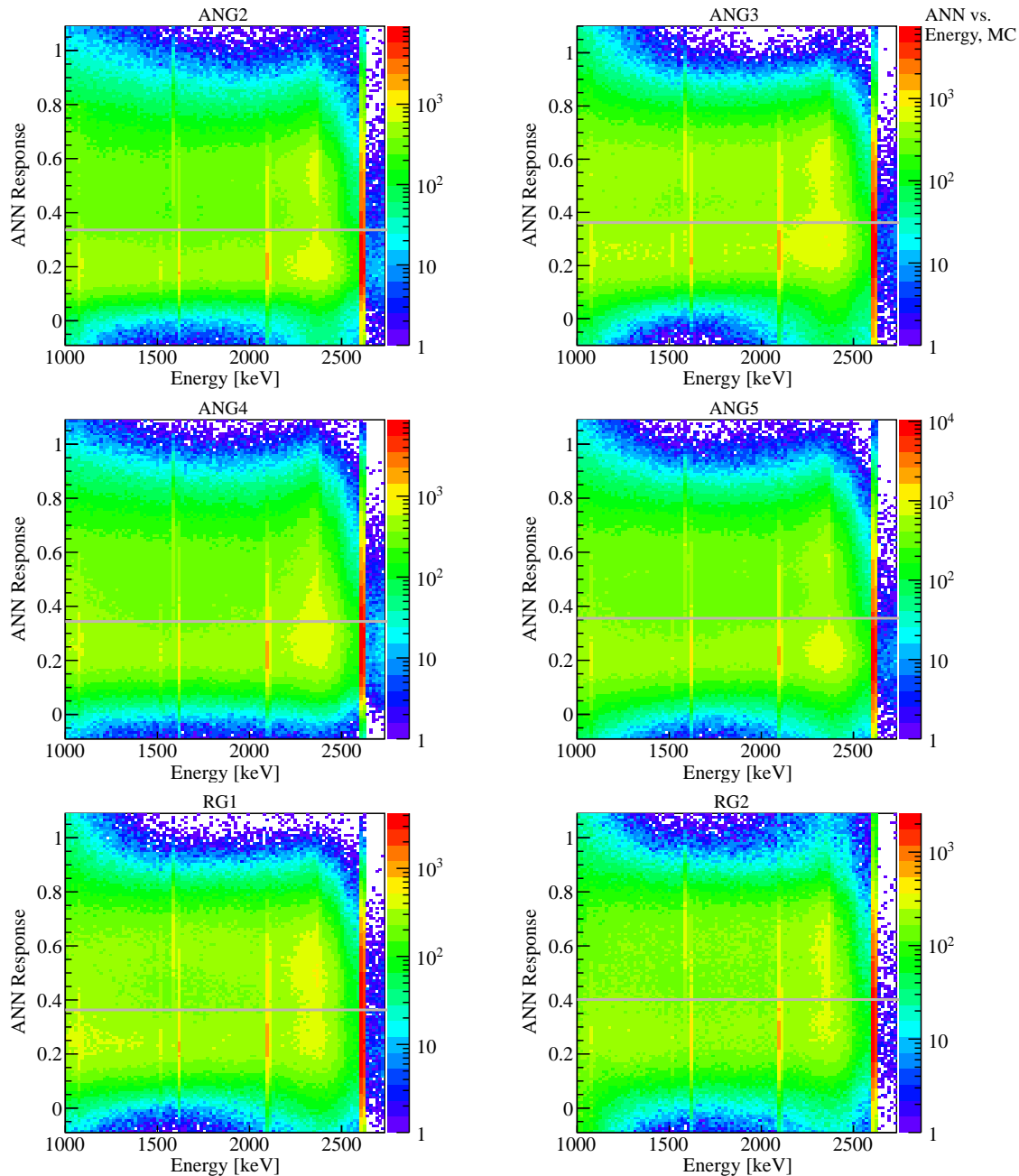
B.3.4   ANN Response versus Energy from MC

Figure B.20: ANN classifier response versus energy distribution for ^{228}Th calibration events of the semi-coaxial detectors and the simulated data set. The horizontal gray line illustrates the position where 90 % of the DEP events are retained.
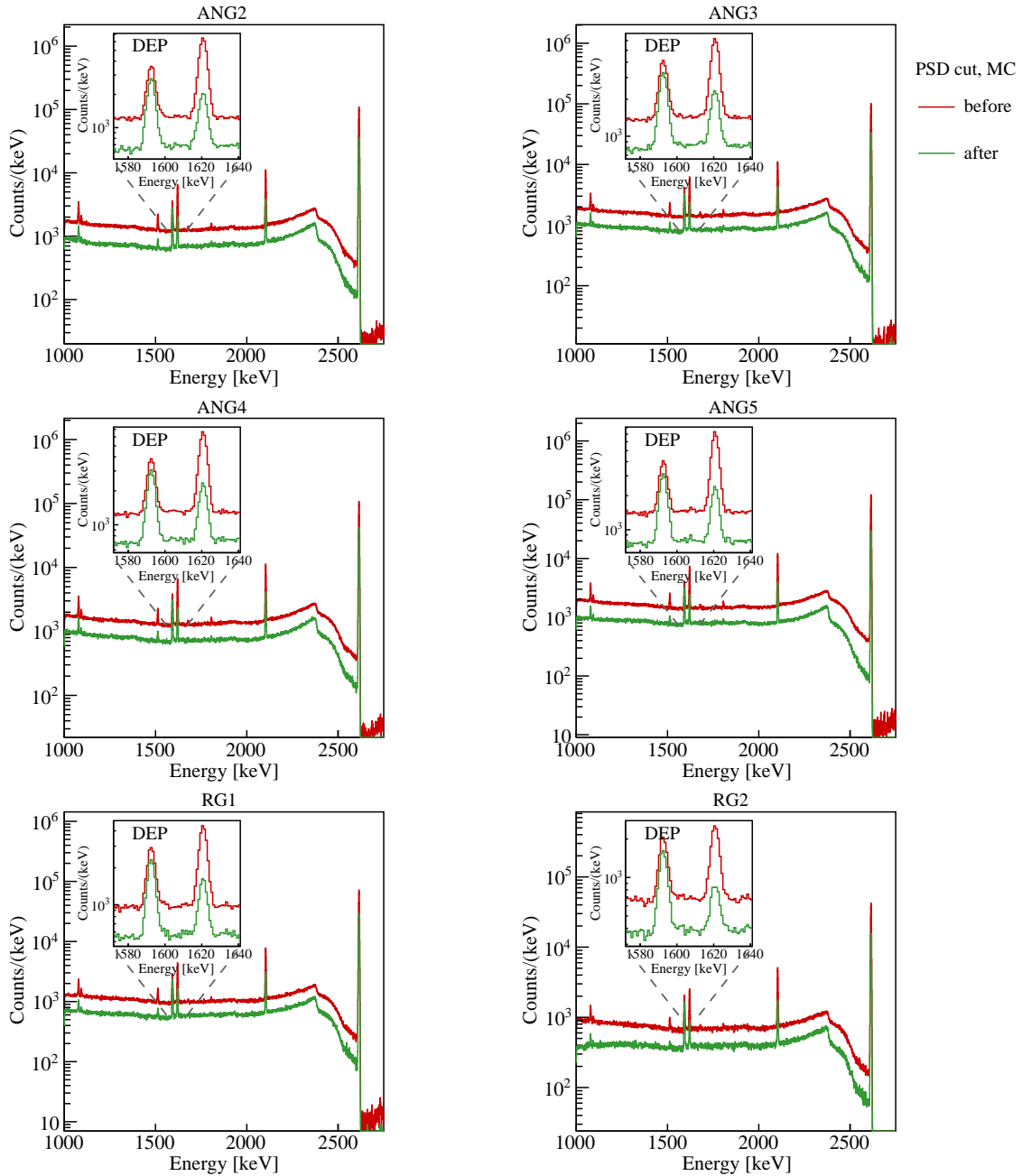
B.3.5 ANN cut on calibration for MC

Figure B.21: ^{228}Th calibration spectrum without (red) or with (green) PSD cut for the semi-coaxial detectors and the simulated data set, where the cut is fixed for a survival fraction of 90 % in the DEP (see inset).

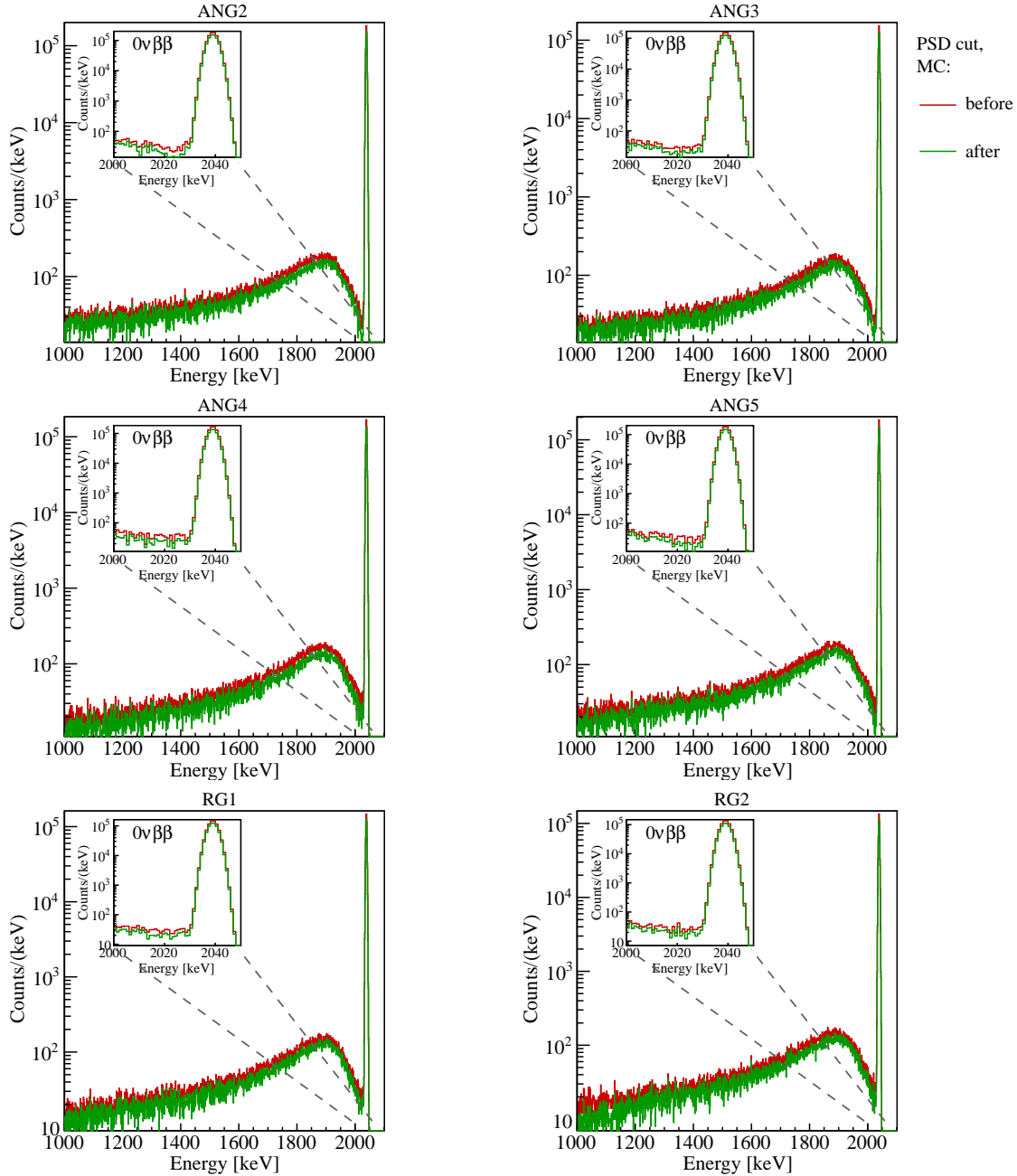**B.3.6   ANN cut on $0\nu\beta\beta$-signal from MC**

Figure B.22: Simulated $0\nu\beta\beta$ spectrum without (red) or with (green) PSD cut for the semi-coaxial detectors. A close-up on the full energy peak at $Q_{\beta\beta}$ in the energy interval $2000 - 2050$ keV is shown in the small inset on the top left margin.

Bibliography

[Aal02] C. Aalseth *et al.*, *The IGEX Ge-76 neutrinoless double beta decay experiment: Prospects for next generation experiments*, Phys. Rev. D, **65**, 092007, 2002.

[Aal04] C. Aalseth *et al.*, *The IGEX experiment reexamined: A response to the critique of Klapdor-Kliengrothaus, Dietz, and Krivosheina*, Phys. Rev. D, **70**, 078302, 2004.

[Abe12] Y. Abe *et al.*, *Indication of Reactor ν_e Disappearance in the Double Chooz Experiment*, Phys. Rev. Lett., **108**, 131801, 2012.

[Abd99] J. N. Abdurashitov *et al.* for the SAGE collaboration, *Measurement of the solar neutrino capture rate by SAGE and implications for neutrino oscillations in vacuum*, Phys. Rev. Lett., **83**, 4686-4689, 1999.

[Abt04] I. Abt *et al.*, GERDA*: The GERmanium Detector Array for the search of neutrinoless $\beta\beta$ decays of ^{76}Ge at LGNS*, Proposal, URL: `http://www.mpi-hd.mpg.de/gerda/reportsLNGS/proposal_21sept.pdf`, last modified: 16. July 2013.

[Abt08] I. Abt *et al.*, *Test of pulse shape analysis using single Compton scattering events*, Eur. Phys. J. C, **54**, 425-433, 2008.

[Ack13] K.H. Ackermann *et al.*, *The* GERDA *experiment for the search of $0\nu\beta\beta$ decay in ^{76}Ge*, EPJC, **73**, 2583, 2013.

[Agl87] M. Aglietta *et al.*, *On the Event Observed in the Mont Blanc Underground Neutrino Observatory during the Occurrence of Supernova 1987a*, Europhys. Lett., **3**, 1315-1320, 1987.

[Ago03] S. Agostinelli *et al.* for the GEANT4 Collaboration, *Geant4 - a simulation toolkit*, Nucl. Instrum. and Meth. A, **506**, 250-303, 2003.

[Ago11a] M. Agostini *et al.*, *Signal modeling of high-purity Ge detectors with a small read-out electrode and application to neutrinoless double beta decay search in $1176Ge$*, J. Instrum., **6**, P03005, 2011.

[Ago11b] M. Agostini *et al.*, *GELATIO: a general framework for modular digital analysis of high-purity Ge detector signals*, J. Instrum., **6**, P08013, 2011.

[Ago11c] M. Agostini, A.B. Machado, B. Schwingenheuer and S. Schönert, *Pulse shape simulation of a GTF detector*, GERDA Scientific Technical Reports, GSTR-11-001, 2011.

[Ago12] M. Agostini, L. Pandola and L. Zavarise, *Off-line data processing and analysis for the GERDA experiment*, J. Phys. Conf. Ser., **368**, 012047, 2012.

[Ago13a] M. Agostini *et al.* for the GERDA Collaboration, *Results on Neutrinoless Double-$\beta\beta$ Decay of ^{76}Ge from Phase I of the GERDA Experiment*, Phys. Rev. Lett., **111**, 122503, 2013.

[Ago13b] M. Agostini, *Signal and background studies for the search of neutrinoless double beta decay in GERDA*, PhD thesis, University of Munich, 2013.

[Ago13c] M. Agostini *et al.* for the GERDA Collaboration, *The background in the $0\nu\beta\beta$ experiment* GERDA, Eur. Phys. J. C, **74**, 2764, 2014.

[Ago13d] M. Agostini *et al.* for the GERDA Collaboration, *Pulse shape discrimination for GERDA Phase I*, Eur Phys. J. C, **73**, 2583, 2013.

[Ahm02] Q.R. Ahmad *et al.*, *Direct Evidence for Neutrino Flavour Transformation from Neutral-Current Interactions in the Sudbury Neutrino Observatory*, Phys. Rev. Lett., **89**, 011301, 2002.

[Akk12] S. Akkoyun *et al.*, *AGATA - Advanced Gamma Tracking Array*, Nucl. Instr. Methods A, **668**, 26-58, 2012.

[Alb14] J.B Albert *et al.* for the EXO Collaboration, *Search for Majorana neutrinos with the first two years of EXO-200 data*, arXiv:1402.6956, 2014.

[Ale87] E.N. Alekseev *et al.*, *Possible Detection of a Neutrino Signal on 23 February 1987 at the Baksan Undergound Scintillation Telescope of the Institute for Nuclear Reasearch*, JETP Lett., **45**, 589-592, 1987.

[Ali75] R.C. Alig and S. Bloom, *Electron-Hole-Pair Creation Energies in Semiconductors*, Phys. Rev. Let., **35**, 1522-1525, 1975.

[All06] J. Allison *et al.* for the GEANT4 Collaboration, *Geant4 developments and applications*, IEEE Trans. Nucl. Sci., **53(1)**, 270-278, 2006.

[Alt00] M. Altmann *et al.* for the GNO Collaboration, *GNO Solar neutrino observations: results for GNO*, I. Phys. Lett. B, **490**, 16-26, 2000.

[Ama05] K. Amako *et al.*, *Comparison of Geant4 Electromagnetic Physics Models Against the NIST Reference Data*, IEEE Trans. Nucl. Sci., **52**, 910-918, 2005.

[An12] F.P. An *et al.*, *Observation of Electron-Antineutrino Disappearance at Daya Bay*, Phys. Rev. Lett., **108**, 171803, 2012.

[And33] C.D. Anderson, *The Positive Electron*, Phys. Rev., **43**, 491-494, 1933.

[And11] E. Andreotti *et al.*, ^{130}Te *neutrinoless double-beta decay with CUORICINO*, Astropart. Phys., **34**, 822-831, 2011.

[Ara06] T. Araki *et al.*, *Search for the Invisible Decay of Neutrinos with KamLand*, Phys. Rev. Lett. , **96**, 101802, 2006.

[Ard06] F. Ardellier *et al.*, *Double Double Chooz, A Search for the Neutrino Mixing Angle θ_{13}*, arXiv:hep-ex/0606025, 2006.

[Aug12] M. Auger *et al.* for the Exo Collaboration, *Search for Neutrinoless Double-Beta Decay in ^{136}Xe with EXO-200*, Phys. Rev. Lett. , **109**, 032505, 2012.

[Avi08] F. Avignone *et al.*, *Double beta decay, Majorana neutrinos, and neutrino mass*, Rev. Mod. Phys. , **80**, 481-516, 2008.

[Bah68] J.N. Bahcall, N.A. Bahcall and G. Shaviv, *Present Status of the Theoretical Predictions for the ^{37}Cl Solar-Neutrino-Experiment*, Phys. Rev. Lett., **20**, 1209-1212, 1968.

[Bah87] J.N. Bahcall and S.L. Glashow, *Upper limit on the mass of the electron neutrino*, Nature, **326**, 476-477, 1987.

[Bah05] J.N. Bahcall and A.M. Serenelli, *New Solar Opacities, Abundances, Helioseismology and Neutrino FLuxes*, A. Phys. Journ., **621**, L85-88, 2008.

[Bar09a] J. Barea and F. Iachello, *Neutrinoless double-beta decay in the microscopic interacting boson model*, Phys. Rev. C, **79**, 044301, 2009.

[Bar09b] M. Barnabé Heider, *Performance and stability tests of bare high purity germanium detectors in liquid argon for the GERDA experiment*, PhD thesis, University of Heidelberg, 2009.

[Bar09c] I. Barabanov *et al.*, *Shielding of the GERDA experiment against external gamma background*, Nucl. Instr. Methods A, **606**, 790-794, 2009.

[Bar11] A.S. Barabash, *Double beta decay experiments*, Phys. Part. Nucl., **42**, 613, 2011.

[Bar12] A.S. Barabash for the SuperNemo Collaboration, *SuperNEMO double beta decay experiment*, J. Phys. Conf. Ser., **375**, 042012, 2012.

[Bar13] A.S. Barabash, *Average and recommended half-life values for two neutrino double beta decay: upgrade-2013*, AIP Conf. Proc., **1572**, 11, 2013.

[Bau99] L. Baudis *et al.*, *Limits on the Majorana Neutrino Mass in the 0.1 eV Range*, Phys. Rev., **83**, 41-44, 1999.

[Bec96] H. Becquerel, *Sur diverses propriétés des rayons uraniques*, C.R. Acad. Sci., **122**, 855-858, 1896.

[Bec14]   N. Becerici-Schmidt, *Title unknown*, PhD thesis, University of Munich, 2014.

[Ber05]   M.J. Berger *et al.*, *ESPAR, PSTAR, and ASTAR: Computer programs for Calculating Stopping-Power and Range Tables for Electrons, Protons, and Helium Ions*, NIST Standard Reference Database 124, online, (last update) 2005.

[Ber10]   M.J. Berger *et al.*, *XCOM: Photon Cross Sections Database*, NIST Standard Reference Database 8, online, (last update) 2010.

[Ber12]   J. Beringer *et al.* (Particle Data Group), *Review of Particle Physics*, Phys. Rev. D, **86**, 010001, 2012.

[Bre84]   L.Breiman *et al.*, *Classification and Regression Trees*, Chapman & Hall/CRC, 1984.

[Bil87]   S.M. Bilenky and S.T. Petkov, *Massive neutrinos and neutrino oscillations*, Rev. Mod. Phys., **59**, 3, 1987.

[Bil12]   S.M. Bilenky and C. Giunti, *Neutrinoless double-beta decay. A brief review*, Mod. Phys. Lett. A, **27**, 1230015, 2012.

[Bio87]   R.M. Bionta *et al.*, *Observation of a neutrino burst in coincidence with supernova 1987A in the Large Magellanic Cloud*, Phys. Rev. Lett., **58**, 1494-1496, 1987.

[Bod15]   T. Bode, *Title unknown*, PhD thesis, University of Munich, 2015.

[Bos11]   M. Boswell *et al.*, *MaGe - a Geant4-based Monte Carlo Application Framework for Low-background Germanium Experiments*, IEEE Trans. Nucl. Sci., **58**, 1212-1220, 2011.

[Bjo64]   J.D. Bjorken and S.D. Drell, *Relativistic Quantum Mechanics and Relativistic Quantum Fields*, McGraw-Hill, New York, 1964.

[Bro70]   C.G. Broyden, *The Convergence of a Class of Double-rank Minimization Algorithms*, J. Inst. of Math. and App., **6**, 76, 1970.

[Bru00]   V.B. Brudanin *et al.*, *Search for double beta decay of ^{48}Ca in the TGV experiment*, Phys. Lett. B, **495**, 63-68, 2000.

[Bru08]   R. Brun and F. Rademakers, *ROOT - An Object Oriented Data Analysis Framework*, Users Guide, URL: `http://root.cern.ch/download/doc/ROOTUsersGuideA4.pdf`, 2008.

[Bru06a] B. Bruyneel, P. Reiter and G. Pascovici, *Characterization of large volume HPGe detectors. Part I: Electron and hole mobility parameterization*, Nucl.. Instrum. Meth. A, **569**, 764-773, 2006.

[Bru06b] B. Bruyneel, P. Reiter and G. Pascovici, *Characterization of large volume HPGe detectors. Part II: Experimental results*, Nucl.. Instrum. Meth. A, **569**, 774-789, 2006.

[Bru06c] B. Bruyneel, *Characterization of Segmented Large Volume, High Purity Germanium Detectors*, Ph.D. thesis, University of Cologne, 2006.

[Bru12] B. Bruyneel, Detector Simulation Software ADL, URL: `http://www.ikp.uni-koeln.de/research/agata/index.php?show=dpwnload`, last modified: 04. September 2012.

[Bud09] D. Budjáš *et al.*, *Pulse shape discrimination studies with a Broad-Energy Germanium detector for signal identification and background suppression in the GERDA double beta decay experiment*, J. Instrum., **4**, P10007, 2009.

[Cab63] N. Cabibbo, *Unitary Symmetry and Leptonic Decays*, Phys. Rev. Lett., **10**, 531-533, 1963.

[Cal09] A. Caldwell, D. Kollar and K. Kroñinger, *BAT - The Bayesian Analysis Toolkit*, Nucl. Comput. Phys. Commun., **180**, 2197-2209, 2009.

[Can75] C. Canali *et al.*, *Electron and hole drift velocity measurements in silicon and their empirical relation to electric field and temperature*, IEEE Trans. on Elec. Devices, **22**, 045-1047, 1975.

[Cha14] J. Chadwick, *Über das β-Strahlenspektrum von ThB + C*, Verh. d. deutschen Phys. Ges., **16**, 383, 1914.

[Chk08] O. Chkvorets, *Search for double beta decay with HPGe detectors at the Gran Sasso underground laboratory*, PhD Thesis, University of Heidelberg, 1914.

[Cir10] G.A.P. Cirrone *et al.*, *Validation of the Geant4 electromagnetic photon cross-sections for elements and compounds*, Nucl. Instrum. Methods A, **618**, 315-322, 2010.

[Cot07] W.N. Cottingham and D.A. Greenwood, *An Introduction to the Standard Model of Particle Physics*, Cambridge University Press, 2007.

[Dav68] R. Davis, D.S. Harmer and K.C. Hoffman, *Search for Neutrinos from the Sun*, Phys. Rev. Lett., **20**, 1205-1209, 1968.

[Dir27] P. Dirac, *The Quantum Theory of the Emission and Absorption of Radiation*, Proc. R. Soc. A, **114**, 243, 1927.

[Dir28] P. Dirac, *The Quantum Theory of the Electron*, Proc. R. Soc. Lond. A, **117**, 610-624, 1928.

[Due11] M. Duerr, M. Lindner, and A. Merle, *On the quantitative impact of the Schechter-Valle theorem*, JHEP, **1106**, 091, 2011.

[Dwy12] D. Dwyer for the Reno Collaboration, talk at *Neutrino 2012*.

[Ell06] S.R. Elliot *et al.*, *Pulse shape analysis in segmented detectors as a technique for background reduction in Ge double-beta decay experiments*, Nucl. Instrum. Meth. A, **558**, 504-510, 2006.

[Fae12] A. Feassler *et al.*, *Nuclear matrix elements for neutrinoless double-beta decay and double-electron capture*, J. Phys. G, **92**, 830-831, 1953.

[Fel98] G. Feldman and R. Cousins, *Unified approach to the classical statistical analysis of small signals*, Phys. Rev. D, **57**(7), 3873-3889, 1998.

[Fer34] E. Fermi, *An attempt of a theory of beta radiation*, Zeitschrift für Physik, **39**, 124006, 2012.

[Fer50] E. Fermi, *Nuclear Physics, University of Chicago*, Press, Chicago, 142, 1950.

[Fey49] R.P. Feynman, *Space-Time Approach to Quantum Electrodynamics*, Phys. Rev., **76**, 769-789, 1949.

[Fle70] R. Fletcher, *A New Approach to Variable Metric Algorithms*, Computer J., **13**, 317, 1970.

[Fog12] G.L. Fogli *et al.*, *Gobal analysis of neutrino masses, mixings and phases: entering the era of leptonic CP violation searches*, Phys. Rev. D, **86**, 013012, 2012.

[Fro12] F. Froborg, *Calibration of Phase I of the GERDA Double Beta Decay Experiment*, PhD thesis, University of Zürich, 2012.

[Fuk01] S. Fukuda *et al.* for the Super-Kamiokande Collaboration, *Solar ^8B and hep Neutrino Measurements from 1258 Days of Super-Kamiokande Data*, Phys. Rev. Lett., **86**, 5651-5655, 2001.

[Fur39] W.H. Furry, *On Transition Probabilities in Double Beta-Disintegration*, Phys. Rev., **56**, 1184-1193, 1939.

[Gan13] A. Gando *et al.* for the KamLAND-Zen Collaboration, *Limit on Neutrinoless $\beta\beta$ Decay of Xe-136 from the First Phase of KamLAND-Zen and Comparison with the Positive Claim in Ge-76*, Phys.Rev.Lett., **110**, 062502, 2013.

[Gat06] F. Gatti *et al.*, *MARE - Microcalorimeter Arrays for a Rhenium Experiment*, Proposal, 2006.

[Gla61] S.L. Glashow, *Partial Symmetries of Weak Interaction*, Nucl. Phys., **22**, 579-588, 1961.

[Goe35] M. Goeppert-Mayer, *Double beta-disintegration*, Rhys. Rev., **48**, 512-516, 1935.

[Gol58]   M. Goldhaber *et al.*, *Helicity of Neutrinos*, Rhys. Rev., **1015-1017**, 491-494, 1958.

[Gol70]   D. Goldfarb, *A Family of Variable Metric Updates Derived by Variational Means*, Math. Comp., **24**, 23, 1970.

[Gom12]   J.J. Gòmez Cadenas, J. Martin-Albo, M. Mezzetto, F. Monrabal, and M. Sorel, *The search for neutrinoless double beta decay*, Riv. Nuovo Cimento Soc. Ital. Fis., **35**, 29, 2012.

[Gon03]   D. Gonzalez *et al.*, *Pulse shape discrimination in the* IGEX *experiment*, Nucl. Instrum. Meth. A, **515**, 634-643, 2003.

[Gor12]   P. Gorla for the CUORE Collaboration, *The CUORE experiment: status an prospects*, J. Phys. Conf. Ser., **375**, 042013, 2012.

[Gri69]   V. Gribov and B. Pontecorvo, *Neutrino Experiment and the Problem of Conservation of Leptonic Charge*, Phys. Lett. B, **28**, 493, 1969.

[Gri09]   D. Griffiths, *Introduction to Elementary Particles*, 6th ed., WILEY-VCH Verlag GmbH & Co. KGaA, Weinheim, 2009.

[Gro90]   K. Grotz and H.V. Klapdor, *The Weak Interaction in Nuclear, Particle and Astrophysics*, Hilger, Bristol, 1990.

[Ham99]   W. Hampel *et al.* for the GALLEX Collaboration, *GALLEX Solar neutrino observations: results for GALLEX*, IV. Phys. Lett. B, **447**, 127-133, 1999.

[Har12]   J. Hartnell for the SNO+ Collaboration, *Neutrinoless Double Beta Decay with SNO+*, J. Phys. Conf. Ser., **375**, 042015, 2012.

[He01]   Z. He, *Review of the Shockley-Ramo theorem and its application in semiconductor gamma-ray detectors*, Nucl. Instrum. Methods Phys. Res. A, **463**, 250-267 , 2001.

[Hei11]   M. Heisel, *LArge - A liquid aargon scintillation veto for* GERDA, PhD thesis, University of Heidelberg, 2011.

[Hem14]   S. Hemmer, *Title unknown*, PhD thesis, Università di Padova, 2014.

[Hir87]   K.S. Hirata *et al.* for the KAMIOKANDE-II Collaboration, *Observation of a Neutrino Burst from the Supernova SN 1987a*, Phys. Rev. Lett., **58**, 1490-1494, 1987.

[Hir92]   K.S. Hirata *et al.*, *Observation of a Small ν_μ/ν_e Ratio in Kamiokande*, Phys. Lett. B, **280**, 146-152, 1992.

[Hoe07]   A. Hoecker *et al.*, *TMVA 4 - Toolkit for Multivariate Data Analysis with ROOT*, arXiv::physics/0703039, 2007.

[Hun11]   S. Hunklinger, *Festkörperphysik*, 3rd ed. (in german), Oldenbourg Verlag, 2011.

[Iac11]   F. Iachello, J. Barea and J. Kotila, *Advances in the theory of 0ν beta beta decay*, AIP Conf. Proc., **1417**, 62-68, 2011.

[Kim08]   S.B. Kim *et al.* for the RENO Collaboration, *RENO: reactor experiment for neutrino oscillation at Yonggwang*, Journal of Physics: Conference Series, **120**(5), 052025, 2008.

[Kim12]   S.B. Kim for the RENO Collaboration, talk at *Neutrino 2012*.

[Kla95]   H.V. Klapdor-Kleingrothaus and A. Staudt, *Non-accelerator Particle Physics*, B.G. Teubner Stuttgart, 1995.

[Kla01]   H.V. Klapdor-Kleingrothaus *et al.*, *Latest results from the HEIDELBERG-MOSCOW double beta decay experiment*, Eur. Phys. J. A, **12**, 147-154, 2001.

[Kla04]   H.V. Klapdor-Kleingrothaus *et al.*, *Search for neutrinoless double beta decay with enriched ^{76}Ge in Gran Sasso $1990-2003$*, Phys. Lett. B, **586**, 198-212, 2004.

[Kla06]   H.V. Klapdor-Kleingrothaus and I.V. Krivosheina, *The evidence for the observation of 0nu beta beta decay: The identification of 0nu beta beta events from the full spectra*, Mod. Phys. Lett. A, **21**, 1547-1566, 2006.

[Kna09]   M.A. Knapp, *Design, Simulation und Aufbau des GERDA-Myonvetos*, PhD thesis (in german), University of Tübingen, 2009.

[Kno89]   G.F. Knoll, *Radiation Detection and Measurement*, 2nd ed., Wiley, New York, 1989.

[Kot12]   J. Kotila and F. Iachello, *Phase-space factors for double-β decay*, Phys. Rev. C, **85**, 034316, 2012.

[Kob73]   M. Kobayashi and T. Maskawa, *CP-Violation in the Renormizable Theory of Weak Interaction*, Prog. Theor. Phys., **49**, 652-657, 1973.

[Kra05]   C. Kraus *et al.*, *Final results from phase II of the Mainz neutrino mass search in tritium β-decay*, Europ. Phys. Journ. C, **40**, 447-468, 2005.

[Lim11]   M. Limon *et al.*, *Wilkinson Microwave Anisotropy Probe (WMAP): Seven-Year Explanatory Supplement*, Greenbelt, MD: NASA/GSFC, 2011.

[Lob03]   V.M. Lobashev, *The search for the neutrino mass by direct method in the tritium β-decay and perspectives of study it in the project KATRIN*, Nucl. Phys. A, **719**, 153c-160c, 2003.

[Maj37] E. Majorana, *Teoria simmetrica dell'elettrone e del positrone*, Nouvo Cimento, **14**, 171, 1937.

[Maj99] B. Majorovits and H..V. Klaptor-Kleingrothaus, *Digital pulseshape analysis by neural networks for the Heidelberg-Moscow-Double-Beta-Decay-Experiment*, Eur. Phys. J. A, **6**, 463-469, 1999.

[Mak62] Z. Maki, M. Nakagawa and S. Sakata, *Remarks on the Unified Model of Elementary Particles*, Prog. Theor. Phys., **28**, 870-880, 1962.

[Men09] J. Menendez *et al.*, *Disassembling the Nuclear Matrix Elements of the Neutrinoless beta beta Decay*, Nucl. Phys. A, **818**, 139-151, 2009.

[Men11] J. Menendez *et al.*, *Neutrinoless Double Beta Decay: The Nuclear Matrix Elements Revisited*, J. Phys. Conf. Ser., **312**, 072005, 2011.

[Mic06] D.G. Michael *et al.*, *Observation of Muon Neutrino Disappearance with the MINOS Detectors in the NuMI Neutrino Beam*, Phys. Rev. Lett., **97**, 191801, 2006.

[Mih00] L. Mihailescu *et al.*, *The influence of anisotropic electron drift velocity on the signal shapes of closed-end HPGe detectors*, Nucl. Instr. and Meth. A, **447**, 350-360, 2000.

[Mik86] S.P. Mikheyev and A.Y. Smirnov, *Resonance enhancemen of oscillations in matter and Solar neutrino spectroscopy*, Soviet Journal of Nucl. Phys., **42**, 913-917, 1986.

[Miz13] MIZZI Computer Software GmbH, URL: http://www.mizzi-computer.de

[Mon12] F. Monrabal for the NEXT Collaboration, *Discovering neutrinoless double beta decay with NEXT100 detector*, J. Phys. Conf. Ser., **375**, 042019, 2012.

[Mor12] M. Moresco *et al.*, *New constraints on cosmological parameters and neutrino properties using the expansion rate of the Universe to $z \sim 1.75$*, J. Cosmol. Astropart. Phys., JCAP(2012)053, 2012.

[Mou10] B.J. Mount, M. Redshaw, and E.G. Myer, *Double-β-decay Q values of ^{74}Se and ^{76}Ge*, Phys. Rev. C, **81**, 032501, 2010.

[Mus13] M.T. Mustonen and J. Engel, *Large-Scale calculations of the double-beta decay of ^{76}Ge, ^{130}Te, ^{136}Xe, and ^{150}Nd in the deformed self-consistent Skyrme quasiparticle random-phase approximation*, Phys. Rev. C, **87**, 064302, 2013.

[Oga12] I. Ogawa *et al.*, *New constraints on cosmological parameters and neutrino properties using the expansion rate of the Universe to $z \sim 1.75$*, J. Phys. Conf. Ser., **375**, 042018, 2012.

[Old12]   C. Oldorf, *Recent progress of the COBRA experiment*, J. Phys. Conf. Ser., **375**, 042012, 2012.

[Pau30]   W. Pauli, *Open Letter to Radioactive Persons*, 1930.

[Pet93]   F. Petry *et al.*, *Background recognition in Ge detectors by pulse shape analysis*, Nucl. Instrum. Meth. A, **332**, 107-112, 1993.

[Pir81]   T. Piran, *Mass and Detection of Neutrino Supernova Bursts*, Phys. Lett. B, **102**, 299-302, 1981.

[Pon67]   B. Pontecorvo, *Neutrino Experiment and the Problem of Conservation of Leptonic Charge*, J. Exptl. Theoret. Phys., **53**, 1717, 1967.

[Pon00]   O.A. Ponkratenko, V.I. Tretyak and Yu.G. Zdesenko, *The event generator DECAY4 for simulation of double beta processes and decay of radioactive nuclei*, Phys. Atom Nucl., **63**, 1282-1287, 2000.

[Poo05]   E. Poon and F. Verhaegen, *Accuracy of the photon and electron physics in GEANT4 for radiotherapy applications.*, Med. Phys, **32**, 1696-1711, 2005.

[Pov08]   B. Povh, K. Rith, C. Scholz and F. Zetsche, *Particles and Nuclei - An Introduction to the Physical Concepts*, 6th ed., Springer Verlag, Berlin, Heidelberg, 2008.

[Pre95]   W.H. Press *et al.*, *Numerical Recipes in C*, Cambridge University Press, URL: http://www.nrbook.com/a/bookcpdf.php, 1995.

[Ran12]   P. C.-O. Ranitzsch *et al.*, *Development of Metallic Magnetic Calorimeters for High Precision Measurements of Calorimetric ^{187}Re and ^{163}Ho Spectra*, J. Low Temp. Phys., **167**, 1004, 2012.

[Rat10]   P.K. Rath *et al.*, *Uncertainties in nuclear transition matrix elements for neutrinoless $\beta\beta$ decay within the projected-Hartree-Fock-Bogoliubov model*, Phys. Rev. C, **82**, 064310, 2010.

[Reg77]   L. Reggiani *et al.*, *Hole Drift Velocity in Germanium*, Phys. Rev. B, **16(6)**, 2781-2791, 1953.

[Rei53]   F. Reines and C.L. Cowan, Jr., *Detection of the free neutrino*, Phys. Rev., **92**, 830-831, 1953.

[Rib10]   S. Riboldi *et al.*, *A Low-Noise Charge Sensitive Preamplifier for Ge Spectroscopy operating at Cryogenic Temperature in the GERDA Experiment*, IEEE, Nuclear Science Symposium Conference Record (NSS/MIC), 1386-1388, 2010.

[Rod10] T.R. Rodriguez and G. Martinez-Pinedo, *Energy density functional study of nuclear matrix elements for neutrinoless $\beta\beta$ decay*, Phys. Rev. Lett., **105**, 252503, 2010.

[Rod11] W. Rodejohann, *Neutrino-less Double Beta Decay and Particle Physics*, Int. J. Mod. Phys. E, **20**, 1833, 2011.

[Rit11] F. Ritter, *Analysis of the Gerda Muon Veto: First Light*, PhD thesis, University of Tübingen, 2011.

[Sal68] A. Salam, *Elematary Particle Theory*, ed N. Svartholm, Almquist and Wiksel, 1968.

[Sal13] M. Salathe, *Report about PSD for coaxial detectors*, Talk at GERDA Collaboration Meeting in Dubna, Russia, 12.-14. June 2013.

[Sal15] M. Salathe, *Title unknown*, PhD thesis, University of Heidelberg, 2015.

[Sch13] B. Schwingenheuer, *Status and prospects of searches for neutrinoless double beta decay*, Ann. Phys., **525**, 269-280, 2013.

[Sch14] B. Schwingenheuer, *Limit on neutrinoless double beta decay of ^{76}Ge by the GERDA experiment*, submitted to Physics Procedia, 2014.

[Sch82] J. Schechter and J. Valle, *Neutrinoless double-β decay in SU(2)×U(1) theories*, Phys. Rev. D, **25**, 2951-2954, 1982.

[Sch70] D.F. Shannon, *Conditioning of Quasi-Newton Methods for Function Minimization*, Math. Comp., **24**, 647, 1970.

[Sci09] N.D. Scielzo *et al.*, *Double-beta decay Q values of ^{130}Te, ^{128}Te, and ^{120}Te*, Phys. Rev. C, **80**, 025501, 2009.

[Sim12] L. Simard *et al.* for the NEMO-3 Collaboration, *The NEMO-3 results after completion of data taking*, J. Phys. Conf. Ser., **375**, 042011, 2012.

[Sim09] F. Simkovic *et al.*, *The 0nbb-decay nuclear matrix elements with self- consistent short-range correlations*, Phys. Rev. C, **79**, 055501, 2009.

[Sim13] F. Simkovic *et al.*, *Neutrinoless double beta decay and double beta decay nuclear matrix elements, quasiparticle random-phase approximation, and isospin symmetry restoration*, Phys. Rev. C, **87**, 045501, 2013.

[Smi99] S.W. Smith, *The Scientist and Engineer's Guide to Digital Signal Processing*, 2nd ed., California Technical Publishing, San Diego (California), 1999.

[Smo10] A. Smolnikov and P. Grabmayr, *Conversion of experimental half-life to effective electron neutrino mass in $0\nu\beta\beta$ decay*, Phys. Rev. C, **81**, 028502, 2010.

[Suh98] J. Suhonen and O. Civitarese, *Weak-Interaction and Nuclear-Structure Aspects of Nuclear Double Beta Decay*, Phys. Rep., **300**, 123-214, 1998.

[Suh10] J. Suhonen and O. Civitarese, *Effects of orbital occupancies and spin-orbit partners on 0 nu beta beta-decay rates*, Nucl.Phys. A, **847**, 207-232, 2010.

[Tar12] M. Tarka, *Studies of Neutron Flux Suppression from a γ-ray Source and the GERDA Calibration System*, PhD thesis, University of Zürich, 2012.

[Ver12] J. D. Vergados, H. Ejiri, and F. Simkovic, *Theory of neutrinoless double-beta decay*, Rep. Prog. Phys., **75**, 106301, 2012.

[Vol12] O. Volynets, *Methods to improve and understand the sensitivity of high purity germanium detectors for searches of rare events*, PhD thesis, University of Munich, 2012.

[Vos07] H. Voss *et al.*, *TMVA, the Toolkit for Multivariate Data Analysis with ROOT*, Proc. of Sci., PoS (ACAT), 040, 2007.

[Wan09] W. Wang *et al.* for the DAYABAY Collaboration, *The hunt for θ_{13} at the Daya Bay nuclear power plant*, arXiv:0910.4605v1, 2009.

[Weg14] A.C. Wegmann, *Title unknown*, PhD thesis, University of Heidelberg, 2014.

[Wei67] S. Weinberg, *A Model of Leptons*, Phys. Rev. Lett., **19**, 1264-1266, 1967.

[Wei02] C. Weinheimer for the KATRIN Collaboration, *KATRIN, a next generation tritium β decay experiment in search for the absolute neutrino mass scale*, Progress in Particle and Nuclear Physics, **48**, 141-150, 2002.

[Wil12] J.F. Wilkerson *et al.*, *The MAJORANA DEMONSTRATOR: A Search for Neutrinoless Double-beta Decay of Germanium-76*, J. Phys. Conf. Ser., **375**, 042010, 2012.

[Wil38] S.S Wilks, *The Large-Sample Distribution of the Likelihood Ratio for Testing Composite Hypotheses*, Ann. Math. Statist., **9**, 60-62, 1938.

[Wol78] L. Wolfenstein, *Neutrino oscillations in matter*, Phys. Rev. D, **17**, 2369-2374, 1978.

[Wu57] C.S. Wu *et al.*, *Experimental Test of Parity Conservation in Beta Decay*, Phys. Rev., **105**, 1413-1415, 1957.

[Zav12] L. Zavarise *et al.*, *Off-line data quality monitoring for the GERDA experiment*, J. Phys. Conf. Ser., **375**, 042028, 2012.

Danksagung

An dieser Stelle möchte ich die Gelegenheit nutzen all denjenigen Personen zu danken, die mich während meiner Promotionszeit unterstützt und auf vielfältige Art und Weise zum Gelingen dieser Arbeit beigetragen haben. Mein besonderer Dank gilt...

- Herrn Prof. Dr. Werner Hofmann für die freundliche Aufnahme in seine Arbeitsgruppe, die interessante Themenstellung sowie die Möglichkeit auf dem Gebiet der Teilchenphysik innerhalb eines so spannenden Projektes wie dem GERDA Experiment aktiv mitarbeiten zu können.

- Herrn Prof. Dr. Norbert Herrmann für die freundliche Übernahme des Zweitgutachtens dieser Arbeit.

- Dr. Bernhard Schwingenheuer für seine tatkräftige Unterstützung, seine wertvollen Ratschläge sowie seine fortwährende, unermüdliche Hilfe. Durch sein umfassendes Wissen, die langjährige Erfahrung und den gewissen "Blick fürs Wesentliche" konnte er in den entscheidenden Momenten der vergangenen Jahre stets wichtige Impulse für den Fortschritt dieser Arbeit setzen. Die unzähligen Diskussionen im Büro, in der Kaffeeecke oder aber auf den Autofahrten nach Gran Sasso haben Richtung und Inhalt meiner Promotion entscheidend geprägt. Für all das sowie für die sorgfältige Durchsicht und die kritischen Kommentare in den letzten Wochen des Zusammenschreibens bin ich Ihm zu großem Dank verpflichtet!

- Dr. Thomas Kihm für seine enorme Hilfsbereitschaft mit der er mich unter seine Fittiche genommen hat und sein unentwegter softwaretechnischer Beistand. Erst anhand seines rastlosen Engagements im Wechselspiel mit einer schier endlosen Begeisterung konnte so manches mal "Unmögliches" möglich gemacht werden. Insbesondere möchte ich mich daher bei Ihm für sein stets offenes Ohr und die Gespräche - ob programmierbezogen oder aber auch fernab der Arbeit - bedanken, die ich in keinster Weise missen möchte und durch die ich viel lernen und neue Ansichten gewinnen konnte.

- Meinen Büro-Kollegen Prof. Dr. Konrad Bernlöhr sowie Dr. Raquel de los Reyes López für die angenehme Atmosphäre und die vielen anregenden Diskussionen, die mich immer wieder im alltäglichen Arbeitsablauf neu motiviert haben. Ebenso möchte ich mich bei Dr. Markward Britsch, Dr. German Hermann, Andreas Hillert, Dr. Joachim Hahn, Prof. Dr. Karl-Tasso Knöpfle und den vielen anderen GERDA-H.E.S.S.-LHCb-CTA-übergreifenden wissenschaftlichen Mitarbeitern aus dem Bothe-Labor für die unzähligen kürzeren oder

längeren Gespräche auf dem Flur, in der Küche oder bei Kaffee-und-Kuchen bedanken aus denen ich stets neuen kreativen Input schöpfen konnte.

- Ruth Crespo, der guten Seele der Abteilung, dafür, dass sie mir so viel administratives "Drum herum" (wie z.B. Visumsangelegenheiten, Reisekostenanträge oder -abrechnungen, Zugansberechtigungen für IT, etc.) abgenommen hat, und ich mich dadurch auf meine Arbeit fokussieren durfte. Danke auch insbesondere für Ihre freundliche, herzliche Art mit der sie täglich im großen Maße zum harmonischen Zusammenhalt in der Arbeitsgruppe beiträgt.

- Prof. Dr. Manfred Lindner, seinem Arbeitskreis und Anja Bernheiser auf der anderen Seite des Instituts im Gentner-Labor bei denen ich mich immer als "adoptiertes" Gruppenmitglied fühlen durfte. Hierbei dürfen einige Namen natürlich keinesfalls unerwähnt bleiben: Dr. Mark Heisel, Marco Salathe, Victoria ("Vici") Wagner, Anne Wegmann, Dr. Werner Maneschg und Dr. Alexey Lubashevskiy mit denen ich im Laufe der letzten Jahre sowohl auf unzähligen Dienstreisen, im Labor, oder während der Mittagspausen als auch so manches Mal außerhalb des Instituts bei geselligen Abenden eine wunderbare Zeit verbringen durfte und deren Unterstützung ebenfalls weitgehend zum Erfolg dieser Arbeit beigetragen hat.

- Der gesamten GERDA Kollaboration, welche sich aus der Begeisterung für die Physik heraus gebildet und auf dem gemeinsamen Bestreben zahlreicher Personen basiert. Ohne den Beitrag eines jeden Einzelnen währe ein solch großes experimentelles Unterfangen - und darin involviert auch diese Arbeit - niemals möglich gewesen.

Zum Schluss gilt mein ganz besonderer Dank meiner Familie, im Speziellen meinen Eltern und Großmüttern, die mir dieses Studium erst ermöglicht und meine Wahl immer unterstützt haben. Ihre Erziehung, bedingungslose Liebe und Vorbild haben mich seit jeher geprägt und mir schlußendlich zu all dem verholfen was ich in meinem Leben erreichen durfte. Gleichzeitig danke ich auch Dir, Henrik. Danke dafür, dass Du immer an mich gelaubt und in allen Phasen meines Studiums sowie der Doktorarbeit gefördert hast. Du hast mich motiviert, wenn ich motiviert werden musste und schaffst es darüber hinaus mit Deiner Art am Ende doch immer die richtigen Worte zu finden, mir an jedem einzelnen Tag das Gefühl zu geben etwas Besonderes zu sein.